Metabolite Mapping of the Human Brain at 9.4T

Dissertation

zur Erlangung des Grades eines
Doktors der Naturwissenschaften

der Mathematisch-Naturwissenschaftlichen Fakultät
und
der Medizinischen Fakultät
der Eberhard-Karls-Universität Tübingen

vorgelegt
von

Sahar Nassirpour
aus *Teheran*, *Iran*

June - 2018

Tag der mündlichen Prüfung: .....

Dekan der Math.-Nat. Fakultät: Prof. Dr. W. Rosenstiel
Dekan der Medizinischen Fakultät: Prof. Dr. I. B. Autenrieth

1. Berichterstatter: Prof. Dr. Anke Henning

2. Berichterstatter: Prof. Dr. Fritz Schick

Prüfungskommission: .....

.....…

.....…

.....…

Erklärung / Declaration:

Ich erkläre, dass ich die zur Promotion eingereichte Arbeit mit dem Titel:

„…….…….…….....

.....….....….“

selbständig verfasst, nur die angegebenen Quellen und Hilfsmittel benutzt und wörtlich oder inhaltlich übernommene Stellen als solche gekennzeichnet habe. Ich versichere an Eides statt, dass diese Angaben wahr sind und dass ich nichts verschwiegen habe. Mir ist bekannt, dass die falsche Abgabe einer Versicherung an Eides statt mit Freiheitsstrafe bis zu drei Jahren oder mit Geldstrafe bestraft wird.

I hereby declare that I have produced the work entitled "……", submitted for the award of a doctorate, on my own (without external help), have used only the sources and aids indicated and have marked passages included from other works, whether verbatim or in content, as such. I swear upon oath that these statements are true and that I have not concealed anything. I am aware that making a false declaration under oath is punishable by a term of imprisonment of up to three years or by a fine.

Tübingen, den ....

Datum / Date Unterschrift /Signature

Abstract

Proton magnetic resonance spectroscopic imaging (^{1}H MRSI) is a powerful technique for mapping the spatial distribution of metabolites in the human body, essentially, allowing researchers and clinicians to perform "virtual biopsy" in a non-invasive manner. These metabolite maps can provide sensitive markers of disease and injury, or can be used to provide insight into the neurochemical processes of the brain. ^{1}H MRSI, therefore, has great potential for clinical diagnostics, as well as biomedical and neuroscience research.

Perhaps the greatest hindrance to the application of MRSI in research and clinics is the time-consuming nature of such experiments. Even though acquiring reliable MRSI data with high spatial resolution and more tissue coverage is desirable for answering many neuroscientific or clinical questions, this comes at the price of even more prolonged scan times.

Compared to lower field strengths, MRSI at ultra-high field strengths has the advantage of higher signal-to-noise-ratio (SNR) as well as increased spectral resolution. These advantages enable the quantification of more metabolites with greater accuracy in the brain. Furthermore, some of the additional SNR can be traded off for shorter scan times through acceleration techniques. However, to be able to benefit from these advantages at ultra-high fields, there are many technical challenges that should be overcome.

The focus of this thesis is, therefore, to develop acquisition sequences, image reconstruction methods, and acceleration techniques to overcome these challenges and enable high resolution whole brain metabolic imaging in the human brain by magnetic resonance spectroscopic imaging at 9.4T. In doing so, we hope to bring metabolic imaging through ^{1}H MRSI one step closer to clinical practice.

Contents

List of Figures

1 Synopsis

1.1 Introduction

Magnetic resonance imaging (MRI) is a non-invasive medical imaging modality that enables the acquisition of high quality images with excellent soft-tissue contrast. The underlying principle of MRI lies in the interaction of matter with electromagnetic radiation. The proton nucleus (^{1}H) is the most commonly used nucleus in MRI due to its high sensitivity and natural abundance (in humans and animals). For imaging, the total signal from the protons in water is used to form the image. However, nuclei of the same element in different molecules experience different chemical environments. This, in turn, results in slightly different resonant frequencies, albeit small in amplitude. MR spectroscopy is a sub-branch of MR imaging that attempts to measure these smaller resonances. Although MR spectroscopy with other nuclei (such as carbon and phosphorous) is possible, proton spectroscopy dominates the field. The scope of this thesis is limited to proton (^{1}H) spectroscopy.

The advantage of spectroscopy[1] is that it allows us to detect several different metabolites and their concentrations *in vivo* while keeping the tissue intact. However, since the metabolite resonances are much smaller (in fact, orders of magnitude smaller) than the dominating water resonance peak, detecting these metabolites reliably and accurately is challenging. Fortunately, recent advances in hardware and MR technology have considerably improved the sensitivity of spectroscopy. Better radio frequency (RF) coils and higher field strengths, particularly the introduction of ultra high field strength (UHF) MRI scanners, give MR spectroscopy a hopeful future. Ultra high field strengths (7T and higher) offer much higher signal-to-noise ratio (SNR). In fact, the SNR increases super-linearly with the field strength [1]. Additionally, the higher spectral resolution as a result of the higher field strength, allows us to better separate the resonance peaks.

So far the majority of MR spectroscopy studies have often been conducted as single voxel spectroscopy (SVS). This means that a single spectrum is usually acquired from a specific

[1] In the remainder of this thesis, the term "spectroscopy" refers to "^{1}H MR spectroscopy" and will be used interchangeably.

voxel in the region of interest (ROI). This is largely due to the fact that the required scan time for measuring a single voxel is rather short and high SNR data can be acquired from rather large voxels in a reasonable scan time. Since historically, the inherent low SNR of spectroscopy required multiple averages of the signal, this meant that multi-voxel spectroscopy imaging was deemed to be too time-consuming. Nevertheless, magnetic resonance spectroscopic imaging (MRSI) or chemical shift imaging (CSI) is slowly drawing attention in the MR community.

MRSI acquires a spectrum from each voxel in the imaging region, in this way, giving us both spatial and spectral information from the tissue at hand. It goes without saying that the advantage of MRSI over SVS is that it covers a much larger area and allows us to see full images rather than a single spectrum. However, the required scan time for MRSI is much more than SVS, since spectra from multiple voxels are being acquired. It can be argued that the reason for a renewed interest in MRSI is largely due to the introduction of UHF MRI scanners. The higher SNR provided by UHF MRI scanners results in better spectral quality and more reliable quantification of a larger number of metabolites. Some of this additional SNR can be traded off for more spatial resolution (smaller voxels) and shorter scan times (acceleration).

The goal of this thesis is to advance spectroscopic imaging methodology at ultra-high fields towards high resolution and whole-brain metabolite mapping in the hopes of eventual common-place use in clinics. The acquisition and data processing techniques used for overcoming the technical challenges at UHF to enable the acquisition of high resolution MRSI data at UHF, specifically 9.4T, is described further in section 1.2.

Perhaps the biggest drawback of MRSI is the long scan duration that is required. This is often the reason that makes this modality less attractive for clinical applications. The reason that MRSI is more difficult to accelerate than other MR imaging applications is, once again, attributed to the lower available SNR. 3D sequences can offer more SNR than 2D sequences, however, the application of 3D sequences is more challenging at UHF due to static (B_0) magnetic field and radio frequency field (B_1) inhomogeneities. Furthermore, due to B_0 inhomogeneities, dynamic slice-wise shim updating is an attractive method for improving the shim quality. However, this technique only works for 2D multi-slice sequences.

The focus of this thesis is on 2D sequences for this reason, even though multi-band [2] and 3D sequences such as EPSI [3] could potentially offer more acceleration[2]. Therefore, the scope of this thesis is limited to in-plane acceleration.

Aside from the low SNR, another challenge that arises in accelerating MRSI data from the human brain, is the lipid signal originating from the subcutaneous lipid region that is orders of magnitudes larger than the metabolites of interest within the brain. This causes a problem for parallel imaging methods such as SENSE [4] and GRAPPA [5] that result in structured aliasing artifacts, as the aliased lipids can be hard to resolve and any small unresolved trace of the aliasing will completely overshadow the metabolites of interest. Naturally, lipid suppression or outer volume suppression pulses can be employed to reduce the lipid signal strength, but this would again drastically lengthen the scan duration. Outer volume suppression schemes are lengthy in nature due to the many pulses required, in contrast lipid suppression usually require only one or two inversion pulses (single and double inversion recovery, respectively). However, at UHF, the specific absorption rate (SAR) requirements for adiabatic inversion pulses typically used for lipid suppression is much more demanding and result in long repetition times (TR) due to safety concerns. We investigated an alternative low-SAR inversion pulse using a single inversion recovery scheme for lipid suppression in [6]. However, we concluded that there is a trade off between the achieved lipid suppression factor and the length of TR, which in the end proved not to be beneficial for the overall achieved acceleration factor. Another major drawback of this type of global lipid suppression is that they will also suppress the lipids in pathologies (e.g. tumors, necrosis) which would otherwise be valuable information in the spectral content.

With this in mind, this thesis focused on in-plane acceleration of multi-slice 2D phase-encoded MRSI data from the brain with neither lipid suppression nor outer volume suppression. Conventional parallel imaging methods such as SENSE and GRAPPA were improved upon and tailored for this application with a focus on controlling the artifacts. This is de-

[2]It should also be noted that sequences such as EPSI require large gradient strengths and slew rates. At UHF, these requirements are even greater and exceed what the hardware of most scanners can provide. This is due to the fact that the required spectral bandwidth is much larger at higher field strengths, and, therefore, there is very little time between the sampling points for the gradients to change. The limitations of EPSI are further discussed in the appended publications.

scribed in further detail in section 1.3. We also investigated the compressed sensing approach for acceleration utilizing the concept of sparsity and random undersampling, which is also described further in section 1.3. Our findings showed that after optimizing, an acceleration factor of 4 was easily feasible for all of these acceleration/reconstruction methods, despite the presence of the unsuppressed lipid signals. However, some of the investigated methods could achieve an even higher in-plane acceleration factor.

Although the absolute quantification of metabolite concentrations is outside the scope of this thesis, three aspects relating to quantification are addressed here. As mentioned before, the small resonances of metabolites are usually overshadowed by the large water resonance peak. Therefore, water suppression is often employed to enable the detection of the metabolites. Water suppression schemes typically excite a narrow bandwidth around the water peak and use spoiler gradients to de-phase the signal, thereby, reducing the effective water signal. For better suppression, additional excitation pulses and spoiler gradients can be used [7]. However, there has been evidence that water suppression pulses may result in chemical exchange, and therefore alter the detected concentrations of the metabolites that undergo chemical exchange [8, 9, 10]. Although not a common method, non-water suppressed spectroscopy is a feasible alternative. The problem with non-water suppressed spectroscopy, besides the large water peak, is the gradient modulation side-bands artifacts that become more prominent. Gradient modulation side bands occur as spurious peaks in the spectra due to mechanical vibrations of the gradient coils [11]. In water suppressed MRSI, these artifacts are less problematic. However, in non-water suppressed MRSI these resonances can cause severe problems and hinder the accurate quantification of some of the metabolites of interest. Nevertheless, non-water suppressed MRSI is still possible with methods such as metabolite-cycling [12, 13]. This method is discussed in more detail in section 1.4.1. Eventually, this methodology allows us to study the effects of chemical exchange resulting from water suppression.

Next, we looked at the macromolecules and how they affected the quantification of the metabolite signals. Due to the ultra short echo times of the sequences used in our studies, the macromolecular signals are large, and contribute greatly to the acquired spectra. The

findings of this investigation can be found in conference proceedings and are described in more detail in section 1.4.

Lastly, we present a method for very high acceleration of a water reference spectroscopic image. One of the common methods for spectroscopy quantification is to use an internal water reference. However, this means that the MRSI scan needs to be repeated once more without the water suppression pulses. This doubles the scan time required for an MRSI study. To reduce the required scan time, a low resolution water reference is typically acquired (usually a resolution of 2x2 lower than the MRSI data). However, in this thesis we present a method for even higher acceleration of the water reference which retains the original spatial resolution and can be used for eddy current correction and internal water referencing (section 1.4).

A disadvantage of MRSI over SVS is that achieving a homogeneous magnetic field over a large region is more difficult. Inhomogeneities in the static (B_0) magnetic field result in multiple problems. Image distortion and signal dropouts are some problems that occur, not only for MRSI but also for MRI [14, 15]. For spectroscopy, poor B_0 homogeneity also leads to line-broadening of the spectral peaks which make quantification less reliable. In addition, any spectrally selective RF pulses, such as water suppression pulses, are affected by the shift in the central water frequency which can cause undesirable effects. At this point, it is also worth noting that although ultra high field strengths have much higher SNR, the magnetic field is also more inhomogeneous due to larger B_0 susceptibility effects. Improved B_0 homogeneity can be attained using slice-wise dynamic shim updating rather than whole-volume static shimming [16, 17, 18]. However, this method is only applicable to 2D multi-slice sequences where each slice can be individually shimmed. In `Publication 7` we further investigated the effects and limitations of B_0 shimming on metabolite mapping using both a very high order spherical harmonics B_0 shimming system and a dedicated multi-coil setup.

At last, we reach the final goal of this thesis, that is: metabolite mapping of the whole brain at UHF. In `Publication` 7, we present metabolite maps for the whole brain acquired at 9.4T. Many of the methods presented in the thesis culminated to this point and were utilized in the final metabolite maps. In particular, dynamic B_0 shimming was used to acquire all the data to ensure sufficiently good B_0 homogeneity; a modified GRAPPA (as described in 1.3.3)

was used to acquire the accelerated MRSI data; the water reference was acquired using very high acceleration (as described in 1.4.3) and finally the data were processed and fit using the methods described in the first publication presented in this thesis.

We present for the first time, arguably, the best whole brain metabolite maps acquired from healthy volunteers utilizing the advantages offered by a 9.4T field strength. We hope that, in doing so, MRSI becomes not only feasible and practical for clinical use but also a more attractive imaging modality for neuroscience studies in general.

1.2 High and Ultra High Resolution Metabolite Mapping at Ultra High Field Strengths

As mentioned in the previous section, there are two main advantages of higher field strengths for spectroscopy: higher SNR and higher spectral resolution. To illustrate the benefits of ultra high field strengths, our first study investigated the feasibility of a free induction decay (FID) MRSI [19, 20] for ultra high resolution single slice spectroscopic imaging at 9.4T. In this study, a slice-selective ultra-short echo time (TE) and ultra-short repetition time (TR) ^{1}H FID MRSI sequence without lipid suppression and without outer volume suppression (OVS) was used. Lipid suppression and OVS were omitted to keep the TR short (TR=220ms) which in turn kept the scan duration short. Another advantage of the FID sequence is that it makes it possible to use ultra-short TEs (TE=1.56ms) which means that the SNR loss due to T_2 relaxation is minimal. This makes more metabolites detectable compared to sequences with longer TEs. Furthermore, since only a slice selection is used for localization, there is no in-plane chemical shift displacement.

In `Publication 1`, two spatial resolutions were used for metabolite mapping: a voxel size of 97 μL (3.12x3.12x10 mm^3) and 24.3 μL (1.56x1.56x10 mm^3) which corresponded to in-plane matrix sizes of 64x64 and 128x128, respectively. A custom numerically optimized water suppression scheme was used. It consisted of 3 pulses and the flip angles were optimized to be robust against a B_1^+ inhomogeneity range of 50% to 150%. The residual water peak was less than 1% on the whole slice. An automatic post-processing pipeline was developed which included steps such as automatic eddy current correction, zero and first order

phase correction, as well as residual water removal and retrospective lipid removal using L2 regularization [21]. The final spectra were fit using LCModel [22] with a basis set simulated using the PyGAMMA library [23].

We showed that 12 metabolites (NAA, NAAG, Cho (PCh + GPC), tCre (PCr + Cr), mI, Glu, Gln, GABA, GSH, Tau, Scyllo, and Asp) could be reliably mapped with a resolution of 97 µL. The reproducibility was shown by repeating the scan on multiple subjects. Significant gray/white matter contrast that corresponded to the underlying anatomical structure could be observed in the metabolite maps (e.g. tCho, GSH, Glu, Gln, mI, NAAG). Similar contrasts can be seen for the higher resolution of 24.3 µL. Although higher spatial resolution can be discerned in these maps, the robustness of the fits was less reliable than for the 97 µL resolution. Higher spatial resolution means that the voxels are smaller and hence have less SNR. The reduced SNR results in less reliable fits. Figure 1 shows some of the metabolite maps for the two resolutions. The quality of these maps is unmatched compared to what is currently published in the literature. This is largely due to the higher field strength (9.4T) used in this study.

This study served two purposes: 1) to outline the necessary data acquisition and post-processing steps required for reliable metabolite mapping at UHF and 2) to illustrate the quality of high and ultra-high resolution metabolite maps that can be obtained using a 9.4T MRI scanner in a reproducible manner.

1.3 Acceleration

Perhaps the biggest drawback to MRSI is the long scan duration that are required. In light of this, we investigated multiple acceleration methods for use at UHF MRI scanners. For reasons discussed earlier, the focus was only put on in-plane acceleration methods. Undersampling was not performed in the time domain but only in the k-space domain. This is largely due to the fact that undersampling the time domain is typically done by moving to another point in k-space from sample to sample (therefore undersampling simultaneously in time and one k-space direction), however, the gradient slew rates required for this is much higher at UHF

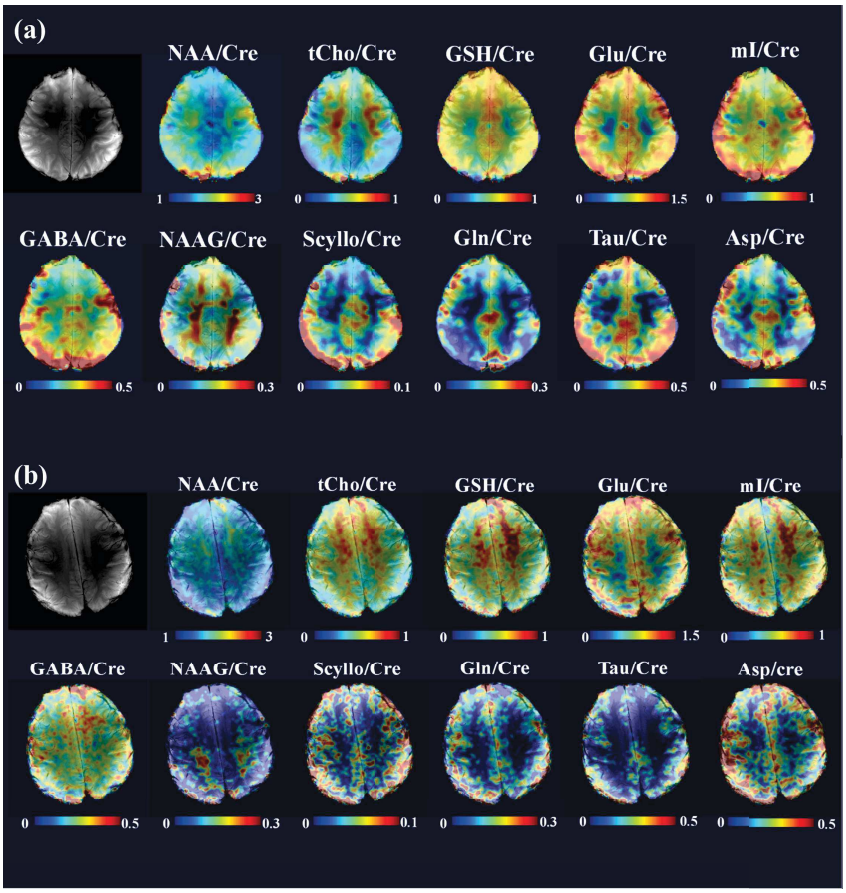

Figure 1: Representative ratio metabolite maps (/Creatine) acquired at high (a) and ultra-high (b) spatial resolutions at 9.4T. The nominal voxel size is 97 μL and 24.3 μL, respectively.

scanners[3]. In contrast, undersampling in k-space could be achieved relatively easily since both k-space directions were phase encoded and any of the sample points could be dropped.

1.3.1 Compressed Sensing

MR signals are sparse by nature, this means that much of the contained information is compressible. One can exploit this concept to only partially acquire the MR signal and recover the full image using sparse reconstruction techniques. This is the underlying concept behind acceleration through sparse sampling. Compressed sensing [24] is one such method that has proven to be a promising acceleration technique in the MR imaging community. Compressed sensing utilizes two principles to reconstruct the missing k-space points: 1) random undersampling and 2) sparsity of information. The random undersampling in k-space results in noise-like aliasing artifacts, as opposed to the structured aliasing artifacts in parallel imaging methods such as sensitivity encoding (SENSE) [4] or the generalized auto-calibrating partially parallel acquisition (GRAPPA) [5] (Figure 2). Secondly, the data is assumed to be sparse and therefore by enforcing sparsity constraints on the data, the missing k-space points can be reconstructed.

However, compressed sensing has not been used extensively in spectroscopic imaging applications. Using compressed sensing for MRSI is difficult because the SNR is much lower than for regular imaging. The SNR needs to be sufficiently high for the peaks of interest to be resolved from the noise-like aliasing artifacts. In addition, finding a good sparsity transform for the overlapping spectral peaks for proton spectroscopy in the frequency domain can be difficult. For x-nuclei spectroscopy on the other hand, the spectral peaks are better separated and hence more sparse in the frequency domain. This allows the data to be better compressed in the frequency domain. Therefore, most applications of compressed sensing in spectroscopy have been for x-nuclei [25, 26, 27].

We implemented compressed sensing at UHF for non-lipid-suppressed ^{1}H MRSI data by randomly undersampling k-space and tailoring a sparse reconstruction algorithm to the

[3]The gradient slew rates need to be higher because the sampling frequency of the ADC needs to be higher at UHF to cover the larger frequency range of interest. Therefore, there is less time between the sample points of the ADC to move to a different location in k-space.

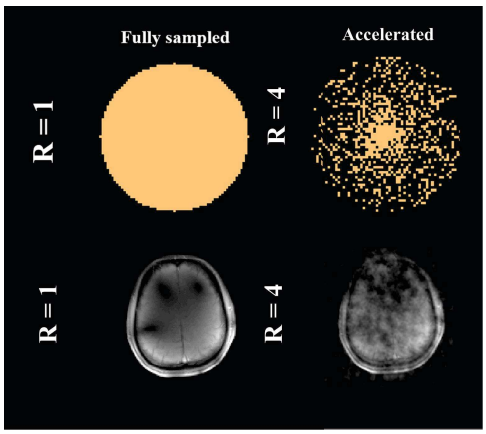

Figure 2: Effect of random undersampling: if the k-space is undersampled in a random manner, the aliasing artifacts will be noise-like. The k-space masks of the fully sampled (right) and the randomly undersampled case with an effective acceleration factor of R = 4 (left) are shown in the top row. All k-space masks include the elliptical shuttering. The light orange color marks the k-space points that are acquired. The bottom row shows the resulting brain images.

problem at hand. By taking advantage of the higher SNR of UHF, we could achieve better reconstruction for high acceleration factors. In `Publication 3`, we showed that reconstruction could only be achieved by coil-combining the data in the image domain and applying a sparsity minimization optimization. Performing a coil-by-coil reconstruction did not provide enough SNR for the reconstruction to be successful. Sparsity was minimized in the image domain using a 2D wavelet transform and was also minimized in the image and time domain using a 3D total variation. Data consistency was enforced in the k-space domain. The minimization problem was thus:

$$\min_x \|F_u x - y\|_2 + \lambda_1 \|\Psi x\|_1 + \lambda_2 \|TV(x)\|_1$$

Where F_u is the undersampled Fourier transform, y is the measured k-space data (used for enforcing data consistency), Ψ is the 2D wavelet transform in the two spatial dimensions, TV is the 3D total variation, and λ_1,λ_2 are tuning parameters that were optimized and found to be 0.001 and 0.003, respectively. A conjugate gradient descent algorithm was used for

the reconstruction. Further details of the reconstruction can be found in `Publication 3`. Random variable density masks were used to undersample the k-space data and different acceleration factors were investigated. The post-processing and fitting steps were the same as described in section 1.2 and `Publication 1`.

Indeed, we could achieve reasonable metabolite maps using acceleration factors of R=4 or 5. As the acceleration increased, the maps became noisier. The higher noise level was due to the lipid signals from the subcutaneous fat that could not be properly resolved and since the undersampling resulted in noise-like aliasing, this resulted in noise in the fitted metabolite maps. In `Publication 3`, we also looked at a low-rank method that enforces sparsity in the k-space domain (SAKE [28])and obtained similar results to compressed sensing. However, the reconstruction time for the SAKE method was an order of magnitude longer than compressed sensing, and hence compressed sensing was deemed to be the more practical option. High resolution metabolite maps obtained from compressed sensing with an acceleration factor of R=5 (scan time ~ 3 minutes for a single slice) are shown in Figure 3.

1.3.2 SENSE Revisited

One of the most common approaches for acceleration in the MR community is parallel imaging. Essentially, in parallel imaging, the localized receive coil sensitivity profiles are used as an extra spatial encoding technique. Using prior knowledge about the sensitivity profiles, the k-space is only partially sampled during the acquisition, and the missing k-space points are later filled in. One such technique for filling the missing points in k-space is SENSE [4]. When k-space is undersampled in a Cartesian manner, the aliasing artifacts appear as repeated versions of the image overlaying the actual signal in a shifted manner (Figure 4). The reconstruction problem in this case reduces down to resolving the aliased versions of the image from the actual underlying signal. With SENSE, explicit knowledge of the coil sensitivity profiles are used to solve the system of linear equations to unalias the image.

Conventional algorithms used for solving SENSE equations [4] are usually able to resolve the aliasing artifacts to an acceptable level for moderate in-plane acceleration factors. Depending on the RF coil geometry, noise amplification can become problematic as the accel-

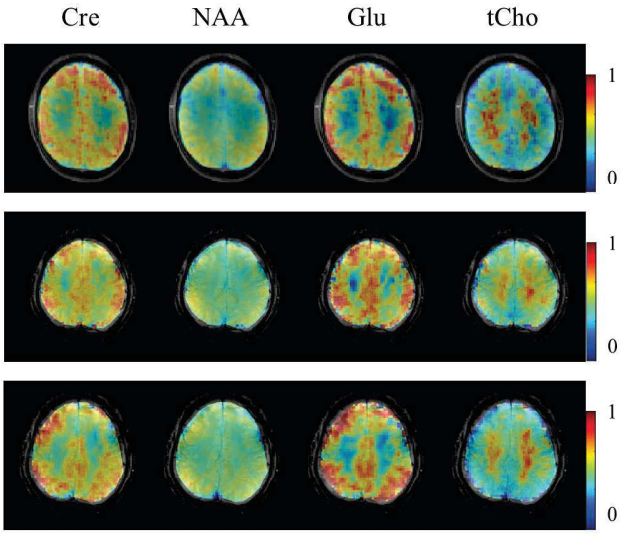

Figure 3: High resolution (in-plane matrix size of 64x64) metabolite maps of four major metabolites obtained using compressed sensing with an acceleration factor of R=5 (scan time of 3 minutes) from the brains of three healthy volunteers.

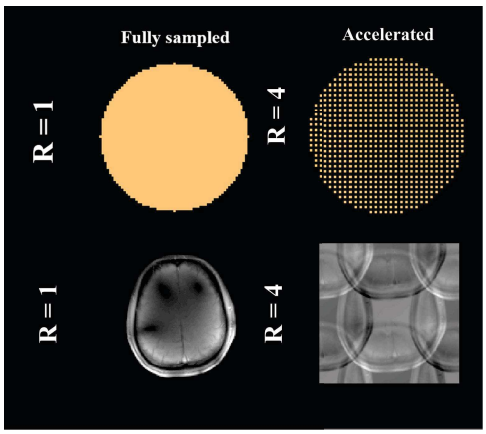

Figure 4: Effect of Cartesian undersampling: if the k-space is undersampled in a cartesian manner, the aliasing artifacts will be repeated versions of the image overlaying the actual signal. The k-space masks of the fully sampled (right) and the regularly undersampled case with an acceleration factor of R = 4 (left) are shown in the top row. All k-space masks include elliptical shuttering. The light orange color marks the k-space points that are acquired. The bottom row shows the resulting brain images.

eration factor increases. Apart from the lower available SNR in MRSI data, what makes the application of SENSE to non-lipid-suppressed ^{1}H MRSI challenging, is the presence of strong unsuppressed lipid signals originating from the subcutaneous lipid region near the skull. Any small traces of unresolved aliasing artifact (resulting from the ill-conditioning of the SENSE problem) which may be tolerable for other imaging applications, becomes a severe problem for non-lipid-suppressed MRSI quantification. The reason for this, is that the aliased signal stemming from the lipid region is orders of magnitude larger than the signal from inside the brain. This means that an improved and robust version of the SENSE reconstruction technique is necessary for this application.

Recently, Kirchner et al [29], presented an improved version of SENSE which includes solving a regularized optimization problem on an over-discretized spatial grid. Unaliasing the accelerated data in this manner accounts for sub-voxel coil sensitivity variations which helps with resolving the aliasing artifacts more efficiently. Furthermore, by directly controlling the shape of the spatial response function (SRF), the near- and far-reaching lipid bleeding

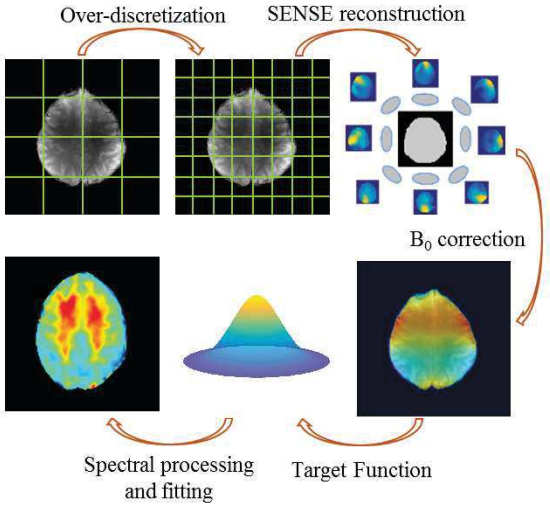

Figure 5: Reconstruction process shown in a clock-wise order: (1) original MRSI grid, (2) over-discretized MRSI grid achieved by zero-padding in k-space, (3) high resolution coil sensitivity maps used for SENSE reconstruction, (4) high resolution B_0 map used for frequency shift correction on a sub-voxel level, (e) target function used to combine voxels to go back to the original MRSI resolution, (f) resulting metabolite maps after spectral processing and fitting.

artifacts are minimized. In an intermediate step, a high resolution B_0 field map can be used to correct for intra-voxel frequency shifts. This will also decorrelate the noise covariance of the neighboring voxels, which in turn will result in a boost in SNR [30]. The process of this reconstruction technique is summarized in the schematic shown in Figure 5.

Given the advantages of this robust SENSE reconstruction technique, in this thesis we decided to investigate its benefits for accelerating non-lipid-suppressed and high resolution ^{1}H MRSI data. The performance of the algorithm (in terms of residual aliasing artifacts, the resulting SNR, and the accuracy of the metabolite maps) was compared to a conventional SENSE algorithm for different acceleration factors, the details of which can be found in `Publication` 4. As expected, compared to conventional SENSE, the over-discretized algorithm proved to be more efficient in resolving the lipid aliasing artifacts. In fact, up to an acceleration factor of four (R = 2x2) the aliasing artifacts were almost completely re-

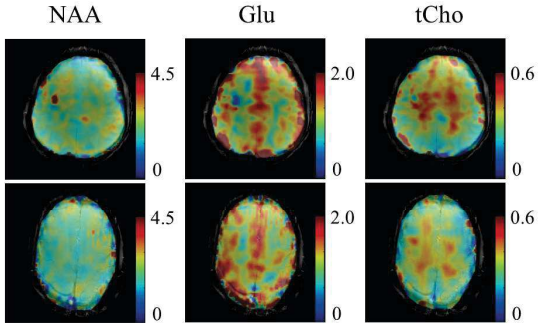

Figure 6: Accelerated (R=2x2) metabolite mapping using the over-discretized SENSE reconstruction at 9.4T: Ratio metabolite maps of three major metabolites (/Creatine) acquired from two healthy volunteers are shown.

solved. Additionally, an SNR boost of ~20% was observed for all acceleration factors when the over-discretized SENSE method is used. This enabled the reproducible acquisition of high resolution metabolite maps in 3.75 minutes (Figure 6). For any acceleration factor higher than two in any phase encoding direction, even the improved SENSE algorithm was not able to resolve all the lipid aliasing artifacts. This limits the highest in-plane acceleration factor achievable through this method. However, the SNR boosting technique used in this reconstruction method is a powerful tool that can be combined with other acceleration techniques to correct for intra-voxel frequency shifts and increase the SNR.

1.3.3 GRAPPA Revisited

GRAPPA [5] is another parallel imaging method that is commonly used for acceleration. Points in k-space are dropped in a regular Cartesian manner during acquisition and then filled in during the reconstruction process. In this way, SENSE and GRAPPA are solutions to the same acceleration problem. However, instead of using the explicit coil sensitivity profiles as the prior knowledge for reconstructing the missing points, GRAPPA directly fills in the missing k-space points by interpolating over the measured points with an optimized kernel. The relationship between the missing point and its neighboring measured point is approximately linear and can be predicted accordingly.

In order to estimate the linear relationship between the missing point and neighboring points, a calibration step needs to be performed. This calibration can be performed externally on a separately acquired image such as an anatomical image that is usually acquired in every study. The k-space data can be used to regress the relationship between the missing points and neighboring points. Alternatively, a region in k-space can be fully sampled and this fully sampled region can be used to calibrate for the kernel and then predict the missing points in the rest of the k-space[4].

In `Publication 5`, we explored GRAPPA to see if the reconstruction could be improved by reducing the aliasing artifacts. As mentioned previously, one of the most problematic aspects with accelerating non-lipid-suppressed ^{1}H MRSI is that subcutaneous fat signal is orders of magnitude larger than the metabolites of interest within the brain. Resolving the aliased lipids requires a robust method for predicting the missing k-space points. With this in mind, we investigated a machine learning approach using neural networks. The neural networks were trained on an anatomical image in the calibration phase. The networks were then used to predict the missing k-space points. We showed in the publication that training neural networks proved to be more robust than using the conventional linear regression method for GRAPPA.

Furthermore, to achieve even higher acceleration factors, we recognized the fact that the more important k-space information is in the center of k-space and that noise and higher spatial frequency information is encoded in outer k-space[5]. We defined different regions in k-space: 1) a center region that was fully sampled, 2) a mid-region that was undersampled at a factor of R=4, and 3) finally an outer region that was heavily undersampled at a factor of R=16. Different neural networks were trained for each region, the details of which can be found in `Publication 5`. The process of reconstructing the missing points is shown in Figure 7.

Our proposed method (called MultiNet PyGrappa) consisting of a combination of variable

[4]This is normally referred to as "self-calibration" because the calibration is performed on the same data that needs to be reconstructed.

[5]Note that this principle is often used in compressed sensing. Even though random undersampling is performed, the center of k-space is more densely sampled than outer k-space.

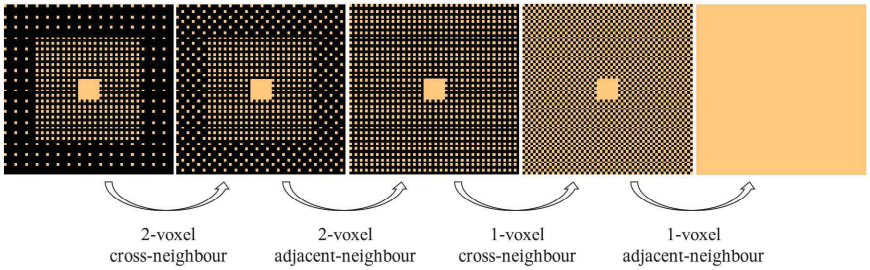

Figure 7: Step-by-step process of the proposed reconstruction technique is shown in this schematic. The missing kspace points are shown in black. Four different neural networks are trained: First, a 2-voxel cross-neighbour neural network fills in some of the missing points in the outer region of kspace. Then, a 2-voxel adjacent-neighbour is used to predict more of the missing points in the outer region so that now almost all of the kspace is undersampled by a factor of 2x2. Next, a 1-voxel cross-neighbor neural network is trained and used to fill in the central missing point in each small grid, and finally, a 1-voxel adjacent-neighbour fills in the rest of the missing points to form the reconstructed data.

density sampling and training multiple neural networks for reconstructing the missing k-space points, resulted in very high in-plane acceleration factors. In the article, we showed that acceleration factors of up to R=9 could be achieved with the resulting metabolite maps having good agreement with the fully sampled metabolite maps. Metabolite maps using this reconstruction are shown in Figure 8 for acceleration factors of R=7 and R=9. Therefore, the total scan duration for a k-space matrix size of 64x64 with R=7 was approximately 2.5 minutes. This is the fastest reported acquisition time (with TR = 300ms) achieved through in-plane acceleration.

1.4 On the Concerns of Quantification

As mentioned before, absolute quantification of the fitted metabolite maps is outside the scope of this thesis since it needs a comprehensive correction of $B_1{}^{+/-}$, coil loading effects, and T_1/T_2 relaxation times [31]. Nevertheless, some aspects of quantification were studied in this work. Firstly, we investigated chemical exchange effects due to water suppression pulses by performing non-water-suppressed MRSI. Next, we looked at the effect of the macromolecular

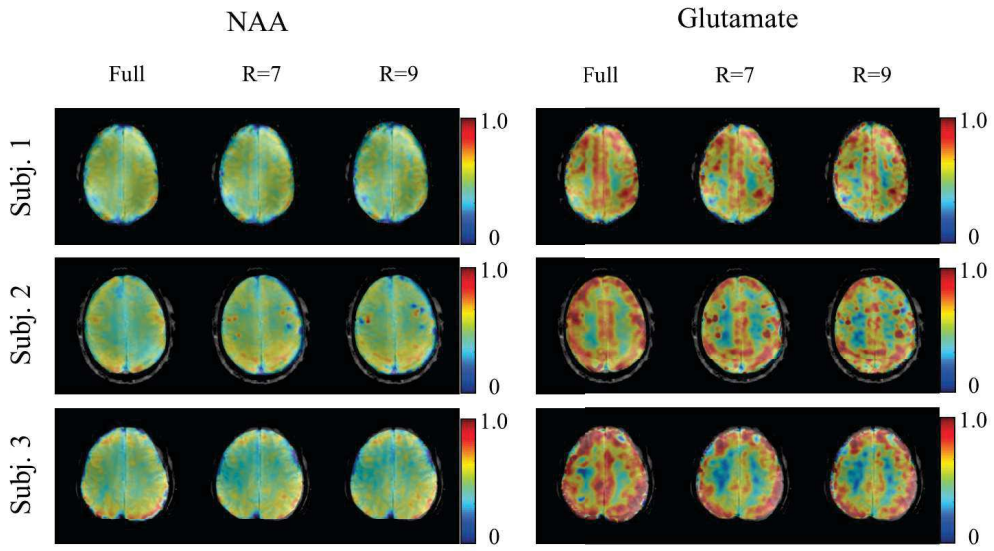

Figure 8: Accelerated (R=7 and R=9) metabolite mapping using the multiNet PyGRAPPA reconstruction at 9.4T: Metabolite maps of two major metabolites acquired from three healthy volunteers are shown. The fully sampled metabolite maps are also shown for comparison

baseline on the fitting of the spectra; i.e. how the macromolecule signals affect the accuracy and quantification of the metabolites. This is important because the FID MRSI sequence that was used throughout the study, used very short TE and TRs and hence the macromolecular baseline significantly affects the acquired spectra. Finally, we investigated the acceleration of water reference acquisition, which can be used for eddy current correction, as well as for quantification using internal water referencing [32].

1.4.1 Non-water Suppressed MRSI

Most MRS studies use water suppression pulses to reduce the water signal so that the water peak does not overshadow the smaller metabolite peaks. However, there is some interest in the community to investigate whether or not the water suppression pulses affect the spectra. Additionally, the simultaneous acquisition of water and metabolite signals is advantageous in that the water peak can be used for internal referencing in quantification as well as frequency shift and eddy current correction. Despite this, non-water suppressed spectroscopy is not commonly done because it introduces more challenges than water suppressed MRS. Firstly, the large water peak makes it difficult to sample the entire signal range unless a high resolution analog-to-digital converter (ADC) is available. Fortunately, with the advances in hardware, this problem is becoming less and less of a concern. Secondly, the large water peak is usually broad and overlaps with the metabolite peaks making it difficult to disentangle the metabolites from the water signal. Since the T_2^* relaxation time is typically lower at higher field strengths, the water peak is broader at UHF, which makes this even more problematic. Thirdly, the unsuppressed water peak results in large gradient modulation side-bands in the spectra [11]. The gradient modulation side-bands can lie on top of the metabolite signals and this can confuse the fitting algorithm. This being said, there have been methods developed to remove the gradient modulation side-band artifacts both prospectively and retrospectively.

In this thesis, we focused on prospective methods for removing gradient modulation side-bands. One such method is the metabolite cycling method [10, 13]. It involves alternately acquiring an inverted and non-inverted spectra. The inverted spectra are effectively inverted over the spectral range of the metabolites of interest. The two spectra can then be subtracted

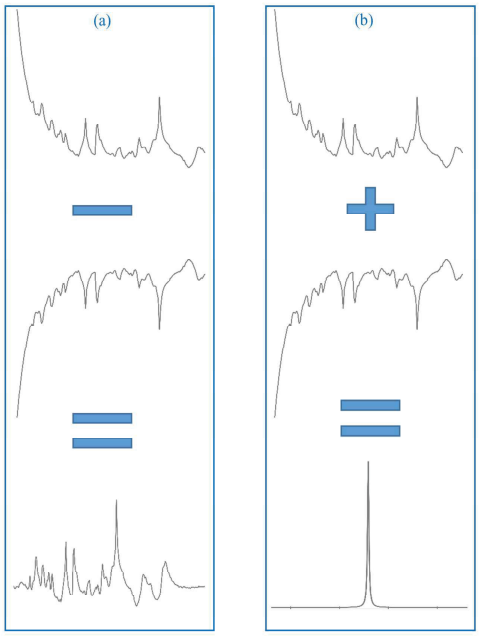

Figure 9: Schematic representation of metabolite cycling: (a) the inverted and non-inverted spectra are subtracted to retain only the metabolite signal. (b) the inverted and non-inverted spectra are added to retain only the water peak.

to retain only the metabolite signals (Figure 9) and in doing so the water peak as well as the gradient modulation side-bands are removed. By adding the two acquired spectra, the metabolite signals are canceled out, leaving the water peak which can be used as a reference.

Although metabolite cycling has been utilized in a number of studies for SVS, it has not been used much for spectroscopic imaging. Since inverted and non-inverted spectra need to be acquired, this makes the scan duration twice as long. Furthermore, at UHF, the adiabatic inversion pulse used in this method causes problems due to the strict SAR restrictions and thus sequences with very short TR are impossible to implement without exceeding the RF safety constraints. In `Publication 2`, we designed a low SAR adiabatic inversion pulse for metabolite cycling at 9.4T and 3T. This allowed us to study the effects of water suppression and if or how it differs from non-water suppressed MRSI.

In this study, we implemented a metabolite cycling scheme with FID MRSI for the first

time. A comparison of the water suppressed and non-water suppressed metabolite maps showed that there were significant differences in the concentration of creatine. There has been evidence in previous SVS studies that suggest that the measured concentrations of creatine may be affected by the water suppression pulses due to chemical exchange effects [8, 9]. Our findings also showed similar differences at 3T and 9.4T. The concentration ratio of creatine/NAA was approximately 0.1 higher for non-water suppressed MRSI at both field strengths.

1.4.2 Macromolecules

Due to the complex nature of macromolecules, very little is known about their properties and their regional differences. Therefore, simulating basis sets for the macromolecules is difficult, which makes their incorporation into the fitting routine for quantification purposes very challenging. Previous studies [33, 34, 35] have measured the macromolecular baseline by nulling the metabolite signals and thereafter used the measured baseline as part of the basis set in the fitting algorithm. This is sensible for single voxel spectroscopy, however, for spectroscopic imaging where there may be regional differences in the macromolecular content (e.g. differences between the macromolecular signals for white and gray matter), a single macromolecular baseline may not be the best approach. In [36] a single measured macromolecule baseline was used for fitting spectroscopic imaging data and differences between white and gray matter for the concentration of the macromolecular signal were found, thus, indicating that concentrations of macromolecules may differ for different regions. In addition to regional differences, there might be relaxation time differences between different macromolecular components in different tissue types. For sequences with ultra short TRs and TEs such as the ^{1}H FID MRSI sequence, this makes the use of a single macromolecular baseline even less justified. If different components of the macromolecular baseline relax at different rates, the shape of the macromolecule baseline will change depending on the TE and TR values. Taking all these factors into consideration, it seems like the best approach for the accurate quantification of our spectroscopic data is to have a model of different macromolecular components rather than a single measured baseline. Using this model, we can then also

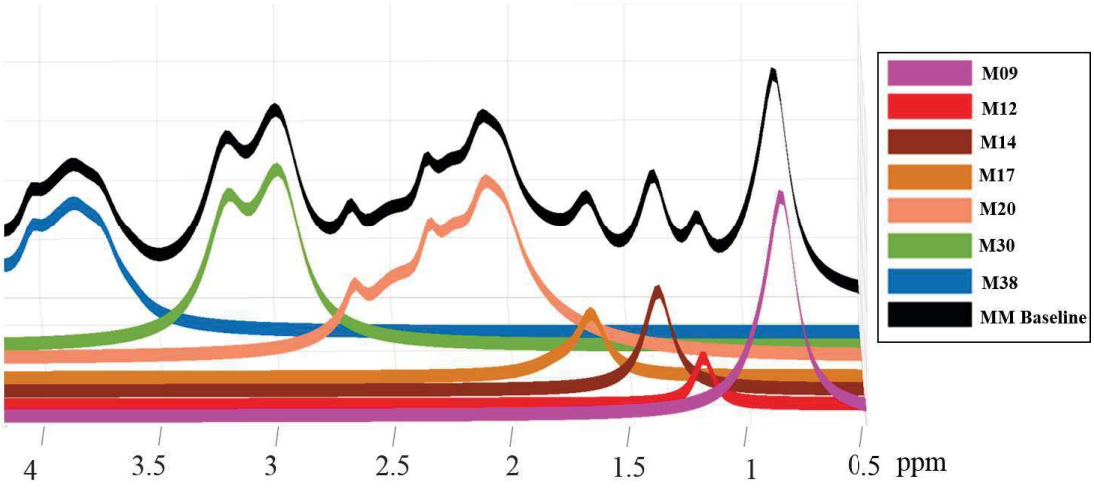

Figure 10: Different macromolecule components used to model the complex structure of the acquired macromolecule baseline (shown in black).

map different macromolecule components across the brain.

To this end, we first acquired a macromolecular baseline using the double inversion recovery (DIR) technique with wide-band, uniform rate, and smooth truncation (WURST) pulses, with a similar method as described in [36]. MRSI data with a moderate spatial resolution (in-plane matrix size of 32x32) was acquired since the high SAR of the WURST pulses required the repetition times to be very long (TR = 4550ms). It should be noted, that due to the high SAR at UHF, acquiring macromolecular baselines for the full MRSI matrix is infeasible as the scan duration would be much too long. The details of the pulse and sequence of the DIR are described in [37] (`Publication` 7 of section 2.2.2). We then parameterized the macromolecular baseline by fitting Lorentzian peaks to the spectra based on [38]. To prevent overfitting, we then combined highly correlated peaks to simplify the model. The resulting components of the macromolecular baseline were then incorporated into the basis set used for the fitting procedure and can be found in Figure 10.

By fitting the modeled macromolecular baseline to the high resolution MRSI data, we were able to map the spatial variations of the different components. These maps (shown in Figure 11) revealed regional differences in the concentration of different macromolecule com-

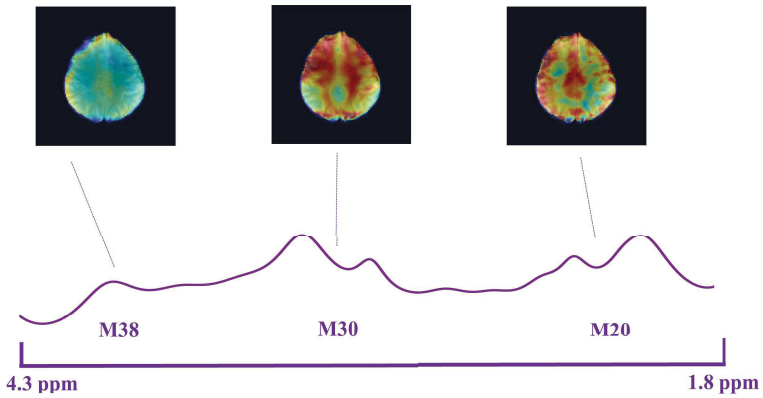

Figure 11: Maps of three individual macromolecule components obtained from the brain of a representative healthy subject by fitting the acquired spectroscopic imaging data with our modeled macromolecule basis set.

ponents. Furthermore, they showed that the gray/white matter contrast can vary between different macromolecule components.

In the next step, the parameterized model of the macromolecular baseline was fit to MRSI data acquired at different flip angles. In addition, due to $B_1{}^+$ inhomogeneity, the voxels of each MRSI dataset experienced a range of flip angles. This allowed us to estimate the T_1 relaxation effects by fitting a curve between the flip angle and the concentrations. MRSI data with two different TRs were acquired for this purpose (300 ms and 500 ms) and the spectra were fit with the macromolecular baseline components included in the basis set. The measured and fit data for the relaxation effects are shown in Figure 12. The results show that different macromolecule components have different relaxation times, and furthermore there are relaxation time differences between different tissue types.

Finally, we compared the metabolite concentration levels resulting from fitting the MRSI data with three different basis-sets: without macromolecules, with a single measured macromolecule baseline, and with our modeled macromolecule baseline (Figure 13). The results showed that if the macromolecular baseline is not incorporated, the concentrations of many metabolites are estimated higher than when the macromolecules are incorporated into the baseline. Using a single molecular baseline can improve the accuracy of the quantification.

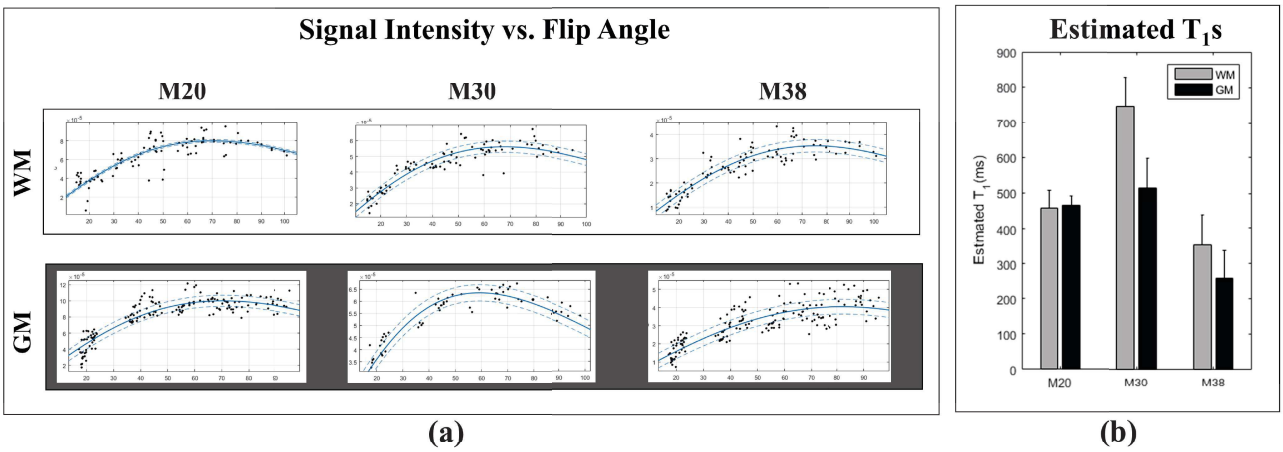

Figure 12: (a) Signal intensity vs. flip angle: The signal intensity of three macromolecule components measured at different flip angles are shown for white (WM) and gray matter (GM) separately. The fitted curves along with the confidence intervals are also shown on each plot in blue. (b) The estimated T_1values for the three macromolecule components resulting from the fitted curves.

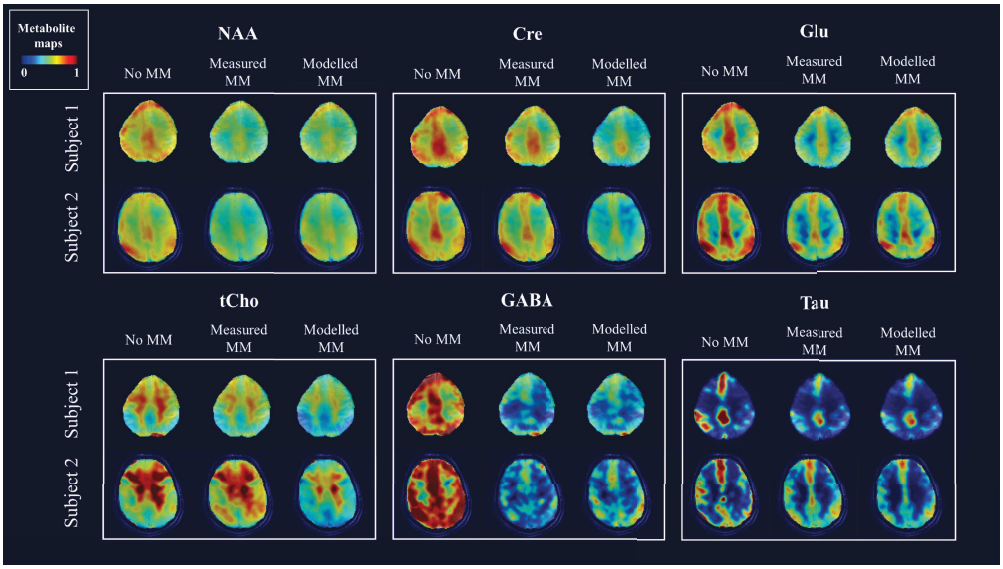

Figure 13: Metabolite maps resulting from fitting with no macromolecule component (No MM), with the single MM baseline (Measured MM) and with our proposed MM model (Modelled MM), shown for 6 metabolites for two different subjects.

However, since there are regional and relaxation time differences between different macromolecular components in different tissue types, only using a modeled macromolecular baseline can account for all these variations. It was shown that this results in different contrasts and concentration levels for the different TRs due to the T_1 relaxation effects [39] (`Publication` 10 of section 2.2.3).

In summary, macromolecules can affect the accuracy of the quantification of metabolites. Furthermore, relaxation effects and regional differences of individual macromolecular components also significantly affect the quantification, especially for ultra-short TR and TE spectroscopic imaging applications. In future, this can be used to better quantify the macromolecules and metabolites in MR spectroscopy.

1.4.3 Water Reference Acquisition

Unsuppressed water spectra are often acquired for MRSI studies to be used as an internal reference for quantification, as well as for eddy current and phase correction purposes. In

order to shorten the total scan time, this water reference image is typically acquired at a lower resolution than the actual MRSI data. However, it has previously been shown [40] that the acquisition of a full resolution water reference can be reliably accelerated using SENSE [4]. Higher accuracy can be achieved this way compared to the low resolution acquisition. However, only moderate acceleration factors were achieved in that study and this was only done for low resolution MRSI applications. In this study, we investigated accelerating the acquisition of a high resolution water reference even further using compressed sensing.

Compressed sensing is a good candidate for accelerating the water reference acquisition, since the amplitude of the signal is within the same order of magnitude across the brain. Therefore, in this regard, the data for the water reference is much sparser. Furthermore, we are mostly interested in recovering the water peak which is very sparse in nature. Also, for the application of eddy current and phase correction, only the phase of the FID signal is important and the phase in the image and time domain is also very sparse.

In `Publication 6`, we investigated an acceleration factor of R=14 and R=28 and used the same reconstruction method as described in section 1.3.1 (also see `Publication 3`). Comparison of the water reference with an acceleration factor of R=14 and a reduced resolution water reference (2x2 times lower resolution than the MRSI data) showed that the Bland-Altman plots indicate very similar results. The water reference maps (integrated over the spectra) are shown in Figure 14. Therefore, we could achieve an acceleration factor of R=14 that performed similarly to the reduced resolution water reference (effectively R=4), even though it is 3.5 times faster. This greatly reduces the overhead scan time.

Furthermore, for the purpose of eddy current and zeroth order phase correction, an acceleration factor of R=28 was achievable, since the phase of the signals is much sparser than the magnitudes. Performing eddy current correction with the accelerated water reference (R=28) was comparable to using the reduced resolution water reference (Figure 15). The differences in the metabolites could not visibly be seen, and the Bland-Altman plots showed minimal differences.

Therefore, a water reference image could be acquired for a 64x64 k-space matrix in under 1 minute.

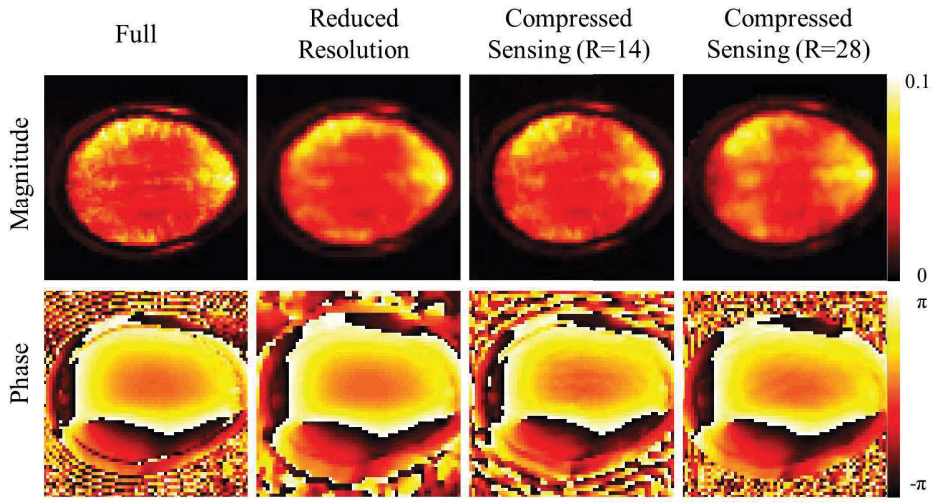

Figure 14: Magnitude (top row) and phase (bottom row) of the water reference image acquired at full resolution, four times reduced resolution, and full resolution accelerated using compressed sensing with a factor of R=14 and R=28.

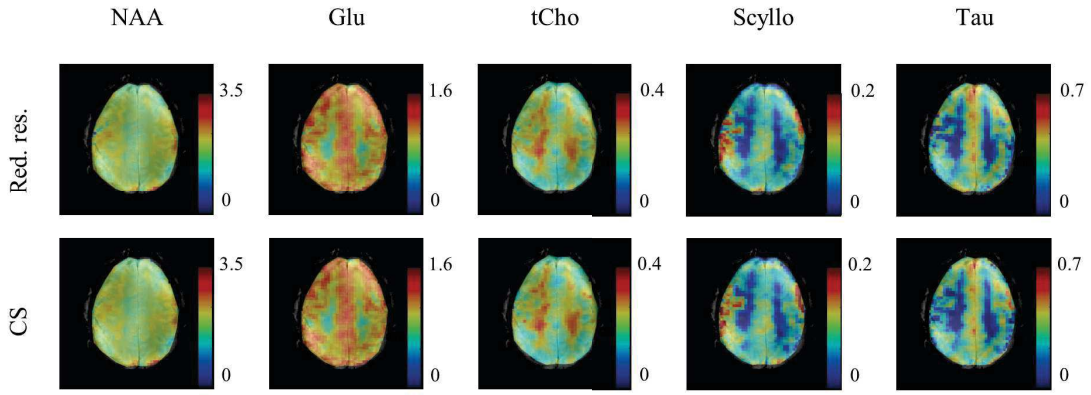

Figure 15: Comparison of eddy current and phase correction using the reduced resolution (R=4) versus compressed sensing (R=28) water reference images for metabolite mapping: ratio metabolite maps (/Creatine) of five metabolites from a healthy volunteer are shown.

1.5 Whole-Brain Metabolite Mapping

Needless to say, the extensive investigation of accelerating MRSI acquisition was not without purpose. The culmination of our studies were to reach a point where we could eventually performing whole brain metabolite mapping in a feasible scan time at 9.4T. Although whole brain metabolite maps have previously been shown at 3T scanners [41, 42] using EPSI [3], these maps are often limited in their SNR and resolution, and the data from several voxels cannot be analyzed due to poor B_0 homogeneity. The metabolite maps are often aggregated over multiple volunteers and lack good spatial specificity. This is largely due to the low SNR of MRSI at 3T. While this can be useful for group studies, this is very limiting in a clinical setting. If good quality single subject metabolite maps can be obtained, this will be clinically more relevant as it would allow diagnosis on single subjects/patients. In this study, we showed that we can achieve high resolution metabolite maps that are much richer in spatial information and more reliable than any previously shown whole brain metabolite maps from single volunteers.

As mentioned multiple times throughout this thesis, we focused on 2D sequences so that we could perform dynamic slice-wise B_0 shimming to acquire good quality metabolite maps. In `Publication` 7, we first investigated the effect of B_0 shimming on the acquired metabolite maps at 9.4T using two different shimming approaches: a very high order spherical harmonics (up to 4^{th} degree) B_0 shim system versus a 16-channel multi-coil system. The results showed that the metabolite maps benefit greatly from advanced B_0 shimming approaches. Dynamic shimming performed using a 4^{th} degree spherical harmonic shim system resulted in a similar quality as the 16-channel multi-coil system combined with 2^{nd} degree spherical harmonic shims.

An 18Tx/32Rx transceiver head RF coil was used to acquire the whole brain MRSI data since it provided good B_1 coverage across the whole brain [43]. The water reference scan required 45 sec per slice using compressed sensing for reconstruction (section 1.4.3) and the MRSI scan required approximately 2.5 mins per slice using the neural network GRAPPA reconstruction (section 1.3.3). A scan protocol of 10 slices with a slice thickness of 8 mm (no distance factor) was used to cover the entire cerebrum. Therefore, the MRSI data was

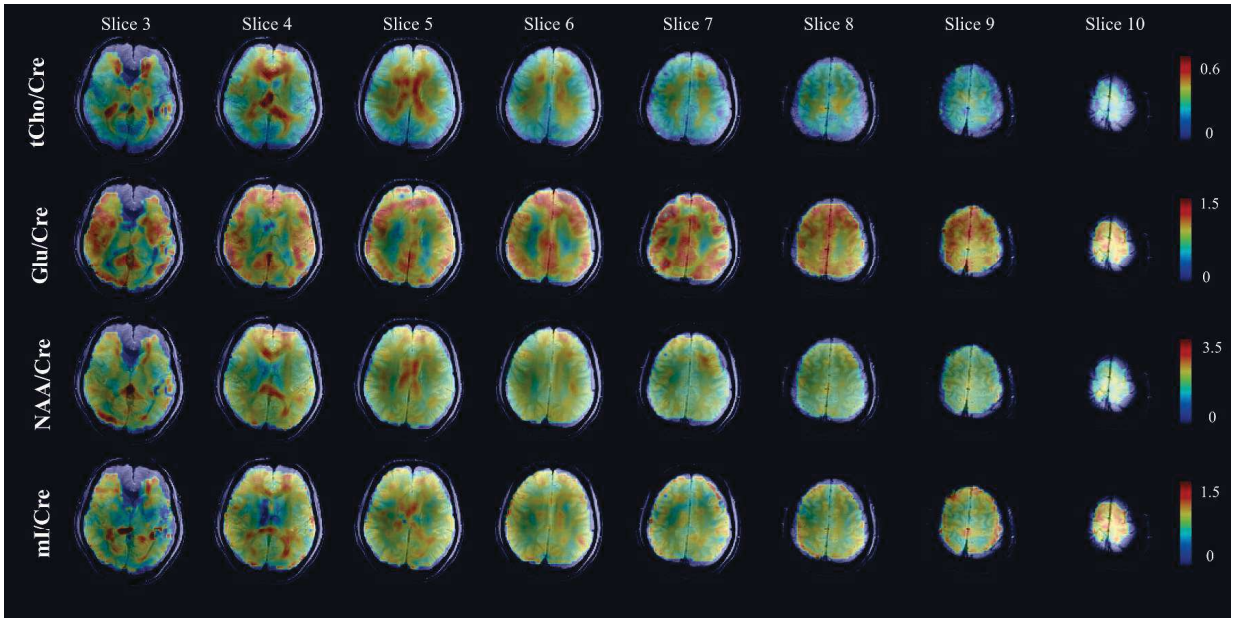

Figure 16: Whole-brain metabolite maps of four major metabolites (/Cre) acquired from a healthy subject at 9.4T using a multi-slice 2D phase-encoded ^{1}H FID MRSI sequence with ultra-short TE and TR along with dynamic B_0 shimming are shown.

acquired in 25 mins, which is comparable to the scan duration for the EPSI sequence for whole brain MRSI at 3T. The water reference was acquired in 7 mins. Each slice was dynamically B_0 shimmed. The processing and fitting of the data was the same as the process described in section 1.2.

Finally, in `Publication 7`, we showed metabolite maps for the whole brain acquired at 9.4T. This is the first time that whole brain metabolite mapping has been performed at UHF. Due to the higher SNR of UHF, the metabolite maps are of much higher quality than the metabolite maps for 3T shown in previous studies. The publication also shows the achieved B_0 maps for acquiring these metabolite maps. Some of the maps are shown in Figure 16 to demonstrate the quality of metabolite maps that could be achieved. Figure 17 shows the sagittal and coronal view of the maps.

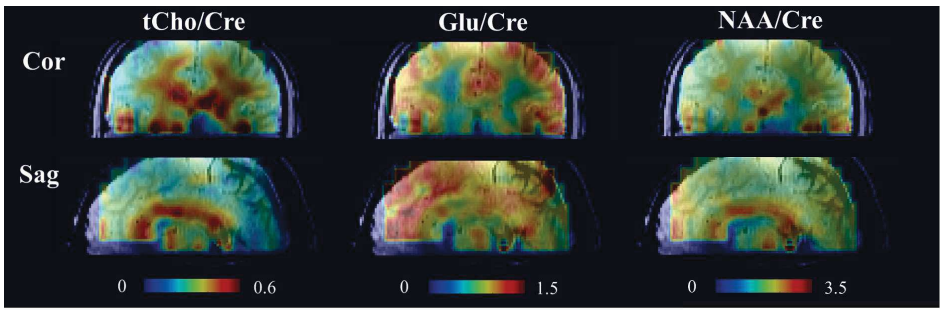

Figure 17: Metabolite maps of three major metabolites (/Cre) shown from the same volunteer as in Figure 16 on the central sagittal and coronal slices.

1.6 Summary and Outlook

In this thesis, a variety of aspects regarding human brain metabolite mapping at 9.4T using MR spectroscopic imaging was addressed. Robust acquisition and reconstruction techniques were employed to acquire high and ultra-high resolution metabolite maps of several metabolites. The effect of water suppression on the metabolite concentrations in comparison to non-water suppressed MRSI was also studied. Other aspects pertaining to metabolite mapping, namely the contribution of macromolecules, as well as the accelerated acquisition of a high resolution water reference image were investigated. Furthermore, various acceleration techniques were introduced and optimized to achieve high in-plane acceleration factors. Finally, by combining a robust acceleration technique with dynamic B_0 shim updating, high quality whole-brain metabolite maps acquired in about 25 minutes at 9.4T were presented.

Despite the remarkable advances in the field of MR spectroscopic imaging, there are still some aspects that must be further investigated. One of the main issues remains to be the quantification of the metabolite levels in absolute units. Indeed, one of the major limitations of the current thesis was that the acquired MRSI data were not absolutely quantified. This is due to the extremely challenging nature of MRSI quantification at ultra-high fields, which requires a comprehensive correction for B_1^+ and B_1^- field inhomogeneity, relaxation times, and partial volume effects. Another important aspect that can greatly benefit the quality of the acquired MRSI data is the use of parallel radio frequency transmission. Using multiple radio frequency power amplifiers instead of one, can help overcome B_1^+ inhomogeneity,

especially at ultra-high fields.

We believe that the comprehensive study of acceleration and MRSI for metabolite mapping in this thesis has demonstrated the potential of UHF scanners for metabolite mapping. The rich information that MR spectroscopy offers has great potential for applications in neuroscience, psychology and clinics. The ability to measure metabolites in the brain could enlighten us to the neurochemical processes of the brain. There is also diagnostic potential in measuring and mapping metabolites to investigate causes and treatments of diseases such as multiple sclerosis, depression and mental disorders. We hope that the investigations and results presented in this thesis can further improve and progress the study of brain function, and bring MRSI one step closer to its commonplace application in research and clinics.

References

[1] A. Pfrommer and A. Henning, "On the superlinear increase of the ultimate intrinsic signal-to-noise ratio with regard to main magnetic field strength in a spherical sample," in *International Conference on Electromagnetics in Advanced Applications IEEE-APS Topical Conference on Antennas and Propagation in Wireless Communications*, 2017.

[2] M. Barth, F. Breuer, P. J. Koopmans, D. G. Norris, and B. A. Poser, "Simultaneous multislice (SMS) imaging techniques," *Magnetic Resonance in Medicine*, vol. 75, no. 1, pp. 63–81, 2016.

[3] S. Posse, G. Tedeschi, R. Risinger, R. Ogg, and D. L. Bihan, "High speed ^{1}H spectroscopic imaging in human brain by echo planar spatial-spectral encoding," *Magnetic Resonance in Medicine*, vol. 33, no. 1, pp. 34–40, 1995.

[4] K. P. Pruessmann, M. Weiger, M. B. Scheidegger, P. Boesiger *et al.*, "SENSE: sensitivity encoding for fast MRI," *Magnetic Resonance in Medicine*, vol. 42, no. 5, pp. 952–962, 1999.

[5] M. A. Griswold, P. M. Jakob, R. M. Heidemann, M. Nittka, V. Jellus, J. Wang, B. Kiefer, and A. Haase, "Generalized autocalibrating partially parallel acquisitions (GRAPPA)," *Magnetic Resonance in Medicine*, vol. 47, no. 6, pp. 1202–1210, 2002.

[6] P. Chang, S. Nassirpour, and A. Henning, "Low SAR lipid suppression for MRSI at ultra-high fields," *Magnetic Resonance Materials in Physics, Biology and Medicine*, vol. 30, no. Supplement 1, p. 471, 2017.

[7] I. Tkáč, Z. Starčuk, I.-Y. Choi, and R. Gruetter, "In vivo ^{1}H NMR spectroscopy of rat brain at 1 ms echo time," *Magnetic Resonance in Medicine*, vol. 41, pp. 649–656, 1999.

[8] D. Leibfritz and W. Dreher, "Magnetization transfer MRS," *NMR in Biomedicine*, vol. 14, no. 2, pp. 65–76, 2001.

[9] M. Kruiskamp, R. De Graaf, J. van Der Grond, R. Lamerichs, and K. Nicolay, "Magnetic coupling between water and creatine protons in human brain and skeletal muscle, as measured using inversion transfer ^{1}H-MRS," *NMR in Biomedicine*, vol. 14, no. 1, pp. 1–4, 2001.

[10] W. Dreher, D. G. Norris, and D. Leibfritz, "Magnetization transfer affects the proton creatine/phosphocreatine signal intensity: in vivo demonstration in the rat brain," *Magnetic Resonance in Medicine*, vol. 31, no. 1, pp. 81–84, 1994.

[11] D. B. Clayton, M. A. Elliott, J. S. Leigh, and R. E. Lenkinski, "^{1}H spectroscopy without solvent suppression: characterization of signal modulations at short echo times," *Journal of Magnetic Resonance*, vol. 153, no. 2, pp. 203–209, 2001.

[12] W. Dreher and D. Leibfritz, "New method for the simultaneous detection of metabolites and water in localized in vivo ^{1}H nuclear magnetic resonance spectroscopy," *Magnetic Resonance in Medicine*, vol. 54, no. 1, pp. 190–195, 2005.

[13] E. L. MacMillan, D. G. Chong, W. Dreher, A. Henning, C. Boesch, and R. Kreis, "Magnetization exchange with water and T_1 relaxation of the downfield resonances in

human brain spectra at 3.0 T," *Magnetic Resonance in Medicine*, vol. 65, no. 5, pp. 1239–1246, 2011.

[14] L. N. Baldwin, K. Wachowicz, S. D. Thomas, R. Rivest, and B. G. Fallone, "Characterization, prediction, and correction of geometric distortion in 3T MR images," *Medical Physics*, vol. 34, no. 2, pp. 388–399, 2007.

[15] P. Jezzard, "Physical basis of spatial distortions in magnetic resonance images," in *Handbook of Medical Imaging.* Academic Press, Inc., 2000, pp. 425–438.

[16] C. Juchem, T. W. Nixon, S. McIntyre, V. O. Boer, D. L. Rothman, and R. A. de Graaf, "Dynamic multi-coil shimming of the human brain at 7T," *Journal of Magnetic Resonance*, vol. 212, no. 2, pp. 280–288, 2011.

[17] K. M. Koch, S. McIntyre, T. W. Nixon, D. L. Rothman, and R. A. de Graaf, "Dynamic shim updating on the human brain," *Journal of Magnetic Resonance*, vol. 180, no. 2, pp. 286–296, 2006.

[18] V. O. Boer, D. W. Klomp, C. Juchem, P. R. Luijten, and R. A. de Graaf, "Multislice ^{1}H MRSI of the human brain at 7T using dynamic B_0 and B_1 shimming," *Magnetic Resonance in Medicine*, vol. 68, no. 3, pp. 662–670, 2012.

[19] A. Henning, A. Fuchs, J. B. Murdoch, and P. Boesiger, "Slice-selective FID acquisition, localized by outer volume suppression (FIDLOVS) for ^{1}H-MRSI of the human brain at 7T with minimal signal loss," *NMR in Biomedicine*, vol. 22, no. 7, pp. 683–696, 2009.

[20] W. Bogner, S. Gruber, S. Trattnig, and M. Chmelik, "High-resolution mapping of human brain metabolites by free induction decay ^{1}H MRSI at 7T," *NMR in Biomedicine*, vol. 25, no. 6, pp. 873–882, 2012.

[21] B. Bilgic, I. Chatnuntawech, A. P. Fan, K. Setsompop, S. F. Cauley, L. L. Wald, and E. Adalsteinsson, "Fast image reconstruction with L2-regularization," *Journal of Magnetic Resonance Imaging*, vol. 40, no. 1, pp. 181–191, 2014.

[22] S. W. Provencher, "Estimation of metabolite concentrations from localized in vivo proton NMR spectra," *Magnetic Resonance in Medicine*, vol. 30, no. 6, pp. 672–679, 1993.

[23] S. Smith, T. Levante, B. H. Meier, and R. R. Ernst, "Computer simulations in magnetic resonance. an object-oriented programming approach," *Journal of Magnetic Resonance, Series A*, vol. 106, no. 1, pp. 75–105, 1994.

[24] M. Lustig, D. L. Donoho, J. M. Santos, and J. M. Pauly, "Compressed sensing MRI," *IEEE Signal Processing Magazine*, vol. 25, no. 2, pp. 72–82, 2008.

[25] P. Cao, P. J. Shin, I. Park, C. Najac, I. Marco-Rius, D. B. Vigneron, S. J. Nelson, S. M. Ronen, and P. E. Larson, "Accelerated high-bandwidth MR spectroscopic imaging using compressed sensing," *Magnetic Resonance in Medicine*, vol. 76, no. 2, pp. 369–379, 2016.

[26] B. J. Geraghty, J. Y. Lau, A. P. Chen, and C. H. Cunningham, "Accelerated 3D echo-planar imaging with compressed sensing for time-resolved hyperpolarized ^{13}C studies," *Magnetic Resonance in Medicine*, vol. 77, no. 2, pp. 538–546, 2017.

[27] M. L. Maguire, S. Geethanath, C. A. Lygate, V. D. Kodibagkar, and J. E. Schneider, "Compressed sensing to accelerate magnetic resonance spectroscopic imaging: evaluation and application to ^{23}Na-imaging of mouse hearts," *Journal of Cardiovascular Magnetic Resonance*, vol. 17, no. 1, p. 45, 2015.

[28] P. J. Shin, P. E. Larson, M. A. Ohliger, M. Elad, J. M. Pauly, D. B. Vigneron, and M. Lustig, "Calibrationless parallel imaging reconstruction based on structured low-rank matrix completion," *Magnetic Resonance in Medicine*, vol. 72, no. 4, pp. 959–970, 2014.

[29] T. Kirchner, A. Fillmer, J. Tsao, K. P. Pruessmann, and A. Henning, "Reduction of voxel bleeding in highly accelerated parallel ^{1}H MRSI by direct control of the spatial response function," *Magnetic Resonance in Medicine*, vol. 73, no. 2, pp. 469–480, 2015.

[30] T. Kirchner, A. Fillmer, and A. Henning, "Mechanisms of SNR and line shape improvement by B_0 correction in overdiscrete MRSI reconstruction," *Magnetic Resonance in Medicine*, vol. 77, no. 1, pp. 44–56, 2017.

[31] N. Zölch, "High precision external reference standards for quantitative in vivo magnetic resonance spectroscopy," Ph.D. dissertation, ETH Zurich, 2016.

[32] P. B. Barker, B. J. Soher, S. J. Blackband, J. C. Chatham, V. P. Mathews, and R. N. Bryan, "Quantitation of proton nmr spectra of the human brain using tissue water as an internal concentration reference," *NMR in Biomedicine*, vol. 6, no. 1, pp. 89–94, 1993.

[33] K. L. Behar, D. L. Rothman, D. D. Spencer, and O. A. Petroff, "Analysis of macromolecule resonances in ^{1}H NMR spectra of human brain," *Magnetic Resonance in Medicine*, vol. 32, no. 3, pp. 294–302, 1994.

[34] M. Craveiro, V. Clément-Schatlo, D. Marino, R. Gruetter, and C. Cudalbu, "In vivo brain macromolecule signals in healthy and glioblastoma mouse models: ^{1}H magnetic resonance spectroscopy, post-processing and metabolite quantification at 14.1T," *Journal of Neurochemistry*, vol. 129, no. 5, pp. 806–815, 2014.

[35] B. Schaller, L. Xin, and R. Gruetter, "Is the macromolecule signal tissue-specific in healthy human brain? a ^{1}H MRS study at 7 Tesla in the occipital lobe," *Magnetic Resonance in Medicine*, vol. 72, no. 4, pp. 934–940, 2014.

[36] M. Považan, G. Hangel, B. Strasser, S. Gruber, M. Chmelik, S. Trattnig, and W. Bogner, "Mapping of brain macromolecules and their use for spectral processing of ^{1}H-MRSI data with an ultra-short acquisition delay at 7T," *NeuroImage*, vol. 121, pp. 126–135, 2015.

[37] S. Nassirpour, P. Chang, and A. Henning, "High resolution maps of individual macromolecule components in the human brain at 9.4T," in *25^{th} Annual Meeting and Exhibition of the International Society for Magnetic Resonance in Medicine (ISMRM 2017), Honolulu, HI, USA*, 2017.

[38] S.-T. Hong, D. Z. Balla, G. Shajan, C. Choi, K. Uğurbil, and R. Pohmann, "Enhanced neurochemical profile of the rat brain using in vivo ^{1}H NMR spectroscopy at 16.4T," *Magnetic Resonance in Medicine*, vol. 65, no. 1, pp. 28–34, 2011.

[39] S. Nassirpour, P. Chang, and A. Henning, "The necessity of parametrizing macromolecules for accurate quantification of ultra-short TE and TR ^{1}H FID MRSI data at 9.4T," *Magnetic Resonance Materials in Physics, Biology and Medicine,*, vol. 30, no. Supplement 1, pp. 473–474, 2017.

[40] R. Birch, A. C. Peet, T. N. Arvanitis, and M. Wilson, "Sensitivity encoding for fast ^{1}H MR spectroscopic imaging water reference acquisition," *Magnetic Resonance in Medicine*, vol. 73, no. 6, pp. 2081–2086, 2015.

[41] A. A. Maudsley, V. Govind, and K. Arheart, "Associations of age, gender and body mass with ^{1}H MR-observed brain metabolites and tissue distributions," *NMR in Biomedicine*, vol. 25, no. 4, pp. 580–593, 2012.

[42] A. Lecocq, Y. Le Fur, A. A. Maudsley, A. Le Troter, S. Sheriff, M. Sabati, M. Donnadieu, S. Confort-Gouny, P. J. Cozzone, M. Guye *et al.*, "Whole-brain quantitative mapping of metabolites using short echo three-dimensional proton MRSI," *Journal of Magnetic Resonance Imaging*, vol. 42, no. 2, pp. 280–289, 2015.

[43] N. Avdievich, I. Giapitzakis, A. Pfrommer, T. Borbath, and A. Henning, "Combination of surface and vertical loop elements improves receive performance of a human head transceiver array at 9.4 T," *NMR in Biomedicine*, 2018.

2 List of Publications

2.1 Appended Publications

1. **S Nassirpour**, P Chang, A Henning, "High and ultra-high resolution metabolite mapping of the human brain using ^{1}H FID MRSI at 9.4T" *NeuroImage*, 2016, doi: 10.1016/j.neuroimage.2016.12.065.

2. P Chang*, **S Nassirpour***, N Avdievich, A Henning, "Non-water Suppressed ^{1}H FID-MRSI at 3T and 9.4T" *Magnetic Resonance in Medicine*, 2017, doi:10.1002/mrm.27049.

3. **S Nassirpour***, P Chang*, N Avdievich, A Henning, "Compressed Sensing for High-Resolution Non-lipid Suppressed ^{1}H FID MRSI of the Human Brain at 9.4T" *Magnetic Resonance in Medicine*, 2018, doi: 10.1002/mrm.27225.

4. **S Nassirpour***, P Chang*, A Henning, "Over-discretized SENSE reconstruction and B_0 correction for accelerated non-lipid suppressed ^{1}H FID MRSI of the human brain at 9.4T" *NMR in Biomedicine*, 2018 *(in review).*

5. **S Nassirpour***, P Chang*, A Henning, "MultiNet PyGRAPPA: Multiple Neural Networks for Reconstructing Variable Density GRAPPA (a ^{1}H FID MRSI Study)" *NeuroImage*, 2018 *(in review).*

6. **S Nassirpour***, P Chang*, A Henning, "Accelerated Water Reference Acquisition for ^{1}H MRSI using Compressed Sensing" *(in preparation).*

7. P Chang*, **S Nassirpour***, A Aghaeifar, A Henning, "In Vivo Whole Brain Proton Spectroscopic Imaging at 9.4T: A Focus on Dynamic Slice-wise B_0 Shimming" *(in preparation).*

*Equal contributions to the publication

2.2 Other Recent Publications

2.2.1 Journal Articles

1. **S Nassirpour***, P Chang*, A Fillmer, A Henning, "A Comparison of Optimization Algorithms for Localized *In Vivo* B_0 Shimming" *Magnetic Resonance in Medicine*, 2017, doi: 10.1002/mrm.26758.

2. P Chang*, **S Nassirpour***, A Henning, "Modeling Real Shim Fields for Very High Degree (and Order) B_0 Shimming of the Human Brain at 9.4T" *Magnetic Resonance in Medicine*, 2017, doi:10.1002/mrm.26658.

3. P Chang, **S Nassirpour**, M Eschelbach, K Scheffler, A Henning, "Constrained Optimisation for Position Calibration of a NMR Field Camera" *Magnetic Resonance in Medicine*, 2017, doi:10.1002/mrm.27010.

4. P Chang, **S Nassirpour**, A Henning, "Controller Design for Feedback of B_0 Shim Systems" *(in preparation).*

2.2.2 Talks

1. **S Nassirpour**, P Chang, A Henning, "Whole Brain High Resolution Metabolite Mapping Using ^{1}H FID MRSI with Slice-wise B_0 Shim Updating at 9.4T", *Proc. of the 26th Annual Meeting of the International Society for Magnetic Resonance in Medicine*, 2018.

2. P Chang, **S Nassirpour**, A Aghaeifar, K Scheffler, A Henning, "Dynamic B_0 Shimming for Multi-Slice Metabolite Mapping at Ultra-High Field in the Human Brain: Very High Order Spherical Harmonics vs. Multi-Coil", *Proc. of the 26th Annual Meeting of the International Society for Magnetic Resonance in Medicine*, 2018.

3. **S Nassirpour**, P Chang, A Henning, "High resolution whole brain metabolite mapping at 9.4T"*, University Hospital Tuebingen's Workshop on Proton MR Spectroscopy in Neuroradiological Diagnostics, 2018.*

4. P Chang, **S Nassirpour**, A Henning, "B_0 shimming for the entire spectrum of spectroscopy applications", *University Hospital Tuebingen's Workshop on Proton MR Spectroscopy in Neuroradiological Diagnostics, Tuebingen, 2018.*

5. **S Nassirpour**, P Chang, A Henning, "Over-discrete SENSE and B_0 Correction for Accelerated ^{1}H FID MRSI of the Human Brain at 9.4T", *Proc. of the 34th Annual Meeting of the European Society of Magnetic Resonance in Medicine and Biology*, 2017.

6. P Chang, **S Nassirpour**, A Henning, "ConsTru: an Optimal B_0 Shimming Solution", *Proc. of the 34th Annual Meeting of the European Society of Magnetic Resonance in Medicine and Biology*, 2017.

7. **S Nassirpour**, P Chang, A Henning, "High resolution maps of individual macromolecule components in the human brain at 9.4T", *Proc. of the 25th Annual Meeting of the International Society for Magnetic Resonance in Medicine*, 2017.

8. **S Nassirpour**, P Chang, A Henning, "Pushing the limits of ultra-high field MRSI: benefits and limitations of 9.4T for metabolite mapping of the human brain", *Proc. of the 25th Annual Meeting of the International Society for Magnetic Resonance in Medicine*, 2017.

9. **S Nassirpour**, P Chang, A Henning, "Multi-slice metabolite mapping with Very-High Degree Dynamic B_0 Shim Updating at 9.4T using Accelerated ^{1}H FID MRSI", *Proc. of the 25th Annual Meeting of the International Society for Magnetic Resonance in Medicine*, 2017.

10. P Chang, **S Nassirpour**, A Henning, "Fast non-water suppressed metabolite cycled ^{1}H FID MRSI at both 3T and 9.4T", *Proc. of the 25th Annual Meeting of the International Society for Magnetic Resonance in Medicine*, 2017.

11. **S Nassirpour**, P Chang, A Henning, "Metabolite Mapping of the Human Brain Using ^{1}H FID MRSI at 9.4T", *ISMRM Workshop on MR Spectroscopy: From Current Best Practice to Latest Frontiers*, 2016.

12. **S Nassirpour**, P Chang, A Henning, "A Comparison of Optimization Algorithms for Localized In-Vivo Shimming", *ISMRM Workshop on MR Spectroscopy: From Current Best Practice to Latest Frontiers*, 2016.

13. P Chang, **S Nassirpour**, A Henning, "Very High-Order B_0 Shimming for Ultra-High Field Magnetic Resonance", *ISMRM Workshop on MR Spectroscopy: From Current Best Practice to Latest Frontiers*, 2016.

14. **S Nassirpour**, P Chang, A Henning, "A Comparison of Optimization Algorithms for Localized *in-vivo* B_0 Shimming", *Proc. of the 24th Annual Meeting of the International Society for Magnetic Resonance in Medicine*, 2016.

15. IA Giapitzakis, **S Nassirpour**, N Avdievich, R Keis, A Henning, "^{1}H Single Voxel Spectroscopy at Occipital Lobe of Human Brain at 9.4T", *Proc. of the 32rd Annual Scientific Meeting of the European Society of Magnetic Resonance in Medicine and Biology*, 2015.

16. IA Giapitzakis, **S Nassirpour**, A Henning, "Short Duration Water Suppression using Optimised Flip Angles (SODA) at Ultra High Fields", *Proc. of the 32rd Annual Scientific Meeting of the European Society of Magnetic Resonance in Medicine and Biology*, 2015.

2.2.3 Posters

1. **S Nassirpour**, P Chang, A Henning, "MultiNet PyGRAPPA: A Novel Method for Highly Accelerated Metabolite Mapping", *Proc. of the 26th Annual Meeting of the International Society for Magnetic Resonance in Medicine*, 2018.

2. **S Nassirpour**, P Chang, A Henning, "Over-discretized SENSE reconstruction and B_0 correction for accelerated non-lipid suppressed ^{1}H FID MRSI of the human brain at 9.4T", *Proc. of the 26th Annual Meeting of the International Society for Magnetic Resonance in Medicine*, 2018.

3. **S Nassirpour**, P Chang, N Avdievitch, A Henning, "SNR Requirements for Successful Application of Compressed Sensing Acceleration to Non-lipid suppressed ^{1}H MRSI at Ultra-High Fields", *Proc. of the 26th Annual Meeting of the International Society for Magnetic Resonance in Medicine*, 2018.

4. P Chang, **S Nassirpour**, A Henning, "Highly Accelerated (R=14) Water Reference Acquisition for High Resolution ^{1}H MRSI using Compressed Sensing", *Proc. of the 26th Annual Meeting of the International Society for Magnetic Resonance in Medicine*, 2018.

5. P Chang, **S Nassirpour**, A Henning, "Measuring Eddy Currents Induced by Switching Gradient/Shim Currents", *Proc. of the 26th Annual Meeting of the International Society for Magnetic Resonance in Medicine*, 2018.

6. A Aghaeifar, Paul Chang, **S Nassirpour**, M Eschelbach, A Henning, K Scheffler, "A true comparison of B_0 shimming with a very high order spherical harmonic based setup and a multi-coil shim array", *Proc. of the 26th Annual Meeting of the International Society for Magnetic Resonance in Medicine*, 2018.

7. A Wright, **S Nassirpour**, P Chang, A Henning,"Toward Absolute Quantification Using External Reference Standards at 3T and 9.4T", *Proc. of the 26th Annual Meeting of the International Society for Magnetic Resonance in Medicine*, 2018.

8. **S Nassirpour**, P Chang, A Henning, "Pushing the limits of MR spectroscopic imaging: benefits and limitations of ultra-high field strengths for metabolite mapping of the human brain", *Proc. of the 12th European Society for Molecular Imaging Winter Conference "hot TOPIics in IMaging": Imaging Metabolism (TOPIM 2018), 2018.*

9. P Chang, **S Nassirpour**, A Henning, "Magnetic Field Homogeneity for Small Volume MR Spectroscopy", *Proc. of the 12th European Society for Molecular Imaging Winter Conference "hot TOPIics in IMaging": Imaging Metabolism (TOPIM 2018), 2018.*

10. **S Nassirpour**, P Chang, A Henning, "The Necessity of Parametrizing Macromolecules for Accurate Quantification of Ultra-short TE and TR ^{1}H FID MRSI Data at 9.4T", *Proc. of the 34th Annual Meeting of the European Society of Magnetic Resonance in Medicine and Biology*, 2017.

11. P Chang, **S Nassirpour**, A Henning, "Low SAR Lipid Suppression for MRSI at Ultra-high Fields", *Proc. of the 34th Annual Meeting of the European Society of Magnetic Resonance in Medicine and Biology*, 2017.

12. P Chang, **S Nassirpour**, A Henning, "Compressed Sensing for ^{1}H MRSI in the Human Brain", *Proc. of the 34th Annual Meeting of the European Society of Magnetic Resonance in Medicine and Biology*, 2017.

13. **S Nassirpour**, P Chang, A Henning, "Comparison of different acceleration methods for high-resolution metabolite mapping using ^{1}H FID MRSI at 9.4T", *Proc. of the 25th Annual Meeting of the International Society for Magnetic Resonance in Medicine*, 2017.

14. P Chang, **S Nassirpour**, A Henning, "Decoupling Controller Design for Real-time Feedback of B_0 Shim Systems", *Proc. of the 25th Annual Meeting of the International Society for Magnetic Resonance in Medicine*, 2017.

15. P Chang, **S Nassirpour**, A Henning, "Dynamic B_0 Shim Controller for Digital Pre-emphasis with Sub-millisecond Update Rate", *Proc. of the 25th Annual Meeting of the International Society for Magnetic Resonance in Medicine*, 2017.

16. P Chang, **S Nassirpour**, A Henning, "Flexible General-Purpose Embedded System for Real-time Feedback and Dynamic B_0 Shimming", *Proc. of the 25th Annual Meeting of the International Society for Magnetic Resonance in Medicine*, 2017.

17. P Chang, **S Nassirpour**, A Henning, "Limitations of NMR Field Cameras for B_0 Field Monitoring", *Proc. of the 25th Annual Meeting of the International Society for Magnetic Resonance in Medicine*, 2017.

18. P Chang, **S Nassirpour**, A Fillmer, A Henning, "Correcting Geometric Distortion in B_0 Mapping", *Proc. of the 24th Annual Meeting of the International Society for Magnetic Resonance in Medicine*, 2016.

19. P Chang, **S Nassirpour**, A Henning, "Very High Order B_0 Shimming of the Human Brain at 9.4T Considering Real B_0 Shim Fields" *Proc. of the 24th Annual Meeting of the International Society for Magnetic Resonance in Medicine*, 2016.

20. P Chang, **S Nassirpour**, A Henning, "Very High-order B_0 Shimming for Single-Shot EPI at 9.4T in the Human Brain", *ISMRM Workshop on Ultra High Field MRI: Technological Advances and Clinical Applications*, 2016.

21. **S Nassirpour**, T Kirchner, IA Giapitzakis, A Henning, "Accelerated Multi-slice ^{1}H FID-MRSI in the Human Brain", *Proc. of the 23rd Annual Meeting of the International Society for Magnetic Resonance in Medicine*, 2015.

22. IA Giapitzakis, **S Nassirpour**, N Avdievich, R Kreis, A Henning, "Metabolite Cycled Single Voxel ^{1}H Spectroscopy at 9.4T", *Proc. of the 23th Annual Meeting of the International Society for Magnetic Resonance in Medicine*, 2015.

23. IA Giapitzakis, **S Nassirpour**, R Kreis, N Avdievich, A henning, "Metabolite Cycled Proton Magnetic Resonance Spectroscopy at 9.4T", *Proc. of the 10th Annual Meeting of the* European Society *for Molecular Imaging*, 2015.

3 Statement of Contributions

3.1 High and ultra-high resolution metabolite mapping of the human brain using ^{1}H FID MRSI at 9.4T

An ultra-short TE and TR ^{1}H FID MRSI sequence was optimized for use at 9.4T. A robust and optimized water suppression scheme was incorporated in the sequence. MRSI datasets at high (nominal voxel size 97µL) and ultra-high (nominal voxel size 24µL) spatial resolutions were acquired from the brains of healthy subjects at 9.4T. The reconstruction and post-processing steps necessary for robust quantification of the data were implemented. Finally, high quality metabolite maps of 12 metabolites at both high and ultra-high spatial resolutions were presented and evaluated.

- **S. Nassirpour** - Optimized the water suppression scheme and implemented it in the pulse sequence. Tested the sequence with phantom experiments. Enabled the acquisition of ultra-high spatial resolution MRSI matrices in the pulse sequence. Collected the in-vivo MRSI data at 9.4T. Implemented the reconstruction scripts and post-processing steps. Implemented the lipid removal post-processing technique. Analyzed the MRSI data and metabolite maps. Wrote the majority of the manuscript.
- **P. Chang -** Optimized and modified the gradients in the pulse sequence to achieve the shortest echo time. Collected MRSI data at 9.4T. Implemented parts of the post-processing steps.
- **A. Henning -** Supervised and advised on the manuscript.

3.2 Non-water Suppressed ^{1}H FID-MRSI at 3T and 9.4T

This study demonstrated the first implementation of the metabolite cycling technique in the FID MRSI sequence for performing non-water suppressed ^{1}H spectroscopic imaging with ultra-short TE at both 3T and 9.4T. A low-SAR asymmetric adiabatic inversion pulse was designed and optimized for use at both field strengths which resulted in reasonable TR values

and scan times. The data quality as well as the *in-vivo* metabolite concentrations measured with this method were compared to the ones obtained from a water suppressed ^{1}H FID MRSI sequence at both 3T and 9.4T.

- **S. Nassirpour** - Optimized the required inversion times and pulse duration at both field strengths through numerical simulations. Fine-tuned the required inversion times and necessary transmit powers through phantom and preliminary *in-vivo* experiments at both 9.4T and 3T. Collected the *in-vivo* MRSI data both water suppressed and non-water suppressed at 9.4T and 3T. Wrote reconstruction scripts to process the non-water suppressed MRSI data. Quantified and analyzed the acquired water-suppressed and non-water suppressed data from both field strengths and performed statistical analyses. Wrote parts of the manuscript.

- **P. Chang -** Designed and optimized the low-SAR adiabatic pulse through Bloch simulations for both 3T and 9.4T. Implemented the optimized metabolite cycling pulse into the pulse sequence for both field strengths. Finalized scan protocols for data acquisition at both field strengths. Collected the *in-vivo* MRSI data both water suppressed and non-water suppressed at 9.4T and 3T. Wrote reconstruction scripts to process the non-water suppressed MRSI data. Wrote parts of the manuscript.

- **N. Avdievich -** Provided the RF coil for 9.4T.

- **A. Henning -** Supervised and advised on the manuscript.

3.3 Compressed Sensing for High-Resolution Non-lipid-Suppressed ^{1}H FID MRSI of the Human Brain at 9.4T

This study is the first report of using sparse sampling for acceleration of high resolution non-lipid-suppressed ^{1}H MRSI data. Two different methods, namely compressed sensing and low-rank reconstruction, are investigated for reconstructing the randomly undersampled data. The two methods are compared based on performance techniques such as speed, accuracy of the resulting metabolite maps, lipid contamination, and reliability of fit. The effect of matrix

size on the achievable acceleration factor is studied. Acceleration factors of up to 4 or 5 are successfully achieved and reproducible high resolution metabolite maps acquired with this technique at 9.4T are presented.

- **S. Nassirpour** - Designed the optimized variable density undersampling masks. Designed test criteria for comparing the two reconstruction algorithms. Collected *in-vivo* MRSI data both accelerated and fully sampled at 9.4T. Compared coil-by-coil versus coil combined compressed sensing and incorporated the SENSE coil combination into the compressed sensing reconstruction. Implemented and optimized the low-rank reconstruction method. Studied the effect of matrix size on the reconstruction performance. Quantified and analyzed the accelerated MRSI data and performed statistical analyses. Wrote parts of the manuscript.

- **P. Chang -** Implemented different random undersampling masks in the pulse sequence to modify the sampling scheme. Implemented and optimized the compressed sensing reconstruction method. Designed test criteria for comparing the two reconstruction algorithms. Collected *in-vivo* MRSI data both accelerated and fully sampled at 9.4T. Investigated and compared the performance of two different RF coils for acceleration of the MRSI data using random undersampling. Quantified and analyzed the accelerated MRSI data and performed statistical analyses. Wrote parts of the manuscript.

- **N. Avdievich -** Provided the RF coil for 9.4T.

- **A. Henning -** Supervised and advised on the manuscript.

3.4 Over-discretized SENSE reconstruction and B_0 correction for accelerated non-lipid-suppressed ^{1}H FID MRSI of the human brain at 9.4T

In this study, high resolution non-lipid-suppressed ^{1}H MRSI data were accelerated using an improved over-discretized SENSE reconstruction. The benefit of the over-discretized method

compared to a conventional SENSE reconstruction was investigated for 7 different acceleration factors. An SNR boosting technique using over-discretized B_0 correction was also implemented and evaluated for each acceleration factor. The highest achievable acceleration factor was found to be R=2x2. The improved SENSE reconstruction as compared to GRAPPA for this acceleration factor. Reproducible metabolite maps acquired at 9.4T using this technique were presented.

- **S. Nassirpour** - Designed the performance criteria for evaluating the accelerated data. Implemented the conventional and over-discretized SENSE reconstruction scripts for the 9.4T datasets. Collected *in-vivo* MRSI data both accelerated and fully sampled at 9.4T. Quantified the acquired data. Implemented GRAPPA and performed the comparison. Performed the acceleration factor comparison. Wrote the majority of the manuscript.
- **P. Chang -** Designed the performance criteria for evaluating the accelerated data. Implemented the undersampling masks in the pulse sequence. Contributed to the implementation of the improved SENSE reconstruction and optimized the scripts for memory and speed. Performed statistical analyses on the reconstructed data. Collected *in-vivo* MRSI data both accelerated and fully sampled at 9.4T. Wrote parts of the manuscript.
- **T. Kirchner -** Provided advice on the over-discretized reconstruction.
- **A. Henning -** Supervised and advised on the manuscript.

3.5 MultiNet PyGRAPPA: Multiple Neural Networks for Reconstructing Variable Density GRAPPA (a ^{1}H FID MRSI Study)

In this study, a novel acceleration/reconstruction approach suitable for accelerating the acquisition of non-lipid-suppressed ^{1}H FID MRSI data is presented. The proposed method is an improved version of the parallel imaging acceleration method known as GRAPPA. By combining variable density undersampling together with multiple neural networks, a robust

reconstruction of accelerated data for acceleration factors of up to 7 and 9 is presented. This is the highest in-plane acceleration factor achieved for non-lipid-suppressed MRSI data. High resolution metabolite maps acquired with this technique at 9.4T in about 2.5 minutes are presented.

- **S. Nassirpour** - Implemented parts of the neural network reconstruction. Suggested the variable density sampling scheme to achieve higher acceleration. Compared different acceleration factors. Collected *in-vivo* MRSI data at 9.4T. Implemented conventional GRAPPA for comparison with the proposed method. Performed all the comparisons between different acceleration factors. Analyzed and quantified the acquired data. Wrote parts of the manuscript.

- **P. Chang -** Optimized the variable density undersampling masks through simulation. Implemented the undersampling masks in the pulse sequence. Implemented parts of the neural network reconstruction. Analyzed and quantified the acquired data. Collected *in-vivo* MRSI data at 9.4T. Wrote parts of the manuscript.

- **A. Henning -** Supervised and advised on the manuscript.

3.6 Accelerated Water Reference Acquisition for ^{1}H MRSI using Compressed Sensing

This study investigated the acceleration of high resolution water reference acquisition for ^{1}H MRSI studies. Compressed sensing was employed for achieving very high acceleration factors (up to R=28). The accelerated water reference images were compared to the most common approach of acquiring a reduced resolution water image. It was shown that for eddy current and phase correction purposes an acceleration factor of 28 can be used. For internal water referencing purposes, a more moderate acceleration factor of 14 is recommended. With this technique, high resolution water reference images can be acquired from each MRSI slice in under a minute.

- **S. Nassirpour** - Studied the sparsity of the water reference signal for potential compressed sensing application through simulation studies. Collected *in-vivo* MRSI data and water references at 9.4T. Performed all the comparisons between different acceleration factors. Evaluated the performance of the proposed method compared to the reduced resolution approach for eddy current and phase correction purposes. Wrote parts of the manuscript.

- **P. Chang -** Implemented the random undersampling masks in the sequence. Collected *in-vivo* MRSI data and water references at 9.4T. Optimized the compressed sensing reconstruction for water reference acquisition. Performed the Bland-Altman analyses. Wrote parts of the manuscript.

- **A. Henning -** Supervised and advised on the manuscript.

3.7 In Vivo Whole Brain Proton Spectroscopic Imaging at 9.4T: A Focus on Dynamic Slice-wise B_0 Shimming

Dynamic B_0 shimming using a very high degree spherical harmonic shim system and a multi-coil shim system were compared. Advantage of dynamic shimming over static global shimming was shown in the human brain. Applications in proton spectroscopic imaging were shown for both shim systems. Dynamic B_0 shimming was then used to show whole brain metabolite maps acquired at 9.4T. For the first time, we show whole brain metabolite maps from ultra high field strengths at high spatial resolution.

- **S. Nassirpour** - Developed the acceleration and reconstruction schemes for MRSI acquisition. Collected the MRSI data with the very high order shim system. Processed and analyzed the MRSI data. Wrote the parts of the manuscript.

- **P. Chang -** Implemented all the hardware/software interface with the very high order B_0 shim system. Implemented the dynamic shim updating pipeline. Collected the MRSI data with the very high order shim system. Performed the processing and analysis for B_0 shim comparisons. Wrote the parts of the manuscript.

- **A. Aghaeifar -** Provided the multi-coil shim setup and helped collect the in vivo data with the multi-coil.
- **A. Henning -** Supervised and advised on the manuscript.

4 Appended Publications

Publication I

"High and ultra-high resolution metabolite mapping of the human brain using ^{1}H FID MRSI at 9.4T"

S Nassirpour, P Chang, A Henning

NeuroImage, 2016, DOI: https://doi.org/10.1016/j.neuroimage.2016.12.065

NeuroImage (xxxx) xxxx–xxxx

Contents lists available at ScienceDirect

NeuroImage

journal homepage: www.elsevier.com/locate/neuroimage

High and ultra-high resolution metabolite mapping of the human brain using ^{1}H FID MRSI at 9.4T

Sahar Nassirpour[a,b,*], Paul Chang[a,b], Anke Henning[a]

[a] Max Planck Institute for Biological Cybernetics, Spemannstr. 41, Tuebingen 72076, Germany
[b] IMPRS for Cognitive and Systems Neuroscience, Eberhard Karls University of Tübingen, Tübingen, Germany

ARTICLE INFO

Keywords:
Spectroscopic imaging
Ultra-high magnetic field
Human brain
Metabolite mapping
9.4 T
FID MRSI

ABSTRACT

Magnetic resonance spectroscopic imaging (MRSI) is a promising technique for mapping the spatial distribution of multiple metabolites in the human brain. These metabolite maps can be used as a diagnostic tool to gain insight into several biochemical processes and diseases in the brain. In comparison to lower field strengths, MRSI at ultra-high field strengths benefits from a higher signal to noise ratio (SNR) as well as higher chemical shift dispersion, and hence spectral resolution. This study combines the benefits of an ultra-high field magnet with the advantages of an ultra-short TE and TR single-slice FID-MRSI sequence (such as negligible J-evolution and loss of SNR due to T_2 relaxation effects) and presents the first metabolite maps acquired at 9.4 T in the healthy human brain at both high (voxel size of 97.6 μL) and ultra-high (voxel size of 24.4 μL) spatial resolutions in a scan time of 11 and 46 min respectively. In comparison to lower field strengths, more anatomically-detailed maps with higher SNR from a larger number of metabolites are shown. A total of 12 metabolites including glutamate (Glu), glutamine (Gln), N-acetyl-aspartyl-glutamate (NAAG), Gamma-amino-butyric acid (GABA) and glutathione (GSH) are reliably mapped. Comprehensive description of the methodology behind these maps is provided.

1. Introduction

Magnetic resonance spectroscopic imaging (MRSI) is a non-invasive imaging method which combines both spectroscopic and imaging techniques to acquire spatially resolved spectra. These spectra can be used to map the distribution of brain metabolites (termed the "neurochemical profile"). The spatial resolution in MRSI studies is usually limited by the available signal to noise ratio (SNR) and lengthy scan times, and hence is much lower than those of other imaging applications. Ideally, by reliably mapping a large number of metabolites at a high spatial resolution, one can achieve valuable insight into diseases with complex and local distribution of metabolites such as multiple sclerosis, tumors or focal ischemia (Mlynárik et al., 2008).

It has been shown previously that MRSI can benefit greatly from ultra-high field strengths and a number of MRSI studies at ultra-high fields on human brain have already been reported (7 T and initial results on 9.4 T) (Scheenen et al., 2008; Henning et al., 2009; Posse et al., 2013; Boer et al., 2012; Bogner et al., 2012; Chadzynski et al. 2015). The higher chemical shift dispersion, spectral resolution and signal to noise ratio achievable at higher field strengths was shown to greatly enhance the information content of the spectra (Henning et al., 2009; Bogner et al., 2012). Earlier studies at 7 T and above reported the detection of a comprehensive neurochemical profile only by single voxel spectroscopy (Tkac et al., 2001; Deelchand et al., 2010) and at lower field strengths either by 2D MRS methods (Schulte et al., 2006; Thomas et al., 2003; Fuchs et al. 2014) or spectral editing (Rothman et al., 1984; Hetherington et al., 1985; Rothman et al., 1993; Mescher et al., 1998; de Graaf and Rothman, 2001; Zhu et al., 2011).

Additionally, by using ultra short echo time (TE) sequences such as Free Induction Decay (FID) MRSI (Henning et al., 2009; Bogner et al., 2012; Boer et al., 2012), the SNR loss due to T_2 relaxation effects can be reduced. As a result, low concentrated and J-coupled metabolites such as Glutamate (Glu) and Myo-inositol (mI) can also be reliably detected (Henning et al., 2009; Bogner et al., 2012). Studies on 7 T using such sequences have hence shown to enable the mapping of a larger number of metabolites at higher spatial resolutions as compared to lower fields or even the studies performed at higher fields but with different sequences such as STEAM or semi-LASER localization (Ryner et al., 1995; Scheenen et al., 2008; Chadzynski et al., 2015;).

Another factor affecting the quality of the metabolite maps is the spatial resolution in which the MRSI study is performed. Due to decreased size of the side lobes of the point spread function (PSF) at

* Corresponding author at: Max Planck Institute for Biological Cybernetics, Spemannstr. 41, Tuebingen 72076, Germany.
E-mail address: sahar.nassirpour@tuebingen.mpg.de (S. Nassirpour).

http://dx.doi.org/10.1016/j.neuroimage.2016.12.065
Received 24 July 2016; Accepted 22 December 2016

higher spatial resolutions, signal bleeding from far-reaching voxels is reduced. Furthermore, the smaller voxel size translates into decreased partial volume effects and better local B_0 homogeneity (Gruber et al., 2003; Kirchner et al., 2016). As a result, metabolite maps acquired at higher spatial resolutions are more accurate and reveal more anatomical details. The typical in-plane matrix size of clinical MRSI studies at 3 T used for metabolite mapping in the brain is usually rather low with matrix sizes of about 16×16 or 20×20 (Hanson et al., 2000). This roughly translates to an in-plane voxel size of 20 mm×20 mm. Recently higher resolution maps have also been published at 7 T with matrix sizes of 32 × 32 which roughly translates to an in-plane voxel size of 6.2 mm×6.2 mm (Henning et al., 2009) or 64×64 (~3.1 mm×3.1 mm in-plane resolution) (Bogner et al., 2012; Boer et al., 2015). Acquiring at higher spatial resolutions directly translates into longer scan times which might not be practical in a clinical setting. Recently, Hangel et al. (2016) proposed that by using an optimized short TR and TE sequence such as FID-MRSI on a 7 T magnet, one can acquire MRSI data at an ultra-high spatial resolution of 128×128 (~1.5 mm×1.5 mm in-plane resolution) in a scan time of 41 min.

Considering the advantages offered by an ultra-high field magnet and an optimized short TR and TE FID-MRSI sequence, it is therefore proposed that high quality spectra from the human brain with high spectral resolution and ultra-high spatial resolution can be acquired at 9.4 T and can be used to map the spatial distribution of several metabolites in a reasonable scan time. In this paper, we present the first metabolite maps of 12 metabolites acquired at 9.4 T in the healthy human brain using a FID-MRSI sequence and provide a comprehensive description of the methodology and post-processing techniques behind them. For comparison purposes we acquired the maps both at a high spatial resolution of 64×64 (which translates into a nominal voxel size of 97.6 μL) and an ultra-high spatial resolution of 128×28 (nominal voxel size of 24.4 μL). The results are then compared and the competing effects of high spatial resolution and lower SNR are discussed.

2. Methods

All experiments were conducted on a 9.4 T whole-body scanner (Siemens, Erlangen, Germany) with an in-house developed 16 channel transmit (operating in circularly polarized (CP) mode) and 31 channel receive coil (Shajan et al., 2014). In-vivo single-slice ^{1}H FID MRSI datasets were acquired from brains of 10 healthy volunteers (5 for the high-resolution study and 5 for the ultra-high resolution one) using a customized FID MRSI sequence (Henning et al., 2009; Bogner et al., 2012). In all studies, the slice position was chosen to run through the periventricular white matter parallel to the Corpus Callosum. All studies in volunteers were approved by the local ethics committee and all volunteers gave their written informed consent. The details of the study are described in the sections below.

2.1. Data acquisition

As with any short TR MRSI sequence that uses water suppression, it is necessary to use the shortest possible water suppression scheme that would sufficiently suppress the water peak (residual water peak < 2% was empirically proven to be sufficient for avoiding baseline distortions resulting from the residual water peak and gradient modulation sideband artefacts). Additionally, for water suppression at 9.4 T, it is necessary to optimize the scheme such that it is insensitive to both T_1 variations and B_1^+ inhomogeneity, as the latter is more severe at higher fields. This would ensure that the water suppression scheme would work equally well across the entire volume of interest, and hence avoid ghosting artifacts caused by unsuppressed water peak residuals from the neighboring voxels.

A numerical optimization was hence performed using a non-linear constrained optimization algorithm performed by MATLAB's *fmincon* function (The Mathworks, Natick, MA, USA) to find the optimal number of pulses and the flip angles of the water suppression scheme. The objective of the minimization problem was that the residual water signal should be minimized over a range of T_1 values (1~3 seconds) corresponding to those occurring in the brain at 9.4 T and a range of B_1^+ values (assuming up to 50% inhomogeneity). As a result of this optimization and in the interest of keeping the water suppression scheme as short as possible, a 3-pulse water suppression scheme was found to be the optimal choice and was incorporated in the sequence prior to excitation. The water suppression pulses were unmodulated Hanning-filtered Gaussian pulses with a bandwidth of 180 Hz, duration of 5 ms and flip angles of 90°, 79.5° and 159° respectively. The inter-pulse delay between the three water suppression pulses as well as between the last water suppression pulse and the excitation pulse were all 20 ms. These pulses were interleaved with spoiler gradients with a spoiling momentum of 168 ms.mT/m which is sufficient for spoiling the signal (Bernstein et al., 2004). The entire water suppression scheme was 62.2 ms long. No additional fat or outer volume suppression was applied in this experiment in the interest of keeping the scan time clinically feasible and also avoiding high values of specific absorption rates (SAR) at 9.4 T.

An image-based second-order B_0 shimming on a rectangular shimming volume (with the same dimensions as the imaging volume) was performed for these studies using the vendor implemented B_0 shim routine. The following parameters were used for the FID-MRSI sequence: FOV 200×200 mm^2, slice thickness 10 mm, acquisition delay (TE) 1.5 ms, nominal flip angle 28 degrees (calculated according to Ernst formula for a T_1 value of about 1800 ms) that had to be scaled to 47 degrees in the protocol because the average flip angle produced by the coil across the slice was 55% of the nominal flip angle, TR 220 ms, spectral bandwidth 4000 Hz and 512 complex data points (acquisition time 128 ms which causes no truncation artifacts due to the shorter T_2 relaxation times at 9.4 T). To further reduce the scan-time, an elliptical k-space shuttering scheme was used for the phase encoding. For comparison of high versus ultra-high spatial resolution MRSI protocols, two different studies were performed: one with a matrix size of 128×128 leading to a nominal voxel size of 1.56×1.56×10 mm^3, and the other with a matrix size of 64×64 leading to a nominal voxel size of 3.12×3.12×10 mm^3. These scan protocols resulted in a scan time of 46 min for the 128×128 scan, and about 11 min for the 64×64 scan.

For eddy current and zero-order phase correction purposes, a water reference scan using the same sequence without incorporating the water suppression scheme was acquired from each subject. In order to avoid lengthy scan times, this water reference scan had half the spatial resolution of the original MRSI slice in each direction leading to one fourth of the original acquisition time. This way an additional 11 min and an additional 2.5 min scan time was added to the 128×128 and the 64×64 scan respectively. Afterwards in post-processing, the same water signal from each voxel in the water reference scan was used to correct the eddy current artifacts in a grid of 4 neighboring voxels in the original scan.

After each MRSI examination, a T_2-weighted 2D FLASH scout image (TR 312 ms, TE 9 ms, flip angle 25°) was recorded as an anatomical reference with the same slice position and properties as the MRSI study. Additionally, a contrast-minimized gradient echo image of the same slice was acquired with a short-TE 3D FLASH sequence (TR 5 ms, TE 0.8 ms, flip angle 15°). This image was later used for B_1^- correction (Wang et al., 2005), i.e., to compensate for the signal intensity variations induced by receiver inhomogeneity. Since tissue contrast cannot be completely eliminated even in the contrast-minimized image because of variations in the relaxation times of different tissue compartments, spatial low-pass Gaussian filtering was used to reduce the residual contrast. For visualization purposes, B_0 and B_1 maps were also acquired from the same slice with the same B_0 shim settings. For B_0 mapping a 2D gradient echo sequence with TR of 100 ms and delta TE of 0.76 ms was used. For B_1 mapping, an Actual

Flip Angle Imaging sequence (AFI) (Yarnykh, 2007) with a flip angle of 60 degrees, TR_1/TR_2 of 20 ms/100 ms and TE of 4 ms.

2.2. Reconstruction and spectral processing

All spectra were processed using a custom script written in MATLAB. The reconstruction steps were conducted in the following order and included spatial Hamming filtering, eddy current and zero-order phase correction using the low resolution water reference image (Klose, 1990) and coil combination using the singular-value-decomposition (SVD) method (Bydder et al., 2008). Post-processing steps included prediction of the missing points at the beginning of the FIDs using a backward linear prediction autoregressive algorithm (AR) based on Burg's method (Kay, 1998) and residual water peak removal using Hankel Lanczos (HLSVD) method (Cabanes et al., 2001) using 10 decaying sinusoids in the range of 4.4–5 ppm. Since the basis-set chosen for the fitting procedure in the next step of the analysis was not truncated and hence its linear phase did not match that of the acquired spectra, the predication of the missing points was performed to remove the linear phase introduced by the acquisition delay from all the spectra. The removal of the residual water peak was also necessary to avoid baseline distortions resulting from the previous steps (Henning et al., 2009). Lastly, in order to reduce the lipid artifacts introduced by the bleeding of the subcutaneous fat signal into the voxels of interest, an L_2-regularized fat suppression algorithm was applied to the reconstructed spectra (Bilgic et al., 2014). According to this non-iterative and fast method, by dividing the image into a brain and a fat region and requiring the lipid and metabolite spectra to be approximately orthogonal, effective lipid artifact reduction is achieved. The masks required for this method were defined manually using MATLAB's graphical user interface. No additional apodization or phase correction was applied.

2.3. Fitting

The spectra were fitted using the LCMODEL software (Provencher, 1993) in the range of 1.5 to 4.2 ppm. The basis-set was simulated using the GAMMA library (https://scion.duhs.duke.edu/vespa/gamma) and included spectra of 18 brain metabolites (namely GPC, Tau, Cre, Glc, Naa, Asc, Lac, GABA, NAAG, GSH, Glu, PE, mI, PCh, Ala, Gln, Scyllo and Asp) with a linewidth of 5 Hz. Metabolite maps were then created in MATLAB using the fitting results. In order to account for the strong receive inhomogeneity, the metabolite maps were corrected using the contrast-minimized gradient echo image. Alternatively, ratio maps (normalized to the Creatine (Cr) map) were also calculated.

3. Results

The results of each step of this study are presented in the following subsections.

3.1. B_1 and B_0 homogeneity

As mentioned in the previous section, for visualization purposes and in order to show the level of homogeneity of the fields that were present during the acquisition of these MRSI studies, B_0 and B_1^+ field maps were acquired at the end of each MRSI scan. Fig. 1 shows one example of such shimmed B_0 map along with the $B1^+$ map. The location of the slice is also shown in this figure. The standard deviation of the frequency shifts in the shimmed B_0 map across all 10 volunteers was 29.40 Hz. This level of B_0 homogeneity resulted in a voxel-wise full line width at half maximum (FWHM) as reported by LCMODEL for total Creatine (3.03 ppm) equal to 20.03 ± 0.55 Hz (mean ± standard deviation) averaged over the entire FOV of all 5 respective volunteer datasets for the high resolution scan (64×64) and 16.30 ± 0.88 Hz for the ultra-high resolution one (128×128). The spatial variation of the B_1 field resulted in variable flip angles across the brain with a mean flip angle equal to 56% ± 10% of the nominal flip angle across the entire FOV of all 10 volunteers.

3.2. Water suppression

To assess the performance of the proposed water suppression scheme, water suppression maps were produced by dividing the amplitude of the residual water peak in each voxel after water suppression to the original unsuppressed water peak of the same voxel. Fig. 1 shows an example of such map. The proposed water suppression scheme achieves an average suppression of 99.49% ± 0.17% of the original peak across the entire slice and all 10 volunteer datasets.

3.3. Prediction of the missing FID points

The missing point prediction procedure was found to solve the linear phase problem introduced by the missing points at the beginning of the FID due to the acquisition delay in all spectra. As a representative example, Fig. 2 shows an example reconstructed spectrum after all the processing steps mentioned in the Methods section are applied once with and once without the linear backward prediction of the missing point.

3.4. Retrospective fat suppression using L_2 regularization method

The fast L_2-regularized lipid suppression method was used with a Beta of 0.65 (as suggested in Bilgic et al. (2014)) and resulted in effective lipid signal artifact reduction. Fig. 3 shows example spectra from four different regions of the brain: three voxels from a region near the skull where the contamination is the largest and one from a more benign central region. The entire fat suppression algorithm after manually defining the masks of the brain and fat region, took 1.67 seconds on the whole dataset for the 64 × 64 study and 3.4 seconds for the128 × 128 dataset. These run times are based on a 2.3 GHz 6-core Intel CPU.

3.5. Spectra and metabolite maps

In order to show the quality and the information content of the acquired spectra, Fig. 4 shows representative sample spectra along with their fitting results from both the high resolution and the ultra-high resolution scan, both picked from the same position in the brain. The voxel position is also shown on the anatomical reference image for each case. As can be seen from this figure by visual inspection of the sample spectra we can distinguish up to12 metabolite peaks. The SNR of the high resolution dataset appears to be higher than that of the ultra-high resolution. This is also confirmed by the SNR values calculated from the reconstructed spectra right after the HLSVD water removal as the ratio between the absolute NAA peak maximum between 1.8 and 2.2 ppm and the root mean square of the residual of a linear fit to the real part of the spectrum between 10 and 11 ppm: an average of 121.6 ± 7.02 for the 64×64 scan versus 75.02 ± 3.55 for the 128 × 128 scan across the entire brain slice and all volunteers.

Fig. 5 shows the contrast-minimized image used for B_1^- correction before and after Gaussian spatial filtering, along with two sample metabolite maps from the high resolution scan before (left) and after (right) B_1^- correction. Some spatial variations of the metabolite levels in the uncorrected maps (especially in the periphery of the slice) appear to have the same pattern and can be traced back to the receiver inhomogeneity that is also apparent in the contrast-minimized image. This artifact seems to be compensated for after B^-_1 correction using the contrast-minimized image and the spatial variations seen in the corrected maps (right), such as higher Glu concentrations in gray matter and higher NAAG concentrations in white matter, are in better agreement with the anatomical reference.

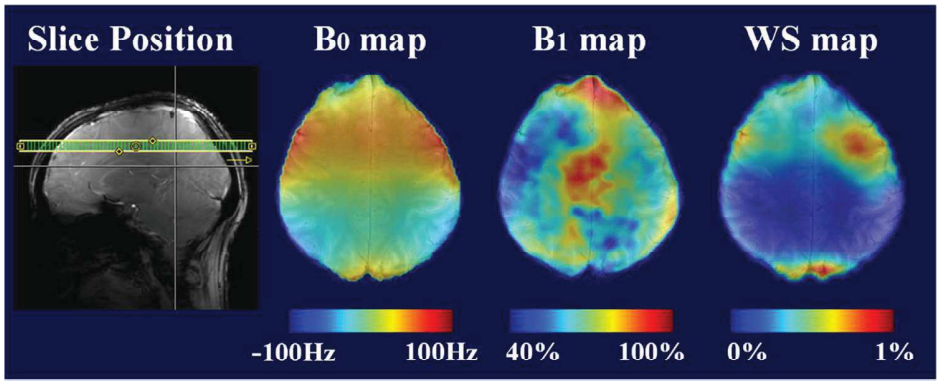

Fig. 1. The slice position along with the measured B_0, B_1^+ and water suppression quality maps. The B_1 values are shown as a percentage of the nominal flip angle of 90 degrees. The water suppression quality map shows the amplitude of the residual water peak as a percentage of the original unsuppressed one.

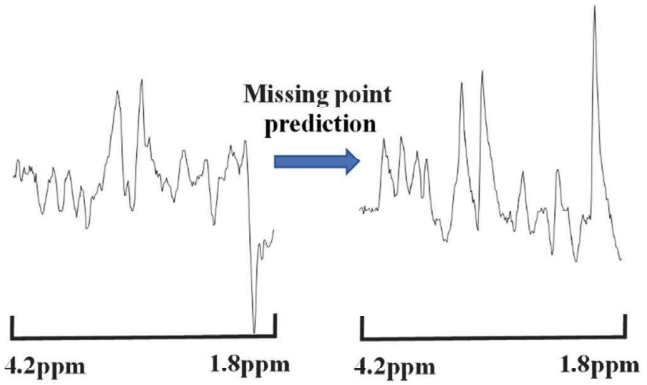

Fig. 2. sample reconstructed spectrum before (left) and after (right) the prediction of the missing FID points. This spectrum was selected from the central voxel of the 64 × 64 resolution study.

The B_1^- -corrected metabolite maps from 12 different metabolites along with their Cramer-Rao lower bound (CRLB) maps are shown for the high resolution and the ultra-high resolution studies of two representative volunteers in Figs. 6 and 8 respectively. As can be seen, the CRLB values of most of the metabolites (i.e. NAA, Cre, tCho, GSH, Glu, mI and GABA) in both high and ultra-high resolution datasets are lower than 20 in practically all voxels across the brain. This results in reliable quantification of the peaks. However, for the following lower concentrated metabolites: Scyllo, Gln, Tau, Asp (and NAAG for the ultra-high resolution dataset) the CRLB maps are shown on a different scale. The reason for this is due to higher CRLB values in some of the voxels where the fitting is not as reliable. The same maps but this time normalized to the Creatine (Cre) peak are shown again in Figs. 7 and 9 for both cases.

The metabolite maps from all 12 metabolites are shown in Fig. 10 for 4 additional volunteers (an additional 2 for the high-resolution case and an additional 2 for the ultra-high resolution one). The maps indicate good reproducibility of the study as similar spatial patterns are

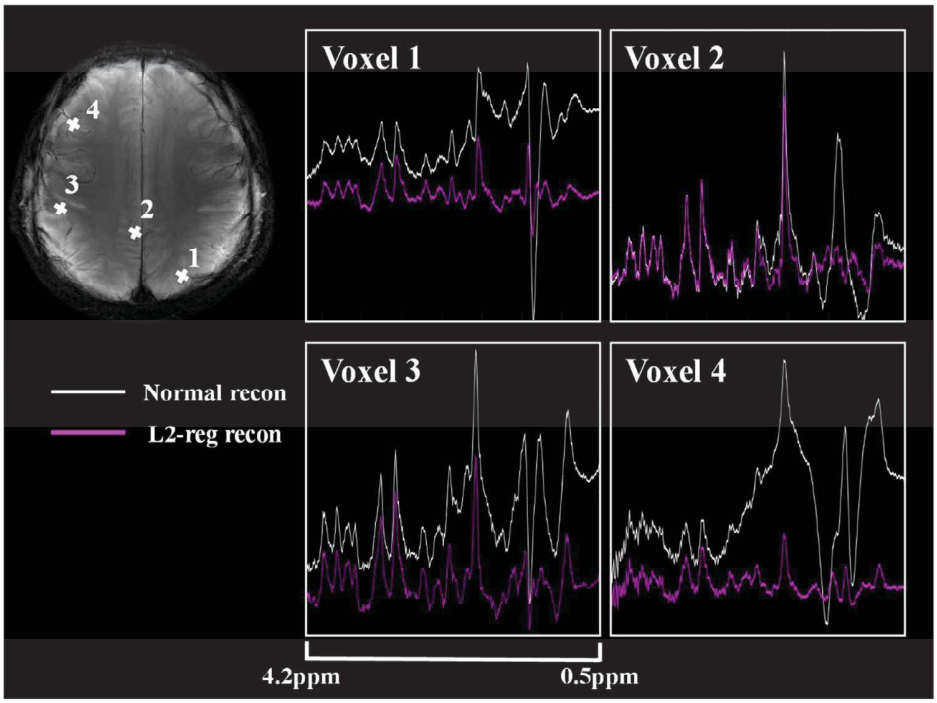

Fig. 3. Four representative spectra from different positions in the brain with (magenta) and without (white) applying the L_2-regularized fat suppression algorithm. The position of these voxels are indicated in white on the anatomical reference image (top left).

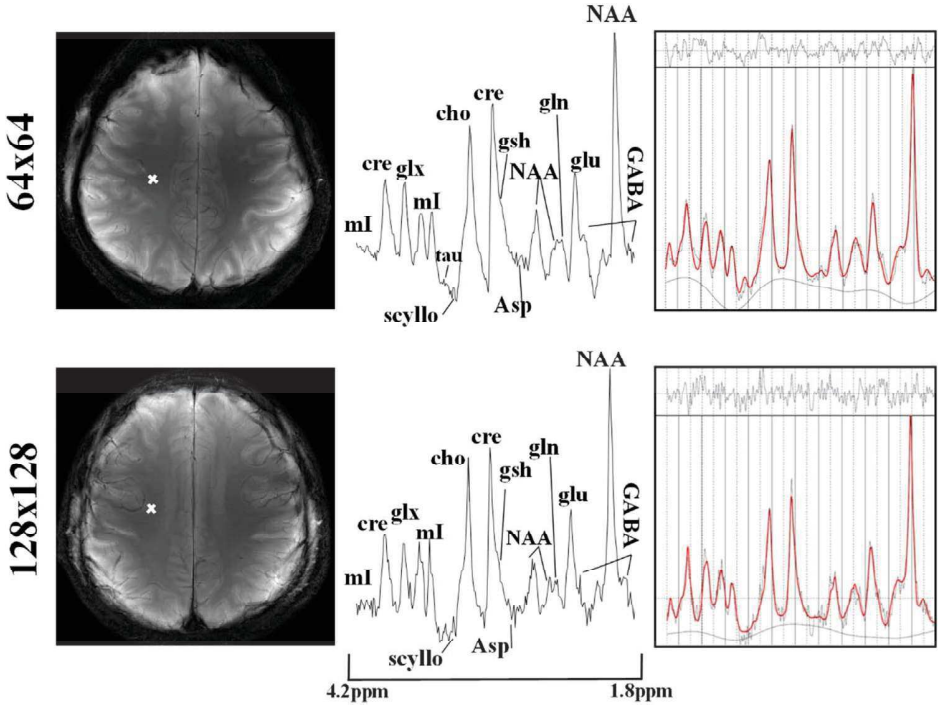

Fig. 4. Comparison of sample spectra from the high resolution (top row) versus ultra-high resolution scan (bottom row). Each row shows the position of the voxel were the spectrum was chosen from (left), the visual inspection of the spectrum (middle) and the LCMODEL fit results (right). All spectra are shown in the range of 1.8 to 4.2ppm.

observed across volunteers.

Finally, the water suppression quality (defined as the percentage of the original unsuppressed water peak that has been suppressed), SNR, FWHM (as reported by LCMODEL for total Creatine), as well as the CRLB and metabolite concentration ratio between a gray and white matter-rich region of interest are summarized in Table 1 for the high and ultra-high resolution datasets separately. The results are averaged across all volunteers. Note that the metabolite ratio between gray and white matter has not been reported for some of the lower concentrated metabolites as due to the lack of that metabolite in gray or white matter, LCMODEL has not fitted anything to them. This is also clear from the high CRLB values indicated in red in the same table.

4. Discussion

Single-slice FID MRSI on human brain at 9.4 T was performed in this study and was used to map the spatial distribution of several brain metabolites. Two different spatial resolutions were compared: a high spatial resolution of 64 × 64 and an ultra-high resolution of 128 × 128. By optimizing the water suppression scheme and without applying any additional fat suppression we were able to shorten the scan to a clinically acceptable scan time. The high spectral resolution and SNR offered by the ultra-high field strength of 9.4 T as well as the benefits of the FID sequence such as low signal loss and negligible J-evolution combined with effective reconstruction and post processing steps enabled reliable quantification of spectra from a larger number of voxels which resulted in maps with better anatomical correspondence as compared to previous 7 T results for low concentrated metabolites such as Gln and GABA (Henning et al., 2009; Bogner et al., 2012).

Of course the benefits of an ultra-high field magnet come at a price. As was shown in Fig. 1, there is a strong B_1^+ inhomogeneity that affects the signal levels in different areas of the brain. Furthermore, as can be seen even from the gradient echo anatomical image there is a strong receive sensitivity variation that affects the signal intensity (especially in the periphery) of the slice. Some spatial variations of the metabolite levels in the uncorrected maps can be traced back to these inhomogeneities. To compensate for this, B_1^- correction was done using a contrast-minimized gradient echo image, which has spatial signal intensity modulations that are dominated by the receive sensitivity B_1- as it is acquired at a very low flip angle. It should be noted that a comprehensive correction for both the B_1^+ and B_1^- profiles requires more sophisticated methods, for example (Zoelch and Henning, 2016) suggests using B_1^+ maps to perform Bloch simulations to determine the excitation profile. A combination of the latter with the herein described B_1^- maps reflects the resulting signal intensity modulation of the real data even more precisely and may be performed in future studies. Alternatively, Cr ratio metabolite maps, that intrinsically include B_1^+ and B_1^- corrections, were calculated in addition to the B_1^--corrected ones.

One solution to the B_1 inhomogeneity problem would be to use parallel transmit (pTX) pulses designed for B_1 inhomogeneity compensation which would result in a more homogenous excitation profile as well as a better quality of water suppression (Boer et al., 2012). Additionally, by designing spatial-spectral pulses we can selectively excite only regions of the spectrum and the brain (i.e. excluding the lipid) that we are interested in (Waxmann et al., 2016).

Even though the 2nd order B_0 shimming available at our scanner provided a reasonable FWHM of the peaks, still we see that the water suppression performance is affected in the regions where the B_0 variations are higher (3.1). By using higher-order and degree shimming (Pan et al., 2012) we can reduce this problem in future studies. Better B_0 shimming would also mean narrower peaks and better separation of the metabolites (Pan et al., 2012). Additionally, by modifying the shim routine such that an arbitrary volume of interest can be shimmed, we may improve the shimming results by better tailoring the shim region to the MRSI slice and by shimming the lipid region as a region of less interest (ROLI) (Boer et al., 2012; Fillmer et al., 2015).

The resulting water suppression map after applying the numerically optimized 3-pulse scheme in Fig. 1 shows a sufficient suppression of the water peak (< 1%) while keeping the duration of the scheme reasonably short (62.2 ms). The performance is indeed T_1 and B_1 insensitive as it results in equally well performance across all the

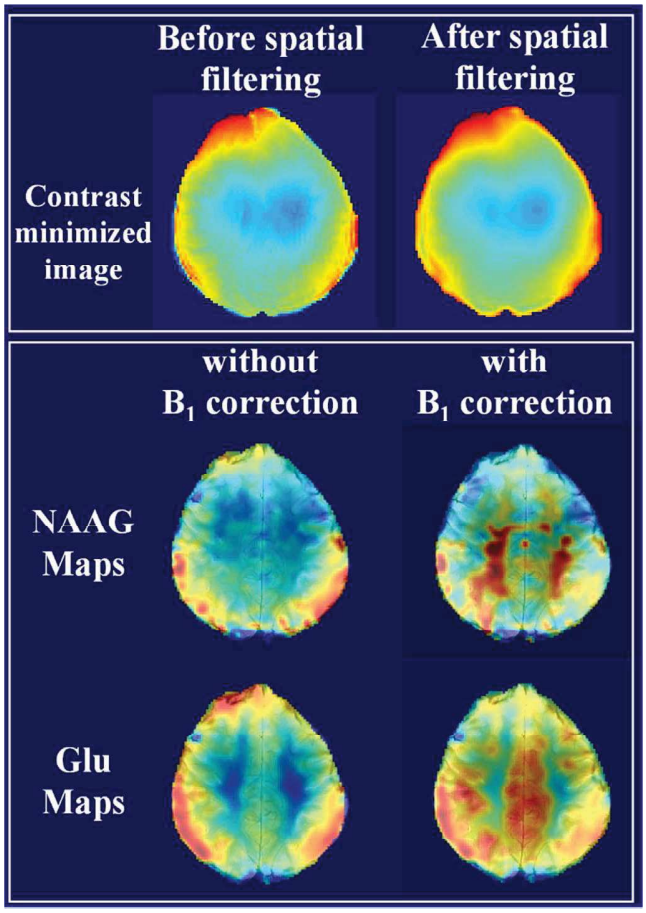

Fig. 5. Top: The contrast-minimized image used for B1-correction before and after spatial filtering, Bottom: Comparison of B_1-corrected versus uncorrected metabolite maps for two metabolites. The maps have been chosen from the high resolution MRSI dataset (64×64).

voxels. This will eliminate the gradient modulation side bands and prevent them from contaminating the spectra and being mistaken as real peaks (Henning et al., 2009).

Even though the acquisition delay was chosen to be as short as possible (1.5 ms), still the missing points at the beginning of the FID introduce a linear phase on the spectrum which makes it difficult to visually distinguish the peaks and also might cause the fitting software to fail if the basis-set is not truncated to match the phase of the acquired spectra (Henning et al., 2009). The post processing step of predicting the missing points via linear backward prediction solves this problem and puts all the peaks back in phase (3.3).

The studies were performed without the use of any lipid suppression techniques. Therefore spectral bleeding of the extracranial lipids due to the non-ideal SRF shape causes severe artifacts especially in regions close to skull. By using the L_2-regularized fat suppression reconstruction method (Bilgic et al., 2014) it was shown that these artifacts can be effectively reduced without reducing SNR or deteriorating the metabolite quality. This method is non-iterative, not computationally demanding and hence very fast. However, it should be noted that a limitation of this method is that because of the alteration of the lipid range of the spectra, it can no longer be used to assess the macromolecule or lipid content alterations of the spectra. Furthermore, the exact quantification of peaks close to this range such as GABA and NAAG might be affected.

The resulting processed spectra from both the high and ultra-high resolution MRSI data show high information content even by visual inspection (3.5). It can be seen that while the high resolution spectra (64×64) show higher SNR, the ultra-high resolution scan results in narrower. By comparing these values to the results reported for a similar study performed at 7 T (64 × 64 FID MRSI sequence) (Bogner et al., 2012; Povazan et al., 2015; Hangel et al., 2015; Strasser et al., 2016) we can readily see the SNR gain offered by the higher field strength. However, naturally, due to the increased field inhomogeneity at 9.4 T the linewidths reported at 7 T are lower (20.03 ± 0.5 Hz at 9.4 T versus 14 ± 3 Hz at 7 T).

The spectra were then fed into LCMODEL for fitting analysis. As a result, for the first time at 9.4 T, high and ultra-high resolution maps of 12 metabolites including NAA, NAAG, Cho (PCh + GPC), tCre (PCr + Cr), mI, Glu, Gln, GABA, GSH, Tau, Scyllo and Asp in human brains presented. The high SNR and quality of the spectra along with the precise localization of the sequence, resulted in minimized artifacts which in turn resulted in maps that are in good agreement with the anatomical reference. Characteristic differences between gray and white matter are evident for certain metabolites from the metabolite maps and the quantitative analysis in a gray versus white matter rich region of interest across volunteers. The results are in good agreement with previously reported maps on lower field strengths (such as higher Cre, Glu, GSH and mI concentration in gray matter (Gasparovic et al., 2006; Srinivasan et al., 2009; Henning et al., 2009; Maudsley et al., 2009; Emir et al., 2012; Bogner et al., 2012; Povazan et al., 2015; Hangel et al., 2015; Strasser et al., 2016; Maudsley et al., 2012), higher NAAG concentration in white matter (Henning et al., 2009; Povazan et al., 2015) as well as higher GABA concentration in gray matter (Emir et al., 2012), but show more anatomical details due to higher spatial resolution and also as a result of LCMODEL being able to fit a higher number of voxels reliably due to the high quality of the spectra.

The comparison of high versus ultra-high resolution metabolite maps (3.5) shows that even though for higher concentrated metabolites (such as NAA, Cre, mI and Cho) both resolutions lead to low CRLB values (lower than 10 in almost all voxels across the whole FOV), naturally the ultra-high resolution one reveals more anatomical details, but appears slightly noisier.

In comparison to lower field strengths, the added value of 9.4 T becomes more obvious in the case of metabolites like Glu, Gln, GABA and GSH. Studies on 7 T either did not show the maps for GABA and GSH (Bogner et al., 2012; Povazan et al., 2015; Hangel et al., 2015; Strasser et al., 2016) or showed very patchy maps (Henning et al., 2009). Furthermore, at 9.4 T we were able to quantify and map Glu and Gln separately whereas in previous studies they are often shown in one map (Glx) (Bogner et al., 2012; Povazan et al., 2015; Hangel et al., 2015; Strasser et al., 2016). The comparison of high versus ultra-high resolution maps for these metabolites shows that for Glu and mI both resolutions result in reliable maps which have CRLB values lower than 12 in all voxels across the slice. In case of GABA, still the maps are highly reliable for both resolutions (CRLBS lower than 20), but the high resolution map has a lower average CRLB compared to the ultra-high case.

However, in the case of lower concentrated metabolites (such as Gln, Asp, NAAG, Scyllo and Tau) there is a trade-off between having higher spatial resolution and having more voxels reliably mapped (with low CRLB values). As an example of this we can look at the NAAG and Taurine maps and compare it between the two resolutions. The CRLB values reveal that a larger area of the brain was mapped reliably in the lower resolution MRSI dataset. This trade-off stems from the lower SNR of the ultra-high resolution scan which in turn is a result of smaller voxel size (Gruber et al., 2012).

The aforementioned trade-off between highly spatially resolved maps and being able to map a greater number of metabolites including those with small concentrations, can be mediated by acquiring more averages in the high resolution study to compensate for the reduced SNR caused by smaller voxel sizes. However this will increase the scan time and make it impractical for clinical settings. One solution to this would be to take advantage of parallel imaging techniques and combine

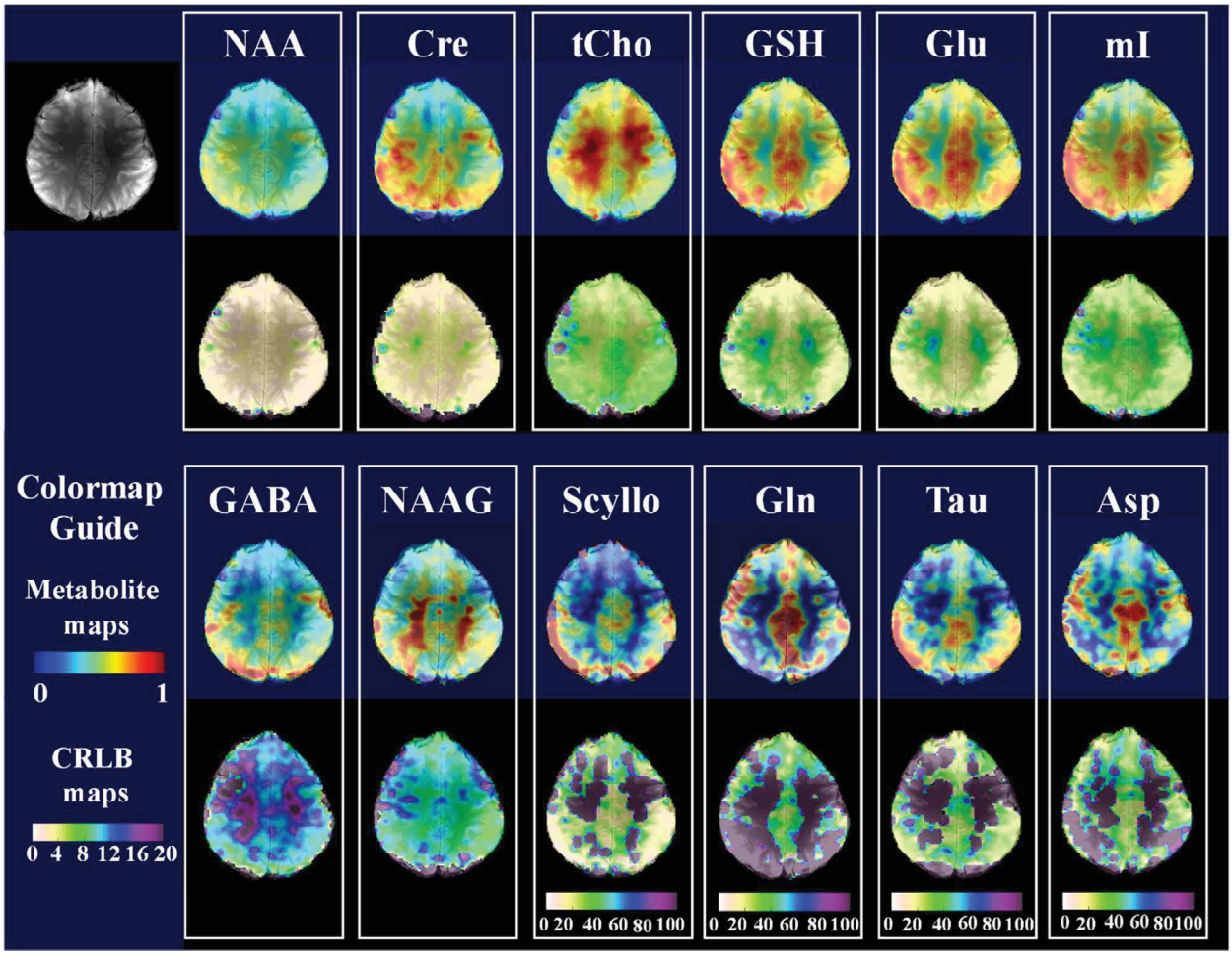

Fig. 6. High resolution (64×64) metabolite maps for 12 different metabolites along with the anatomical reference scan (top left). The CRLB maps are shown below the metabolite map in each box. Note the different scaling of the CRLB maps in the last four metabolites (Scyllo, Gln, Tau and Asp).

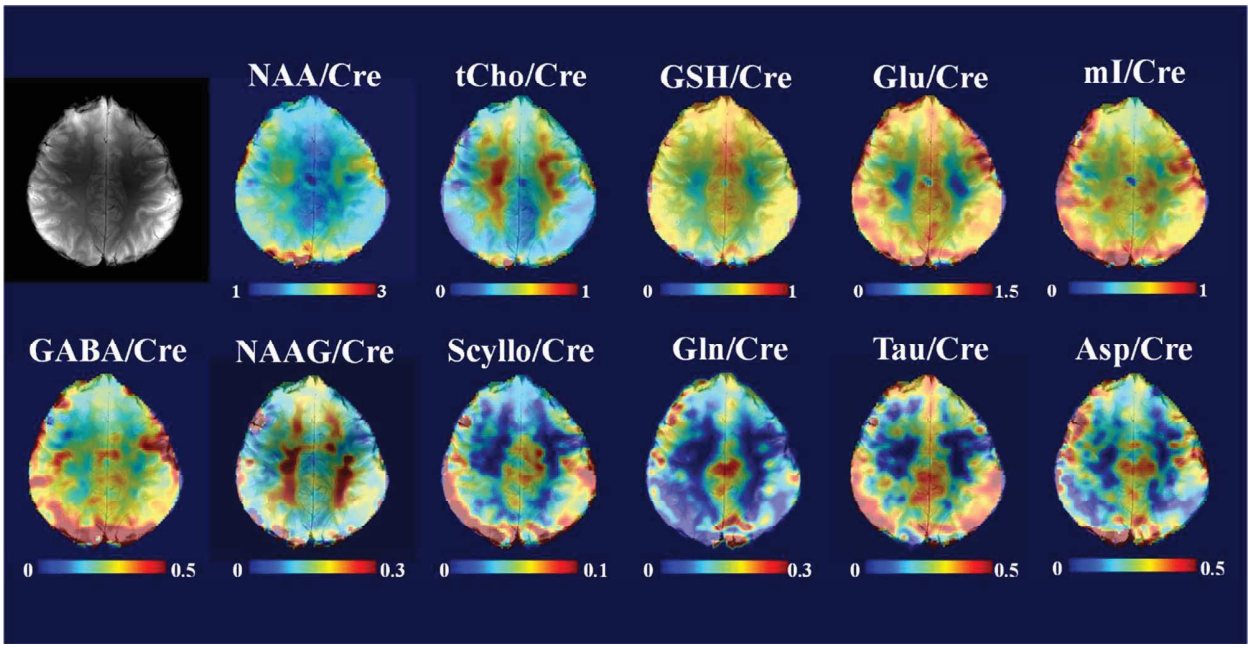

Fig. 7. High resolution (64×64) ratio maps for 11 different metabolites along with the anatomical reference scan (top left).

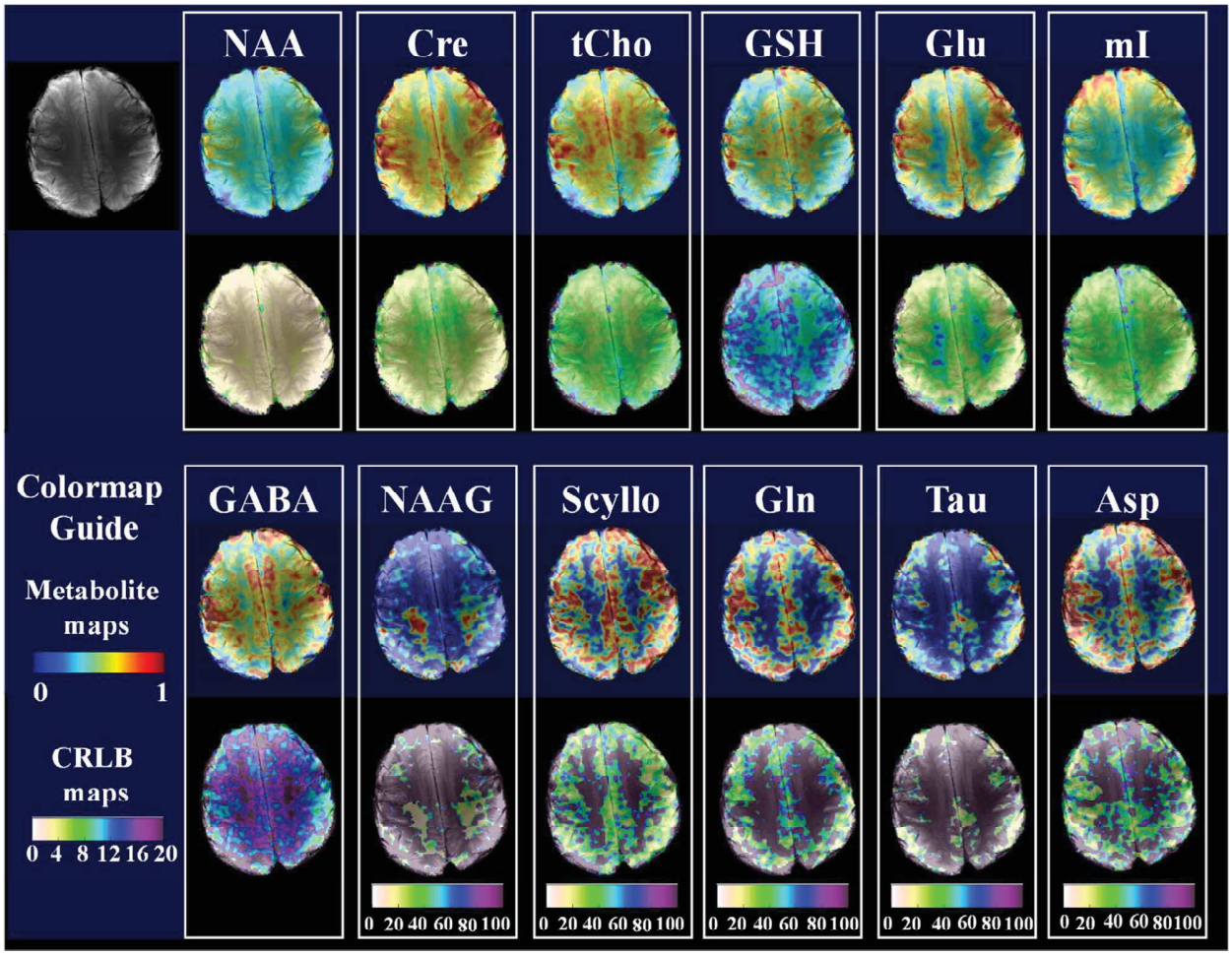

Fig. 8. Ultra-high resolution (128×128) metabolite maps for 12 different metabolites along with the anatomical reference scan (top left). The CRLB maps are shown below the metabolite map in each box. Note the different scaling of the CRLB maps in the last five metabolites (Scyllo, NAAG, Gln, Tau and Asp).

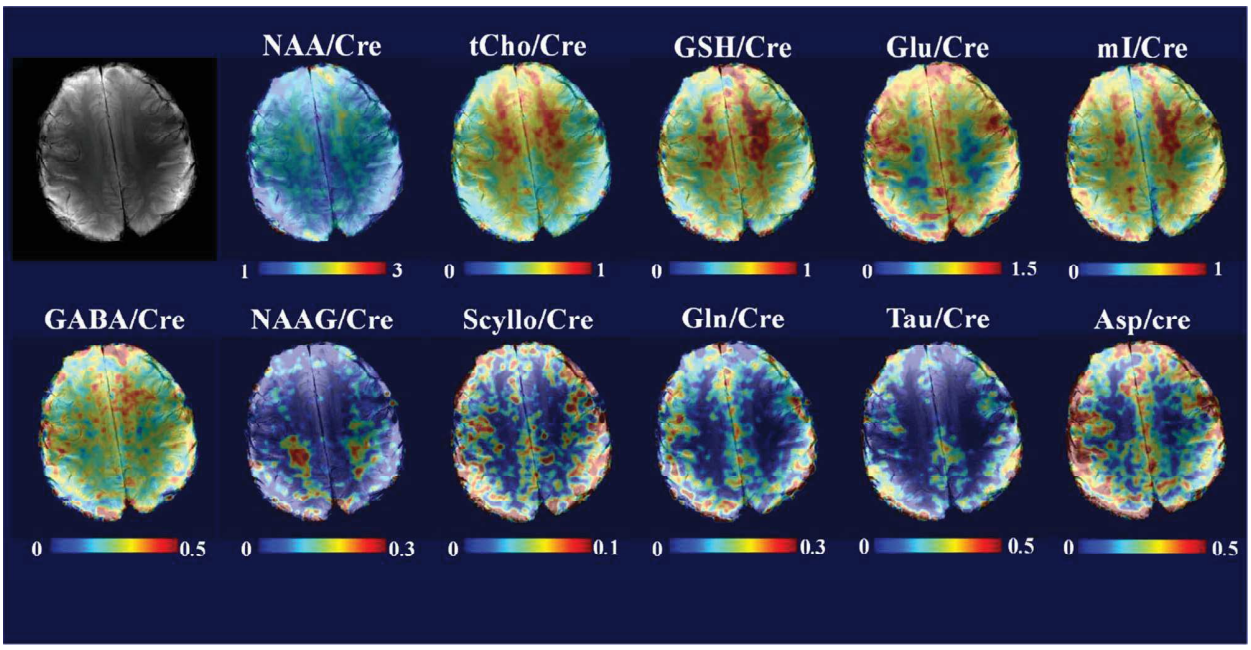

Fig. 9. Ultra-high resolution (128×128) ratio maps for 11 different metabolites along with the anatomical reference scan (top left).

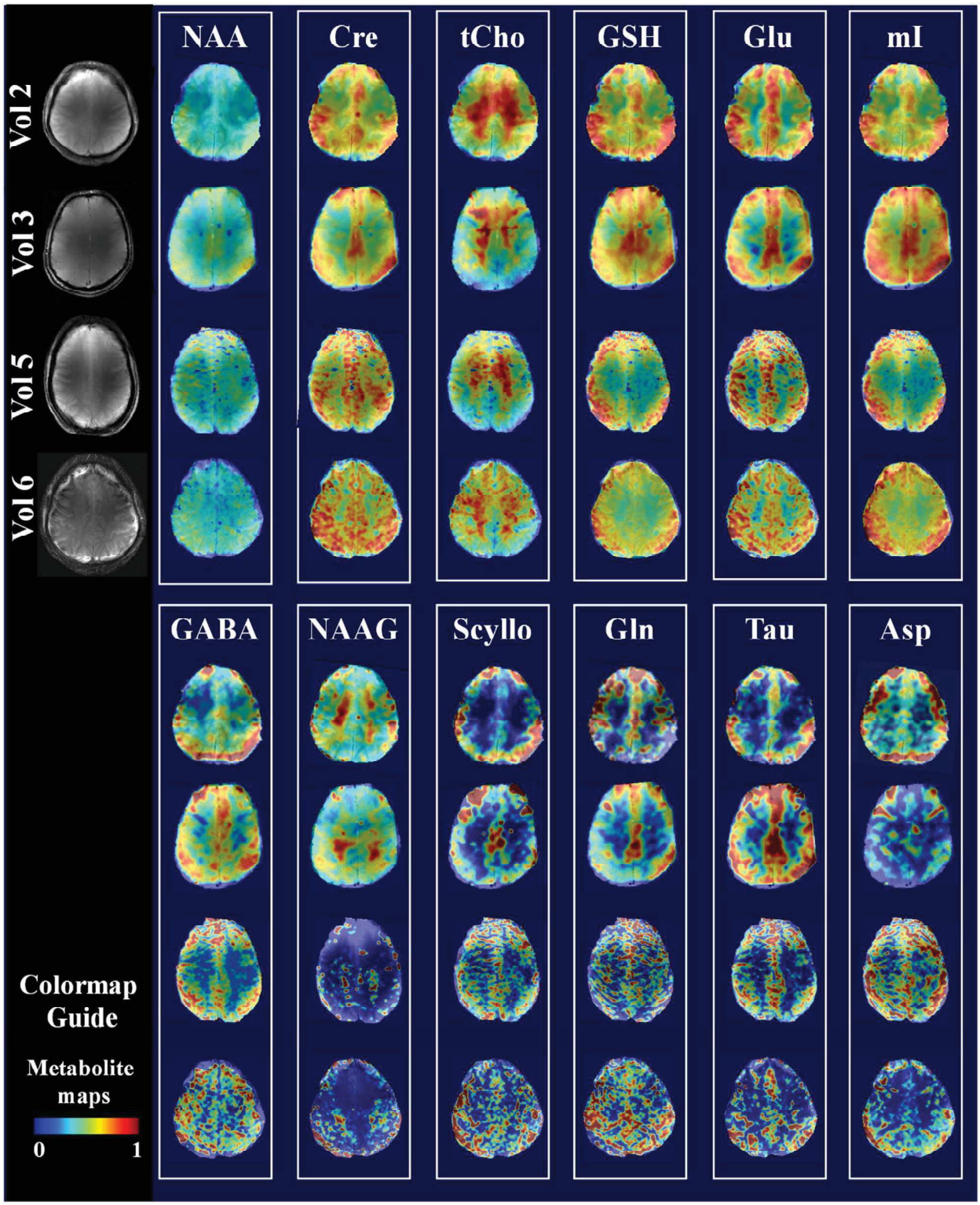

Fig. 10. Qualitative reproducibility assurance shown for 4 additional volunteers. Volunteers 2 and 3 have been scanned at a high spatial resolution of 64×64, while volunteers 5 and 6 have been scanned at the ultra-high spatial resolution of 128×128.

the FID MRSI sequence with acceleration techniques such as SENSE (Kirchner et al., 2015), GRAPPA (Hangel et al., 2015), EPSI (Maudsley et al., 2012) or CAIPIRINHA (Strasser et al., 2016). By using special reconstruction and SNR boosting techniques, this combination was shown to be able to accelerate the scan without deteriorating the SNR at 7 T (Kirchner et al., 2015; Kirchner et al., 2016). It has yet to be studied how these would work in the high spatial resolution cases and how they will affect the quality of the metabolite maps.

It should be noted that even though this study was performed at a short TE of 1.5ms, there is a strong T_1 weighting due to the short TR. One solution to this would be to apply tissue segmentation followed by a voxel-wise relaxation attenuation correction that would account for

Table 1
Quantitative comparison of high versus ultra-high resolution metabolite mapping at 9.4 T.

	64x64	128x128
SNR	121.6 ± 7.02	75.02 ± 3.55
Water supp. factor	99.46 ± 0.23	99.65 ± 0.15
FWHM	20.03 ± 0.55	16.30 ± 0.80

	CRLB (%) (GM ± SD : WM ± SD)		Met. Conc. Ratio. (GM/WM ± SD)	
	64x64	128x128	64x64	128x28
NAA	2.32±0.49 : 2.18±0.73	3.31±0.92 : 3.06±1.72	1.09 ± 0.03	1.10 ± 0.05
Cre	1.99±0.63 : 2.16±0.65	5.21±1.86 : 5.27±2.71	1.22 ± 0.12	1.28 ± 0.14
tCho	5.39±1.5 : 4.61±0.42	8.0±2.83 : 6.11±1.70	0.77 ± 0.06	0.76 ± 0.09
GSH	3.90±0.10 : 4.42±0.35	11.31±2.49 : 16.64±4.30	1.25 ± 0.07	1.17 ± 0.29
Glu	3.43±1.01 : 5.90±0.42	7.44±2.16 : 10.79±5.44	1.51 ± 0.04	1.54 ± 0.05
mI	4.85±1.05 : 5.22±1.42	6.40±2.35 : 7.36±1.62	1.23 ± 0.08	1.20 ± 0.78
GABA	11.13±2.01 : 20.67±0.97	15.78±4.03 : 25.55±8.11	1.35 ± 0.11	1.24 ± 0.20
NAAG	12.80±2.41 : 9.90±0.5	16.06±3.26 : 532±216.07	0.53 ± 0.09	N/A
Scyllo	24.19±1.43 : 287±85.08	35.69±10.23 : 435±157.98	N/A	N/A
Gln	28.05±6.62 : 310±79.21	55.18±14.19 : 536±379.21	N/A	N/A
Tau	26.57±2.51 : 90.90±9.9	35.72±5.62 : 417±145.86	N/A	N/A
Asp	33.14±1.19 : 304±50.84	69.89±12.93 : 338±139.75	N/A	N/A

differences in the relaxation times across different tissues (Gasparovic et al. 2006; Zoelch and Henning, 2016). Additionally, due to the short TE and TR of the sequence, it is advisable to include the macromolecules in the basis-set for more reliable quantification of the metabolites (Povazan et. al, 2015; Geades et al., 2016).

As a final note, the slice thickness used in this study was relatively thick (10mm) as this was a single-slice study and resolution in the sagittal direction was not of concern. However, to match the in-plane resolution and in future multi-slice studies, a thinner slice thickness could be used.

5. Conclusion

In this study we showed for the first time that ^{1}H FID MRSI of the human brain at 9.4 T along with LCMODEL analysis allows for the visualization of the spatial distribution of 12 metabolites in a scan time. By optimizing the water suppression scheme and other scan parameters combined with robust reconstruction techniques, high quality spectra were acquired. This enabled the mapping of a larger number of metabolites including low concentrated ones such as NAAG, Tau, Asp, Scyllo, Gln, and GABA at high (97.6 μL) and ultra-high (24.2 μL) spatial resolutions with high reproducibility. The maps had higher SNR and corresponded better to the underlying anatomy as compared to previous 7 T results (Henning et al., 2009; Bogner et al., 2012; Povazan et al., 2015; Hangel et al., 2015; Strasser et al., 2016).

Comparison of high versus ultra-high spatial resolution maps showed that while the ultra-high resolution MRSI data results in anatomically detailed maps for major metabolites, the decreased SNR makes it more difficult to map the lower concentrated metabolites reliably in all the voxels.

Acknowledgements

The authors would like to thank Dr. Rolf Pohmann for the implementation of the AFI sequence, Dr. Shajan Gunamony for providing the RF coil and Dr. Grzegorz Chadzynski for helpful information regarding the prediction of the missing FID points. This study was supported by the European Research Council Starting grant, project SYNAPLAST MR #679927.

References

Bernstein, M., King, K., Zhou, X., 2004. Correction Gradients in Handbook of MRI Pulse Sequences, Elsevier.

Bilgic, B., Chatnuntawech, I., Fan, A.P., Setsompop, K., Cauley, S.F., Wald, L.L., Adalsteinsson, E., 2014. Fast image reconstruction with L2-regularizationJ. Magn. Reson. Imag. 40, 181–191.

Boer, V.O., Klomp, D.W.J., Juchem, C., Luijten, P.R., de Graaf, R.A., 2012. Multislice ^{1}H MRSI of the human brain at 7 T using dynamic B_0 and B_1 shimming. Magn. Reson. Med. 68, 662–670.

Boer, V.O., Van de Lindt, T., Luijten, P.R., Klomp, D.W.J., 2015. Lipid suppression for brain MRI and MRSI by means of a dedicated crusher coil. Magn. Reson. Med. 73, 2062–2068.

Bogner, W., Gruber, S., Trattnig, S., Chmelik, M., 2012. High-resolution mapping of human brain metabolites by free induction decay 1H MRSI at 7 T. NMR Biomed. 25 (6), 873–882.

Bydder, M., Hamilton, G., Yokoo, T., Sirlin, C.B., 2008. Optimal phased-array combination for spectroscopy. Magn. Reson. Imaging 26 (6), 847–850.

Cabanes, E., Confort-Gouny, S., Le Fur, Y., Simond, G., Cozzone, P.J., 2001. Optimization of residual water signal removal by HLSVD on simulated short echo time proton MR spectra of the human brain. J. Magn. Reson. 150 (2), 116–125.

Chadzynski, G.L., Pohmann, R., Shajan, G., Kolb, R., Bisdas, S., Klose, U., Scheffler, K., 2015. In vivo proton magnetic resonance spectroscopic imaging of the healthy human brain at 9.4 T: initial experience. Magn. Reson. Mater. Phys. 28, 239–249.

Deelchand, D.K., Van de Moortele, P.F., Adriany, G., Iltis, I., Andersen, P., Strupp, J.P., Vayghan, T., Ugurbil, K., H PG, 2010. In vivo 1H NMR spectroscopy of the human brain at 9.4 T: initial results. J. Magn. Reson. 1, (74:80).

de Graaf, R.A., Rothman, D.L., 2001. Detection of gamma-aminobutyric acid (GABA) by longitudinal scalar order difference editing. J. Magn. Reson. 152, 124–131.

Emir, U.E., Auerbach, E.J., Van De Moortele, P.F., Marjanska, M., Ugurbil, K., Terpstra, M., Tkac, I., Oza, G., 2012. Regional neurochemical profiles in the human brain measured by 1H MRS at 7 T using local B1 shimming. NMR Biomed. 25 (1), 152–160.

Fillmer, A., Kirchner, T., Cameron, D., Henning, A., 2015. Constrained image-based B_0 shimming accounting for "local minimum traps" in the optimization and field inhomogeneities outside the region of interest. Magn. Reson. Med. 73, 1370–1380.

Fuchs, A., Boesiger, P., Schulte, R.F., Henning, A., 2014. Profit revisited. Magn. Reson. Med. 71 (2), 458–468.

Gasparovic, C., Song, T., Devier, D., Bockholt, H.J., Caprihan, A., Mullins, P.G., Posse, S., Jung, R.E., Morrison, L.A., 2006. Use of tissue water as a concentration reference for proton spectroscopic imaging. Magn. Reson. Med. 55 (6), 1219–1226.

Geades, N., Wismans, C., Damen, M., Gowland, P., Hoogduin, H., Boer, V., Klomp, D., Wijnen, J., 2016. Evidence for regional and spectral differences of macromolecule signals in human brain using a crusher coil at 7 T. Proc. ISMRM.

Gruber, S., Mlynarik, V., Moser, E., 2003. High-resolution 3D proton spectroscopic imaging of the human brain at 3 T: snr issues and application for anatomy-matched voxel sizes. Magn. Reson. Med. 49, 299–306.

Hangel, G., Strasser, B., Povazan, M., Gruber, S., Chmelik, M., Gajdosik, M., Trattnig, S., Bogner, W., 2015. Lipid suppression via double inversion recovery with symmetric frequency sweep for robust 2D-GRAPPA-accelerated MRSI of the brain at 7 T. NMR Biomed.. http://dx.doi.org/10.1002/nbm.3386.

Hangel, G., Strasser, B., Považan, M., Heckova, E., Hingerl, L., Boubela, R., Gruber, S., Trattnig, S., Bogner, W., 2016. Ultra-high resolution brain metabolite mapping at 7 T by short-TR Hadamard-encoded FID-MRSI. Neuroimage. http://dx.doi.org/10.1016/j.neuroimage.2016.

Hanson, L.G., Adalsteinsson, E., Pfefferbaum, A., Spielman, D.M., 2000. Optimal voxel size for measuring global gray and white matter proton metabolite concentrations using chemical shift imaging. Magn. Reson Med. 44 (1), 10–18.

Henning, A., Fuchs, A., Murdoch, J.B., Boesiger, P., 2009. Slice-selective FID acquisition, localized by outer volume suppression (FIDLOVS) for 1H-MRSI of the human brain at 7 T with minimal signal loss. NMR Biomed. 22 (7), 683–696.

Hetherington, H.P., Avison, M.J., Shulman, R.G., 1985. 1H homonuclear editing of rat brain using semiselective pulses. Proc. Natl. Acad. Sci. USA 82, 3115–3118.

Kay, S.M., 1998. Modern Spectral Estimation: theory and Application. Prentice Hall, Englewood Cliffs, NJ.

Kirchner, T., Fillmer, A., Tsao, J., Pruessman, K.P., Henning, A., 2015. Reduction of voxel bleeding in highly accelerated parallel ^{1}H MRSI by direct control of the spatial response function". Magn. Reson. Med. 73, 469–480.

Kirchner, T., Fillmer, A., Henning, A., 2016. Mechanisms of SNR and line shape improvement by B_0 correction in over discrete MRSI reconstruction. Magn. Reson. Med.. http://dx.doi.org/10.1002/mrm.26118.

Klose, U., 1990. In vivo proton spectroscopy in presence of eddy currents. Magn. Reson. Med. 14 (1), 26–30.

Maudsley, A.A., Domenig, C., Govind, V., Darkazanli, A., Studholme, C., Arheart, K., Bloomer, C., 2009. Mapping of brain metabolite distributions by volumetric proton MR spectroscopic imaging (MRSI). Magn. Reson. Med. 61 (3), 548–559.

Maudsley, A.A., Govind, V., Arheart, K.L., 2012. Associations of age, gender and body mass with 1H MR-observed brain metabolites and tissue distributions. NMR Biomed. 25 (4), 580–593.

Mescher, M., Merkle, H., Kirsch, J., Garwood, M., Gruetter, R., 1998. Simultaneous in-vivo spectral editing and water suppression. NMR Biomed. 11, 266–272.

Mlynárik, V., Kohler, I., Gambarota, G., Vaslin, A., Clarke, P.G.H., Gruetter, R., 2008. Quantitative proton spectroscopic imaging of the neurochemical profile in rat brain with microliter resolution at ultra-short echo times. Magn. Reson Med. 59 (1), 52–58.

Pan, J.W., Lo, K.M., Hetherington, H.P., 2012. Role of very high order and degree B_0 shimming for spectroscopic imaging of the human brain at 7 T. Magn. Reson. Med. 1, 1007–1017.

Posse, S., Otazo, R., Dager, S.R., Alger, J., 2013. MR spectroscopic imaging: principles and recent advances. J. Magn. Reson. Imaging 37, 1301–1325.

Povazan, M., Hangel, G., Strasser, B., Gruber, S., Chmelik, M., Trattnig, S., Bogner, W., 2015. Mapping of brain macromolecules and their use for spectral processing of 1H-MRSI data with an ultra-short acquisition delay at 7 T. NeuroImage. http://dx.doi.org/10.1016/j.neuroimage.2015.07.042.

Provencher, S.W., 1993. Estimation of metabolite concentrations from localized in vivo proton NMR spectra. Magn. Reson. Med. 30, 672–679.

Rothman, D.L., Behar, K.L., Hetherington, H.P., Shulman, R.G., 1984. Homonuclear 1H double-resonance difference spectroscopy of the rat brain in vivo. Proc. Natl. Acad. Sci. USA 81 (20), 6330–6334.

Rothman, D.L., Petroff, O.A., Behar, K.L., Mattson, R.H., 1993. Localized 1H NMR measurements of gamma-aminobutyric acid in human brain in-vivo. Proc. Natl. Acad. Sci. USA 90, (5662:5666).

Ryner, L.N., Sorenson, J.A., Thomas, M.A., 1995. 3D localized 2D NMR spectroscopy on an MRI scanner. J. Magn. Reson. B 107, 126–137.

Scheenen, T.W.J., Heerschap, A., Klomp, D.W.J., 2008. Towards 1H-MRSI of the human brain at 7T with slice-selective adiabatic refocusing pulses. MAGMA 21, 95–1001.

Schulte, R.F., Lange, T., Beck, J., Meier, D., Boesiger, P., 2006. Improved two dimensional J-resolved spectroscopy. NMR Biomed. 19, 264–270.

Shajan, G., Kozlov, M., Hoffmann, J., Turner, R., Scheffler, K., Pohmann, R., 2014. A 16-channel dual-row transmit array in combination with a 31-element receive array for human brain imaging at 9.4 T. Magn. Reson. Med. 71, 870–879.

Srinivasan, R., Ratiney, H., Hammond-Rosenbluth, K.E., Pelletier, D., Nelson, S.J., 2010. MR spectroscopic imaging of glutathione in the white and gray matter at 7 T with an application to multiple sclerosis. Magn. Reson. Med. 28, 163–170.

Strasser, B., Povazan, M., Hangel, G., Hingerl, L., Chmelik, M., Gruber, S., Trattnig, S., Bogner, W., 2016. (2+1)D-CAIPIRINHA accelerated MR spectroscopic imaging of the brain at 7 T. Magn. Reson. Med.. http://dx.doi.org/10.1002/mrm.26386.

Thomas, M.A., Hattori, N., Umeda, M., Sawada, T., Naruse, S., 2003. Evaluation of two-dimensionam L-COSY and JPRESS using a 3 T MRI scanner: from phantoms to human brain in vivo. NMR Biomed. 16, 245–251.

Tkac, I., Andersen, P., Adriany, G., Merkle, H., Ugurbil, K., Gruetter, R., 2001. In vivo 1H NMR spectroscopy of the human brain at 7 T. Magn. Reson. Med. 46, 451–456.

Wang, J., Qiu, M., Yang, Q.X., Smith, M.B., Constable, R.T., 2005. Measurement and correction of transmitter and receiver induced nonuniformities in vivo. Magn. Reson. Med. 53, 408–417.

Waxmann, P., Mekle, R., Schubert, F., Bruhl, R., Kuehne, A., Lindel, T.D., Seifert, F., Speck, O., Ittermann, B., 2016. A new sequence for shaped voxel spectroscopy in the human brain using 2D spatially selective excitation and parallel transmission. NMR Biomed.. http://dx.doi.org/10.1002/nbm.3558.

Yarnykh, V.L., 2007. Actual flip-angle imaging in the pulsed steady state: a method for rapid three-dimensional mapping of the transmitted radiofrequency field. Magn. Reson. Med. 57 (1), 192–200.

Zhu, H., Edden, R.A.E., Ouwerker, R., Barker, P., 2011. High resolution spectroscopic imaging of GABA at 3 T. Magn. Reson. Med. 65 (3), 603–609.

Zoelch, N., Henning, A., 2016. High Precision External Reference Standards for Quantitative in Vivo Magnetic Resonance Spectroscopy, Dissertation ETH Zurich No. 23482.

Publication II

"Non-water Suppressed ^{1}H FID-MRSI at 3T and 9.4T"

P Chang*, **S Nassirpour***, N Avdievich, A Henning

Magnetic Resonance in Medicine, 2017, DOI: https://doi.org/10.1002/mrm.27049

FULL PAPER

Magnetic Resonance in Medicine 00:00–00 (2017)

Non-Water-Suppressed ^{1}H FID-MRSI at 3T and 9.4T

Paul Chang,[1,2†]* Sahar Nassirpour,[1,2†] Nikolai Avdievitch,[1,3] and Anke Henning[1,3]

Purpose: This study investigates metabolite concentrations using metabolite-cycled ^{1}H free induction decay (FID) magnetic resonance spectroscopic imaging (MRSI) at ultra-high fields.
Methods: A non-lipid-suppressed and slice-selective ultra-short echo time (TE) ^{1}H FID MRSI sequence was combined with a low-specific absorption rate (SAR) asymmetric inversion adiabatic pulse to enable non-water-suppressed metabolite mapping using metabolite-cycling at 9.4T. The results were compared to a water-suppressed FID MRSI sequence, and the same study was performed at 3T for comparison. The scan times for performing single-slice metabolite mapping with a nominal voxel size of 0.4 mL were 14 and 17.5 min on 3T and 9.4T, respectively.
Results: The low-SAR asymmetric inversion adiabatic pulse enabled reliable non-water-suppressed metabolite mapping using metabolite cycling at both 3T and 9.4T. The spectra and maps showed good agreement with the water-suppressed FID MRSI ones at both field strengths. A quantitative analysis of metabolite ratios with respect to N-acetyl aspartate (NAA) was performed. The difference in Cre/NAA was statistically significant, ~0.1 higher for the non-water-suppressed case than for water suppression (from 0.73 to 0.64 at 3T and from 0.69 to 0.59 at 9.4T). The difference is likely because of chemical exchange effects of the water suppression pulses. Small differences in mI/NAA were also statistically significant, however, are they are less reliable because the metabolite peaks are close to the water peak that may be affected by the water suppression pulses or metabolite-cycling inversion pulse.
Conclusion: We showed the first implementation of non-water-suppressed metabolite-cycled ^{1}H FID MRSI at ultra-high fields. An increase in Cre/NAA was seen for the metabolite-cycled case. The same methodology was further applied at 3T and similar results were observed. **Magn Reson Med 000:000–000, 2017. © 2017 International Society for Magnetic Resonance in Medicine.**

Key words: metabolite cycling; MRSI; non-water-suppressed; spectroscopic imaging; ultra-high field strengths

INTRODUCTION

The majority of ^{1}H magnetic resonance spectroscopy (MRS) studies use water suppression to detect the metabolite signals that are much smaller than the water peak. However, there are also a few studies that use non-water-suppressed methods. Non-water-suppressed MRS has certain benefits over water-suppressed MRS. The water signal can be used for internal referencing in quantification, for frequency alignment between averages, and for motion and eddy current correction purposes (1–3). As an example of this, non-water-suppressed spectroscopy has been previously used to improve the signal-to-noise ratio (SNR) and spectral quality in the spinal cord by using the large water signal for frequency alignment between averages (4). Water suppression may cause chemical exchange that result in quantification errors (5–7), whereas, non-water-suppressed spectroscopy can be used in inversion transfer experiments for investigating downfield metabolite peaks (3,8). Water suppression may also result in other signal changes because of the nuclear Overhauser effect (NOE) (9).

Despite the benefits of non-water-suppressed spectroscopy, there are also challenges that need to be overcome. One of the biggest challenges is that non-water-suppressed spectra have large gradient modulation sidebands (10). There are multiple techniques that can be used to remove these sidebands which can be categorized as either post-processing or experimental methods. Sidebands can be removed in post-processing using software methods by taking the modulus of the FID signal, however, this results in line-broadening and a decrease in SNR (11). A more sophisticated approach is to use the theoretical model and algebraically extract the artifacts using Schur decomposition (12). However, these post-processing methods can result in inaccuracies. The sidebands can be simulated based on theoretical models and accounted for retrospectively, but this requires intensive computation and is not guaranteed to be accurate. Other post-processing methods use data acquired from water phantoms as a reference and subtract the resulting spectra from the in vivo measurements (13,14). The disadvantage of using phantom reference scans is that there may be inconsistencies between those and the in vivo measurements. Furthermore, because of weight differences in the loading of the table (i.e., phantoms are generally lighter than humans) the vibration frequencies are different and would, again, result in inaccuracies. An alternative to removing sidebands in post-processing is to use experimental methods to prevent them from happening in the first place. Sideband artifacts can be reduced by reducing the gradient amplitudes in the sequence where possible (15). Another popular method of removing sidebands is metabolite-cycling (MC) (2,3). This method alternately inverts the upfield and downfield metabolites and subtracts the 2 signals to extract the metabolites from the water peak and sidebands. However, this method requires a wide-band sharp-transition inversion pulse that can be very SAR-demanding.

[1]Max Planck Institute for Biological Cybernetics, Tuebingen, Germany.
[2]IMPRS for Cognitive and Systems Neuroscience, Eberhard-Karls University of Tuebingen, Germany.
[3]Department of Physics, University of Greifswald, Germany.
*Correspondence to: Paul Chang, MS.c., Max Planck Institute for Biological Cybernetics, Max-Planck-Ring 11, 72076 Tübingen, Germany.
E-mail: paul.chang@tuebingen.mpg.de
†These authors contributed equally to this work.
Received 4 September 2017; revised 21 November 2017; accepted 27 November 2017
DOI 10.1002/mrm.27049
Published online 00 Month 2017 in Wiley Online Library (wileyonlinelibrary.com).

For spectroscopic imaging (MRSI), the number of non-water-suppressed publications is even sparser than the single voxel studies. Previously, non-water-suppressed MRSI was done without the consideration of gradient modulation sidebands (16). Later, Chadzynski and Klose (15) and Chadzynski et al. (17) successfully acquired non-water-suppressed MRSI data at 3T while accounting for sideband artifacts. This was achieved by acquiring spectra from a water phantom and subtracting this from the in vivo spectra (18) and also by reducing gradient amplitudes (15). However, as mentioned earlier, removing sidebands in post-processing can be inaccurate and hence, insufficient. A recent study implemented non-water-suppressed MRSI using MC at 3T (19). So far, in all the previous studies, non-water-suppressed MRSI has only been done on field strengths up to 3T and with localization methods such as STEAM (19) or PRESS (15,18).

Currently, no implementations of non-water-suppressed MRSI at ultra-high field strengths have been realized. Although there is a large gain in SNR and spectral resolution at higher field strengths, there are also many difficulties such as strong B_0 and B_1 inhomogeneity and higher specific absorption rate (SAR), which increases exponentially as field strength increases. The strict SAR limitations might therefore require longer scan times. For example, the localized MC sequence that requires an adiabatic inversion pulse might end up with long repetition times that is evident from the single voxel studies. At 7T, the pulse repetition time (TR) was 4000 ms (20), which is approximately twice as long as it would be for a similar sequence at 3T (19). Another example at 9.4T is the TR of 3000 ms for MC with STEAM (21).

At lower field strengths, the lengthy MRSI scan times can be reduced by using non-Cartesian trajectories such as in (19), where they used a concentric ring k-space trajectory for performing MC MRSI scans. However, scan duration can be further reduced by removing the localization, outer-volume, and lipid-suppression schemes from the sequence. For example, a slice-selective non-lipid-suppressed ^{1}H FID MRSI sequence has previously been implemented with water suppression to have short TRs of ~200 ms (22,23)and even 57 ms (17). Furthermore, if extra care is taken into designing the MC pulse to reduce its SAR as much as possible, one can combine the advantages of ultra-high fields with non-water-suppressed MC MRSI.

Therefore, in this work, we show the first implementation of non-water- and non-lipid-suppressed ^{1}H FID MRSI at 9.4T using a low-SAR MC RF pulse that greatly reduces the scan time (compared to the conventional MC pulse). We present metabolite maps acquired at 9.4T with this technique, and we perform the same experiments at 3T for comparison. Furthermore, we show that chemical exchange effects are likely causes for differences between water-suppressed and non-water-suppressed MRSI concentrations.

METHODS

Hardware and Equipment

The ultra-high field experiments were performed on a Siemens 9.4T Magnetom whole-body human scanner (Erlangen, Germany) equipped with gradient coils with a nominal maximum amplitude of 40 mT/m and slew rate of 200 mT/m/ms. An in-house developed RF coil with 18Tx/32Rx and maximum B_1^+ of ~35uT (24) was used for the measurements at 9.4T. For the 3T scans, a Siemens Prisma scanner (Erlangen, Germany) with a commercial 64 channel TIM head-and-neck coil was used. Both 3T and 9.4T scanners were equipped with up to 2nd order shim coils for B_0 shimming.

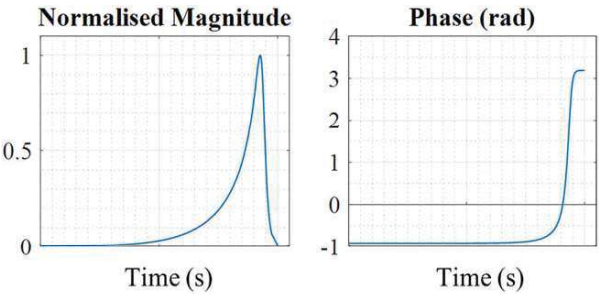

FIG. 1. Magnitude (left) and phase (right) of the adiabatic asymmetric inversion hyper-pulse. The magnitude is normalized to the maximum voltage used for the respective scanner. The time axis is normalized to the total pulse duration.

RF Pulse Design

Adiabatic pulses are typically more SAR demanding than conventional non-adiabatic ones. The adiabatic pulse of a certain duration requires a minimum level of B_1^+ to satisfy the adiabatic condition. While at 3T, a single adiabatic inversion does not cause much SAR problems, at 9.4T even a single pulse results in much longer repetition times. The de facto standard for MC sequences is to use an adiabatic asymmetric inversion sech/tanh pulse (2). In this study, to make the scan times feasible at 9.4T, we instead use a low SAR adiabatic inversion pulse to invert the metabolites. This pulse, referred to as the hyper-pulse from now on, has been shown to be a generalized form of the sech/tanh pulse. It is an analytical solution to a hypergeometric equation and is given as (25):

$$\boldsymbol{\omega}(t) = \Omega_0 \frac{\sqrt{z(1-z)}}{az+b}, \qquad [1]$$

where

$$t = \ln \frac{z^b}{(1-z)^{a+b}}. \qquad [2]$$

For $t \in [-\infty, \infty]$, $z \in [0, 1]$, where Ω_0 is the amplitude of the pulse. The variables a and b are design parameters and were chosen to be 1.3 and 0.12, respectively (as recommended in [25]). The magnitude and phase of the resulting pulse are shown in Figure 1.

Satisfying the adiabatic condition is dependent on the B_1^+ level and the duration of the pulse. Although the B_1^+ field is more or less homogeneous at 3T, at ultra-high fields the B_1^+ homogeneity is rather poor. To account for the strong B_1^+ inhomogeneities, the RF pulse needs to be

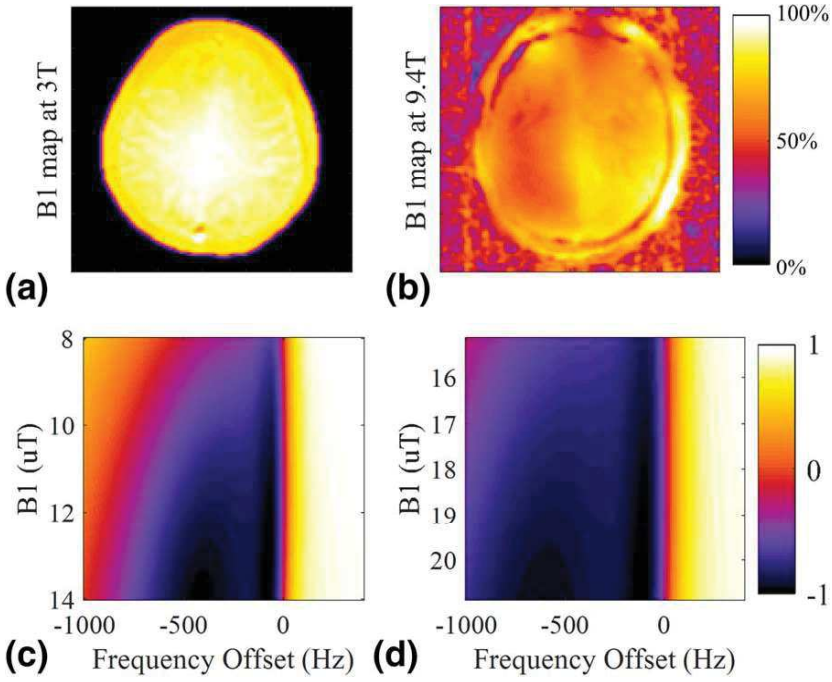

FIG. 2. (A and B) Representative B_1^+ maps acquired at 3T and 9.4T, respectively. The B_1^+ values are shown as a percentage of the nominal flip angle of 60°. (C and D) Inversion profiles of the adiabatic asymmetric inversion hyper-pulse shown as a function of the B_1^+ level and the frequency offset for 3T and 9.4T, respectively.

optimized for a range of B_1^+ values. The pulses were therefore optimized over a range of B_1^+ values for both field strengths. B_1^+ maps were acquired using an actual flip angle imaging (AFI) sequence (26) with the following parameters: flip angle = 60°; $TR_1/TR_2 = 20/100$ ms; TE = 4 ms; matrix size = 128×128; field of view (FOV) = 200×200 mm. The B_1^+ field at 3T was fairly homogeneous. The hyper-pulse was therefore optimized for 3T to operate in a B_1^+ range between 12 uT and 14 uT. The maximum B_1^+ for 9.4T was found to be 33 uT, however, to account for the strong B_1^+ inhomogeneities, the hyper-pulse was optimized over a range of 17 uT to 33 uT. The acquired B_1^+ maps and the spectral inversion profiles for the resulting hyper-pulses are shown in Figure 2.

Frequency Offset Profiling

The center frequency of the designed adiabatic inversion pulse needs to be shifted such that it covers the whole region of the spectrum where the metabolites of interest are located. The frequency offset of this adiabatic asymmetric inversion pulse was therefore calculated and experimentally fine-tuned. Low-resolution MRSI data sets with a matrix size of 16×16 were acquired with an FOV of 200×200 mm and a slice thickness of 10 mm. A non-inverted water image along with multiple metabolite-inverted images were acquired with different frequency offsets. The frequency offsets have to be chosen such that the metabolites in the range of 2.0 ppm to 4.2 ppm are fully inverted. Additionally, to account for B_0 inhomogeneities, inversion of up to 4.5 ppm is necessary. Therefore, a range of frequency shifts of up to 36 Hz for 3T and 120 Hz for 9.4T were tested in this study. The chosen frequency shifts were 0 Hz, −12 Hz, −24 Hz, and −36 Hz for 3T and 0 Hz, −40 Hz, −80 Hz, and −120 Hz for 9.4T. The inversion pulse duration was 14 ms and 9 ms for the 3T and 9.4T, respectively. The applied transmit voltage was 250 V for 3T and 550V for 9.4T.

Data Acquisition

A total of 3 healthy volunteers were scanned with their informed consent and in accordance with the local ethics board committee. The volunteers were scanned at both 3T and 9.4T scanners. For all studies, a 2D ^{1}H FID MRSI sequence (22) was used to acquire single-slice MRSI data with a matrix size of 32×32, in-plane resolution of 6.25×6.25 mm, and a slice thickness of 10 mm. This translates to a nominal voxel size of 0.4 mL. The slice was placed through the periventricular white matter of the cortex and parallel to the corpus callosum in all volunteers. Two variations of the ^{1}H FID MRSI sequence were prepared: a water suppressed version by incorporating an optimized and short 3-pulse water suppression scheme with a duration of 62 ms before the excitation pulse as described in (20), and an MC version by incorporating the designed adiabatic asymmetric inversion hyper pulse before excitation. The excitation pulse occurs directly after the inversion pulse without any delays. Both water-suppressed and MC measurements were performed on each subject in the same session. For a meaningful comparison of the 2 methods, the bandwidth of the water suppression pulses were chosen to be narrow enough so that they did not affect peaks closest to the water peak (myo-inositol and creatine at 4.2 and 4.0 ppm, respectively). Both pulse sequences are illustrated in Figure 3. Because we were not interested in the downfield metabolites in this study, only the upfield metabolites were inverted and this was interleaved with non-inverted FID acquisitions of the water

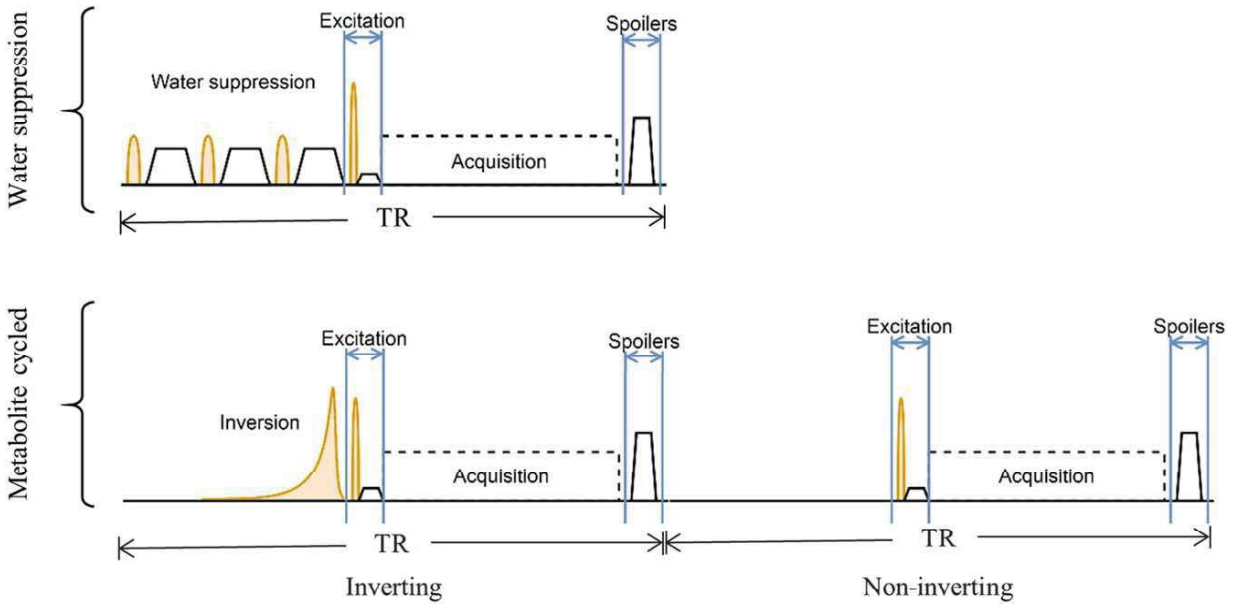

FIG. 3. Schematic representation of the water suppressed (top) and the metabolite-cycled (bottom) ^{1}H FID MRSI sequence.

signal. By only inverting the upfield metabolites, this kept the SAR lower than inverting both the upfield and downfield metabolites.

Additionally, to compare the 2 field strengths, a total of 10 healthy volunteers were scanned at both 3T and 9.4T with the water-suppressed sequence.

The parameters at 3T were: spectral bandwidth = 2400 Hz; acquisition time = 425 ms; TR = 550 ms; acquisition delay = 2.1 ms. The flip angle was 46°, and was calculated from the Ernst formula for a T_1 of 1500 ms. The water suppression scheme for the water-suppressed FID MRSI sequence consisted of 3 pulses with bandwidths of 60 Hz and with a 20-ms delay between each pulse. For the MC FID MRSI sequence, the hyper-pulse was used with a frequency offset of −12 Hz, a pulse duration of 14 ms, and an amplitude of 250 V. The effective inversion bandwidth (defined as more than 90% inversion) for a B_1^+ of 12 uT was ∼450 Hz (or 3.75 ppm). The total scan time for the MRSI sequence at 3T was 14 min for MC.

The spectral resolution between the 2 field strengths were kept the same at ∼55 samples/ppm for consistency, so at 9.4T the acquisition time was 128 ms and the spectral bandwidth was 4000 Hz. The acquisition delay was 1.5 ms and the flip angle was calculated from the Ernst equation for a T_1 of 1800 ms to be 43°. The flip angles of the water-suppression pulses were optimized for 9.4T and had bandwidths of 100 Hz with 20-ms delay between each pulse. For the MC pulse, the maximum voltage was used as the amplitude (550 V) and the inversion pulse had a frequency offset of −40 Hz and a pulse duration of 9 ms. The effective bandwidth of the inversion was ∼1 kHz (2.5 ppm) for the mean B_1^+ amplitude of 25 uT. With the TR set to the minimum possible (700 ms), the total scan time for the MRSI sequence at 9.4T was 17.5 min for MC.

After each measurement, anatomic reference images and B_1^+ maps were also acquired for each subject from the same slice position as the MRSI studies. A T_2-weighted 2D FLASH sequence with the following parameters was used to acquire the scout images: flip angle = 25°; TE = 9 ms; TR = 312 ms; matrix size = 256 × 256; FOV = 200 × 200 mm; slice thickness = 10 mm. The B_1^+ maps were acquired using an AFI sequence with the same parameters as previously stated (in RF Pulse Design). For all studies, an image-based 2nd order B_0 shimming was performed on a shimming volume that had the same dimensions as the imaged slice.

Data Processing

All reconstruction and post-processing steps were implemented in MATLAB (The MathWorks, Natick, MA) First, the data were spatially reconstructed using a spatial Hanning filter before the 2D FFT. The non-water-suppressed images were used for eddy current and 0th order phase correction in both the MC and the water-suppressed data sets (27). The coils were then combined using the singular value decomposition (SVD) coil combination method (28).

The upfield metabolites were calculated from the MC data set by subtracting the inverted signals from the non-water-suppressed signals. To correct for the slight non-uniformities in the inversion profile, the spectra were weighted by the inversion profiles based on the B_1^+ map acquired in the same scan session using the AFI sequence:

$$S_{met}(\omega) = S_{nws}(\omega) - \frac{S_{inv}(\omega)}{\left(1 - magn_{z,inv}(B_1, \omega)\right)}, \qquad [3]$$

where $magn_{z,inv}(B_1, \omega)$ is the inversion profile, the value of which is dependent on the spectral frequency ω and the B_1^+ level at that specific voxel position (as shown in Fig. 2), $S_{nws}(\omega)$ is the non-water-suppressed spectrum,

$S_{inv}(\omega)$ is the metabolite-inverted spectrum, and $S_{met}(\omega)$ is the resulting metabolite-only spectrum.

Further post-processing steps included the removal of the residual water signal using the Hankel-Lanczos (HLSVD) method (29) and automatic first order phase correction by recovering the missing points at the beginning of the FID using linear back prediction with the auto-regressive Burg method (30). No further apodization or phase correction was applied. The metabolites were fit using LCMODEL (31) with a basis set generated from the Gamma library (https://scion.duhs.duke.edu/vespa/gamma) (32) for both the 3T and 9.4T data. The simulated basis-set was generated using the Govindajaru values (33) and included spectra of 18 brain metabolites (namely GPC, Tau, Cre, Glc, Naa, Asc, Lac, GABA, NAAG, GSH, Glu, PE, mI, PCh, Ala, Gln, Scyllo, and Asp) and were line-broadened by 3 Hz for 3T and 5 Hz for 9.4T. The spectra were fit between 1.8 to 4.2 ppm. The metabolite maps shown in the results were overlaid on anatomical images for better visualization.

The SNRs, CRLBs, and FWHMs were calculated from the spectra and spectral fits. The SNR was defined as the absolute peak of NAA over the root mean square of the noise (calculated from the real part of the spectrum between 10 and 11 ppm) in each voxel. The mean and standard deviations of the CRLBs of creatine were calculated for all volunteers at both field strengths. The FWHM of the spectra were acquired from the LCModel.

The metabolite ratios of 5 major metabolites (with respect to NAA) of the water-suppressed and the MC MRSI were compared. The Shapiro-Wilks normality test was used to check that the distributions were sufficiently close to Gaussian and then Welch 2 sample t-tests were performed to test for statistically significant differences between the concentrations of the metabolites resulting from the water-suppressed versus the MC spectra. The *P*-value and statistical power of the t-tests were also evaluated.

RESULTS

Figure 4 shows the results of the frequency offset profiling for 9.4T. At 9.4T, for frequency offsets of −80 Hz and −120 Hz, the transition bandwidth of the inversion pulse is affecting the metabolites at ∼4.4 and 4.2 ppm, respectively. The frequency offset of −40 Hz inverts the spectrum sufficiently, without the transition range affecting the spectrum, for the range of frequencies that we are interested in. Similarly, at 3T, for a frequency offset of −0.1 ppm (−12 Hz), the range of interest is inverted and the transition range does not affect the metabolites close to the water peak. Hence, in all subsequent MC studies, frequency offsets of −40Hz for 9.4T and −12 Hz for 3T were used.

Figure 5 shows representative spectra from 5 voxel positions in the brain of the same volunteer at each of the 2 field strengths. The quality of the spectra look very similar between the water suppressed and the MC acquisitions. The values in Table 1 show the average value for SNR, CRLBs, FWHMs, and metabolite ratios averaged across all the voxels in the brain region and across all volunteers. Statistical comparisons of the SNR, CRLBs, and FWHMs between the 2 field strengths are shown in the Supporting Information for 10 volunteers.

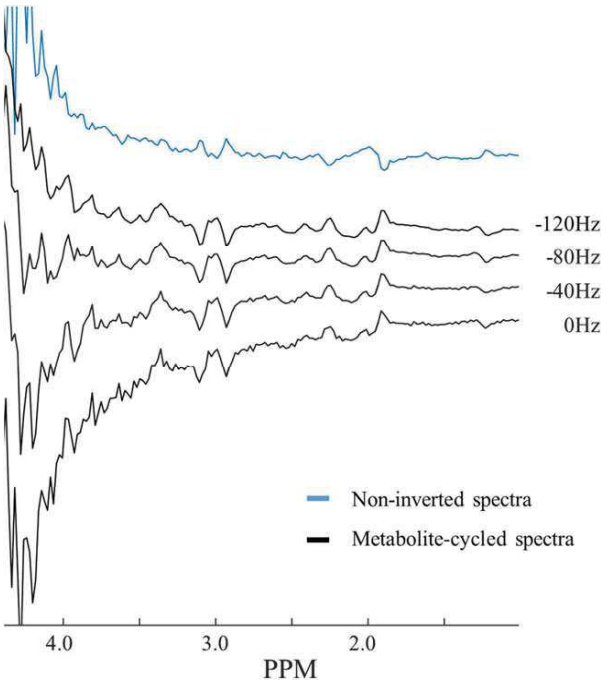

FIG. 4. Results of the frequency offset profiling to find the optimized frequency shift for the adiabatic asymmetric inversion metabolite-cycling pulse at 9.4T.

The metabolite maps for 4 major metabolites, NAA, creatine (Cre), glutamate (Glu), and total choline (tCho), are shown in Figure 6. The water suppressed and MC maps look similar for all volunteers and the tissue contrasts also exhibit similar patterns. The Cramer-Rao lower bound (CRLBs) maps are also shown for both methods in Figure 7.

A quantitative analysis of the metabolite concentrations is shown in Figure 8. The metabolite ratios (with respect to NAA) are shown for both field strengths and both water suppressed and MC data sets. The concentrations of Glu/NAA, tCho/NAA, and GSH/NAA are very similar between water-suppressed and MC spectra. However, the concentrations of Cre/NAA and mI/NAA appear higher when using MC compared to water suppression (Table 2). Furthermore, the variance of the concentrations is slightly higher for MC.

The statistical significance of the differences between the concentrations is shown in Table 2 for both field strengths. The *P*-values of the Shapiro-Wilk normality test show that all distributions are very similar to a normal distribution (except for myo-inositol at 9.4T in the metabolite-cycled case). The Welch 2 sample t-test shows that the differences between the concentrations achieved through water-suppressed versus MC sequences are statistically significant for all metabolites except Glutamate (which has P-values > 0.05). Although all 4 remaining metabolites had high statistical significance, a statistical power test of the t-test shows that only the value for Cre/NAA and mI/NAA has high statistical power. At 3T, the

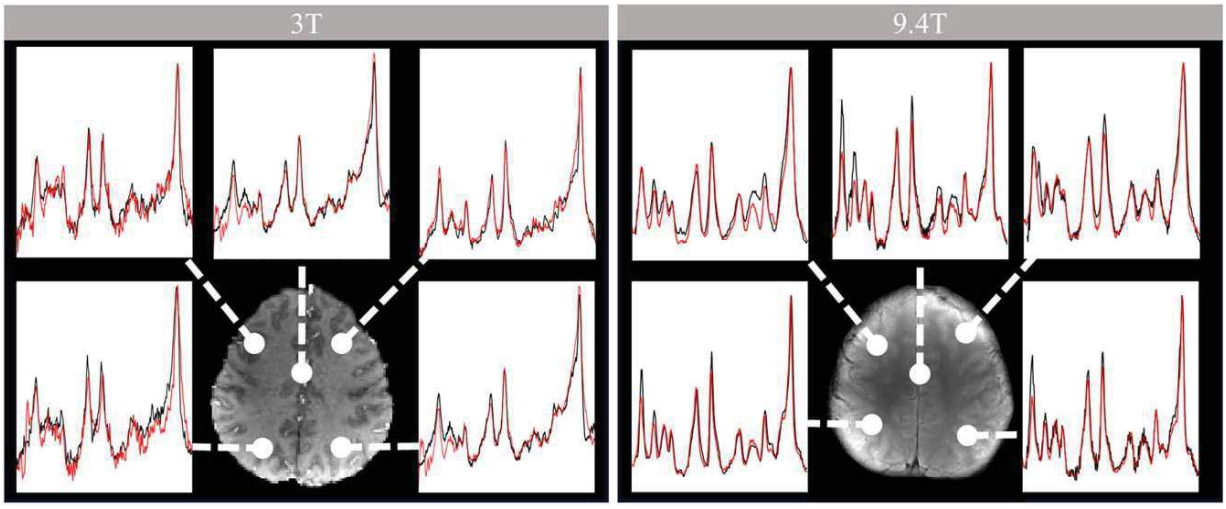

FIG. 5. Representative spectra resulting from the metabolite-cycled MRSI data set (shown in black) overlaid on the corresponding ones acquired through water-suppressed MRSI (shown in red). The spectra are selected from the brain of a healthy volunteer at 5 different voxel positions and are shown for both 3T (left) and 9.4T (right). All spectra are shown between the range of 1.8 ppm and 4.2 ppm.

statistical power of Cre/NAA was 0.275 and at 9.4T was 0.350. The concentration of Cre/NAA was on average 0.739 and 0.687 for MC, and 0.641 and 0.589 for water suppression (for 3T and 9.4T, respectively). From Table 2, *P*-values comparing the MC and water suppression were $<$2.2e-16 for both field strengths (exact values could not be calculated because of the limitations of the R statistical computing software). The difference in mI/NAA was $\sim$0.5 but the statistical power was less and this statistical significance is less reliable.

DISCUSSION

Similar scan times were achieved compared to previously published non-water-suppressed MRSI sequences. At 3T, the TR was 550 ms and total MRSI scan duration was 14 min for a 32×32 matrix size. A previous non-water-suppressed MRSI study (15) had a scan duration of 6 mins at 3T, however, the TR was 3 times longer (1500 ms) and the matrix size was 4 times smaller (16×16). Emir et al. (19) achieved a short scan time using a concentric ring trajectory at 3T. The scan duration was $\sim$8 min for an effective k-space size of 24×24. In this study, we were able to achieve a short scan time by using a non-lipid-suppressed FID sequence with slice-selection, and hence had short repetition times. Furthermore, we achieve higher spatial resolution with the effective voxel size of 0.4 mL while the effective voxel sizes in previous studies were 1.5 mL and 2 mL in (15) and (19), respectively.

The advantage of non-water-suppressed MR spectroscopy is that it is unaffected by potential chemical exchange effects that could occur in sequences with water suppression. Single-voxel spectroscopy studies previously showed significant signal attenuation of creatine and lactate because of chemical exchange (5,6). The exchange between water and total creatine has also been shown in inversion transfer experiments for single-voxel spectroscopy (6). However, so far MRSI studies have been less conclusive. In this study, our results show that there is a statistical significance between the mean metabolite ratios of the water suppressed and MC spectra. However, only the difference in Cre/NAA showed significant statistical power. At 3T, the power of the Welch 2 sample t-test for Cre/NAA was 0.47 and for 9.4T the statistical power was 0.73. The concentration difference of the Cre/NAA is clearer at 9.4T than 3T. At 9.4T, the lower Cre/NAA using water suppression may also be attributed to the higher B_0 inhomogeneity. Higher B_0 inhomogeneity may shift the water suppression pulses to suppress the creatine peak close to the water peak. However, even if this was the case, visible differences in the creatine peak can be seen at 3.0 ppm (lower for water suppression) whereas other metabolite peaks between 3.0 and 4.0 ppm have similar levels of concentration for water-suppressed and MC

Table 1
SNRs, CRLBs, and FWHMs (Averaged across all Voxels in the Brain Region and all the Volunteers) for the Water-Suppressed Versus Metabolite-Cycled MRSI Data Calculated at both 3T and 9.4T

		SNR	CRLB (Cre)	FWHM (Hz)
3T	Water-suppressed	32.7 $\pm$ 4.34	6.05 $\pm$ 1.81	6.45 $\pm$ 2.27
	Metabolite-cycled	29.6 $\pm$ 3.94	9.63 $\pm$ 2.99	7.54 $\pm$ 2.63
9.4T	Water-suppressed	112.6 $\pm$ 17.63	5.65 $\pm$ 5.40	18.99 $\pm$ 5.06
	Metabolite-cycled	125.34 $\pm$ 19.69	5.74 $\pm$ 5.44	23.87 $\pm$ 4.61

The SNR was defined as the absolute peak of NAA over the root-mean-square of the noise (calculated from the real part of the spectrum between 10 and 11 ppm) in each voxel. The CRLBs of creatine and FWHM (as reported by LCModel) are also reported.

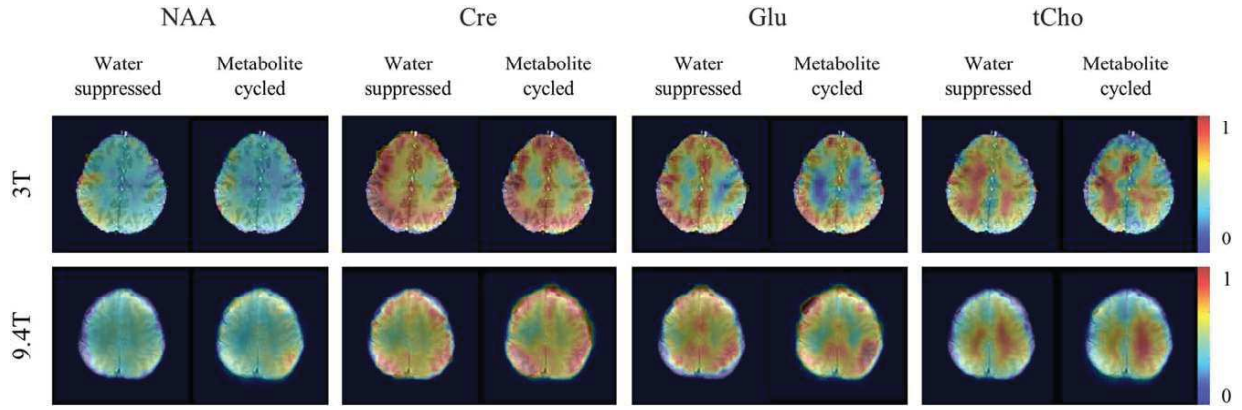

FIG. 6. Metabolite maps of four major metabolites using water suppressed and metabolite-cycled ^{1}H FID MRSI at 3T and 9.4T. All metabolite maps are normalized and shown between 0 and 1.

spectra. Another possible explanation is that because of the B_1^+ inhomogeneity, the lower B_1^+ in some voxels may not be sufficiently inverting the metabolites over the required frequency range. However, these deviations were corrected using a measured B_1^+ map for each volunteer, and furthermore, no other metabolite concentrations showed differences with statistical significance. At 3T, where B_0 and B_1 inhomogeneity are not as big of an issue, a similar result was seen. Emir et al. (19) did not see a significant difference in any of the metabolites at 3T. On the other hand, Chadzynski and Klose (18) saw a slight increase in concentrations for most metabolites when using non-water-suppressed spectroscopic imaging at the same field strength. van der Veen et al. (16) also reported a small increase in creatine concentrations but they also found a similar increase in choline. However, van der Veen et al. (16) used a long echo time, used a different fitting algorithm and also did not fit the creatine peak at 3.9 ppm. These previous studies were all conducted at 3T where the statistical significance of the difference is not as large as for 9.4T. Despite the different results from other MRSI studies, our results were in agreement with single-voxel studies that showed a slight increase in creatine for non-water-suppressed spectroscopy that could be a result of the chemical exchange effect in water-suppressed spectroscopy. Even though only upfield metabolites were studied in this work, same methodology can be used in future on the downfield metabolites to validate chemical exchange saturation transfer (CEST) studies (8,34).

The increase in mI/NAA could be because of B_0 homogeneity or because of an increase in NAA. It is unlikely that the change in mI/NAA is because of chemical exchange. However, it could also be a result of subtraction errors from the non-water-suppressed MRSI. Metabolite peaks closer to water may be more difficult to fit because the residual water peak's tail would affect the baseline under these peaks (especially at 9.4 T). Another explanation could be that the B_0 inhomogeneity could shift the water suppression pulses and reduce the metabolite peaks close to 4.7 ppm. Although this may also be true for the creatine peak at 3.9 ppm, the creatine peak at 3.0 ppm still results in higher concentrations for the non-water-suppressed case. The less reliable fit for myo-inositol for the metabolite-cycled data is reflected by the higher *P*-value for the Shapiro-Wilk normality test. This higher *P*-value indicates that the data for mI/NAA are not distributed normally, and hence the statistical significance shown by the t-test is not very reliable. In contrast, the distributions of the Cre/NAA concentrations follow a normal distribution.

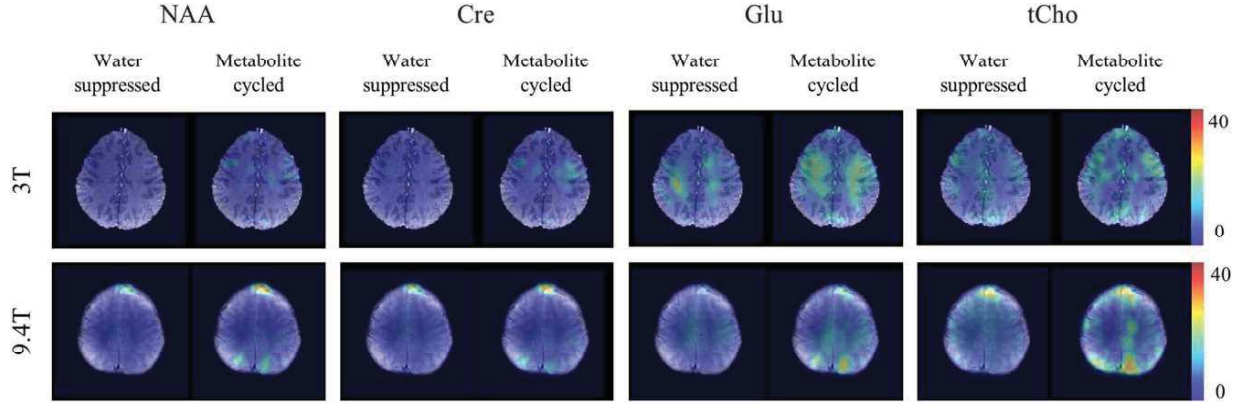

FIG. 7. CRLB maps of 4 major metabolites acquired using water-suppressed and metabolite-cycled ^{1}H FID MRSI at 3T and 9.4T. CRLB maps are shown between 0% and 40%.

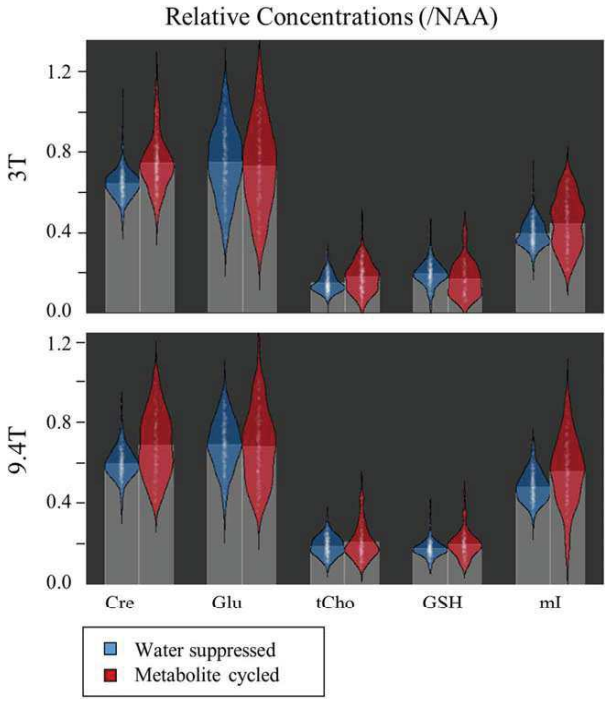

FIG. 8. Quantitative comparison of the metabolite ratios (/NAA) of 5 different metabolites resulting from water-suppressed (blue) versus metabolite-cycled (red) ^{1}H FID MRSI at 3T (top) and 9.4T (bottom). Each box contains the concentration values of all the voxels in the brain region for all the volunteers.

Comparison of the 2 field strengths (Supporting Fig. S1 and Supporting Table S1) show that the SNR of the 9.4T was ~3 times greater than 3T. However, the linewidths of the 9.4T were much larger because of B_0 inhomogeneity and shorter T_2^*. Despite the larger linewidths, the CRLBs of the fits were lower for the 9.4T, especially for the smaller metabolites. This makes the fit results more reliable at higher field strengths.

We also demonstrated the first implementation of non-water-suppressed MRSI at ultra-high fields (9.4T) in the human brain. A reasonable scan-time could be achieved by using a low SAR adiabatic inversion pulse (25) instead of the conventional sech/tanh pulse that is typically used (2). The TR was 700 ms and the scan duration was, therefore, 17.5 min. However, the drawbacks of this pulse compared to the sech/tanh pulse is that the inversion profile is not as flat, and a higher B_1^+ is generally required to reach the required bandwidth. The slight non-uniformities of the inversion profile can be corrected by measuring a B_1^+ map and simulating the inversion profiles at each voxel (as described in this study). This correction was necessary because some regions with low B_1^+ operated in the sub-adiabatic regime. To circumvent this, more B_1^+ efficiency would be required. The retrospective correction is more complex and time-consuming compared to conventional MC methods. However, the benefit of a pulse with lower SAR is that the TR is almost half the duration of the sech/tanh pulse (for a similar bandwidth).

To further reduce the scan duration, non-uniform k-space trajectories can be used (as demonstrated in [19]) along with the short TR. Accelerations methods that under-sample k-space, such as SENSE (35), GRAPPA (36), CAIPIRINHA (23,37), or compressed sensing (38,39) have been demonstrated for the acceleration of water-suppressed ^{1}H MRSI and can also be used to reduce the scan duration.

Limitations

A limitation of using metabolite-cycling is that it is a subtraction method and is therefore sensitive to subtraction errors. If there are slight differences between the inverted and non-inverted spectra then small perturbations arise in the subtracted signal. This can result in baseline distortions and make the spectra more difficult to fit.

The B_0 inhomogeneity is another limitation of ultra-high field strengths. The B_0 inhomogeneity affects the cutoff frequency of the inversion pulse at different voxel positions. This can cause the spectra to be cut off too much and hence affect the myo-inositol peak close to 4.2 ppm. Similarly, a shift in the other direction can

Table 2
Statistical Analyses of the Metabolite Ratio Differences between the Water-Suppressed and the Metabolite-Cycled MRSI Data Sets for 5 Different Metabolites at 3T and 9.4T

	Mean Relative Concentrations (/NAA)		Shapiro-Wilk Normality (*P*-value)		Welch 2 Sample t-Test (*P*-value)	Statistical Power
	Water-Suppressed	Metabolite-Cycled	Water-Suppressed	Metabolite-Cycled		
3T						
Cre	0.641 ± 0.081	0.739 ± 0.135	6.57E-11	4.47E-16	2.20E-16*	0.275*
Glu	0.733 ± 0.179	0.734 ± 0.209	0.243	0.080	0.953	0.046
tCho	0.136 ± 0.045	0.164 ± 0.075	4.44E-06	8.41E-05	5.47E-08*	0.058
GSH	0.187 ± 0.060	0.156 ± 0.080	4.19E-05	2.23E-04	6.72E-05*	0.055
mI	0.391 ± 0.069	0.446 ± 0.133	1.09E-08	3.37E-05	1.45E-07*	0.106*
9.4T						
Cre	0.589 ± 0.073	0.687 ± 0.159	8.11E-08	4.36E-05	2.20E-16*	0.350*
Glu	0.691 ± 0.135	0.701 ± 0.174	0.071	4.33E-03	0.312	0.049
tCho	0.187 ± 0.048	0.196 ± 0.083	6.51E-3	4.36E-10	0.038	0.055
GSH	0.172 ± 0.040	0.199 ± 0.070	5.45E-16	1.01E-05	1.36E-11*	0.067
mI	0.480 ± 0.074	0.539 ± 0.178	1.14E-05	0.100	2.01E-09*	0.146*

*Values with high statistical significant/powerful.

cause more of the water peak to be inverted, which results in more baseline distortion. Furthermore, the challenge of B_0 shimming over a whole slice results in larger linewidths in some voxel positions. Larger linewidths not only decrease the accuracy of the fits but also cause baseline distortion from a broader water peak. Both the 3T and 9.4T data were acquired using 2^{nd} order spherical harmonic B_0 shimming. B_0 homogeneity can be improved using higher order spherical harmonic shimming (40,41) or using the multi-coil approach (42).

Because low repetition times were used, the short TR may result in different saturation effects because of the different T_1 relaxation times for metabolites in different tissue types. The TRs for the water-suppressed and MC sequences were kept the same to account for similar relaxation effects. Corrections for T_1 and T_2 need to be performed in quantification (43), however, this is currently not possible because the T_1 and T_2 values at 9.4T are not known.

To account for B_1^- inhomogeneity, the metabolite ratios (with respect to NAA) were used in the data analysis. However, the NAA maps are also susceptible to fitting uncertainties and relaxation effects. It is still possible that the concentrations of NAA are different between the water suppressed and MC spectra. Leibfritz and Dreher (5) also found that (besides creatine and lactate) certain metabolites such as NAA may be affected by chemical exchange. However, the difference was only slightly above the limits of the experimental error. If NAA does decrease then it could also explain why there may be an increase in mI/NAA. To perform accurate quantification, more sophisticated methods such as the ones described in (44) are required to account for B_1^+/B_1^- variations (that are especially problematic at ultra-high field).

The larger variance of the distribution of concentrations corresponds to the slightly higher CRLBs for MC spectra. The larger variance in the concentrations of some metabolites is mostly because of the larger baseline distortion. The larger water signals for MC were seen to cause more baseline distortion than in the case of water suppression. The larger distortion can make it difficult for the fitting algorithm to fit a spline baseline. Furthermore, because of the ultra-short echo times and the short TRs, macromolecule signals are also significant and contribute to the baseline if they are not accounted for in the fitting routine. Although it is certainly possible to fit the spectra with macromolecules (45), using a single macromolecule baseline is not sufficient for MRSI sequences because of regional differences. Because the MRSI sequence has low TR, there will be different relaxation effects of the individual macromolecules. Using individual macromolecule components is also possible (46), however, it is difficult because the spectra may be over-fit because of over-parametrization and result in less reliable spectral fits. The presence of unsuppressed water peaks in the MC spectra, which are orders of magnitude larger than the metabolite peaks, will result in a much bigger dynamic range of signal amplitudes compared to the water suppressed signals. Depending on the gain of the receiver analog-to-digital convertor (ADC), this may result in quantization noise in the acquired MC data compared to the water suppressed ones. However, by using the large water peak for frequency alignment between averages, previous single-voxel studies showed an improvement of SNR when using MC compared to water suppression methods (4,19). For MRSI applications, however, only 1 average can be acquired because of scan time limitations. Emir et al. (19) reported similar values of SNR for the MC and water-suppressed data acquired at 3T. In this study, we also got similar results and found the SNRs of the 2 techniques to be similar at both field strengths.

CONCLUSIONS

Water suppression can cause chemical exchange effects to occur and hence alter the quantification of the concentrations of metabolites. Non-water-suppressed spectroscopy allows us to measure these exchange effects and also allows us to acquire spectra unaffected by chemical exchange.

In this work, we combined the benefits of a slice-selective and non-lipid-suppressed ^{1}H FID MRSI sequence with a low-SAR adiabatic asymmetric inversion metabolite cycling pulse and were able to achieve low TRs of 550 ms and 700 ms on 3T and 9.4T, respectively. The resulting low TR makes metabolite-cycled MRSI feasible at ultra-high fields. Despite the advantages of non-water-suppressed metabolite-cycling spectroscopic imaging, implementing such technique at ultra-high fields is difficult because of the strong B_0 and B_1 inhomogeneities and the high SAR required for the inversion pulse. Using this technique, we were able to show the first metabolite maps acquired with a metabolite-cycled ^{1}H FID MRSI sequence at 9.4T. We compared the results of this technique to a water-suppressed version of the same sequence and performed the same study at 3T for comparison.

REFERENCES

1. Dong Z, Dreher W, Leibfritz D. Toward quantitative short-echo-time in vivo proton MR. Magn Reson Med 2006;55:1441–1446.
2. Dreher W, Leibfritz D. New method for the simultaneous detection of metabolites and water in localized in vivo 1H nuclear magnetic resonance spectroscopy. Magn Reson Med 2005;54:190–195.
3. MacMillan EL, Chong DG, Dreher W, Henning A, Boesch C, Kreis R. Magnetization exchange with water and T1 relaxation of the downfield resonances in human brain spectra at 3.0 T. Magn Reson Med 2011;65:1239–1246.
4. Hock A, MacMillan E, Fuchs A, Kreis R, Boesiger P, Kollias SS, Henning A. Non-water-suppressed proton MR spectroscopy improves spectral quality in the human spinal cord. Magn Reson Med 2013;69:1253–1260.
5. Leibfritz D, Dreher W. Magnetization transfer MRS. NMR Biomed 2001;14:65–76.
6. Kruiskamp MJ, de Graaf RA, van der Grond J, Lamerichs R, Nicolay K. Magnetic coupling between water and creatine protons in human brain and skeletal muscle, as measured using inversion transfer 1H-MRS. NMR Biomed 2001;14:1–4.
7. Dreher W, Norris DG, Leibfritz D. Magnetization transfer affects the proton creatine/phosphocreatine signal intensity: in vivo demonstration in the rat brain. Magn Reson Med 1994;31:81–84.
8. Fichtner ND, Henning A, Zoelch N, Boesch C, Kreis R. Elucidation of the downfield spectrum of human brain at 7T using multiple inversion recovery delays and echo times. Magn Reson Med 2017;78:11–19.
9. Chen W, Avison MJ, Bloch G, Shulman RG. Proton NMR observation of glycogen in vivo. Magn Reson Med 1994;31:576–579.

10. Clayton DB, Elliott MA, Leigh JS, Lenkinski RE. 1H spectroscopy without solvent suppression: characterization of signal modulations at short echo times. J Magn Reson 2001;153:203–209.
11. Le Fur Y, Cozzone PJ. FID modulus: a simple and efficient technique to phase and align MR spectra. MAGMA 2014;27:131–148.
12. Lin JM, Chuang TC, Chung HW, Tsai SY. Quantitative comparison of post-processing methods for reduction of frequency modulation sidebands in non-water suppression 1H MRS. NMR Biomed 2013;26:400–409.
13. Ozdemir MS, De Deene Y, Fieremans E, Lemahieu I. Quantitative proton magnetic resonance spectroscopy without water suppression. J Instrum 2009;4:P06014.
14. Hurd RE, Gurr D, Sailasuta N. Proton spectroscopy without water suppression: the oversampled j-resolved experiment. Magn Reson Med 1998;40:343–347.
15. Chadzynski GL, Klose U. Proton CSI without solvent suppression with strongly reduced field gradient related sideband artifacts. MAGMA 2013;26:183–192.
16. van der Veen JWC, Weinberger DR, Tedeschi G, Frank JA, Duyn JH. Proton MR spectroscopic imaging without water suppression. Radiology 2000;217:296–300.
17. Chadzynski GL, Bause J, Shajan G, Pohmann R, Scheffler K, Ehses P. Fast and efficient free induction decay MR spectroscopic imaging of the human brain at 9.4 Tesla. Magn Reson Med 2017;78:1281–1295.
18. Chadzynski GL, Klose U. Chemical shift imaging without water suppression at 3 T. Magn Reson Imaging 2010;28:669–675.
19. Emir UE, Burns B, Chiew M, Jezzard P, Thomas MA. Non-water-suppressed short-echo-time magnetic resonance spectroscopic imaging using a concentric ring k-space trajectory. NMR Biomed 2017;30:e3714.
20. MacMillan EL, Kreis R, Fuchs A, Versluis MJ, Boesch C, Boesiger P, Henning A. New technique for metabolite cycled non-water-suppressed proton spectroscopy in the human brain at 7T. In Proceedings of the 19th Annual Meeting of ISMRM, Montreal, Canada, 2011. p 1412.
21. Giapitzakis IA, Shao T, Avdievich N, Mekle R, Kreis R, Henning A. Metabolite-cycled STEAM and semi-LASER localization for MR spectroscopy of the human brain at 9.4T. Magn Reson Med 2017. doi: 10.1002/mrm.26873.
22. Nassirpour S, Chang P, Henning A. High and ultra-high resolution metabolite mapping of the human brain using 1H FID MRSI at 9.4T. Neuroimage 2017. doi: 10.1016/j.neuroimage.2016.12.065
23. Hangel G, Strasser B, Povazan M, Heckova E, Hingerl L, Boubela R, Gruber S, Trattnig S, Bogner W. Ultra-high resolution brain metabolite mapping at 7 T by short-TR Hadamard-encoded FID-MRSI. Neuroimage 2016. doi: 10.1016/j.neuroimage.2016.10.043.
24. Avdievich NI, Giapitzakis IA, Henning A. Optimization of the receive performance of a tight-fit transceiver phased array for human brain imaging at 9.4T. In Proceedings of the 25th Annual Meeting of ISMRM, Honolulu, Hawaii, USA, 2017. Abstract 4309.
25. Rosenfeld D, Phanfil SL, Zur Y. Design of adiabatic pulses for fat-suppression using analytic solutions of the Bloch equation. Magn Reson Med 1997;37:793–801.
26. Yarnykh VL. Actual flip-angle imaging in the pulsed steady state: a method for rapid three-dimensional mapping of the transmitted radiofrequency field. Magn Reson Med 2007;57:192–200.
27. Klose U. In vivo proton spectroscopy in the presence of eddy currents. Magn Reson Med 1990;14:26–30.
28. Bydder M, Hamilton G, Yokoo T, Sirlin CB. Optimal phased-array combination for spectroscopy. Magn Reson Imaging 2008;24:847–850.
29. Cabanes E, Confort-Gouny S, Le Fur Y, Simond G, Cozzone P. Optimization of residual water signal removal by HLSVD on simulated short echo time proton MR spectra of the human brain. J Magn Reson 2001;150:116–125.
30. Kay SM. Modern spectral estimation: theory and application. New Jersey: Prentice Hall; 1998.
31. Provencher SW. Estimation of metabolite concentrations from localized in vivo proton NMR spectra. Magn Reson Med 1993;30:672–679.
32. Smith SA, Levante TO, Meier BH, Ernst RR. Computer simulations in magnetic resonance. An object oriented programming approach. J Magn Reson A 1994;106:75–105.
33. Govindaraju V, Young K, Maudsley AA. Proton NMR chemical shifts and coupling constants for brain metabolites. NMR Biomed 2000;13:129–153.
34. Fichtner N, Giapitzakis IA, Advievich NI, Mekle R, Zaldivar D, Henning A, Kreis R. In vivo characterization of the downfield part of 1H MR spectra of human brain at 9.4T: magnetization exchange with water and relation to conventionally determined metabolite content. Neuroimage 2017. doi: 10.1002/mrm.26968.
35. Kirchner T, Fillmer A, Tsao J, Pruessmann KP, Henning A. Reduction of voxel bleeding in highly accelerated parallel 1H MRSI by direct control of the spatial response function. Magn Reson Med 2014;73:469–480.
36. Hangel G, Strasser B, Povazan M, Gruber S, Chmelik M, Gajdosik M, Trattnig S, Bogner W. Lipid suppression via double inversion recovery with symmetric frequency sweep for robust 2D-GRAPPA-accelerated MRSI of the brain at 7T. NMR Biomed 2015:28:1413–1425.
37. Strasser B, Povazan M, Hangel G, Hingerl L, Chmelik M, Gruber S, Trattnig S, Bogner W. (2 + 1)D-CAIPIRINHA accelerated MR spectroscopic imaging of the brain at 7T. Magn Reson Med 2017;78:429–440.
38. Cao P, Xu EX. Accelerating phase-encoded proton MR spectroscopic imaging by compressed sensing. J Magn Reson Imaging 2015;41:487–495.
39. Geethanath S, Baek HM, Ganji SK, Ding Y, Maher EA, Sims RD, Choi C, Lewis MA, Kodibagkar VD. Compressive sensing could accelerate 1H MR metabolic imaging in the clinic. Radiology 2012;262:985–994.
40. Pan JW, Lo KM, Hetherington HP. Role of very high order and degree B0 shimming for spectroscopic imaging of the human brain at 7 Tesla. Magn Reson Med 2012;68:1007–1017.
41. Chang P, Nassirpour S, Henning A. Modeling real shim fields for very high degree (and order) B0 shimming of the human brain at 9.4T. Magn Reson Med 2017. doi: 10.1002/mrm.26658.
42. Juchem C, Nixon TW, McIntyre S, Boer VO, Rothman DL, de Graaf RA. Dynamic multi-coil shimming of the human brain at 7 T. J Magn Reson 2011;212:280–288.
43. Kreis R. Quantitative localized 1H MR spectroscopy for clinical use. Prog Nucl Magn Reson Spectrosc 1997;31:155–195.
44. Zoelch N, Henning A. High precision external reference standards for quantitative in vivo magnetic resonance spectroscopy [dissertation]. [Zurich]: ETH Zurich. 2016.
45. Povazan M, Hangel G, Strasser B, Gruber S, Chmelik M, Trattnig S, Bogner W. Mapping of brain macromolecules and their use for spectral processing of 1H-MRSI data with an ultra-short acquisition delay at 7 T. Neuroimage 2015;121:126–135.
46. Povazan M, Strasser B, Hangel G, Heckova E, Gruber S, Trattnig S, Bogner W. Simultaneous mapping of metabolites and individual macromolecular components via ultra-short acquisition delay 1H MRSI in the brain at 7T. Magn Reson Med 2017. doi: 10.1002/mrm.26778.

SUPPORTING INFORMATION

Additional Supporting Information may be found in the online version of this article.

Fig. S1. CRLBs, SNR, and FWHM of 3T and 9.4T averaged across 10 volunteers.
Table S1. Statistical comparison of the SNR, FWHM, CRLBs, and metabolite ratios between 3T and 9.4T for 10 volunteers.

Table S1. Statistical comparison of the SNR, FWHM, CRLBs and metabolite ratios between 3T and 9.4T for 10 volunteers.

		3T	9.4T	t-test	
				p-value	Stat. power
FWHM		5.61±1.42	23.49±7.71	0.0	1.0
SNR		30.42±9.89	107.38±36.93	0.0	1.0
CRLB	NAA	4.80±1.06	4.54±0.80	2.06E-04	0.937
	Cre	5.86±0.69	5.65±0.79	3.56E-04	0.76
	Glu	11.52±4.59	6.84±1.78	0	1.0
	tCho	9.47±1.85	7.37±1.45	0	1.0
	GSH	18.82±7.26	14.55±2.81	0	1.0
	mI	10.61±1.75	8.95±2.51	0	1.0
Concentration (/NAA)	Cre	0.643±0.049	0.608±0.074	7.74E-12	0.077
	Glu	0.699±0.180	0.661±0.122	9.95E-04	0.074
	tCho	0.156±0.044	0.206±0.057	2.20E-16	0.103
	GSH	0.170±0.039	0.157±0.029	2.90E-07	0.045
	mI	0.375±0.049	0.44±0.076	2.20E-16	0.124

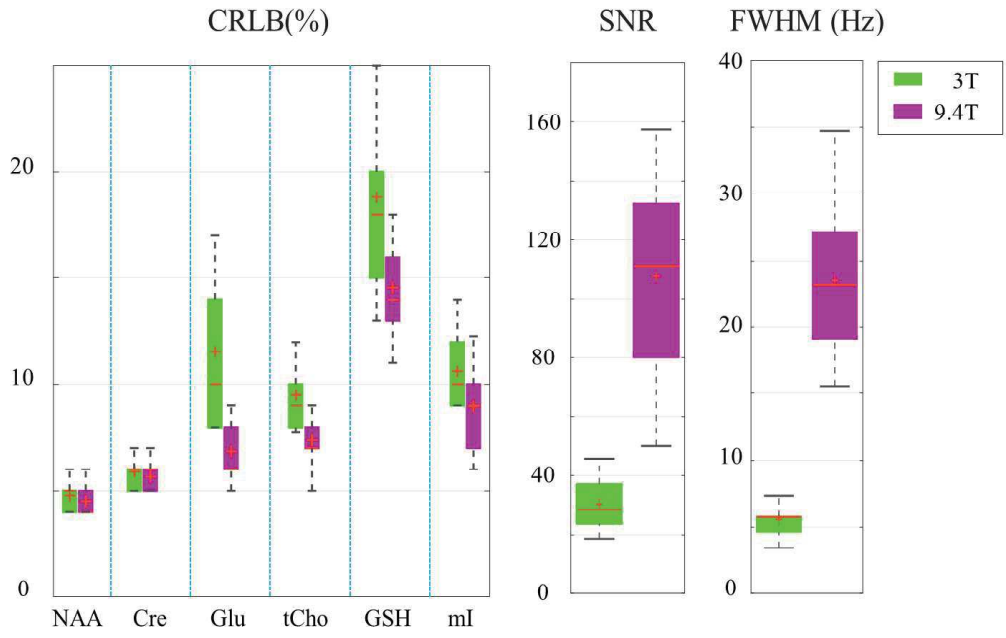

Figure S1. CRLBs, SNR and FWHM of 3T and 9.4T averaged across 10 volunteers.

Publication III

"Compressed Sensing for High-Resolution Non-lipid Suppressed ^{1}H FID MRSI of the Human Brain at 9.4T"

S Nassirpour*, P Chang*, N Avdievich, A Henning

Magnetic Resonance in Medicine, 2018, DOI: 10.1002/mrm.27225

Received: 15 September 2017 | Revised: 6 March 2018 | Accepted: 26 March 2018

DOI: 10.1002/mrm.27225

FULL PAPER

Magnetic Resonance in Medicine

Compressed sensing for high-resolution nonlipid suppressed ^{1}H FID MRSI of the human brain at 9.4T

Sahar Nassirpour[1,2*] | Paul Chang[1,2*] | Nikolai Avdievitch[1,3] | Anke Henning[1,3]

[1] Max Planck Institute for Biological Cybernetics, Tuebingen, Germany

[2] IMPRS for Cognitive and Systems Neuroscience, Eberhard-Karls University of Tuebingen, Germany

[3] Institute of Physics, Ernst-Moritz-Arndt University Greifswald, Greifswald, Germany

Correspondence
Sahar Nassirpour, Max Planck Institute for Biological Cybernetics, Spemannstrasse 41, 72076 Tübingen, Germany.
Email: sahar.nassirpour@tuebingen.mpg.de

Funding information
Grant sponsor: European Research Council Starting, Grant Number: SYNAPLAST MR #679927; Grant sponsor: Horizon 2020, Grant Number: CDS_QUAMRI #634541

Purpose: The aim of this study was to apply compressed sensing to accelerate the acquisition of high resolution metabolite maps of the human brain using a nonlipid suppressed ultra-short TR and TE ^{1}H FID MRSI sequence at 9.4T.

Methods: X-t sparse compressed sensing reconstruction was optimized for nonlipid suppressed ^{1}H FID MRSI data. Coil-by-coil x-t sparse reconstruction was compared with SENSE x-t sparse and low rank reconstruction. The effect of matrix size and spatial resolution on the achievable acceleration factor was studied. Finally, in vivo metabolite maps with different acceleration factors of 2, 4, 5, and 10 were acquired and compared.

Results: Coil-by-coil x-t sparse compressed sensing reconstruction was not able to reliably recover the nonlipid suppressed data, rather a combination of parallel and sparse reconstruction was necessary (SENSE x-t sparse). For acceleration factors of up to 5, both the low-rank and the compressed sensing methods were able to reconstruct the data comparably well (root mean squared errors [RMSEs] $\leq$ 10.5% for Cre). However, the reconstruction time of the low rank algorithm was drastically longer than compressed sensing. Using the optimized compressed sensing reconstruction, acceleration factors of 4 or 5 could be reached for the MRSI data with a matrix size of 64 $\times$ 64. For lower spatial resolutions, an acceleration factor of up to R$\sim$4 was successfully achieved.

Conclusion: By tailoring the reconstruction scheme to the nonlipid suppressed data through parameter optimization and performance evaluation, we present high resolution (97 μL voxel size) accelerated in vivo metabolite maps of the human brain acquired at 9.4T within scan times of 3 to 3.75 min.

KEYWORDS
MRSI, ultra-high field strengths, compressed sensing, acceleration, metabolite mapping

1 | INTRODUCTION

Proton ^{1}H MRSI is a powerful tool for mapping the metabolites of the human brain that can benefit greatly from ultra-high field strengths. Among the commonly used ^{1}H MRSI sequences, slice-selective ultra-short TE ^{1}H FID MRSI[1-7] is fast, and not gradient intensive. In addition to offering high SNR, it is able to detect metabolites with short T_2^*, and has low chemical shift displacement. This makes it a very suitable candidate for fast and high resolution metabolite mapping at ultra-high fields (UHF).

*Sahar Nassirpour and Paul Chang contributed equally to this work.

Nevertheless, MRSI scans even with such a fast sequence, still suffer from lengthy scan times. This problem has been mitigated at lower field strengths by the use of acquisition schemes such as echo-planar spectroscopic imaging (EPSI) [8-11] or non-Cartesian trajectories.[12] Furthermore, recently several approaches based on the principle of low-rank and the spatio-spectral correlations of the MRSI data were proposed and incorporated in the EPSI sequence to further accelerate the acquisition.[13-18] However, applying the same methods at UHFs is challenging due to the higher sampling bandwidth requirements that will in turn require stronger gradient systems.

Several approaches have been investigated for accelerating the ^{1}H FID MRSI sequence at ultra-high fields. In-plane acceleration using parallel imaging (PI) can be done by means of GRAPPA,[19] SENSE,[20] or CAIPIRINHA.[3,4] However, the acceleration factors are limited by the SNR of the spectra and the g-factor related noise amplification. Additionally, depending on how the calibration data are acquired, it will add to the scan time, such that the effective acceleration factor is usually lower than the nominal one.

Several efforts have been made to optimize the acquisition of the FID MRSI sequence as well as the reconstruction process of the PI methods to enable higher acceleration factors. Kirchner et al[20] used SENSE acceleration together with an over-discrete reconstruction scheme to achieve an acceleration factor of 4. However, because specific absorption rate demanding outer volume suppression pulses were still used in this study, the scan time was 42 min for a matrix size of 20×16 at 7T. Hangel et al[19] chose GRAPPA and showed that for efficient 2D GRAPPA acceleration, the lipid signal should be suppressed. They performed a specific absorption rate-efficient double inversion recovery lipid suppression and were able to achieve an acceleration factor of 9. For a matrix size of 64×64, their required scan time was 8 min at 7T. Note that the use of lipid suppression schemes lengthened the TR in these studies due to the increased specific absorption rate. To acquire fast high resolution MRSI data at UHF, no lipid suppression scheme should be applied. This enables the use of ultra-short TRs. However, because the unsuppressed subcutaneous lipid signal is orders of magnitude larger than the metabolites of interest inside the brain, any residual aliasing artifact from the lipid ring will overshadow the metabolites in the brain and prevent accurate quantification. Therefore, for the nonlipid suppressed ^{1}H FID MRSI, more advanced acceleration methods are required.

Strasser et al[3] used a controlled aliasing PI method (CAIPIRINHA) on the nonlipid suppressed FID MRSI sequence to control the lipid signal better than the conventional PI methods. They combined the 2D CAIPIRINHA with slice CAIPIRINHA and introduced (2+1)D CAIPIRINHA for FID MRSI, which enabled the acquisition of a 64×64 matrix size in an effective scan time of 3.75 min at 7T. Hangel et al[4] used the same strategy to acquire ultra-high resolution MRSI data with a matrix size of 100×100 in an effective time of 4.25 min at 7T. To date, these are the fastest reported ^{1}H FID MRSI data acquisitions at UHF. Note that these studies used acceleration also in the third spatial direction by simultaneous excitation of multiple slices (multi-band excitation) and resolving the slices later. Given the strong B_0 inhomogeneities at ultra-high fields, this method has the disadvantage that slice-wise dynamic shim updates cannot be used, rather several slices have to be acquired with the same B_0 shim setting.

Another approach for acceleration which does not rely on the structured nature of the aliasing artifact for recovering the original signal, is compressed sensing (CS). The concept of CS was introduced by Candes et al[21] in 2005 and picked up by the MR community shortly after.[22,23] Essentially, CS is a technique for recovering missing data points from an undersampled dataset by exploiting two key concepts: sparsity (or transform sparsity) of the underlying signal, and incoherent, noise-like undersampling artifacts in the sparse domain. Due to the inherent sparsity of MR images, CS is a promising technique that can enable higher acceleration factors compared with PI methods. Successful application of CS to any MR imaging method relies on the ability to implement a random (or pseudo-random) undersampling scheme in the acquisition trajectory and the sparsity of the signal.

CS has been applied in the field of MRSI since the early years of its application in MR. Spectroscopic imaging is multi-dimensional: it has two or three spatial dimensions and one temporal dimension and is by nature very sparse. To achieve incoherent aliasing artifacts in the image domain, one can apply random undersampling to one or more of these dimensions. In fact, if the random undersampling is performed across multiple dimensions, CS can perform better.[23] In EPSI sequences,[24] each readout simultaneously acquires one spatial encoded and one temporal dimension, and hence the other incrementally collected spatial dimensions can be randomly undersampled. In J-resolved spectroscopy imaging, there is an additional temporal dimension that can also be randomly undersampled. These undersamplings can be achieved using phase-encoding (PE) blips in the sequence. In conventional chemical shift spectroscopy imaging with multiple PE directions, random undersampling can easily be applied to all PE directions.

The second key factor that has to be considered, is the nature of the signal in the MRSI application at hand, specifically its degree of sparsity. CS has been previously applied to ^{13}C,[25-28] ^{19}F,[29] ^{31}P,[30] and ^{23}Na[31] MRSI, as the very sparse nature of X-nuclei spectra makes them a good candidate for CS. CS has also been applied to accelerate J-resolved MRSI.[32-35] For ^{1}H MRSI, CS has been used to accelerate localized and lipid-suppressed sequences.[36-38] The only account of CS applied to a full-FOV 3D ^{1}H MRSI is in Otazo et al,[39] where it has been used to further accelerate an EPSI sequence by a factor of 4. However, the results show that the

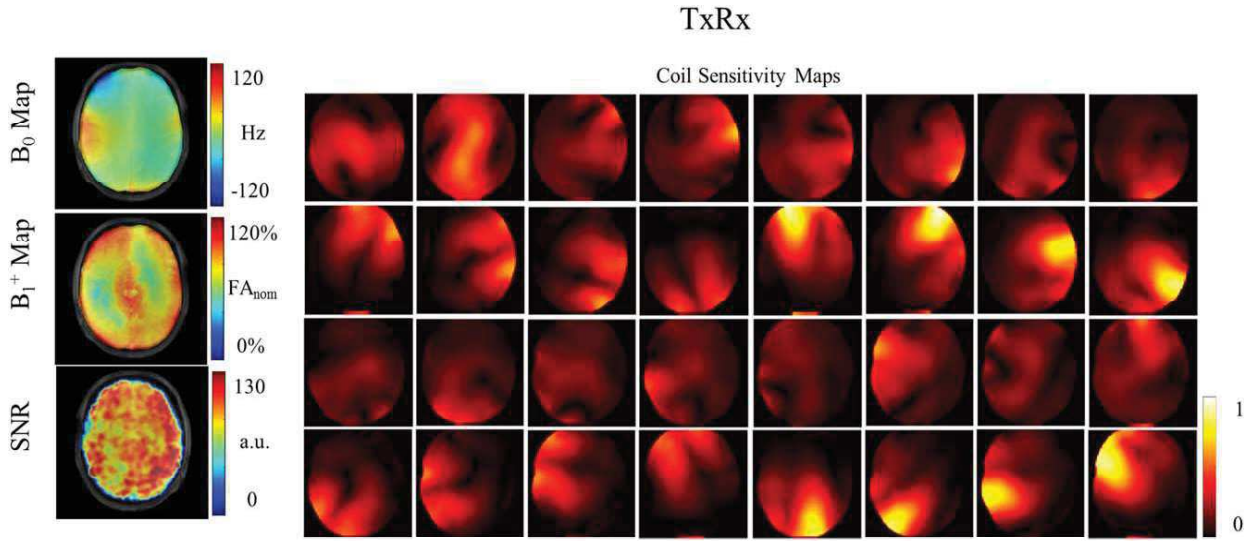

FIGURE 1 Representative B_0, B_1^+, and MRSI SNR maps along with the coil sensitivity maps for the 18Tx/32Rx RF coil used in this study. Coil sensitivity maps are normalized to the maximum receive sensitivity

acceleration is limited by the degree of sparsity of the signal, and possibly the methodology. The problem becomes even worse for a slice-selective and nonlipid suppressed ^{1}H MRSI scheme. The reason is that the presence of strong lipid signals from the subcutaneous lipid ring prevents the CS reconstruction algorithm from recovering the metabolites of interest that have lower SNR in comparison. In fact, the combination of the denoising and sparsifying transforms used in CS reconstruction will treat the strong lipid signal as the major features of the image, and the small metabolite peaks as noise.

Thus, despite the straight-forward implementation of random undersampling in nonlipid suppressed ^{1}H FID MRSI sequences, CS has never been successfully applied to accelerate this imaging technique. In this work, we present a methodology that enables successful application of CS to nonlipid suppressed ultra-short TE and TR ^{1}H FID MRSI for high acceleration factors beyond those achieved through 2D PI. We highlight the key factors leading to a reliable recovery of the signal despite the presence of strong lipid signals, which include the necessity of combining parallel imaging and sparse reconstruction[40] or alternatively using low rank structural matrix completion methods.[41] We study the effect of matrix size and SNR on the achievable acceleration factor using this method, and finally, we present high resolution in vivo metabolite maps of the human brain acquired from an accelerated ^{1}H FID MRSI sequence at 9.4T.

2 | METHODS

2.1 | Data acquisition

All experiments were conducted on healthy volunteers on a 9.4T Siemens whole-body human scanner (Siemens, Erlangen, Germany). A total of six healthy volunteers were scanned for this study. All volunteers gave informed consent according to the local ethics board regulations before the scans. The vendor preimplemented image-based second-order B_0 shimming was performed on a rectangular shimming volume (with the same dimensions as the imaged slice) for all studies. An in-house developed 18Tx/32Rx transceiver RF coil with two dedicated transmit coils, 16 TxRx loops, and 16 dedicated vertical receive loops arranged in two rows on a cylindrical holder was used for data acquisition.[42] Representative B_0, B_1^+, and coil sensitivity maps achieved with this setup in vivo are shown in Figure 1. The B_0 map was acquired using a 2D gradient echo sequence with a TR of 100 ms and a delta TE of 0.76 ms. For B_1 mapping, an actual flip angle imaging sequence (AFI) with a flip angle of 60 degrees, TR_1/TR_2 of 20 ms/100 ms and TE of 4 ms was used.

Fully sampled high resolution single-slice MRSI data were acquired from a nonoblique slice placed above the Corpus Callosum in 3 volunteers using a nonlipid suppressed ultra-short TR and TE ^{1}H FID MRSI sequence.[1-7,43] An optimized three-pulse water suppression scheme with a duration of 62 ms was incorporated in the sequence before excitation as described in.[5] Other parameters of the sequence include: FOV = 200 mm × 200 mm, slice thickness = 10 mm, matrix size = 64 × 64, nominal voxel size = 97 μL, flip angle = 30 degrees, TE = 1.56 ms, TR = 300 ms, spectral bandwidth = 8 kHz, acquisition time = 128 ms, total acquisition time- = 15 min. After each scan, a nonwater suppressed reference scan with the same parameters as the original MRSI scan, but at four times lower spatial resolution was acquired for eddy current and zero-order phase correction.

The ^{1}H FID MRSI sequence used in the study has two spatial, and one temporal dimensions. Therefore, the data can be theoretically undersampled in three dimensions. Because after each excitation and 2D phase-encoding the whole FID

is acquired within one TR, the price paid for fully sampling the temporal dimension is minimal. However, in each TR, the two spatial dimensions are incrementally phase-encoded, and hence easy to undersample in a fully random manner by skipping certain points in k-space without requiring any further modifications to gradients or the ADC read-out. To achieve optimal randomness in the acquisition, variable density sampling masks were designed for different acceleration factors using the method described in Cheng et al.[44] Because the most valuable data with the highest SNR in MR applications are located in the center of k-space, this method divides the kspace into concentric rings and implements random undersampling of increasingly higher degrees as the rings progress toward the outer k-space. The optimal mask was generated using Monte-Carlo simulations that minimizes peak interference. The parameters used to generate all masks were: polynomial degree = 5, radius of fully sampled center- = 0.12, number of Monte-Carlo iterations = 10.

2.2 | CS reconstruction optimization

CS reconstruction can be formulated as an optimization problem where the sparsity of the reconstructed signal is maximized subject to a data consistency constraint. Two sparsity terms were used to enforce x-t sparsity: 3D total variation (over two spatial dimensions and a time dimension) and 2D 4th order Debauchies wavelet with a four-level decomposition over the two spatial dimensions. A norm-1 metric is typically used for the sparsity terms and a norm-2 metric is used for the data consistency constraint. The objective function was, thus, generally:

$$\min_x \|\mathcal{F}_u x - y\|_2 + \lambda_1 \|\Psi x\|_1 + \lambda_2 \|TV(x)\|_1 \qquad (1)$$

where $\mathcal{F}_u$ is the undersampled Fourier transform, y is the measured k-space data (used for enforcing data consistency), Ψ is the 2D wavelet transform in the two spatial dimensions, TV is the 3D total variation, and λ_1, λ_2 are tuning parameters that trade-off data consistency for sparsity and can be tuned to trade-off wavelet sparsity for total variation sparsity (and vice-versa). Also note that the x term is in the image-domain (not k-space) and time-domain.

As mentioned earlier, the strong lipid signals present in a nonlipid suppressed MRSI data, will have significantly higher SNR compared with the metabolites of interest. Therefore, the CS reconstruction should use all the help it can get for increasing the SNR of the metabolites to be higher than the noise-like artifacts resulting from high acceleration factors. This is where CS reconstruction can be combined with PI, where the receive sensitivity maps of the coils are used as an additional tool in reconstruction. It should be noted that despite the obvious advantage of combining parallel imaging with CS, this approach requires a calibration scan to extract the coil sensitivity profiles. Any inconsistencies between the actual MRSI scan and the calibration scan (e.g., patient movement) will reduce the accuracy of the extracted coil sensitivity map.

In this regard, a calibration-less coil-by-coil reconstruction is preferable. With this in mind, we investigated the differences between a coil-by-coil and a SENSE x-t sparse[40] CS reconstruction (for R = 4). A conjugate gradient method was used for solving the optimization problem in both methods. The coil-by-coil reconstruction uses the objective function (defined above) for each of the coil channels separately. The parallel-sparse method combines the coil channels using the coils sensitivity maps when calculating the sparsity measures during the reconstruction. Therefore, in this case, the x term is 3D (that is, two image domain and one time domain) coil-combined data, and $\mathcal{F}_u x$ is a 4D term that also includes the uncombined coil channel data.

For the SENSE x-t sparse reconstruction, the coil sensitivities were extracted from a low resolution 2D FLASH scout image acquired with the same slice position and properties as the MRSI study with the following parameters: TR = 312 ms, TE = 9 ms, flip angle = 25°. The coil sensitivities were extracted from the raw data using ESPIRiT.[45] This method computes the coil sensitivities by eigenvalue decomposition in the image-domain.

For consistency, the data are usually first normalized, so that the same tuning parameters can be applied to differently scaled data. Normalization is typically performed by dividing the variable x by its maximum value. However, in our reconstruction the data were normalized by dividing them by:

$$mean(x) + 2 * std(x) \qquad (2)$$

where x is the undersampled k-space data, and $std(x)$ is the standard deviation of x. This is more robust against noise in the data (in case, $\max(x)$ is an unusually large outlier). However, for most cases, the normalized data using both methods will be on a similar scale and thus the tuning parameters should be compatible for either normalization method.

The tuning parameters λ_1, λ_2 are usually empirically chosen. Typical values for λ are in the range 0.001 to 0.01. In a previous application of compressed sensing to MRSI,[36] λ_2 was larger than λ_1. In this study, we fixed λ_1 as 0.001 and found the optimal λ_2 by iterating over a range of logarithmically-distributed values between $1e^{-4}$ to $1e^{-2}$. The objective function was the norm-2 of the error between the spectra of the fully-sampled data and reconstructed data:

$$\min_{\lambda_2} \|\mathcal{F}_1 \left(x_{full} - x_{accel}(\lambda_2) \right)\|_2 \qquad (3)$$

where $\mathcal{F}_1$ is the 1D Fourier transform in the time-domain and $x_{accel}(\lambda_2)$ is the reconstructed x (using Equation 1) for a given λ_2. The objective function was calculated in the spectral domain between the range 0.5 to 4.5 ppm which includes

the metabolites of interest. This optimization was run (using the conjugate gradient method) on one dataset to find the optimal tuning values and the optimal λ_2 was used for all subsequent reconstructions.

After optimizing the CS reconstruction method, we also compared this reconstruction with a low-rank, structured matrix completion method (simultaneous auto-calibrating and k-space estimation [SAKE]).[41] Unlike the CS method, this method is directly applied to the k-space data and reconstructs the missing points by enforcing low rank and structured matrix properties on the data. SAKE reconstruction was realized using the adopted version of the Cadzow algorithm[46] proposed by Shin et al[41] with the following parameters: kernel-window-size = 6×6, window-normalized number of singular values to threshold = 1.8, eigen-value threshold = 0.9, and 200 iterations.

2.3 | Spectral postprocessing

After the CS reconstruction, the spectra were postprocessed using a custom MATLAB script. The postprocessing steps included: spatial Hamming filtering, eddy current and zero-order phase correction using the low resolution water reference image,[47] coil combination using the singular-value-decomposition (SVD) method,[48] prediction of the missing points at the beginning of the FIDs using a backward linear prediction algorithm[49] and residual water peak removal using Hankel Lanczos singular value decomposition method.[50] No additional apodization or phase correction was applied. The spectra were then fitted using the LCMODEL software.[51] The basis-set was simulated using the GAMMA library (http://www.nmr.ethz.ch/Gamma.html) and included spectra of 18 brain metabolites (namely glycerophosphocholine, taurine, creatine [Cre], glucose, N-acetyl aspartate [NAA], ascorbate, lactate, γ-aminobutyric acid, N-acetylaspartylglutamate, glutathione, glutamate [Glu], phosphoethanolamine, myo-inositol, phosphocholine, alanine, glutamine, scyllo-inositol, and aspartate) with a linewidth of 5 Hz. No T_1 or T_2 attenuation correction was performed on the metabolite maps.

2.4 | Acceleration comparison

To study the effect of increasingly higher acceleration factors, four different undersampling masks (Figure 2) were used. Therefore, the effective acceleration factors and scan times were R = 2, 4, 5, and 10 and acquisition time = 7.5, 3.75, 3, and 1.5 min, respectively.

The metabolite maps of four major metabolites (NAA, Glu, Cre, and total choline [tCho]) were compared for each acceleration factor. Furthermore, because nonlipid suppressed data were used, lipid contamination maps were calculated to compare the effect of different acceleration factors. The lipid maps were defined as the absolute integral of the spectra between 0.3 and 1.8 ppm.

Quantitative comparisons were performed using four metrics. First, the lipid contamination power (LCP) was calculated. This is similar to the artifact power defined in Strasser et al,[3] however, the measure was calculated in the spectral domain between 0.3 to 1.8 ppm. Therefore, the LCP was defined as:

$$LCP = 100 \cdot \frac{\sum_{ch}\sum_{\vec{r}\in mask}\sum_{f\in Fmask}|S_{accel}(ch,\vec{r},f) - S_{full}(ch,\vec{r},f)|}{\sum_{ch}\sum_{\vec{r}\in mask}\sum_{f\in Fmask}|S_{full}(ch,\vec{r},f)|} \quad (4)$$

where *ch* are the different coil channels, *r* is the voxel position, *f* is the spectral point, *mask* is the spatial mask containing only the brain region, *Fmask* is the frequency domain mask (between 0.3 and 1.8 ppm), and S_{accel} and S_{full} are the signals of the accelerated and fully sampled datasets, respectively. The spatial mask was manually defined on each volunteer. Second, an SNR ratio metric similar to the g-factor was calculated from:

$$\frac{RMS(noise_{accel})}{\sqrt{R}\cdot RMS(noise_{full})} \quad (5)$$

where the noise was calculated from the real part of the spectrum between 10 and 11 ppm, and *R* is the effective acceleration factor. Third, RMSE of the metabolite maps were calculated as:

$$RMSE = 100 \cdot \sqrt{\frac{\sum_{\vec{r}\in mask}\left(\frac{C_{accel}(\vec{r}) - C_{full}(\vec{r})}{C_{full}(\vec{r})}\right)^2}{N}} \quad (6)$$

where *C* is the concentration of the metabolite and *N* is the number of voxels in the spatial mask. Lastly, the Cramer-Rao lower-bounds (CRLBs) of the fitted metabolite maps were used as a metric for data fidelity.

2.5 | Effect of matrix size and SNR

It is well known that increasing the spatial resolution of the MRSI data results in two competing effects: on one hand, the SNR decreases as the voxel size decreases which results in noisier spectra, but on the other hand, the FWHM and lipid contamination also decrease which results in more accurate spectra.

So far, all comparisons were done on the high resolution (in-plane matrix size = 64×64) FID MRSI data. To highlight the effect of matrix size and SNR on the highest achievable acceleration factor using CS, the in-plane matrix size of the high resolution fully sampled data was retrospectively reduced to 48×48 and 32×32 and the undersampling

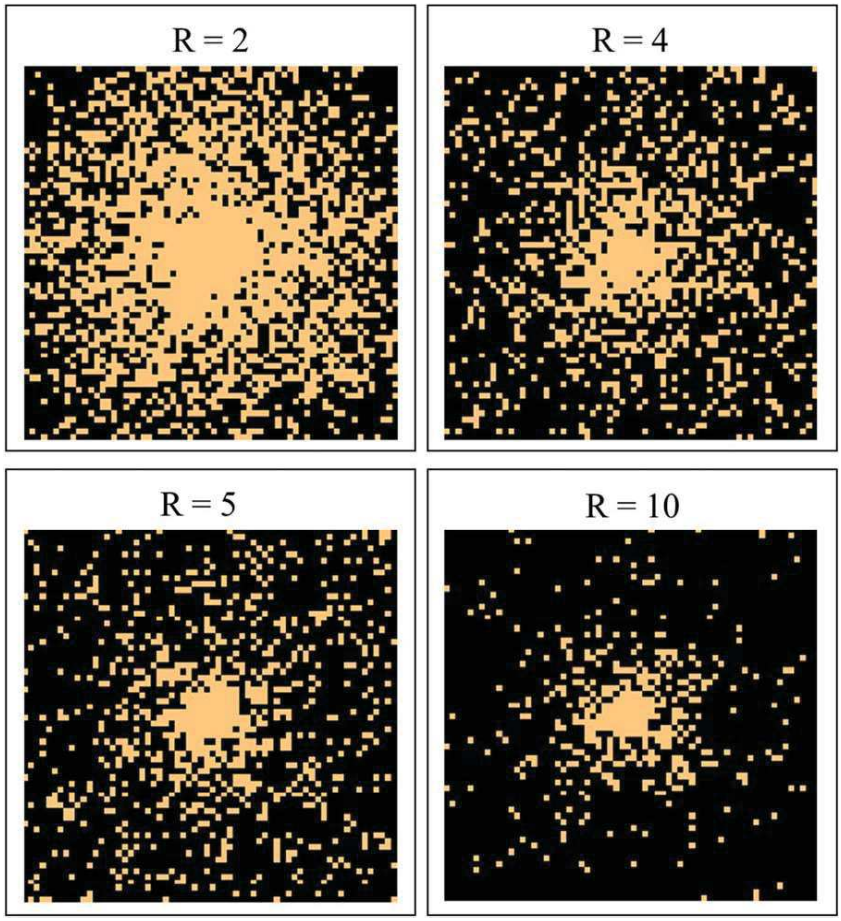

FIGURE 2 Optimal random variable density k-space undersampling masks calculated for different acceleration factors. The light orange color marks the k-space points that are acquired

k-space masks were similarly truncated. The effect of increasingly higher acceleration factors on the resulting metabolite maps on these reduced resolution data was studied and the same quantitative measures were used for the comparison.

3 | RESULTS

3.1 | CS reconstruction optimization

The optimization of the tuning parameters showed that the minimum error value was achieved for $\lambda_2=0.003$. Hence, the parameters $\lambda_1=0.001$ and $\lambda_2=0.003$ were consistently used for the reconstruction of all datasets and acceleration factors.

The reconstructed data for the coil-by-coil x-t sparse and the SENSE x-t sparse method are shown in Supporting Information Figure S1, which is available online. The coil-by-coil x-t sparse reconstruction (red) clearly has large lipid artifacts that distort the spectra while the SENSE x-t sparse reconstruction (black) has reasonable spectra that can be further processed and fitted. The metabolite maps for three major metabolites resulting from the coil-by-coil CS reconstruction are shown in Figure 3. It can be seen that the large distortion in the coil-by-coil CS reconstruction resulted in a complete

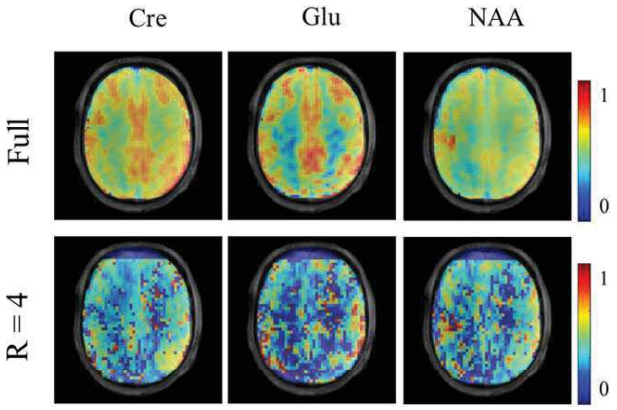

FIGURE 3 Metabolite maps of three major metabolites shown once for the fully sampled case (top row), and once for the R = 4 accelerated case (bottom row) reconstructed with the coil-by-coil sparse reconstruction. The metabolite maps are normalized between 0 and 1. The coil-by-coil reconstruction completely fails in recovering the metabolite of interest. The maps in the bottom row looked cropped at the map because the fitting routine aborted the process due to the failure in fitting the spectra

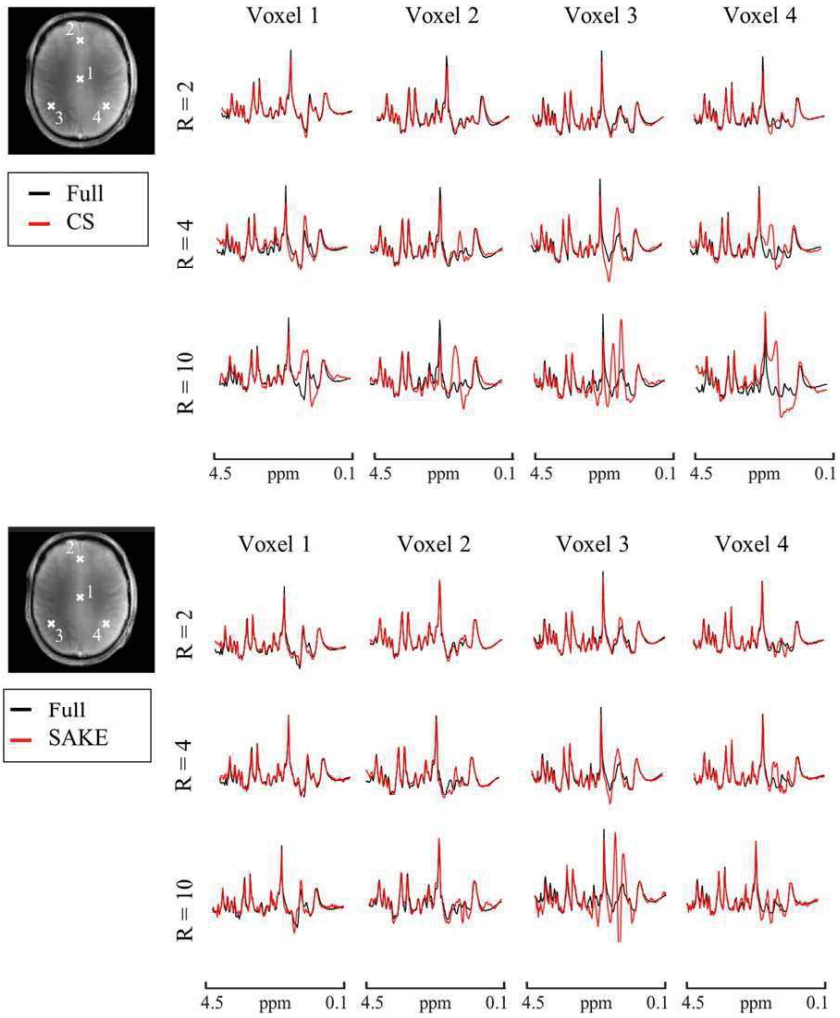

FIGURE 4 Representative spectra from four different positions in the brain shown for twofold (R = 2), fourfold (R = 4), and 10-fold (R = 10) acceleration. The top panel shows the accelerated spectra reconstructed with the SENSE x-t sparse CS reconstruction method, and the bottom panel shows the spectra reconstructed with the SAKE method. Accelerated spectra (red) are overlaid on fully sampled spectra (black) for all cases

failure when quantifying the metabolites. Hence, the coil-by-coil x-t sparse CS reconstruction method was not used any further in the study.

3.2 | Acceleration comparison

Figure 4 shows the results of the acceleration factor comparison done with both the SENSE CS and the low rank reconstruction schemes. For each reconstruction scheme, representative spectra with acceleration factors of R = 2, 4, and 10 are overlaid on the fully sampled spectra for four different positions in the brain. For R = 2, the reconstructed spectra using both the CS and the SAKE reconstruction are very similar to the fully-sampled spectra. For R = 4, the low rank reconstruction was still able to recover the spectra very well, whereas the CS reconstruction showed some deviations in the lipid range in voxels closer to the skull region. As the acceleration factor increases to R = 10, the deviations increase for both methods.

The lipid contamination maps for both reconstruction methods are shown in Figure 5. These maps illustrate how the lipid signal contaminates the signal in the brain as a result of the random undersampling. It can be seen that the lipid contamination gets higher overall as we go to higher acceleration factors. However, unlike PI acceleration methods, the artifact is randomly scattered due to the random undersampling. It can be seen that SAKE resulted in less lipid artifacts than the CS reconstruction (also evident in the spectra shown in Figure 4). However, even for R = 10 in the CS reconstruction, the maximum lipid contamination inside the cortex was approximately 5 to 8% of the maximum lipid signal in the image.

The resulting metabolite maps for the same subject along with the error in the maps compared with the fully sampled case are shown in Figure 6. Note that no spatial smoothing

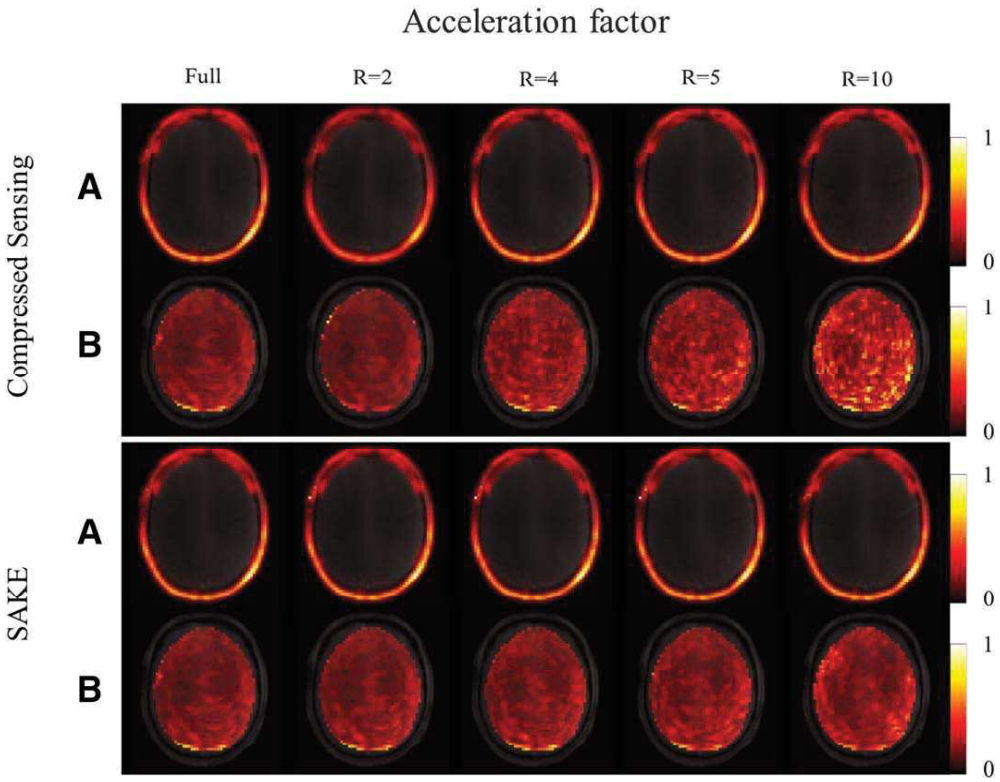

FIGURE 5 Lipid contamination maps resulting from different acceleration factors. The maps in are shown without any thresholding. Row (a) shows the full field of view while in row (b) the skull lipid ring has been set to zero to better visualize the lipid contamination inside the brain. The top panel shows the maps reconstructed with the SENSE x-t sparse CS reconstruction method, and the bottom panel shows the maps reconstructed with the SAKE method

or interpolation was applied to these maps. For both the CS and SAKE reconstruction, the maps show very good reconstruction for R = 2, and acceptable reconstruction for R = 4 and 5. The noise increase is evident as the acceleration factor increases. Although quite noisy, the gray/white matter contrast can clearly be discerned for even high accelerations of R = 10. It can be seen that for higher acceleration factors, the errors in the maps resulting from the SAKE reconstruction are higher than for the CS. The CRLB maps (shown in Figure 7) for the same metabolite confirm this result: the overall CRLB values appear to be higher for the SAKE reconstruction. In general, for each reconstruction scheme, the CRLB maps are similar for all acceleration factors and only slightly increase for higher accelerations. The metabolite maps for three more metabolites (NAA, Glu, and tCho) are shown in Supporting Information Figure S2. It can be seen that for higher acceleration factors, the tCho maps deteriorates so much more for the low-rank reconstruction compared with CS.

The quantitative measures of the reconstruction are shown in Figure 8 and summarized in Table 1. The LCP of the CS reconstruction (solid black line) is clearly higher than the SAKE reconstruction (dotted line). There is also a clear increase in LCP as the acceleration factor, R, increases. The CRLBs of the metabolite maps were calculated for the four major metabolites and were higher for the low-rank reconstruction. Although there was an increase in the CRLBs for higher acceleration, they are only slightly increased. The RMSE of the metabolite maps also increase as R increases. The RMSE of tCho for the SAKE reconstruction is much higher than the CS reconstruction for acceleration factors beyond R = 4.

To show the capability of the proposed method for prospective acceleration, Supporting Information Figure S3 shows the metabolite maps resulting from prospectively applying the CS method to 3 additional volunteers with R = 5 in vivo.

3.3 | Effect of matrix size and SNR

Figure 9 shows the metabolite maps of Cre for two additional resolutions of 48×48 and 32×32 in-plane matrix size with increasingly higher acceleration factors. The accelerated data was reconstructed using the CS reconstruction. The corresponding metabolite maps for three more metabolites (NAA, Glu, and tCho) are shown in Supporting Information Figure S4.

It can be seen that even for the lower resolution cases, the CS reconstruction shows good reconstruction for the

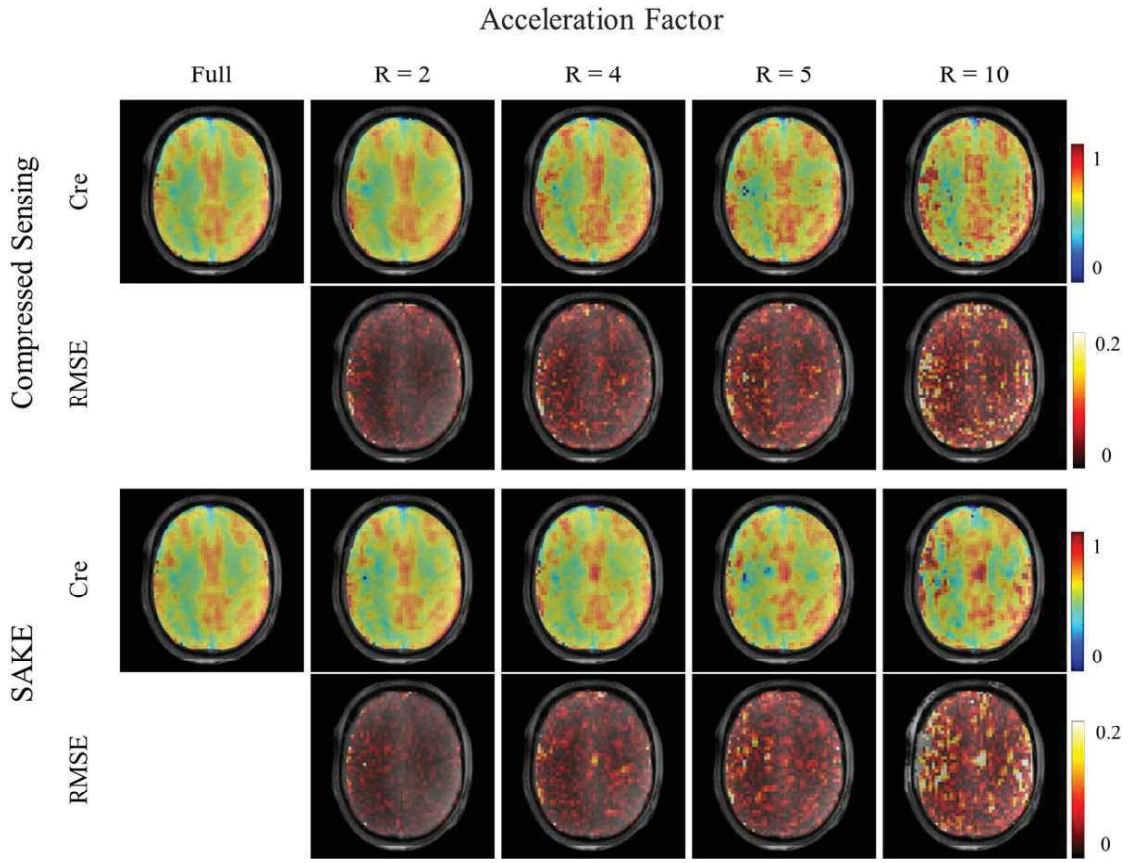

FIGURE 6 Metabolite map of Cre along with the corresponding RMSE between the fully sampled and accelerated cases are shown for different acceleration factors. The top panel shows the maps reconstructed with the SENSE x-t sparse compressed sensing (CS) reconstruction method, and the bottom panel shows the maps reconstructed with the SAKE method. The metabolite maps are normalized between 0 and 1, and the RMSE is shown between 0% and 20% of the metabolite map

R∼4 in both cases. As expected the maps get noisier as the acceleration factor increases.

The nominal voxel size for the different resolutions were 390 μL, 174 μL, and 97 μL for the 32×32, 48×48, and 64×64 case, respectively. The average SNR of the fully sampled data was 210, 164, and 111 for the 32×32, 48×48, and 64×64 case, respectively. The quantitative measures for the two reduced resolutions are also shown in Figure 8 and once again summarized in Table 1. The same trends of increasing LCP, RMSE and CRLB as the

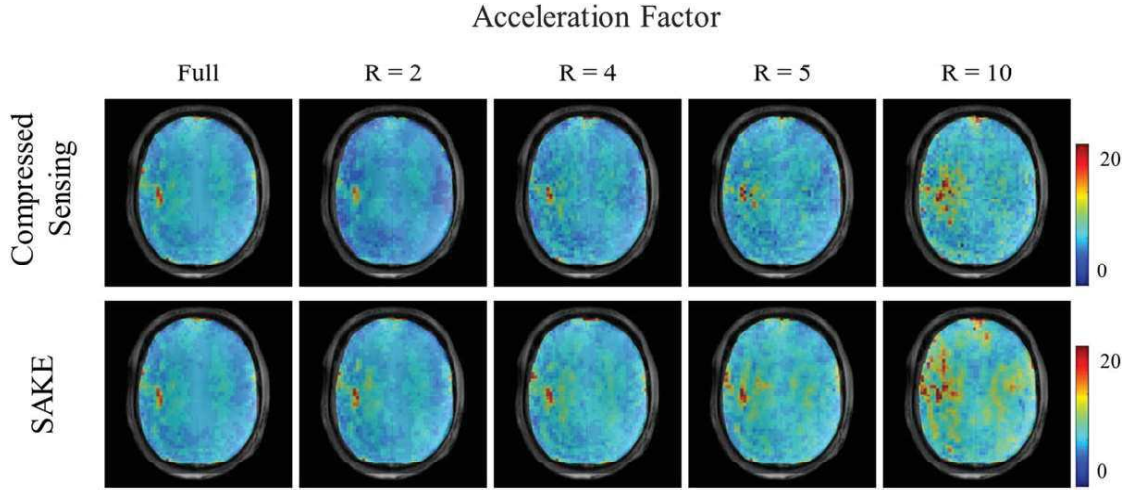

FIGURE 7 CRLB maps corresponding to the metabolite maps of Figure 6 shown for different acceleration factors and reconstruction routines

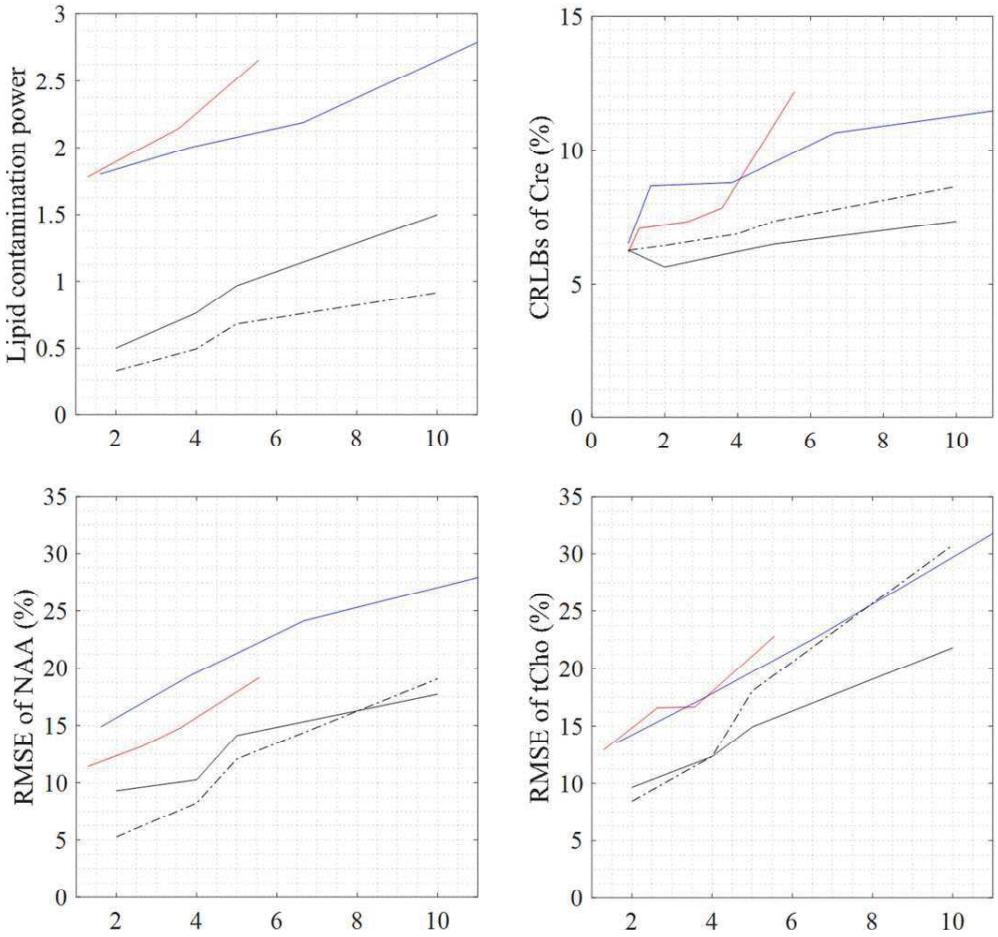

FIGURE 8 Quantitative comparison of different acceleration factors. On each graph, the red and blue line correspond to the in-plane matrix sizes of 32×32 and 48×48 reconstructed with the SENSE x-t sparse compressed sensing reconstruction, respectively. The two black lines correspond to the matrix size of 64×64 once reconstructed with the SENSE x-t sparse compressed sensing reconstruction (solid black), and once with the SAKE method (dotted black). The average value (averaged across the whole slice for the volunteers) is shown for each measure

acceleration factor increases can be seen for the reduced resolution cases. Even though the LCP of the 48×48 case (blue line) was lower than the 32×32 case (red line), the CRLB and RMSE of the maps (up to R∼4) were generally higher for the 48×48 case. This is due to the competing effect of SNR that dominates the quality of the maps. After R∼4, the lipid contamination dominates and the error in the tCho map and the CRLBs become higher for the 32×32 compared with the 48×48 case. Note that, generally, the quantitative measures of the 64×64 case were better than the two reduced resolutions.

4 | DISCUSSION

The motivation for the present work was to explore a different approach of acceleration that does not result in strong and structured residual lipid artifacts, and can provide sufficient and reliable in-plane acceleration to compete with 3D acceleration methods. Because conventional PI acceleration methods cannot satisfy these requirements, we turned to CS for this study and successfully implemented it for acquiring accelerated nonlipid suppressed metabolite maps of the human brain with a matrix size of 64×64 in approximately 3.75 or 3 min (for $R = 4$ and 5, respectively) at 9.4T. To the best of our knowledge, this is the fastest 2D acquisition of ^{1}H FID MRSI data that result in reliable metabolite maps.

Two approaches for reconstructing randomly undersampled data were studied in this work: a compressed sensing approach relying on the principle of data sparsity for recovering the missing points,[23] and a pure k-space based approach relying on the principle that the structured data matrix is low rank.[41] Both methods succeed in recovering the missing data points without introducing additional artifacts in the spectra. Detailed comparisons between the two methods showed that despite the fact that the low-rank reconstruction resulted in lower lipid artifacts, the CS method resulted in better metabolite maps at higher acceleration factors, especially for smaller metabolites such as tCho. This

TABLE 1 Summary of the quantitative measures of different acceleration factors for the 64 × 64 in-plane matrix size once reconstructed with compressed sensing and once with the SAKE method (A), and the two reduced resolutions reconstructed with the CS method (B)[a]

(A)		R = 2	R = 4	R = 5	R = 10
LCP	CS	0.50	0.76	0.97	1.50
	SAKE	0.33	0.49	0.68	0.92
CRLB (Cre)	CS	5.64 ± 1.10	6.21 ± 1.39	6.49 ± 1.88	7.34 ± 2.22
	SAKE	6.44 ± 1.54	6.87 ± 1.44	7.35 ± 2.17	8.65 ± 2.66
CRLB (NAA)	CS	4.18 ± 0.88	4.58 ± 1.10	4.93 ± 2.61	5.37 ± 1.24
	SAKE	4.48 ± 1.48	4.73 ± 0.81	5.19 ± 2.94	5.91 ± 1.59
CRLB (tCho)	CS	7.63 ± 1.66	8.61 ± 2.40	8.96 ± 2.69	10.56 ± 3.98
	SAKE	8.82 ± 2.36	9.38 ± 2.40	10.05 ± 3.04	12.66 ± 8.11
CRLB (Glu)	CS	7.06 ± 2.40	8.41 ± 4.75	9.09 ± 6.45	10.77 ± 7.40
	SAKE	8.48 ± 4.23	9.09 ± 4.24	10.15 ± 5.87	12.57 ± 8.55
RMSE (Cre)	CS	5.76	7.87	10.25	14.86
	SAKE	5.01	7.55	10.46	18.74
RMSE (NAA)	CS	9.31	10.26	14.13	17.71
	SAKE	5.25	8.25	12.06	19.05
RMSE (tCho)	CS	9.65	12.32	14.93	21.82
	SAKE	8.45	12.33	18.04	30.76
RMSE (Glu)	CS	15.21	15.07	21.34	29.88
	SAKE	9.08	14.92	19.53	33.82
Noise factor	CS	0.39 ± 0.31	0.52 ± 0.37	0.57 ± 0.36	0.76 ± 0.55
	SAKE	0.56 ± 0.48	0.58 ± 0.44	0.62 ± 0.52	0.61 ± 0.48

(B)		LCP	CRLB (Cre)	RMSE (NAA)	RMSE (tCho)	Noise factor
48 × 48	Full	-	6.51 ± 1.37	-	-	-
	R = 1.6	1.80	8.67 ± 2.02	14.90	13.52	0.70 ± 0.54
	R = 3.8	2.00	8.79 ± 2.45	19.36	17.52	1.22 ± 0.60
	R = 6.7	2.19	10.65 ± 3.12	24.13	22.87	1.36 ± 0.70
	R = 11	2.80	11.49 ± 3.53	28.02	31.97	0.88 ± 0.70
32 × 32	Full	-	6.17 ± 1.12	-	-	-
	R = 1.3	1.79	7.07 ± 1.82	11.42	12.91	0.71 ± 0.46
	R = 2.6	1.99	7.33 ± 2.32	13.16	16.57	0.88 ± 0.54
	R = 3.6	2.14	7.85 ± 2.70	14.76	16.66	0.97 ± 0.65
	R = 5.6	2.65	12.17 ± 3.02	19.14	22.83	0.81 ± 0.69

Abbreviations: CRLB, Cramer-Rao lower-bound; Cre, creatine; CS, compression sensing; Glu, glutamate; LCP, lipid contamination power; NAA, N-acetyl aspartate; RMSE, root mean squared error; SAKI, simultaneous auto-calibrating and k-space estimation; tCho, total choline;

[a]The lipid contamination power is abbreviated to LCP in the tables. The average value (averaged across the whole slice for the volunteers) is shown for each measure.

can be attributed to the fact that the SAKE reconstruction had more spatial noise resulting from inconsistencies in the prediction of the outer k-space points. These small inconsistencies between the spectra of neighboring voxels confound the fitting routine and result in less accurate metabolite maps. This is evident from the fact that for any acceleration above R = 4, the low rank SAKE method results in large errors in the metabolite maps of tCho.

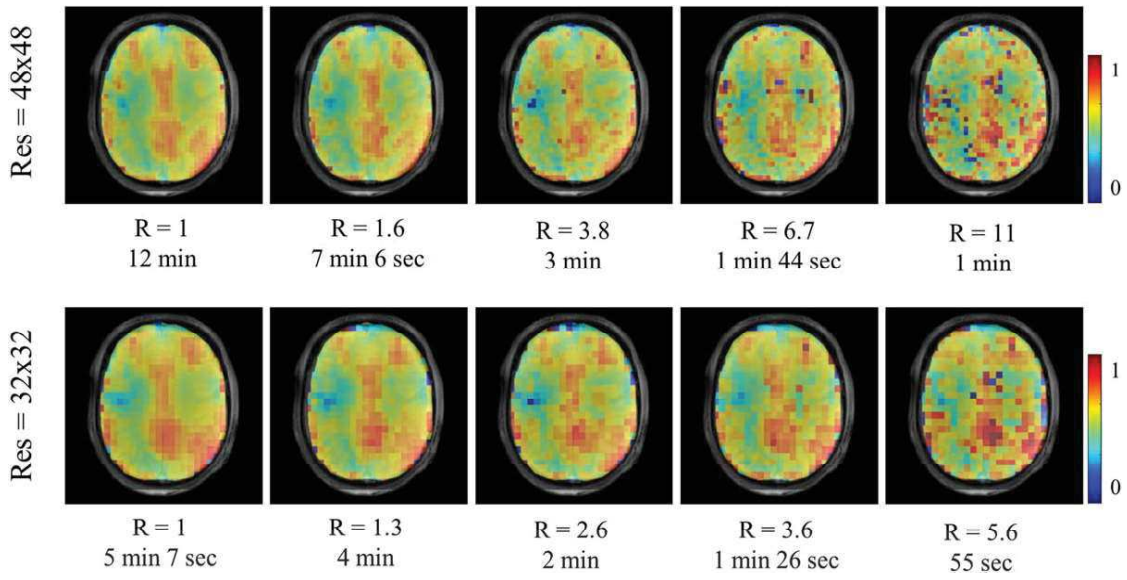

FIGURE 9 Metabolite maps of Cre shown for two different spatial resolutions and with different acceleration factors. The resulting scan times are also noted under each acceleration factor (in minutes). The SENSE x-t sparse compressed sensing reconstruction was used to reconstruction the accelerated data. The metabolite maps are normalized between 0 and 1

In contrast, the CS method manages to recover the data points while simultaneously enforcing spatial smoothness (by minimizing the total variation). Another important difference between the CS and SAKE methods was their speed. The SAKE method suffers from drastically longer reconstruction time (~24 h for the reconstruction of a 64×64 MRSI dataset versus ~20 min when CS was used) due to the computational complexity resulting from high dimensional structured matrices. Hence, we concluded that the CS approach is the more practical way for achieving high acceleration factors for high resolution metabolite mapping of the even the lower concentrated metabolites and the rest of the comparisons in this work were done using CS. It should be noted that by using faster algorithms, or by only performing the low rank reconstruction method on the central part of the k-space and combining it with L1-minimization methods for the rest of k-space,[41] one can reduce the reconstruction time of SAKE. However, the performance of this kind of reconstruction for the application at hand has to be further studied.

For a successful CS implementation, extra care should be taken in selecting the sparsifying transforms tailored to the nature of the data. Total variation function as a sparsity measure is often sufficient to reconstruct randomly undersampled data in most applications, however, it is also known to introduce some smoothing into the final reconstruction. Another commonly used sparsity transform is the wavelet transform. This transform is able to preserve higher frequencies, however, it can sometimes result in patchiness. We have hence combined both of these in the reconstruction problem. We enforced x-t sparsity by performing the wavelet transform over the two spatial dimensions (compared with one spatial and one time domain in Geethanath et al).[36] In addition, we used a 3D total variation whereas Geethanath et al[36] used a 2D total variation over the spatial domains. Additionally, the tuning parameters for similar reconstruction methods in previous studies were only empirically chosen. In this work, the optimal ratio between the tuning parameters were found by directly optimizing the reconstruction error to be $\lambda_1 = 0.001$, $\lambda_2 = 0.003$.

Another important result of this work is work is the requirement for sufficient SNR for CS. Because the metabolite signals are orders of magnitude smaller than the water signal, the SNR of MRSI data is much lower than other imaging applications. As a result, the conventional CS approach (coil-by-coil sparse reconstruction) that successfully recovers the data in other imaging applications, completely failed to reconstruct the MRSI data. This is likely due to the fact that individual coil elements have lower SNR than the coil-combined data or that some individual coil elements pick up more nuisance signal due to their sensitivity profile. Because random undersampling generates noise-like aliasing, the peaks of interest in the spectra have to be above this noise level for the reconstruction algorithm to recover them correctly. Even though the residual water peak is still the biggest signal in the acquired spectra, the main problem is the presence of lipid signals because they have broad peaks that overlap with the metabolites of interest.

The water signal, however, corresponds to low frequencies both spatially and spectrally. Because the central part of the k-space is always fully sampled, this is less of an issue for the reconstruction. On the other hand, due to the presence

of large subcutaneous lipid signals, the reconstruction treats the metabolites as noise and mostly recovers the lipids. Hence, we needed to boost the SNR of the initial data by combining CS with PI[40] and use the SENSE x-t sparse reconstruction. An additional benefit of using a coil-combined method is that the reconstruction time is much faster and the disk memory required is less because the 4D data are now combined into 3D data.

Although we performed the reconstruction in the time domain, it is also possible to use the frequency domain. More terms can be introduced into the optimization function by separating the lipid and metabolite frequency ranges (and possibly also spatially) and using different weights for each term. This strategy offers more flexibility in the reconstruction and can possibly further improve the reconstruction.

A characteristic of compressed sensing is that it denoises the data and, therefore, increases the SNR in the reconstruction. An implication of this is that the spectral noise is approximately constant for all acceleration factors. Unlike PI accelerations, the SNR of the reconstructed data does not decrease with higher acceleration. However, it is evident that the metabolite maps are noisier for higher acceleration. The noise does not stem from lower spectral SNR of the reconstruction (because this remains more or less constant), but rather comes from the higher lipid contamination that the reconstruction is unable to resolve. This is also shown in Figure 8 from the LCP and RMSE graphs. Another implication of the constant spectral noise is that the confidence of the fits remains more or less constant for all acceleration factors. Although the CRLBs do increase slightly, the difference between $R = 2$ and $R = 10$ acceleration is only a few percent. This also explains why the CRLBs and g-factor values for $R = 2$ are in fact lower than the values for the fully sampled data.

Comparison of different acceleration factors showed that for $R = 2$ and 4, the reconstruction does very well. This enabled the reliable acquisition of the 64×64 matrix size in 3.75 and 3 min at 9.4T. However, for $R = 10$, the spectra in the lipid range deviate quite drastically. This indicates that there is more lipid contamination than the reconstruction is able to deal with. Because the temporal dimension was fully sampled, the lipid contamination most-likely comes from the spatial aliasing resulting from strong lipid signal close to the skull region, and hence removing the lipid ring directly from the k-space data after acquisition will have minimal effect on the reconstruction performance.

Furthermore, the random undersampling generates aliasing artifacts that are noise-like (Figure 5) rather than the structured fold-over artifacts that are typical for PI methods such as SENSE. MRSI data acquired with lipid suppression can probably be better reconstructed for the higher acceleration factors; however, as mentioned earlier, lipid suppression methods often drastically increase the scan duration due to strict specific absorption rate limitations. Another possibility is to use a crusher coil[52] to crush the lipid signal from the skull without prolonging the scan time. This will most likely enable higher accelerations with the CS methodology described in the present work.

To study the effects of SNR and spatial resolution on a successful CS implementation, the CS method was successfully applied to two increasingly lower spatial resolutions with in-plane matrix sizes of 48×48 and 32×32 at 9.4T. The results suggested that the x-t sparse CS reconstruction enabled the acquisition of reasonable metabolite maps for both resolutions up to $R \sim 4$. Naturally, compared with the matrix size of 32×32, the 48×48 results in more anatomically detailed maps. The fact that the highest achievable acceleration factor for both reduced resolutions was $R \sim 4$ is likely due to the fact that the degradation in the quality of the maps as a result of CS acceleration stems from two competing effects of more lipid contamination and higher SNR which appear to come to a balance at $R \sim 4$ for the 32×32 and 48×48 matrix sizes.

It is worth mentioning that the use of ultra-high field in this study has positively affected the performance of the CS methodology. The additional SNR offered by higher field strengths plays an important role in enabling higher acceleration factors. For lower field strengths with lower SNRs, other acceleration strategies such as spatio-spectral encoding methods (e.g., references 8-11, 53,54) with inherently faster readouts combined with PI or subspace-based strategies might be a more viable option for fast metabolite mapping. Furthermore, the same method may be used with 3D MRSI sequences which inherently offer more SNR. The combination of PI and CS may result in higher acceleration factors in these cases.

5 | CONCLUSIONS

In this work, we showed that compressed sensing can be used for high in-plane acceleration factors for nonlipid suppressed ^{1}H FID MRSI beyond those of conventional PI methods. The practical considerations of compressed sensing reconstruction (such as parameter tuning, coil-by-coil reconstruction versus combined parallel, and sparse or low rank reconstruction, as well as the effect of SNR and matrix size) were systematically studied. Acceleration factors of 4 or 5 could be reached using a combined parallel imaging with compressed sensing reconstruction (SENSE x-t sparse). Even for higher acceleration factors, the lipid contamination shows an incoherent, noise-like quality and noise in the metabolite maps were the result of spatial noise-like aliasing rather than lower spectral SNR in the accelerated data.

ACKNOWLEDGMENT

This study was supported by the European Research Council Starting grant (project SYNAPLAST MR #679927) and the Horizon 2020 grant (project CDS_QUAMRI #634541).

REFERENCES

[1] Bogner W, Gruber S, Trattnig S, Chmelik M. High-resolution mapping of human brain metabolites by free induction decay ^{1}H MRSI at 7 T. *NMR Biomed.* 2012;25:873-882.

[2] Boer VO, Klomp DWJ, Juchem C, Luijten PR, de Graaf RA. Multislice ^{1}H MRSI of the human brain at 7 T using dynamic B_0 and B_1 shimming. *Magn Reson Med.* 2012;68:662-670.

[3] Strasser B, Povazan M, Hangel G, et al. (2 + 1)D-CAIPIRINHA accelerated MR spectroscopic imaging of the brain at 7T. *Magn Reson Med.* 2017;78:429-440.

[4] Hangel G, Strasser B, Považan M, et al. Ultra-high resolution brain metabolite mapping at 7 T by short-TR Hadamard-encoded FID-MRSI. *Neuroimage.* 2018;168:199-210.

[5] Nassirpour S, Chang P, Henning A. High and ultra-high resolution metabolite mapping of the human brain using ^{1}H FID MRSI at 9.4T. *Neuroimage.* 2016;168:211-221.

[6] Chadzynski GL, Bause J, Shajan G, Pohmann R, Scheffler K, Ehses P. Fast and efficient free induction decay MR spectroscopic imaging of the human brain at 9.4 Tesla. *Magn Reson Med.* 2017;78:1281-1295.

[7] Lam F, Li Y, Clifford B, Liang ZP. Macromolecule mapping of the brain using ultrashort-TE acquisition and reference-based metabolite removal. *Magn Reson Med.* 2018;79:2460-2469.

[8] Posse S, Tedeschi G, Risinger R, Ogg R, Le Bihan D. High speed ^{1}H spectroscopic imaging in human brain by echo planar spatial-spectral encoding. *Magn Reson Med.* 1995;33:34-40.

[9] Posse S, Otazo R, Caprihan A, et al. Proton echo-planar spectroscopic imaging of J-coupled resonances in human brain at 3 and 4 Tesla. *Magn Reson Med.* 2007;58:236-244.

[10] Maudsley AA, Domenig C, Govind V, et al. Mapping of brain metabolite distributions by volumetric proton MR spectroscopic imaging (MRSI). *Magn Reson Med.* 2009;61:548-559.

[11] Lecocq A, Le Fur Y, Maudsley AA, et al. Whole-brain quantitative mapping of metabolites using short echo three-dimensional proton MRSI. *J Magn Reson Imaging.* 2015;42:280-289.

[12] Andronesi OC, Gagoski BA, Sorensen AG. Neurologic 3D MR spectroscopic imaging with low-power adiabatic pulses and fast spiral acquisition. *Radiology.* 2012;262:647-661.

[13] Kasten J, Lazeyras F, Van De Ville D. Data-driven MRSI spectral localization via low-rank component analysis. *IEEE Trans Med Imaging.* 2013;32:1853-1863.

[14] Lam F, Liang ZP. A subspace approach to high-resolution spectroscopic imaging. *Magn Reson Med.* 2014;71:1349-1357.

[15] Ma C, Lam F, Johnson CL, Liang ZP," Removal of nuisance signals from limited and sparse 1H MRSI data using a union-of-subspaces model. *Magn Reson Med.* 2016;75:488-497.

[16] Lam F, Ma C, Clifford B, Johnson CL, Liang ZP. High-resolution (1) H-MRSI of the brain using SPICE: Data acquisition and image reconstruction. *Magn Reson Med.* 2016;76:1059-1070.

[17] Ma Chao, Lam F, Ning Q, Johnson CL, Liang ZP. High-resolution ^{1}H-MRSI of the brain using short-TE SPICE. *Magn Reson Med.* 2016;77:467-479.

[18] Bhattacharya I, Jacob M. Compartmentalized low-rank recovery for high-resolution lipid unsuppressed MRSI. *Magn Reson Med.* 2017;78:1267-1280.

[19] Hangel G, Strasser B, Povazan M, et al. Lipid suppression via double inversion recovery with symmetric frequency sweep for robust 2D-GRAPPA-accelerated MRSI of the brain at 7 T. *NMR Biomed.* 2015;28:1413-1425.

[20] Kirchner T, Fillmer A, Tsao J, Pruessman KP, Henning A. Reduction of voxel bleeding in highly accelerated parallel ^{1}H MRSI by direct control of the spatial response function. *Magn Reson Med.* 2015;73:469-480.

[21] Candes E, Romberg J, Tao T. Robust uncertainty principles: exact signal reconstruction from highly incomplete frequency information. *IEEE Trans Inf Theory.* 2006;52:489-509.

[22] Lustig M, Donoho D, Pauly JM. Sparse MRI: The application of compressed sensing for rapid MR imaging. *Magn Reson Med.* 2007;58:1182-1195.

[23] Lustig M, Donoho D, Santos JM, Pauly JM. Compressed sensing MRI. *IEEE Signal Process Mag.* 2008;25:72-82.

[24] Posse S, DeCarli C, Le Bihan D. Three-dimensional echo-planar MR spectroscopic imaging at short echo times in the human brain. *Radiology.* 1994;192:733-738.

[25] Hu S, Lustig M, Balakrishnan A, et al. 3D compressed sensing for highly accelerated hyperpolarized ^{13}C MRSI with in vivo applications to transgenic mouse models of cancer. *Magn Reson Med.* 2010;63:312-321.

[26] Geraghty BJ, Lau JY, Chen AP, Cunningham CH. Accelerated 3D echo-planar imaging with compressed sensing for time-resolved hyperpolarized ^{13}C studies. *Magn Reson Med.* 2016;77:538-546.

[27] Larson PEZ, Hu S, Lustig M, et al. Fast dynamic 3D MR spectroscopic imaging with compressed Sensing and multiband excitation pulses for hyperpolarized ^{13}C studies. *Magn Reson Med.* 2011;65:610-619.

[28] Cao P, Shin PJ, Park I, et al. Accelerated high-bandwidth MR spectroscopic imaging using compressed sensing. *Magn Reson Med.* 2016;76:369-379.

[29] Kampf T, Fischer A, Basse-Lüsebrink TC, et al. Application of compressed sensing to in vivo 3D ^{19}F CSI. *J Magn Reson.* 2010;207:262-273.

[30] Askin NC, Atis B, Ozturk-Isik E. Accelerated phosphorus magnetic resonance spectroscopic imaging using compressed sensing. *Conf Proc IEEE Eng Med Boil Soc.* 2012;2012:1106-1109.

[31] Maguire ML, Geethanath S, Lygate CA, Kodibagkar VD, Schneider JE. Compressed sensing to accelerate magnetic resonance spectroscopic imaging: evaluation and application to ^{23}Na-imaging of mouse hearts. *J Cardiovasc Magn Reson.* 2015;17:45.

[32] Furuyama JK, Wilson NE, Burns BL, Nagarajan R, Margolis DJ, Thomas MA. Application of compressed sensing to multidimensional spectroscopic imaging in human prostate. *Magn Reson Med.* 2012;67:1499-1505.

[33] Merhej D, Ratiney H, Diab C, Khalil M, Sdika M, Prost R. Fast multidimensional NMR spectroscopy for sparse spectra. *NMR Biomed.* 2014;27:640-655.

[34] Sarma MK, Nagarajan R, Macey PM, et al. Accelerated echo-planar J-resolved spectroscopic imaging in the human brain using compressed sensing: a pilot validation in obstructive sleep apnea. *AJNR Am J Neuroradiol.* 2014;35:81-89.

[35] Iqbal Z, Wilson NE, Thomas MA. 3D spatially encoded and accelerated TE-averaged echo planar spectroscopic imaging in healthy human brain. *NMR Biomed.* 2016;29:329-339.

[36] Geethanath S, Baek HM, Ganji SK, et al. Compressive sensing could accelerate ^{1}H MR metabolic imaging in the clinic. *Radiology.* 2012;262:985-994.

[37] Cao P, Wu EX. Accelerating phase-encoded proton MR spectroscopic imaging by compressed sensing. *J Magn Reson Imaging.* 2015;41:487-95.

[38] Chatnuntawech I, Gagoski B, Bilgic B, Cauley SF, Setsompop K, Adalsteinsson E. Accelerated ^{1}H MRSI using randomly undersampled spiral-based k-space trajectories. *Magn Reson Med.* 2015;74:13-24.

[39] Otazo R, Sodickson DK, Yoshimoto A, Posse S. Accelerated proton echo-planar spectroscopic imaging using parallel imaging and compressed sensing. In Proceedings of the 17th Annual Meeting of ISMRM, Honolulu, HI, 2009. Abstract 331.

[40] Otazo R, Kim D, Axel L, Sodickson DK. Combination of compressed sensing and parallel imaging for highly accelerated first-pass cardiac perfusion MRI. *Magn Reson Med.* 2010;64:767-776.

[41] Shin PJ, Larson PE, Ohliger MA, et al. Calibrationless parallel imaging reconstruction based on structured low-rank matrix completion. *Magn Reson Med.* 2014;72:959-970.

[42] Avdievich N, Giapitzakis I, Pfrommer A, Borbath T, Henning A. Combination of surface and "vertical" loop elements improves receive performance of a human head transceiver array at 9.4T. *NMR Biomed.* 2018; https://doi.org/10.1002/nbm.3878.

[43] Henning A, Fuchs A, Murdoch JB, Boesiger P. Slice-selective FID acquisition, localized by outer volume suppression (FIDLOVS) for ^{1}H-MRSI of the human brain at 7 T with minimal signal loss. *NMR Biomed.* 2009;22:683-696.

[44] Cheng JY, Zhang T, Ruangwattanapaisarn N, et al. Free-breathing pediatric imaging with nonrigid motion correction and acceleration. *J Magn Reson Imaging.* 2015;42:407-420.

[45] Uecker M, Lai P, Murphy MJ, et al. ESPIRiT—an eigenvalue approach to autocalibrating parallel MRI: where SENSE meets GRAPPA. *Magn Reson Med.* 2014;71:990-1001.

[46] Cadzow JA. Signal enhancement—a composite property mapping algorithm. *IEEE Trans Acoust.* 1988;36:49-62.

[47] Klose U. In vivo proton spectroscopy in presence of eddy currents. *Magn Reson Med.* 1990;14:26-30.

[48] Bydder M, Hamilton G, Yokoo T, Sirlin CB. Optimal phased-array combination for spectroscopy. *Magn Reson Imaging.* 2008;26:847-850.

[49] Kay SM. *Modern Spectral Estimation: Theory and Application.* Englewood Cliffs, NJ: Prentice Hall; 1998.

[50] Cabanes E, Confort-Gouny S, Le Fur Y, Simond G, Cozzone PJ. Optimization of residual water signal removal by HLSVD on simulated short echo time proton MR spectra of the human brain. *J Magn Reson.* 2001;150:116-125.

[51] Provencher SW. Estimation of metabolite concentrations from localized in vivo proton NMR spectra. *Magn Reson Med.* 1993;30:672-679.

[52] Boer VO, Van de Lindt T, Luijten PR, Klomp DWJ. Lipid suppression for brain MRI and MRSI by means of a dedicated crusher coil. *Magn Reson Med.* 2015;73:2062-2068.

[53] Adalsteinsson E, Irarrazabal P, Topp S, Meyer C, Macovski A, Spielman DM. Volumetric spectroscopic imaging with spiral-based k-space trajectories. *Magn Reson Med.* 1998;39:889-898.

[54] Schirda CV, Tanase C, Boada FE. Rosette spectroscopic imaging: optimal parameters for alias-free, high sensitivity spectroscopic imaging. *J Magn Reson Imaging.* 2009;29:1375-1385.

SUPPORTING INFORMATION

Additional Supporting Information may be found in the online version of this article.

FIGURE S1. Representative spectra from R = 4 acceleration resulting from the coil-by-coil x-t sparse reconstruction (red) and the SENSE x-t sparse reconstruction (black). For visualization purposes, only every four voxel in the grid has been shown. The spectra are shown between 0.1 and 4.2 ppm

FIGURE S2. Metabolite maps for three major metabolites (NAA, Glu, and tCho) shown for different acceleration factors on the same volunteer as in Figure 6. Metabolite maps are shown for the compressed sensing reconstruction (top) and alternatively for the low rank reconstruction (bottom)

FIGURE S3. Metabolite maps of four major metabolites (NAA, Cre, Glu, and tCho) resulting from applying the CS method for prospective in vivo acceleration (with R = 5) in 3 healthy subjects

FIGURE S4. Accelerated reduced resolution metabolite maps of the same volunteer as Figure 8 using the compressed sensing reconstruction for different acceleration factors. Metabolite maps with in-plane matrix sizes of 48 × 48 and 32 × 32 are shown in the top and bottom panels, respectively. The maps are shown for NAA, Glu, and tCho

How to cite this article: Nassirpour S, Chang P, Avdievitch N, Henning A. Compressed sensing for high-resolution nonlipid suppressed ^{1}H FID MRSI of the human brain at 9.4T. *Magn Reson Med.* 2018;00:1–15. https://doi.org/10.1002/mrm.27225

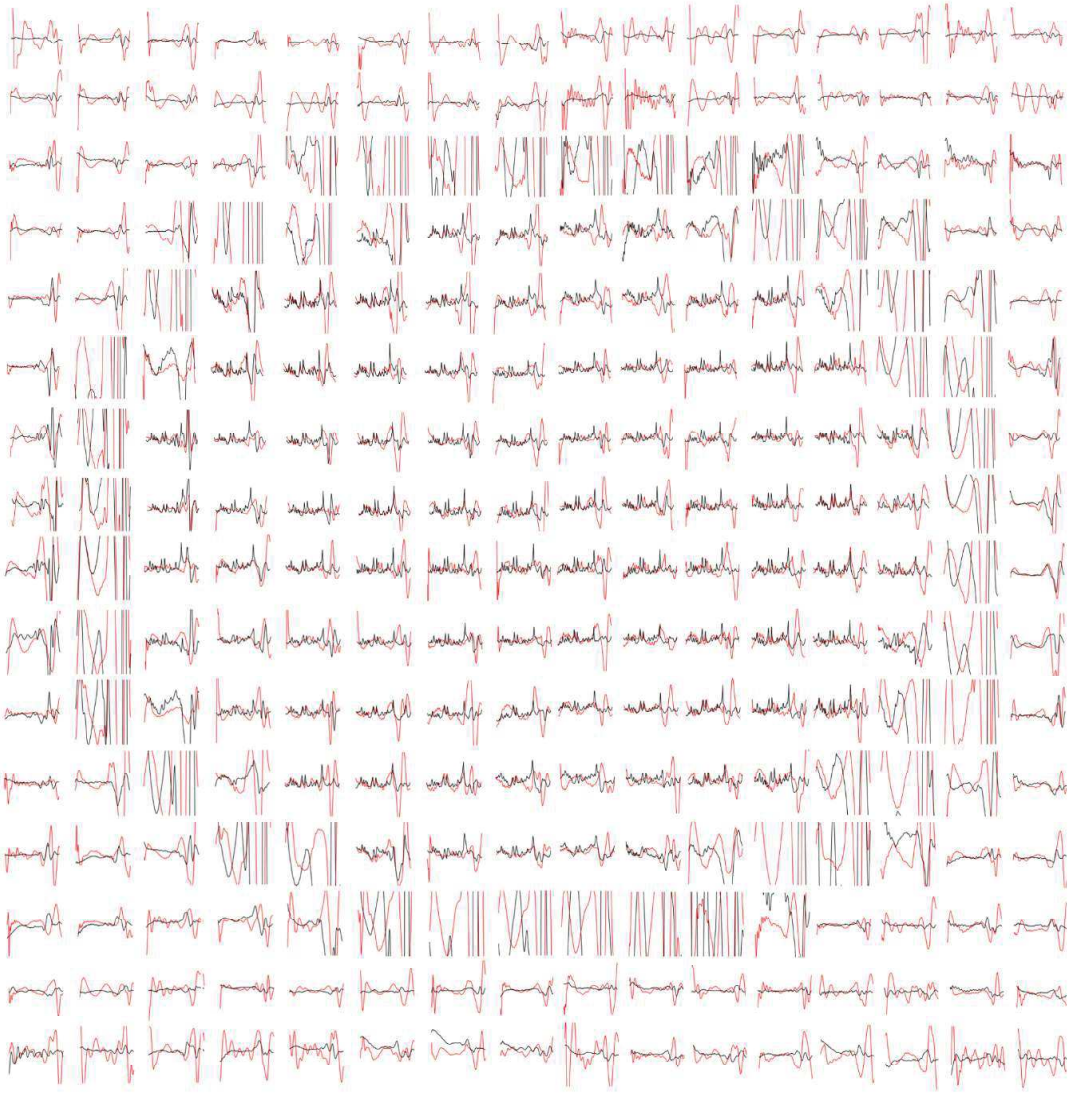

Figure S1- Representative spectra from R=4 acceleration resulting from the coil-by-coil x-t sparse reconstruction (red) and the SENSE x-t sparse reconstruction (black). For visualization purposes, only every four voxel in the grid has been shown. The spectra are shown between 0.1 and 4.2 ppm.

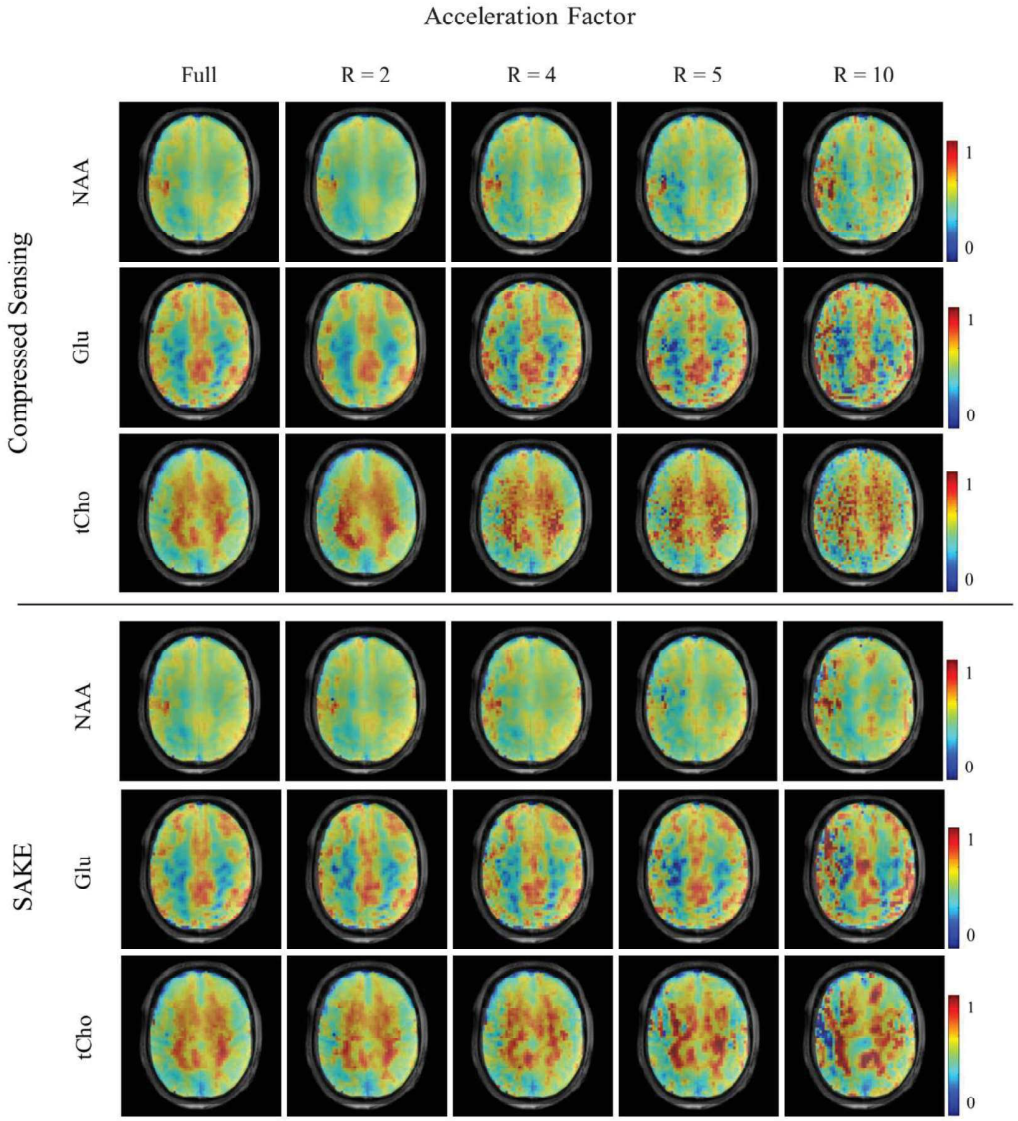

Figure S2- Metabolite maps for three major metabolites (NAA, Glu and tCho) shown for different acceleration factors on the same volunteer as in Figure 6. Metabolite maps are shown for the compressed sensing reconstruction (top) and alternatively for the low rank reconstruction (bottom).

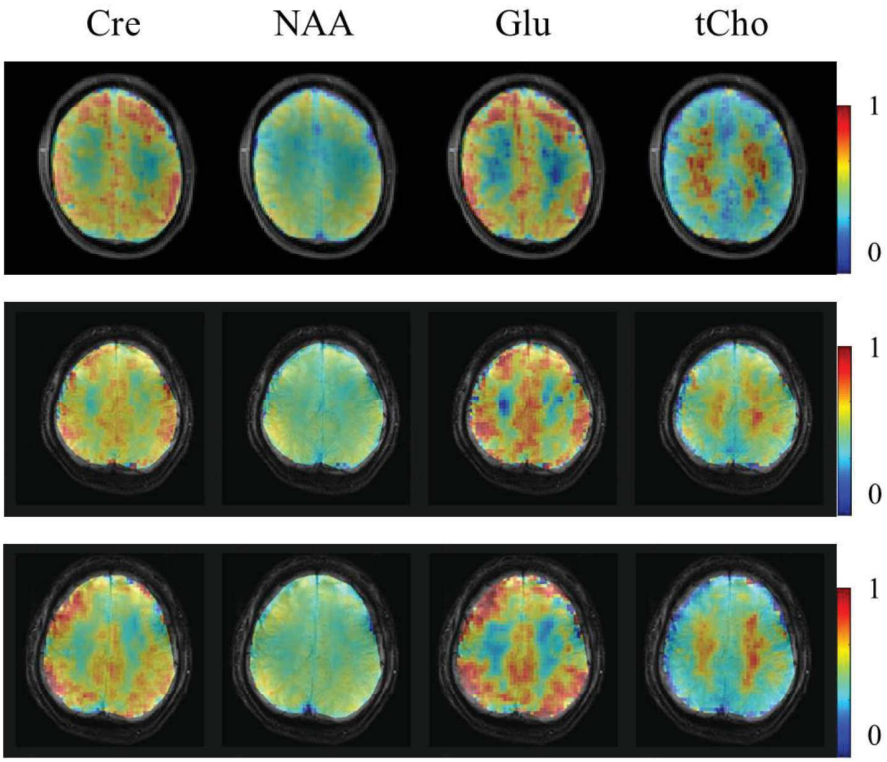

Figure S3- Metabolite maps of four major metabolites (NAA, Cre, Glu and tCho) resulting from applying the CS method for prospective in-vivo acceleration (with R = 5) in 3 healthy subjects.

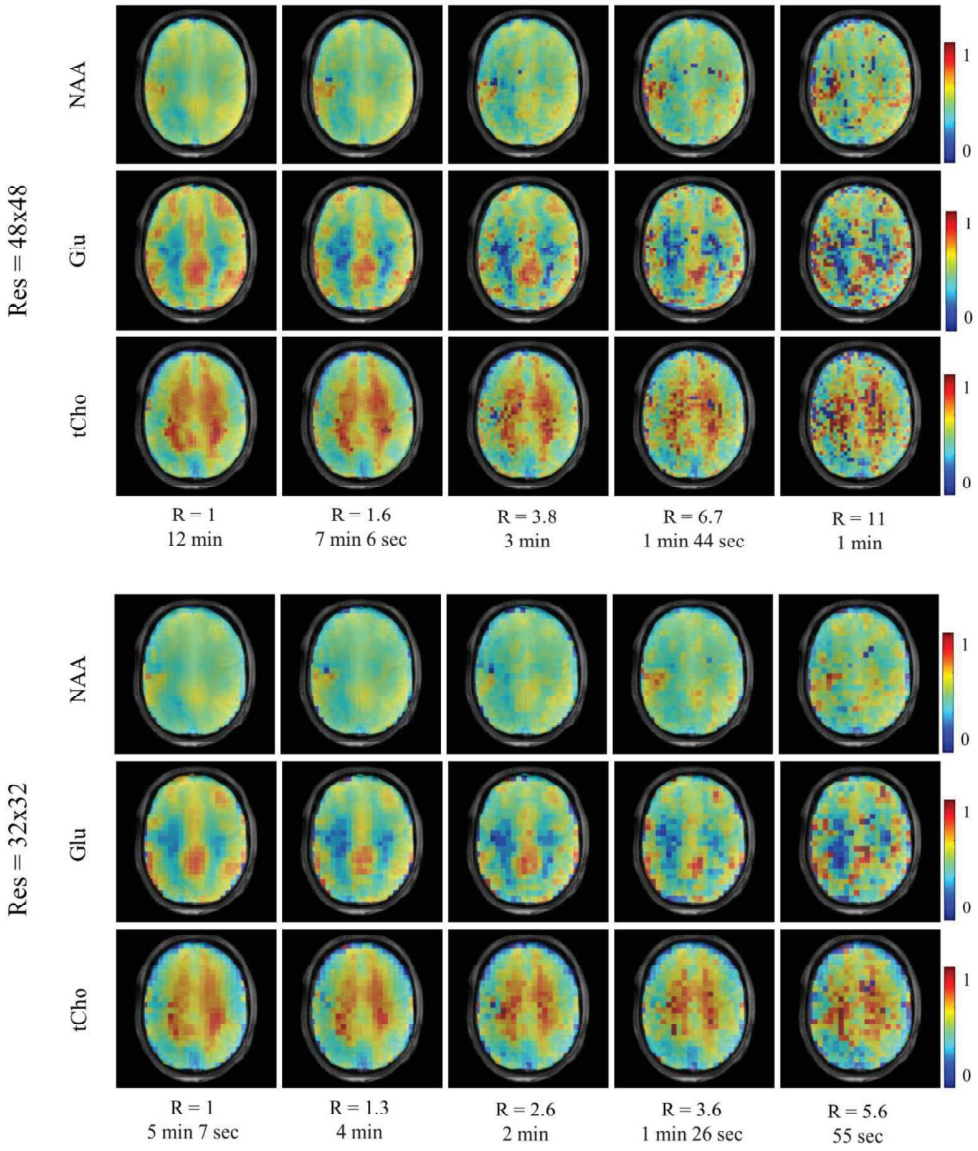

Figure S4- Accelerated reduced resolution metabolite maps of the same volunteer as Figure 8 using the compressed sensing reconstruction for different acceleration factors. Metabolite maps with in-plane matrix sizes of 48x48 and 32x32 are shown in the top and bottom panels, respectively. The maps are shown for NAA, Glu and tCho.

Publication IV

"Over-discretized SENSE reconstruction and B_0 correction for accelerated non-lipid-suppressed ^{1}H FID MRSI of the human brain at 9.4T"

S Nassirpour*, P Chang*, A Henning

[in review]

NMR in Biomedicine

Over-discretized SENSE reconstruction and B_0 correction for accelerated non-lipid-suppressed ^{1}H FID MRSI of the human brain at 9.4T

Journal:	*NMR in Biomedicine*
Manuscript ID	NBM-18-0031.R1
Wiley - Manuscript type:	Research Article
Date Submitted by the Author:	n/a
Complete List of Authors:	Nassirpour, Sahar; Max-Planck-Institut fur biologische Kybernetik; Eberhard Karls University Tuebingen, IMPRS for Cognitive and Systems Neuroscience Chang, Paul; Max-Planck-Institut fur biologische Kybernetik; Eberhard Karls University Tuebingen, IMPRS for Cognitive and Systems Neuroscience Kirchner, Thomas; University and ETH Zurich, Institute for Biomedical Engineering Henning, Anke; Max Planck Institute for Biological Cybernetics, High-Field Magnetic Resonance Center; University and ETH Zurich, Institute for Biomedical Engineering; Ernst-Moritz-Arndt University Greifswald, Institute of Physics
Keywords:	MR Spectroscopy (MRS) and Spectroscopic Imaging (MRSI) Methods < Methods and Engineering, Parallel imaging < Acquisition Methods < Methods and Engineering, Reconstruction < Post-acquisition Processing < Methods and Engineering

Over-discretized SENSE reconstruction and B_0 correction for accelerated non-lipid-suppressed ^1H FID MRSI of the human brain at 9.4T

†Sahar Nassirpour[1, 2], †Paul Chang[1, 2], Thomas Kirchner[3], Anke Henning[1, 3, 4]

[1]*Max Planck Institute for Biological Cybernetics, Tuebingen, Germany*

[2]*IMPRS for Cognitive and Systems Neuroscience, Eberhard-Karls University of Tuebingen, Germany*

[3]*Institute for Biomedical Engineering, University and ETH Zurich, Zurich, Switzerland*

[4]*Institute of Physics, Ernst-Moritz-Arndt University Greifswald, Greifswald, Germany*

Max Planck Institute for Biological Cybernetics

Max-Planck-Ring 11

72076 Tübingen

Phone: +49 7071 939

Email: sahar.nassirpour@tuebingen.mpg.de

† These authors contributed equally to this work.

This study was supported by the European Research Council Starting grant, project SYNAPLAST MR #679927.

Word Count: 5425

Keywords:

SENSE, metabolite mapping, ultra-high field, 9.4T, FID MRSI

Abbreviations used:

ACS auto calibration signal

Ala alanine

AP anterior-posterior

Asc ascorbate

Asp aspartate

CRLB Cramer-Rao lower bound

Cre creatine

ESPIRiT efficient iterative self-consistent parallel imaging reconstruction

FLASH fast low angle shot

FID free induction decay

FOV field of view

GABA γ- aminobutyrate

Glc glucose

Gln glutamine

Glu glutamate

GPC glycerophosphocholine

GRAPPA Generalized autocalibrating partially parallel acquisitions

GRE gradient echo

GSH glutathione

Lac lactate

mI myo-inositol

MRSI magnetic resonance spectroscopic imaging

NAA N-acetylaspartate

NAAG N-acetylaspartylglutamate

OD over-discretized

PCh phosphocholine

PE phosphoethanolamine

PEPSI proton echo planar spectroscopic imaging

PI parallel imaging

RF radio frequency

RL right-left

RMSE root mean square error

SAR specific absorption rate

SENSE sensitivity encoding

SNR signal-to-noise ratio

Tau taurine

tCho total choline

Abstract:

The aim of this work was to use post-processing methods to improve the data quality of metabolite maps acquired on the human brain at 9.4T with accelerated acquisition schemes. This was accomplished by combining an improved SENSE reconstruction with a B_0 correction of spatially over-discretized MRSI data.

Since MRSI scans suffer from long scan duration, investigating different acceleration techniques has recently been the focus of several studies. Due to strong B_0 inhomogeneity and strict SAR limitations at ultra-high fields, the use of a low-SAR sequence combined with an acceleration technique that is compatible with dynamic B_0 shim updating is preferable. Hence, in this study, a non-lipid-suppressed ultra-short TE and TR ^{1}H FID MRSI sequence is combined with an in-plane SENSE acceleration technique to obtain high resolution metabolite maps in a clinically feasible scan time. One of the major issues in applying parallel imaging techniques to non-lipid-suppressed MRSI is the presence of strong lipid aliasing artifacts which, if not thoroughly resolved, will hinder the accurate quantification of the metabolites of interest. To achieve a more robust reconstruction, an over-discretized SENSE reconstruction (with direct control over the shape of the spatial response function) was combined with an over-discretized B_0 correction. This method is compared to conventional SENSE reconstruction for seven acceleration schemes on four healthy volunteers.

The over-discretized method consistently outperformed the conventional SENSE resulting in an average of 23±1.2% more signal-to-noise ratio and 8±2.9% less error in the NAA signal over a whole brain slice. The highest achievable acceleration factor with the proposed technique was determined to be 4. Finally, using the over-discretized method, high resolution (97μL nominal voxel size) metabolite maps can be acquired in 3.75 minutes at 9.4T. This robust acceleration technique will enable the acquisition of high resolution metabolite maps with more spatial coverage at ultra-high fields.

Introduction:

In recent years, magnetic resonance imaging (MRI) methods that have been hindered by low signal-to-noise ratio (SNR) are being revisited and revitalized by the advent of ultra-high field (UHF) MRI scanners (i.e. magnetic field strengths of 7T and higher). In fact, the SNR has been shown to increase at a super-linear rate with respect to the field strength [1, 2]. For magnetic resonance spectroscopic imaging (MRSI), the use of higher field strength can lead to images with higher spatial and spectral resolution [3-5].

Furthermore, the higher SNR allows higher acceleration using, for example, parallel imaging methods such as SENSE [6] and GRAPPA [7]. This is beneficial to MRSI where the scan times are often very lengthy. Reducing the scan times of MRSI studies can pave the way for new research and clinical applications, as it enables metabolite mapping with more tissue coverage (e.g. multi-slice or whole-brain coverage) in a clinically feasible scan time, as well as dynamic time-lapse metabolic imaging.

However, no system offering improvements is without its drawbacks. This, too, is the case for UHF MRI where the technical challenges are in abundance. For instance, the B_1^+ and B_1^- radiofrequency (RF) fields are more inhomogeneous [8, 9], the static magnetic B_0 field is also more inhomogeneous, and there is a higher specific absorption rate (SAR) and hence stricter SAR restrictions. These technical challenges limit the use of certain sequences, acceleration schemes, RF pulses and lipid suppression methods. For example, lipid suppression and outer volume suppression RF pulses typically result in a lot of SAR [8, 9]. This increases the scan duration to something that is impractical for clinical applications. Furthermore, 3D acquisition techniques and simultaneous multi-slice acquisition techniques, such as echo-planar spectroscopic imaging (EPSI) [10] and Hadamard-encoding [11], would be incompatible with dynamic slice-wise B_0 shimming (e.g. Boer et al. [12]), hence limiting the achievable B_0 homogeneity. Additionally, for spectroscopy applications, the required spectral bandwidth is higher, which makes spatial-spectral acquisition schemes for MRSI more difficult [13]. In light of this, a slice-selective FID MRSI without lipid and outer-volume suppression was used in this study [14-16].

At ultra-high field strengths, in-plane PI acceleration methods are favored over 3D acceleration schemes as they are still compatible with dynamic slice-wise B_0 shim updating, without which it would be near impossible to acquire reliable spectroscopy data from lower positions in the brain at ultra-high fields. Among the parallel imaging methods, the two most commonly used are SENSE [6] and GRAPPA [7] (or variants thereof). Both of these methods have been applied previously to accelerate ^{1}H MRSI scans in combination with different sequences (e.g. [17, 18]). However, only GRAPPA has so far been used to accelerate non-lipid-suppressed ultra-short TR and TE ^{1}H FID MRSI [19]. The results of this study suggested that due to the strong unsuppressed lipid signals originating from the subcutaneous lipid region, which interfere with the metabolite signals in the brain when aliased, a reconstruction method that can properly unalias the signals is of utmost importance. Conventional PI reconstruction methods result in noise amplification (especially for higher acceleration factors) and residual aliasing artifacts in the image. The noise amplification will increase the CRLBs and the residual aliasing artefacts will overshadow the metabolite signals from the brain, and make quantification in the affected regions nearly impossible. Hence, it was clear that the reconstruction methods should be improved by controlling the lipid aliasing artifacts to allow for higher acceleration factors.

Recently, Kirchner et al [20] presented an improved SENSE reconstruction method that proved beneficial for reducing the near and far reaching voxel bleeding through a direct control of the shape of the spatial response function (SRF). The reconstruction was done on an over-discretized grid at a higher spatial resolution compared to the acquired MRSI data and coil sensitivity maps of the same higher resolution were used to unalias the image. In this way, the intra-voxel coil sensitivity variations were taken into account. Thereafter, a target function of an optimized shape was used to shape the voxels back into the original resolution. The shape and properties of this target function determined the ultimate shape of the SRF. In a later work by the same authors, they added an additional step before applying the target function, where a high resolution shimmed B_0 field map was used to correct for intra-voxel frequency shifts [21]. This additional step resulted in an increase of SNR and an improvement in the spectral lineshapes. These improvements stemmed not only from more constructive averaging of the sub-voxels, but also from spatial noise decorrelation. This optimized and more accurate reconstruction has so far only been applied to lipid-suppressed ^{1}H FID MRSI where the long TRs (resulting from strict SAR limitations) prevented the acquisition of high resolution metabolite maps. Furthermore, since a lipid suppression scheme was used in the previous study, the benefits of the suggested method for non-lipid-suppressed data have not yet been explored.

In this work, we combine the over-discretized SENSE reconstruction along with the B_0 correction method [20, 21] and apply them for the first time to an ultra-short TR and TE non-lipid-suppressed ^{1}H FID MRSI sequence to enable high resolution metabolite mapping of the human brain at 9.4T in a clinically feasible scan time. The suggested method is extensively compared to conventional SENSE reconstruction for different acceleration factors to demonstrate the advantages, and is then used to acquire accelerated metabolite maps at 9.4T. Finally, the method is also compared to a conventional GRAPPA reconstruction.

Theory:

In any PI method, k-space data is acquired from an array of receive coils that each have a spatially varying receive sensitivity profile. Images are then reconstructed from this multi-channel raw data.

The relationship between the acquired k-space data and the underlying desired image in any MR experiment can be formulated as:

$$s = E\rho + \eta \quad (1)$$

where s is the acquired k-space data, E is the encoding matrix, η is the receiver noise, and ρ is the original image in spatial domain. The encoding matrix includes information about the way data is encoded in k-space and acquired. For a 2D phase-encoded FID MRSI sequence which acquires samples on a Cartesian grid, this reduces down to a discrete Fourier operator. In the SENSE acceleration approach, the spatially varying receive coil sensitivities are used as an additional encoding mechanisms, such that the encoding matrix E is the product of the discrete Fourier operator at each of the acquired points in k-space and the coil sensitivity profiles.

Reconstruction of the original image then comes down to finding the reconstruction operator F such that:

$$\rho = Fs \quad (2)$$

In an ideal experiment (in the absence of noise), the analytic solution to this system of linear equations is:

$$F = (E^H E)^{\dagger} E^H \quad (3)$$

where E^H is the Hermitian adjoint of the encoding matrix, and † indicates the Moore–Penrose pseudoinverse.

In the presence of receiver noise coupling, in a process known as noise pre-whitening, the system of linear equations is first weighted by the inverse square root of the noise covariance matrix of the receive system. So instead of Eq. (2), we solve the new problem posed as:

$$L^{-1}\rho = L^{-1}Fs \tag{4}$$

where L is the square root of the noise covariance matrix ψ (e.g. by Cholesky decomposition) such that:

$$\psi = LL^H \tag{5}$$

The noise covariance between coil elements i and j is calculated as:

$$\psi_{i,j} = < \eta_i, \eta_j >= \overline{\eta_i \eta_j^*} \tag{6}$$

The analytical solution to the new system of equations described in Eq. (4) can thus be written as:

$$F = (E^H \psi^{-1} E)^{\dagger} E^H \psi^{-1} \tag{7}$$

The reconstruction matrix F calculated with Eq. (7) is the conventional SENSE reconstruction operator commonly used [16]. It is hereafter simply referred to as SENSE.

In the over-discretized reconstruction method used in [20] however, the coils sensitivity maps are acquired at a higher resolution compared to the MRSI data, and the MRSI data is first zero-padded in k-space (as shown in Figure 1). The reconstruction problem is hence posed on an over-discrete grid:

$$s_{OD} = E_{OD}\rho + \eta \tag{8}$$

Where the subscript OD (over-discrete) indicates that the denoted matrices have higher resolution compared to the original MRSI data.

Instead of solving the SENSE problem directly as cast in Eq. (8), a target SRF shape is chosen and an objective function is defined and minimized (in the least-square sense) to directly control the deviation of the shape of the resulting SRF from a target shape T (Figure 1):

$$\min \| F E_{OD} - T \|_2^2 \tag{9}$$

The analytical solution to this problem (in the presence of noise coupling) can then be written as:

$$F = T(E_{OD}^H \psi^{-1} E_{OD})^{\dagger} E_{OD}^H \psi^{-1} \tag{10}$$

Essentially, the operator T is used to go back to the original matrix size and shape the voxel in the original resolution by weighing each reconstructed sub-voxel according to the shape of the chosen target function. The shape of this operator indicates the amount of voxel bleeding from the neighboring voxels.

To incorporate the frequency shift correction on a sub-voxel level as described in [21], the operator F described in Eq. (10) is broken into two parts:

$$F = TF_{intermediate} \tag{11}$$

where

$$F_{intermediate} = (E_{OD}^{H}\psi^{-1}E_{OD})^{\dagger}E_{OD}^{H}\psi^{-1} \quad (12)$$

First an intermediate high resolution image, $\rho_{intermidiate}$, is formed by applying the intermediate operator to the zero-padded k-space data:

$$\rho_{intermediate} = F_{intermediate}s_{OD} \quad (13)$$

Then, the high resolution shimmed B_0 field map is used to correct for the inhomogeneity induced frequency shifts on a sub-voxel level,

$$\rho_{intermediate}(r,t) = \rho_{1intermediate}(r,t)e^{-2\pi i\Delta f_0(r).t} \quad (14)$$

Finally, the target averaging operator is again used to shape the voxels back into the original resolution:

$$\rho = F\rho_{intermediate} \quad (15)$$

The reconstruction matrix F calculated with Eqs. (10-15) is the over-discretized target-driven SENSE reconstruction combined with B_0 correction SNR boosting technique that will be investigated in this paper. It is hereafter simply referred to as OD-SENSE and its processing pipeline is depicted in Figure 1.

Methods:

All scans in this study were performed on a 9.4T Siemens whole-body human scanner (Erlangen, Germany) with an in-house developed 18 channel transmit, 32 channel receive RF coil [22]. Fully sampled high resolution ^{1}H MRSI data of a single-slice were acquired from the brains of four healthy volunteers. All volunteers gave their informed written consent prior to the scan in accordance with the regulations of the local ethics committee board. The slice was positioned parallel to the Corpus Callosum and running through the periventricular white matter in all volunteers.

A custom slice-selective and non-lipid-suppressed ultra-short TR and TE ^{1}H FID MRSI sequence was used to acquire the single-slice MRSI data [14-16]. A short and optimized water suppression scheme consisting of 3 pulses (as described in [16]) was incorporated into the sequence prior to the excitation pulse. Other parameters of the sequence were: FOV = 200x200 mm, slice thickness = 10 mm, in-plane matrix size = 64x64, TR = 300 ms, acquisition delay = 1.56 ms, flip angle = 30°, spectral bandwidth = 8000 Hz, and acquisition time = 128 ms. As a result, the total scan time of fully sampled data was 15 mins, and the nominal voxel size was 97μL. B_0 shimming for all scans was performed using the vendor-implemented image-based 2nd order spherical harmonic shimming routine on the same imaging volume as the MRSI data.

In order to perform eddy current and zero-order phase correction, a water reference was acquired for each volunteer using the same sequence but without the water suppression scheme. To avoid lengthy scan times, this water reference scan had half the spatial resolution of the original MRSI slice in each direction (four times faster).

An additional high resolution SENSE anatomical reference image from the same imaging volume as the MRSI data was acquired for each volunteer using a 2D FLASH sequence with the following parameters: TR = 312 ms, TE = 9 ms, flip angle = 25°, in-plane matrix size = 256x256 (four times over-discretized in

each direction with respect to the MRSI image). Additionally, the high resolution shimmed B_0 map of the MRSI imaging volume was acquired using a 2D dual-echo gradient echo (GRE) sequence with the following parameters: TR = 100 ms, ΔTE = 0.76 mm, in-plane matrix size = 256x256, read-out bandwidth = 1400 Hz. So the nominal voxel size of the anatomical image and the shimmed B_0 field map were approximately 6μL (16 times smaller than the MRSI voxel size).

The fully sampled MRSI data were retrospectively undersampled with increasingly higher acceleration factors in both the anterior-posterior and right-left directions. A total of eight different acceleration schemes, namely, 1x1 (fully sampled), 1x2, 2x1, 1x3, 3x1, 2x2, 2x3, and 3x2 were retrospectively implemented on the acquired data where R = nxm denotes acceleration of n in the anterior-posterior direction and m in the right-left direction.

Two different SENSE reconstruction methods (SENSE, and OD-SENSE, as described in the previous section) were used to reconstruct the undersampled data for each of the chosen acceleration factors. Coil sensitivity maps were calculated from the high resolution anatomical reference image using an eigenvalue decomposition based approach known as ESPIRiT [23]. This method calculates robust coil sensitivity maps by forming a calibration matrix from the reference image data and performing eigen-decomposition in the image domain. The receive coil system's noise covariance matrix was calculated using the pixels from a noise-only region in the anatomical reference data.

The OD-SENSE reconstruction was performed on a grid of 256x256 (four times higher resolution than the original data in each direction) and a Gaussian shape with a characteristic width of 0.5 times the original MRSI voxel size (equivalent to 2 sub-voxels) was used as the target SRF shape. The target function was chosen to be Gaussian since Kirchner et al. [20] showed that this was the optimal choice.

After reconstructing the spectra using the two different SENSE reconstruction methods, the spectra were post-processed using the same methodology as described in [16]. This included eddy current correction using the non-water suppressed reference data, automatic phase correction, and residual water peak removal. The processed spectra were then fitted using the LCMODEL software [24]. The basis-set was simulated using the GAMMA library (http://www.nmr.ethz.ch/Gamma.html) and included spectra of 18 brain metabolites (namely GPC, Tau, Cre, Glc, Naa, Asc, Lac, GABA, NAAG, GSH, Glu, PE, mI, PCh, Ala, Gln, Scyllo and Asp) with a linewidth of 5Hz. The fit range was chosen to be between 1.8 and 4.2ppm. The parameter file used for fitting the MRSI data can be found in the supporting materials. Metabolite maps were formed from the results of the fit for each of the datasets.

A number of qualitative and quantitative metrics were used to evaluate the performance of the different acceleration methods. Lipid contamination maps were calculated as the absolute integral of the spectra from 0.3 to 1.8 ppm to assess the amount of far and near voxel-bleeding as well as residual aliasing artifacts resulting from different acceleration factors. The lipid maps were normalized to the maximum lipid signal strength. SNR values were also calculated from the reconstructed spectra as the ratio between the absolute NAA peak maximum between 1.8 and 2.2 ppm and the root mean square of the residual noise between 10 and 11 ppm. Baseline trends in the noise region were removed by subtracting a linear fit in this range. This metric allowed us to evaluate how much noise is introduced as the acceleration factor increases. Another metric used for evaluation was the RMSE of the NAA maps with respect to the fully sampled data. The RMSEs are calculated as ratios of the fully sampled data:

$$RMSE = 100 \cdot \sqrt{\sum_{\vec{r} \in mask} \left(\frac{C_{accel}(\vec{r}) - C_{full}(\vec{r})}{C_{full}(\vec{r})} \right)^2 / N} \qquad (16)$$

where c_{accel} and c_{full} are the concentrations of NAA (from LCMODEL) for the accelerated data and fully sampled data, respectively, $mask$ is the spatial mask defined to include only voxels within the brain and N is the number of voxels inside the spatial mask. The RMSE metric indicates how accurate the metabolite maps are (using the fully sampled data as the benchmark reference). Lastly, the CRLBs of NAA, Glutamate, and total Choline are used as a metric to evaluate the confidence of the fits. The CRLB values were obtained from LCModel.

Next, the most reliable reconstruction with the highest feasible acceleration factor (judging by the results of the comparisons done above) was implemented in the sequence and was used to acquire accelerated high resolution ^{1}H MRSI data from the brain of three healthy volunteers to evaluate the reproducibility of the method on different subjects. For each volunteer, metabolite maps were generated using the same procedure described above.

Finally, the best SENSE reconstruction and acceleration was compared to a conventional GRAPPA reconstruction for the same acceleration factor. GRAPPA reconstruction was done with the 2D-GRAPPA operator method [25], using the central 64x64 grid of k-space data from the anatomical reference image as auto-calibration signal (ACS) to optimize the kernel weights. Metabolite maps from both reconstruction methods were generated and compared.

Results

Figure 2 shows the lipid contamination map for the fully sampled case as well as the accelerated case R=2x2, which was reconstructed with the conventional SENSE and with the OD-SENSE method for a representative volunteer. The SENSE reconstructed map clearly shows the residual aliasing artifact of the lipid signal stemming from the subcutaneous fat. However, the OD-SENSE reconstruction is able to better resolve the aliasing and results in less lipid contamination.

The reduction in the lipid signal due to the advantages of the OD-SENSE reconstruction can also be seen directly in the spectra (Figure 2). Voxels 1 and 5 did not coincide with any of the aliased lipid signal artifacts and there are, therefore, fewer differences in the spectra between the accelerated and fully sampled data. However, the OD-SENSE still shows better data consistency and less lipid contamination. Voxels 2, 3 and 4 are severely affected by the aliasing artifacts and thus have higher lipid signals. For all three voxels, the OD-SENSE has lower lipid contamination than the conventional SENSE reconstruction and is more comparable to the fully sampled spectra. To further appreciate the effect of the OD method on the reconstructed data, representative spectra from white and gray matter regions (along with the LCMODEL fits for Glu, NAA, and tCho) are shown in Figure S1. The residual aliasing artifacts of the conventional SENSE reconstruction have made it impossible for the fitting routine to detect the metabolites of interest, while the OD-SENSE reconstruction has succeeded in recovering the data.

The metabolite ratio maps for three major metabolites (/Cre) are shown in Figure 3 and the corresponding CRLB maps are shown in Figure 4. Note that the CRLB maps are of the metabolites only (not over creatine). These figures show the maps for accelerations in one phase encoding direction (AP) for R=2 and R=3. Figure S2 and S3 of the supporting material show the corresponding metabolite ratio maps and CRLB maps, respectively, resulting from acceleration of R=2 and R=3 in the other phase encoding direction (RL). The effect of the aliasing artifacts is visible in some of the metabolite maps. The advantage of OD-SENSE in reducing the aliasing artifacts can be seen, for example, in the total choline maps for R=2 in the AP direction. The OD-SENSE shows almost no aliasing artifacts, while the conventional SENSE has clear residual aliasing. This is also supported by the quantitative analysis in Table 1 where the number of voxels with a CRLB greater than 15% (for NAA) is much lower for OD-SENSE than SENSE. These voxels are most likely heavily affected by the residual aliasing artifacts. The

metabolite maps for the OD-SENSE are much more similar to the fully sampled data than the conventional SENSE reconstruction. Table 1 shows this quantitatively with the RMSE, where the OD-SENSE reduced the error by up to 10±2% for R=2 and approximately 5±1.4% for R=3. The higher SNR of the OD-SENSE reconstruction can be seen in the CRLB maps. This is supported by the SNR values given in Table 1, where there is an improvement of approximately 20±1% for OD-SENSE.

The metabolite maps for simultaneous acceleration in both AP and RL directions are shown in Figure 5. The respective CRLB maps are shown in Figure 6. Again, the OD-SENSE reconstruction is able to reduce the aliasing artifacts and this also increases the number of voxels that can be fit. The metabolite maps for OD-SENSE are more similar to the fully sampled data than for conventional SENSE. Table 1 shows an improved RMSE of approximately 10±2% for the OD-SENSE. For R=2x2, the amount of the residual lipid aliasing is less than for R=3 using OD-SENSE (Table 1). In other words, aliasing could be better resolved if it is spread over two directions than only in one direction with similar acceleration factor. It appears that the highest acceleration factor in which the OD-SENSE is able to resolve the lipid aliasing artifacts is R=2x2. Accelerating by higher than a factor of 2 in any phase encoding direction results in an excessive amount of residual lipid signals in the brain which makes the mapping of the metabolite in those areas nearly impossible.

The SNR values of NAA were calculated for each voxel and aggregated across the brain region (excluding the skull and subcutaneous fat) for four volunteers. Figure 7 shows the boxplot of the SNR values for the fully sampled, as well as conventional and over-discrete SENSE reconstructions for all seven different acceleration schemes. The noise increases as the acceleration factor increases. However, the SNR for the over-discrete SENSE reconstruction is higher than the conventional SENSE. The exact mean and standard deviations of the noise are given in the first column of Table 1. Paired-sample t-tests were performed to compare the significance of the SNR gain between SENSE and OD-SENSE reconstructions for all acceleration factors. The tests resulted in p-values of $P < 0.01$ across all acceleration factors. To quantify the SNR gain, Cohen effect size values were calculated for each pair and shown in Table 1. The boost in SNR had the highest effect size for R=2 (AP or RL) and R=4. The overall gain in SNR resulting from applying the over-discrete reconstruction in combination with B_0 correction compared to the conventional SENSE reconstruction was on average about 23.14±1.2%.

The RMSEs of the NAA maps and the CRLBs of the NAA, glutamate and choline maps (with respect to the fully sampled data) are shown in Figure 8. Paired-sample t-tests were performed to evaluate the significance of the CRLB reduction between SENSE and OD-SENSE for all acceleration factors. The tests resulted in p-values of $P < 0.01$ across all acceleration factors. To quantify the improvement, Cohen effect size values were again calculated for each pair and shown in Table 1. It can be seen that for all acceleration factors there is a modest effect size of CRLB reduction. The biggest effect is seen for R=2x2, where the OD-SENSE reconstruction is able to greatly reduce the residual aliasing artefacts in both directions. For R=3 the effect size is less. This is due to the fact that when accelerating 3 times in one direction, even with OD-SENSE there are still residual aliasing artefacts.

The three major metabolite ratio maps (/Cre) for two representative volunteers scanned using prospective undersampling of R=2x2 are shown in Figure 9. The maps did not show discernible residual aliasing artifacts. In addition to the metabolite maps, representative spectra from gray and white matter regions are shown for each volunteer.

Figure 10 shows the results of GRAPPA reconstruction for R=2x2. Three major metabolite ratio maps (/Cre) are shown for the same volunteer as in Figure 3 to 6. It is evident that there are more residual aliasing artifacts (arising from subcutaneous lipid ring) that affect the metabolite maps when GRAPPA is used. The lipid traces are indicated by yellow arrows in NAA, Glu and tCho maps. On the contrary, the

OD-SENSE maps show reasonable consistency with the fully sampled maps and do not have strong signs of structured residual aliasing. The SNR of the GRAPPA reconstruction was on average 29±1.7% lower than the OD-SENSE reconstruction.

Discussion

In-plane acceleration using parallel imaging for a non-lipid-suppressed ^{1}H FID MRSI sequence in the human brain is limited due to the presence of strong subcutaneous lipid signals. This problem has so far only been mediated by using post-processing lipid removal methods [26] or moving away from in-plane acceleration to through-plane [27]. In the interest of being able to apply slice-wise B_0 shim updates, and to avoid any artificial lipid removal or global lipid suppression method that removes diagnostically relevant lipid content (e.g. brain tumors) and affects the macromolecular content of the spectra, this study investigated the feasibility of high in-plane acceleration using an improved SENSE reconstruction [20, 21] for high resolution non-lipid-suppressed metabolite mapping of the human brain at 9.4T.

Compared to conventional SENSE reconstruction, over-discrete SENSE combined with over-discrete B_0 correction improves the quality of the reconstruction through 3 major mechanisms: Firstly, the intra-voxel coil sensitivity variations are taken into account by solving the SENSE equations on a much higher resolution grid using high resolution coil sensitivity maps. Secondly, the intra-voxel frequency offsets induced by poor B_0 shimming are corrected for on the same over-discretized grid, and meanwhile, the noise content of these sub-voxels will be de-correlated due to these shifts, which will result in destructive addition of noise in the next step. Finally, the resulting target-driven SRF shape helps reduce the voxel-bleeding by shaping the original voxels in a controlled manner.

This study showed that the OD-SENSE indeed resulted in a more reliable reconstruction of accelerated data and reduced structured aliasing lipid artifacts. The number of voxels with CRLBs of NAA greater than 15% give an indication of how much lipid aliasing artefacts are affecting the metabolite maps. The mean CRLBs give an indication of how much the fits are affected due to the noise introduced by the SENSE reconstruction. This can also be compared by looking at the SNRs of the different reconstruction methods.

The metabolite maps for R=2 were in good agreement with the fully sampled data. The reduction of the aliased lipid artifacts resulted in lower RMSEs of the NAA maps. In comparison, even for R=2, the conventional SENSE reconstruction could have residual aliasing artifacts. It was also shown that R=2x2 acceleration is possible when an OD-SENSE reconstruction is used. The RMSE values for this acceleration factor were about 11% for the NAA map. This is comparable to the 2D CAIPIRINHA acceleration method which results in an RMSE of ~12% on 7T for the same acceleration factor [27]. For higher acceleration factors, such as R=6, the aliasing artifacts became more prominent even when OD-SENSE was used.

As expected, lower spectral noise in the OD-SENSE reconstruction was observed due to the B_0 correction that boosted the SNR of the spectra (on average by ~23%). This, therefore, resulted in lower CRLBs since the spectra could be fit more reliably. As a result, high resolution metabolite maps could be acquired with an acceleration factor of 4 (3.75 minutes scan time) from several volunteers using the OD-SENSE reconstruction and the ^{1}H FID MRSI sequence. Ultrashort TE values (less than 2ms) could be achieved with this sequence. Without lipid suppression, ultra-short TR values could be achieved due to the low-SAR nature of the sequence [11,16]. In addition, the sequence is easily scalable to any field strength.

In comparison, the proton echo-planar spectroscopic imaging (PEPSI) technique [10] has provided a good solution for reducing MRSI scan times by using fast echo-planar readouts. This technique has enabled the

acquisition of metabolite maps from 18 slices with an in-plane matrix size of 50x50 in 25.5 minutes on 3T [28], which in turn has enabled the application of 1H MRSI in clinical studies (e.g. [29,30]). The advantage of this sequence is that firstly it acquires fully sampled data and secondly it uses lipid suppression. Compared to a fully sampled FID MRSI, this sequence would require a total scan time of 165 minutes at a TR of 300 ms (with the same k-space matrix size of 50x50x18), which is obviously not feasible. To achieve comparable scan times, an acceleration factor of ~6.5 is required. Note that PEPSI sequences can potentially also be performed without lipid suppression to reduce scan times. However, to the best of our knowledge, this has not yet been done. The trade-offs between SENSE and EPSI at 3T was investigated by Zierhut et al. [31]. All methods investigated were of comparable quality. It should be noted that in this study a PRESS localization was used for all MRSI sequences.

Although PEPSI is a fully sampled sequence and thus devoid of image aliased artefacts, it becomes more and more difficult to apply at higher field strengths due to the higher receive bandwidth requirements. At 7T, the minimum required bandwidth 4.7 ppm (over the metabolite range) is typically achieved [3]. However this could cause spectral aliasing if there are spectral peaks or other spurious peaks outside the sampling bandwidth.

A great benefit of using a FID MRSI sequence without localization is the higher SNR that can be achieved. The normalized SNRs of the NAA signals is approximately three times higher than previously reported (also after accounting for the field strengths). This is also due to the very short TRs that make the sequence more time efficient.

Aside from SENSE another common PI acceleration method, known as GRAPPA was compared to the OD-SENSE method, which once again demonstrated the advantages of the OD-SENSE reconstruction. Even though SENSE and GRAPPA are similar in nature, they differ in the way they reconstruct the image from the undersampled data. GRAPPA tries to estimate the missing k-space points by forming a kernel that represents the relationship between the neighboring acquired points and the ones missing. The kernel is obtained from some form of calibration data and is applied to predict every missing point in k-space, and finally the unaliased image is formed from the fully reconstructed k-space data. On the other hand,SENSE is among the family called image domain PI that unalias the data using the properties of the image domain itself. Using the explicit receive coil sensitivity maps (in image domain) obtained from a calibration scan, a system of equations is solved to resolve the aliased voxels. Unlike GRAPPA, the SENSE reconstruction equations readily lend themselves to different objective functions and regularization methods [32] and that is why a reconstruction like OD-SENSE can be used to improve the reconstruction and achieve higher accelerations. Even though it is possible to perform regularization also in the GRAPPA reconstruction approach, these methods have been much less explored for GRAPPA compared to SENSE. Our results showed that, indeed, using the OD-SENSE and B_0 correction method, which is by nature an SNR boosting approach that also directly controls the shape of the resulting SRF, the reconstructed data showed less residual aliasing and more SNR (by ~ 29±1.7%) than GRAPPA and hence allowed more reliable fitting for R=4.

Needless to say, achieving higher acceleration factors to further reduce the scan time can be done by combining the OD-SENSE method with through-plane acceleration (such as Hadamard multi-band approaches [27, 33]). Although, as emphasized before, the application of these methods limits the ability of applying dynamic slice-wise B_0 shim updates. It may still be possible to perform this in a benign shimming region like the upper part of the brain. Another approach to achieve higher in-plane only acceleration factors would be to use other acceleration schemes such as compressed sensing [34] that are by nature de-noising mechanisms and result in noise-like aliasing artifacts instead of structured ones. The

advantage of conventional parallel imaging methods like SENSE and GRAPPA over compressed sensing however, is that these methods can be applied in combination with other acceleration schemes such as EPSI as they regularly undersample the data, whereas compressed sensing requires the sampling trajectory to inherently change to realize random or pseudo-random undersampling.

Finally, it is worth noting that the SNR boosting technique (through an over-discrete grid and using the shimmed B_0 map to correct for frequency shifts on a sub-voxel level and then using a target function to shape the original voxel size) is not limited to the investigated acceleration methods in this work, and can be used as an additional step to any other acceleration reconstruction to gain additional SNR and better lineshapes.

Conclusion

In this study, we investigated the feasibility of using SENSE as a method for accelerating the acquisition of non-lipid-suppressed ^{1}H FID MRSI of the human brain at ultra-high fields. An improved SENSE reconstruction method, namely the over-discretized target-driven SENSE reconstruction in combination with B_0 correction was used and compared to conventional SENSE and GRAPPA reconstruction for multiple acceleration factors in two different phase encoding directions. The improved SENSE reconstruction proved advantageous in reducing the residual structured aliasing artifacts resulting from unsuppressed subcutaneous lipid signals and enabled reliable and reproducible acceleration of R=2x2. This resulted in the acquisition of high resolution metabolite maps of the human brain with a nominal voxel size of 97µL at 9.4T in 3.75 minutes.

Acknowledgements

This study was supported by the European Research Council Starting grant, project SYNAPLAST MR #679927.

References:

1) Pohmann R, Speck O, Scheffler K. Signal-to-noise ratio and MR tissue parameters in human brain imaging at 3, 7, and 9.4 Tesla using current receive coil arrays. Magn. Reson. Med. 2016; 75: 801-809.
2) Pfrommer A, Henning A. The ultimate intrinsic signal-to-noise ratio of loop- and dipole-like current patterns in a realistic human head model. Magn. Reson. Med. 2018: 1-17.
3) Otazo R, Mueller B, Ugurbil K, Wald LL, Posse S. Signal-to-noise ratio and spectral linewidth improvements between 1.5 and 7 Tesla in proton echo-planar spectroscopic imaging. Magn. Reson. Med. 2006; 56(6): 1200-1210.
4) Trattnig S, Springer E, Bogner W, Hangel G, Strasser B, Dymerska B, Cardoso PL, Robinson SD. Key clinical benefits of neuroimaging at 7 T. NeuroImage 2016. DOI:10.1016/j.neuroimage.2016.11.031.
5) Henning A. Proton and multinuclear magnetic resonance spectroscopy in the human brain at ultra-high field strength: A review. NeuroImage, 2017. DOI: 10.1016/j.neuroimage.2017.07.017.
6) Pruessman KP, Weiger M, Scheidegger MB, Boesinger P. SENSE: sensitivity encoding for fast MRI. Magn. Reson. Med. 1999; 42(5): 952-962
7) Griswold MA, Jakob PM, Heidemann RM, Nittka M, Jellus V, Wang J, Kiefer B, Haase A. Generalized autocalibrating partially parallel acquisitions (GRAPPA). 2002; 47(6): 1202:1210.
8) Vaughan JT, Garwood M, Collins CM, Liu W, DelaBarre L, Adriany G, Andersen P, Merkle H, Goebel R, Smith MB, Ugurbil K. 7T vs. 4T: RF Power, Homogeneity, and Signal-to-Noise Comparison in Head Images. Magn. Reson. Med. 2001; 46: 24-30.

9) Collins CM, Smith MB. Calculations of B1 Distribution, SNR, and SAR for a Surface Coil Adjacent to an Anatomically-Accurate Human Body Model. Magn. Reson. Med. 2001; 45: 692-699.
10) Posse S, Dager RS, Richards TL, Yuan C, Ogg R, Artru AA, Mueller-Gaertner H-W, Hayes C. In vivo measurement of regional brain metabolic response to hyperventilation using magnetic resonance: proton echo planar spectroscopic imaging (PEPSI). Magn. Reson. Med. 1997; 37(6): 858-865.
11) Hangel G, Strasser B, Považan M, Heckova E, Hingerl L, Boubela R, Gruber S, Trattnig S, Bogner W. Ultra-high resolution brain metabolite mapping at 7 T by short-TR Hadamard-encoded FID-MRSI. NeuroImage. 2016; 168: 199-210.
12) Boer VO, Klomp DW, Juchem C, Luijten PR, de Graaf RA. Multislice ^{1}H MRSI of the human brain at 7 T using dynamic B_0 and B_1 shimming. Magn. Reson. Med. 2012; 68(3): 662-670.
13) Hingerl L, Bogner W, Moser P, Považan M, Hangel G, Heckova E, Gruber S, Trattnig S, Strasser B. Density-Weighted Concentric Circle Trajectories for High Resolution Brain Magnetic Resonance Spectroscopic Imaging at 7T. Magn. Reson. Med. 2018; 79: 2874-2885.
14) Henning A, Fuchs A, Murdoch JB, Boesinger P. Slice-selective FID acquisition, localized by outer volume suppression (FIDLOVS) for 1H-MRSI of the human brain at 7 T with minimal signal loss. NMR Biomed. 2009; 22(7): 683-696.
15) Bogner W, Gruber S, Trattnig S, Chmelik M. High-resolution mapping of human brain metabolites by free induction decay ^{1}H MRSI at 7 T. NMR Biomed. 2012; 25(6): 873–882.
16) Nassirpour S, Chang P, Henning A. High and ultra-high resolution metabolite mapping of the human brain using ^{1}H FID MRSI. NeuroImage 2016. DOI: 10.1016/j.neuroimage.2016.12.065.
17) Lin F, Tsai S, Otazo R, Caprihan A, Wald LL, Belliveau JW, Posse S. Sensitivity-encoded (SENSE) proton echo-planar spectroscopic imaging (PEPSI) in the human brain. Magn. Reson. Med. 2007; 57(2): 249-257.
18) Posse S, Otazo R, Tsai SY, Yoshimoto E, Lin FH. Single-shot magnetic resonance spectroscopic imaging with partial parallel imaging. Magn. Reson. Med. 2009; 61(3): 541-547.
19) Hangel G, Strasser B, Považan M, Gruber S, Chmelík M, Gajdošík M, Trattnig S, Bogner W. Lipid suppression via double inversion recovery with symmetric frequency sweep for robust 2D-GRAPPA-accelerated MRSI of the brain at 7 T. NMR Biomed. 2015; 28(11): 1413-1425.
20) Kirchner T, Fillmer A, Tsao J, Pruessman KP, Henning A. Reduction of voxel bleeding in highly accelerated parallel ^{1}H MRSI by direct control of the spatial response function. Magn. Reson. Med. 2015; 73(2): 469-480.
21) Kirchner T, Fillmer A, Henning A. Mechanisms of SNR and line shape improvement by B_0 correction in overdiscrete MRSI reconstruction. Magn. Reson. Med. 2017; 77(1): 44-56.
22) Avdievich NI, Giapitzakis IA, Pfrommer A, Borbath T, Henning A. Combination of surface and 'vertical' loop elements improves receive performance of a human head transceiver array at 9.4T. NMR in Biomed. 2018
23) Uecker M, Lai P, Murphy MJ, Virtue P, Elad M, Pauly JM, Vasanawala SS, Lustig M. ESPIRiT—an eigenvalue approach to autocalibrating parallel MRI: where SENSE meets GRAPPA Magn. Reson. Med. 2015; 71(3): 990-1001.
24) Provencher SW. Estimation of metabolite concentrations from localized in vivo proton NMR spectra. Magn. Reson. Med. 1993; 30(6): 672-679.
25) Blaimer M, Breuer FA, Mueller M, Seiberlich N, Ebel D, Heidemann RM, Griswold MA, Jakob PM. 2D-GRAPPA-operator for faster 3D parallel MRI. Magn. Reson. Med. 2006; 56(6): 1359-1364.

26) Bilgic B, Chatnuntawech I, Fan AP, Setsompop K, Cauley SF, Wald LL, Adalsteinsson E. Fast image reconstruction with L2-regularization. J. Magn. Reson. Imaging 2014; 40(1): 181-191.
27) Strasser B, Považan M, Hangel G, Hingerl L, Chmelik M, Gruber S, Trattnig S, Bogner W. (2+ 1) D-CAIPIRINHA accelerated MR spectroscopic imaging of the brain at 7T. Magn. Reson. Med. 2017; 78(2): 429-440.
28) Sabati M, Sheriff S, Gu M, Wei J, Zhu H, Barker PB, Spielman DM, Alger JR, Maudsley AA. Multivendor implementation and comparison of volumetric whole-brain echo-planar MR spectroscopic imaging. . Magn. Reson. Med. 2015; 74(5): 1209-1220.
29) Govind V, Gold S, Kaliannan K, Saigal G, Falcone S, Arheart KL, Harris L, Jagid J, Maudsley AA. Whole-brain proton MR spectroscopic imaging of mild-to-moderate traumatic brain injury and correlation with neuropsychological deficits. Journal of neurotrauma 2010; 27(3): 483-496.
30) Ding XQ, Maudsley AA, Sabati M, Sheriff S, Schmitz B, Schütze M, Bronzlik P, Kahl KG, Lanfermann H. Physiological neuronal decline in healthy aging human brain—An in vivo study with MRI and short echo-time whole-brain 1 H MR spectroscopic imaging. NeuroImage 2016; 137: 45-51.
31) Zierhut ML, Oztruk-Isik E, Chen AP, Park I, Vigneron DB, Nelson SJ. 1H Spectroscopic Imaging of Human Brain at 3T: Comparison of Fast 3D-MRSI Techniques. Journ. Magn. Reson. 2009; 30(3): 473-480.
32) Sánchez-González J, Tsao J, Dydak U, Desco M, Boesiger P, Pruessmann KP. Minimum-norm reconstruction for sensitivity-encoded magnetic resonance spectroscopic imaging. Magn. Reson. Med. 2006; 55(2): 287-295.
33) Goelman G, Liu S, Fleysher R, Fleysher L, Grossman RI, Gonen O. Chemical-shift artifact reduction in hadamard-encoded MR spectroscopic imaging ay high (3T and 7T) magnetic fields. Magn. Reson. Med. 2007; 58: 167-173.
34) Cao P, Wu EX. Accelerating phase-encoded proton MR spectroscopic imaging by compressed sensing. J. Magn. Reson. Imaging 2015; 41(2): 487-4

		SNR [a.u.]			CRLB [%] (NAA)				RMSE [%] (NAA)
		Mean	Std.	Cohen Effect Size	Mean	Std.	Cohen Effect Size	Percentage > 15	Mean
R=1x1		133.64	35.85	-	4.10	0.74	-	0	-
R=1x2	SENSE	100.34	30.03	0.61	4.95	1.66	0.26	3.6	20.50
	SENSE-OD	120.47	36.14		4.54	1.33		0.57	10.74
R=2x1	SENSE	96.70	26.59	0.73	4.58	1.12	0.31	0.19	12.08
	SENSE-OD	119.12	34.56		4.27	0.81		0	3.98
R=1x3	SENSE	87.36	52.72	0.30	5.36	1.80	0.24	2.83	23.76
	SENSE-OD	102.80	50.37		4.93	1.59		1.04	17.02
R=3x1	SENSE	85.16	45.63	0.39	5.23	1.76	0.21	5.94	27.49
	SENSE-OD	105.41	57.03		4.88	1.64		2.36	21.22
R=2x2	SENSE	72.71	22.96	0.68	5.34	1.78	0.33	3.96	22.06
	SENSE-OD	89.78	27.06		4.81	1.44		0.57	11.16
R=2x3	SENSE	67.31	48.35	0.23	5.95	1.86	0.25	3.25	26.33
	SENSE-OD	77.32	37.74		5.50	1.67		1.88	15.67
R=3x2	SENSE	64.47	35.36	0.35	6.09	2.17	0.12	10.56	34.54
	SENSE-OD	78.52	43.39		5.84	2.09		7.63	32.07

Table 1- Quantitative comparison of the conventional versus over-discretized SENSE reconstruction approaches for different acceleration factors (R = right-left x anterior-posterior). The mean and standard deviation of SNR and CRLB of NAA as well as the mean of the RMSE of the NAA metabolite maps averaged across all voxels in the brain region of four volunteers are shown for the fully sampled and seven acceleration schemes. T-tests were performed on the SNR and CRLB values of the SENSE and OD-SENSE reconstructions for each acceleration factor. The p-values for all cases were < 0.01. To quantify the statistical significance of the difference of performance between the SENSE and OD-SENSE reconstructions, Cohen effect sizes were calculated and shown in the table. The average percentage of the voxels in the slice having a CRLB greater than 15% are also shown

Figure Legends:

Figure 1- Reconstruction process: (a) original MRSI grid, (b) over-discretized MRSI grid achieved by zero-padding k-space, (c) coil sensitivity maps used for SENSE reconstruction, (d) acquired high resolution B_0 map used for B_0 correction of the spectra on a sub-voxel level, (e) target function used to combine voxels to go back to the original MRSI resolution, (f) resulting metabolite maps after spectral processing and fitting.

Figure 2- Normalized lipid contamination maps (overlaid on anatomical reference images) and representative spectra from five different voxel positions (indicated on the anatomical reference image) resulting from an acceleration factor of R=2x2 reconstructed with conventional, and with OD-SENSE. The corresponding spectra and lipid contamination map for the fully sampled case is also shown for comparison. All lipid maps are calculated as the absolute integral of the spectrum from 0.3 to 1.8 ppm and shown between 0 to 10% of the maximum lipid signal for better visualization. The residual artefacts are indicated with yellow arrows. All spectra are shown between 0.5 and 4.2 ppm.

Figure 3- Effect of different acceleration factors and reconstruction schemes on metabolite mapping: Ratio metabolite maps of three major metabolites (/Cre) resulting from the fully sampled, as well as accelerated datasets (accelerated only in the anterior-posterior direction) reconstructed with conventional SENSE, and with OD-SENSE. The residual artefacts are indicated with yellow arrows.

Figure 4- Effect of different acceleration factors and reconstruction schemes on the confidence of fitting: the CRLB maps of the corresponding metabolites in Figure 3. Note that the CRLB maps are shown for individual metabolites. The maps are shown for the fully sampled, as well as accelerated datasets (accelerated only in the anterior-posterior direction) reconstructed with conventional SENSE, and with OD-SENSE.

Figure 5- Effect of different acceleration factors and reconstruction schemes on metabolite mapping: Ratio metabolite maps of three major metabolites (/Cre) resulting from the fully sampled, as well as accelerated datasets (accelerated in both phase-encoding directions, i.e. R = right-left x anterior-posterior) reconstructed once with conventional SENSE, and once with OD-SENSE. The residual artefacts are indicated with yellow arrows.

Figure 6- Effect of different acceleration factors and reconstruction schemes on the confidence of fitting: the CRLB maps corresponding to the metabolite maps of the three major metabolites in Figure 5. The maps are shown for the fully sampled, as well as accelerated datasets (accelerated in both phase-encoding directions, i.e. R = right-left x anterior-posterior) reconstructed with conventional SENSE, and with OD-SENSE.

Figure 7- Box plot of SNR values resulting from different acceleration factors and reconstruction schemes: Each box includes the SNR values aggregated across the whole slice through the brain for four volunteers. The main acceleration direction (anterior-posterior or right-left) are indicated at the bottom of each box.

Figure 8- Quantitative comparison of the effect of different acceleration factors and reconstruction approaches: The RMSE of the NAA maps (the error between the accelerated and the fully sampled maps) versus different acceleration factors is shown on the left. The dark and light blue bars both correspond to more acceleration in the anterior-posterior (AP) direction, reconstructed with conventional SENSE (dark blue) and with OD-SENSE (light blue). The yellow and brown bars both correspond to more acceleration

in the right-left (RL) direction, once reconstructed with conventional SENSE (yellow) and once with OD-SENSE (brown). The CRLB of NAA, glutamate, and total choline for different acceleration factors are also shown. Only the net acceleration factor is indicated on the x-axis but the exact acceleration factors from left to right written as "R = (right-left) x (anterior-posterior)" are: 1x1, 1x2, 2x1, 1x3, 3x1, 2x2, 2x3, and 3x2.

Figure 9- Accelerated (R=2x2) metabolite mapping using the OD-SENSE reconstruction at 9.4T: Ratio metabolite maps of three major metabolites (/Cre) acquired from two additional healthy volunteers are shown. Representative spectra chosen from white and gray matter voxels are also shown.

Figure 10- Comparison of OD-SENSE and GRAPPA reconstruction for an acceleration factor of 4 (R=2x2): Ratio metabolite maps (/Cre) and the corresponding CRLB maps of three major metabolites reconstructed using a 2D GRAPPA operator are shown for the same subject of which maps are depicted in Figure 3-6. Yellow arrows point to where clear residual aliasing artifacts are present in the maps. On the contrary the same maps obtained using the OD-SENSE reconstruction in Figure 5 and 6 do not show any significant aliasing artifact.

Table 1- Quantitative comparison of the conventional versus over-discretized SENSE reconstruction approaches for different acceleration factors (R = right-left x anterior-posterior). The mean and standard deviation of SNR and CRLB of NAA as well as the mean of the RMSE of the NAA metabolite maps averaged across all voxels in the brain region of four volunteers are shown for the fully sampled and seven acceleration schemes. T-tests were performed on the SNR and CRLB values of the SENSE and OD-SENSE reconstructions for each acceleration factor. The p-values for all cases were < 0.01. To quantify the statistical significance of the difference of performance between the SENSE and OD-SENSE reconstructions, Cohen effect sizes were calculated and shown in the table. The average percentage of the voxels in the slice having a CRLB greater than 15% are also shown.

Supporting Materials Figure 1- Representative spectra (gray) along with their LCMODEL fit (red) from white and gray matter voxels. The spectra are shown for the fully sampled case as well as accelerated with a factor of 4 reconstructed once with conventional and once with OD SENSE. The LCMODEL fit for Glu, NAA, and tCho components are shown in dotted gray lines.

Supporting Materials Figure 2- Effect of different acceleration factors and reconstruction schemes on metabolite mapping: Ratio metabolite maps of three major metabolites (/Cre) resulting from the fully sampled, as well as accelerated datasets (accelerated only in the right-left direction) reconstructed with conventional SENSE, and with OD-SENSE.

Supporting Materials Figure 3- Effect of different acceleration factors and reconstruction schemes on the confidence of fitting: the CRLB maps corresponding to the metabolite maps of the three major metabolites of Figure S1 are shown. The maps are shown for the fully sampled, as well as accelerated datasets (accelerated only in the right-left direction) reconstructed with conventional SENSE, and with OD-SENSE.

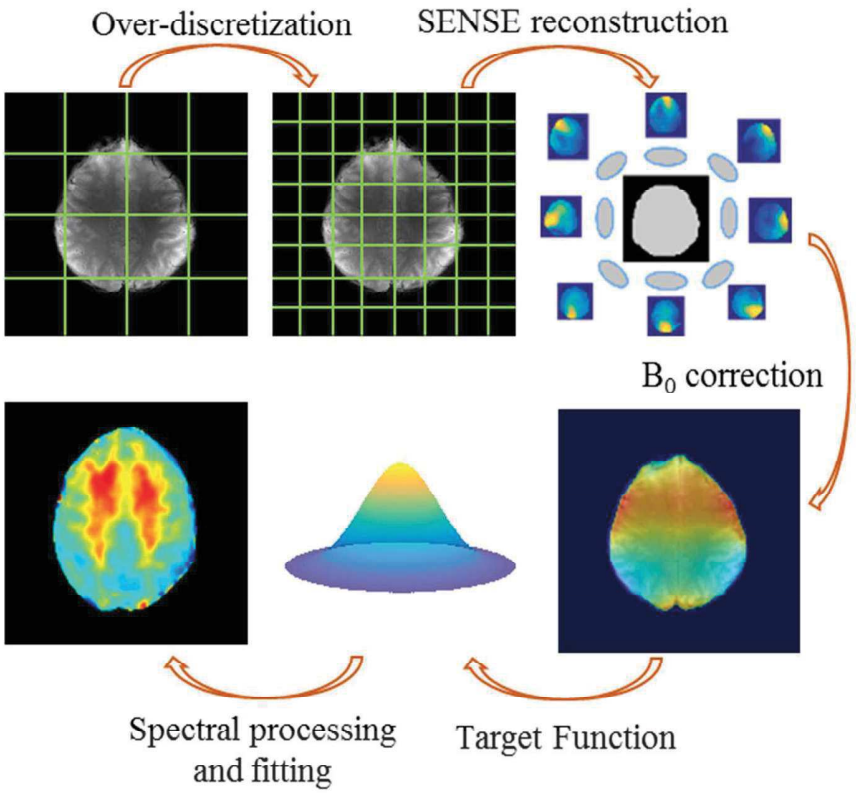

Figure 1- Reconstruction process: (a) original MRSI grid, (b) over-discretized MRSI grid achieved by zero-padding k-space, (c) coil sensitivity maps used for SENSE reconstruction, (d) acquired high resolution B_0 map used for B_0 correction of the spectra on a sub-voxel level, (e) target function used to combine voxels to go back to the original MRSI resolution, (f) resulting metabolite maps after spectral processing and fitting.

60x50mm (300 x 300 DPI)

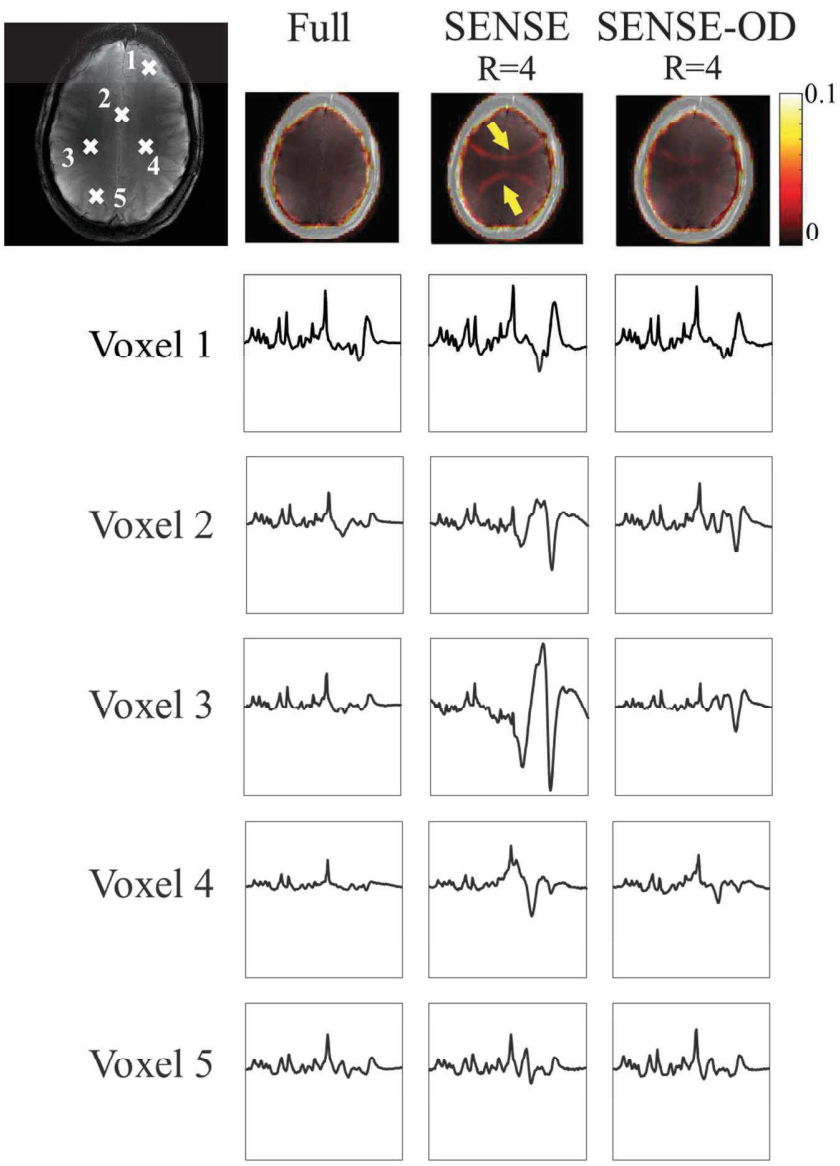

Figure 2- Normalized lipid contamination maps (overlaid on anatomical reference images) and representative spectra from five different voxel positions (indicated on the anatomical reference image) resulting from an acceleration factor of R=2x2 reconstructed with conventional, and with OD-SENSE. The corresponding spectra and lipid contamination map for the fully sampled case is also shown for comparison. All lipid maps are calculated as the absolute integral of the spectrum from 0.3 to 1.8 ppm and shown between 0 to 10% of the maximum lipid signal for better visualization. The residual artefacts are indicated with yellow arrows. All spectra are shown between 0.5 and 4.2 ppm.

86x119mm (300 x 300 DPI)

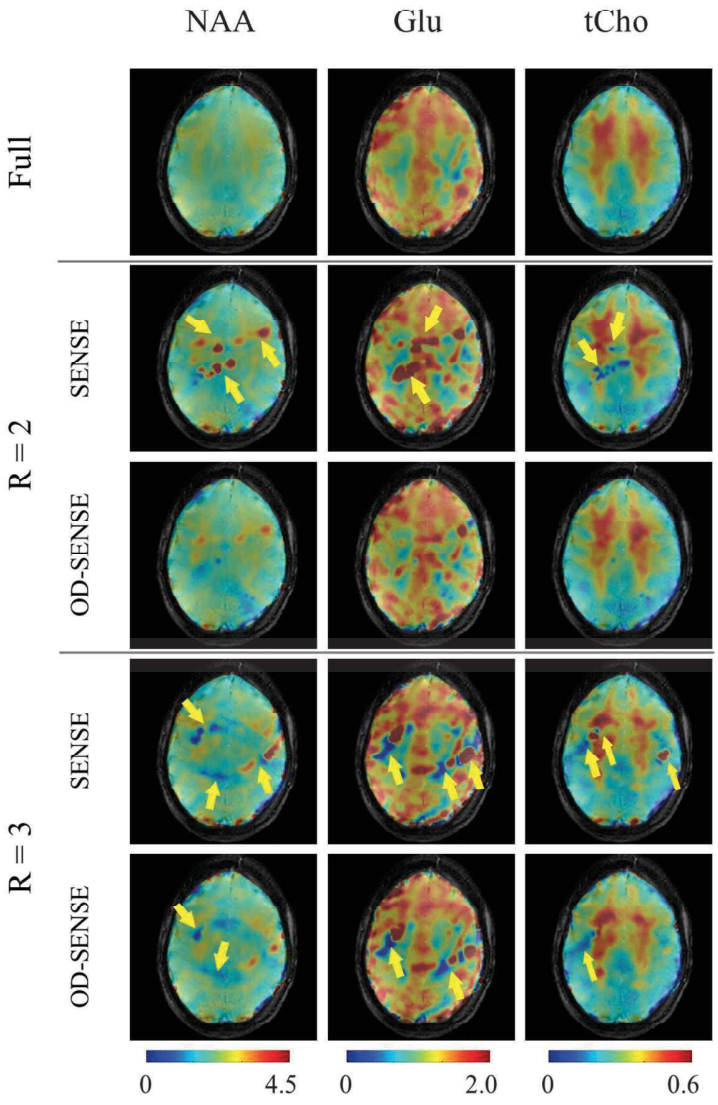

Figure 3- Effect of different acceleration factors and reconstruction schemes on metabolite mapping: Ratio metabolite maps of three major metabolites (/Cre) resulting from the fully sampled, as well as accelerated datasets (accelerated only in the anterior-posterior direction) reconstructed with conventional SENSE, and with OD-SENSE. The residual artefacts are indicated with yellow arrows.

86x127mm (300 x 300 DPI)

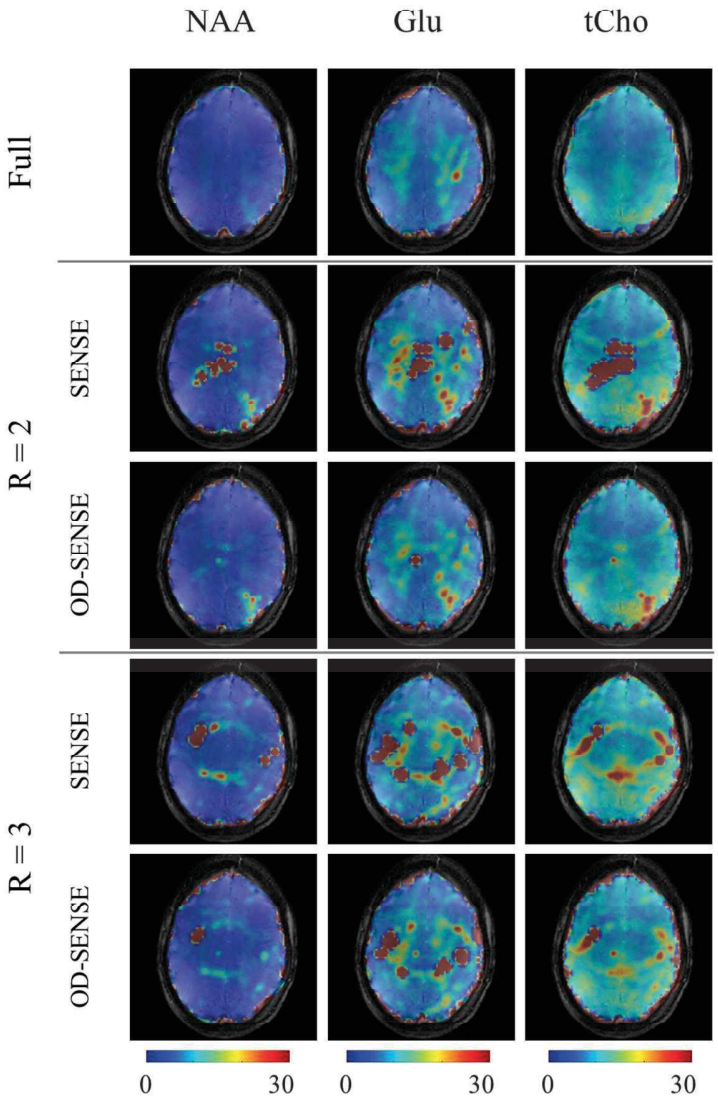

Figure 4- Effect of different acceleration factors and reconstruction schemes on the confidence of fitting: the CRLB maps of the corresponding metabolites in Figure 3. Note that the CRLB maps are shown for individual metabolites. The maps are shown for the fully sampled, as well as accelerated datasets (accelerated only in the anterior-posterior direction) reconstructed with conventional SENSE, and with OD-SENSE.

86x127mm (300 x 300 DPI)

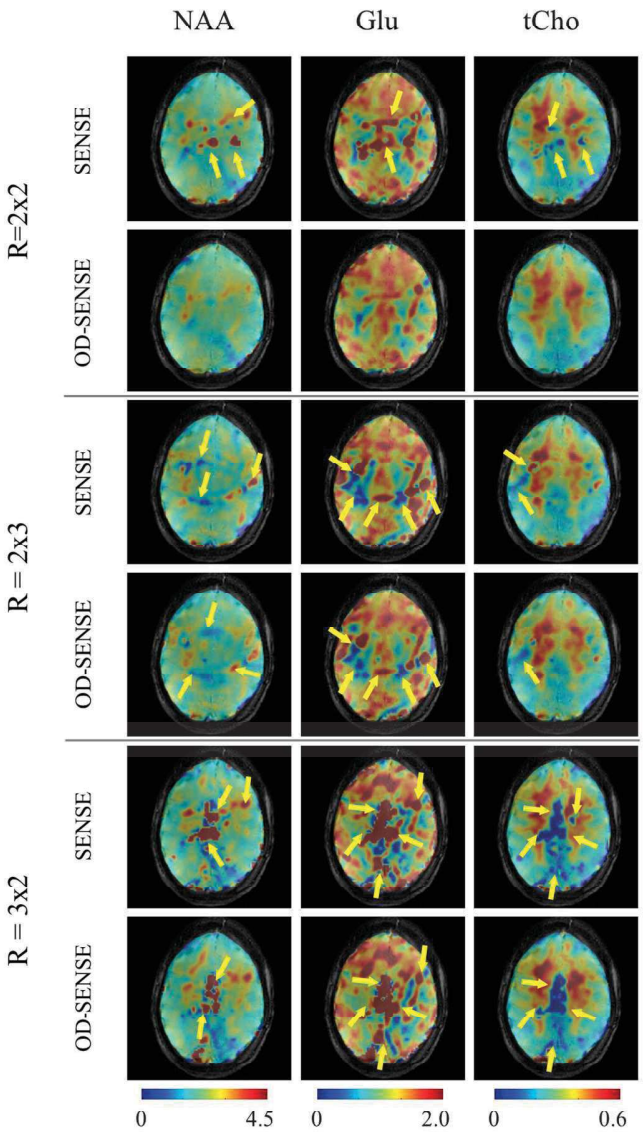

Figure 5- Effect of different acceleration factors and reconstruction schemes on metabolite mapping: Ratio metabolite maps of three major metabolites (/Cre) resulting from the fully sampled, as well as accelerated datasets (accelerated in both phase-encoding directions, i.e. R = right-left x anterior-posterior) reconstructed once with conventional SENSE, and once with OD-SENSE. The residual artefacts are indicated with yellow arrows.

86x144mm (300 x 300 DPI)

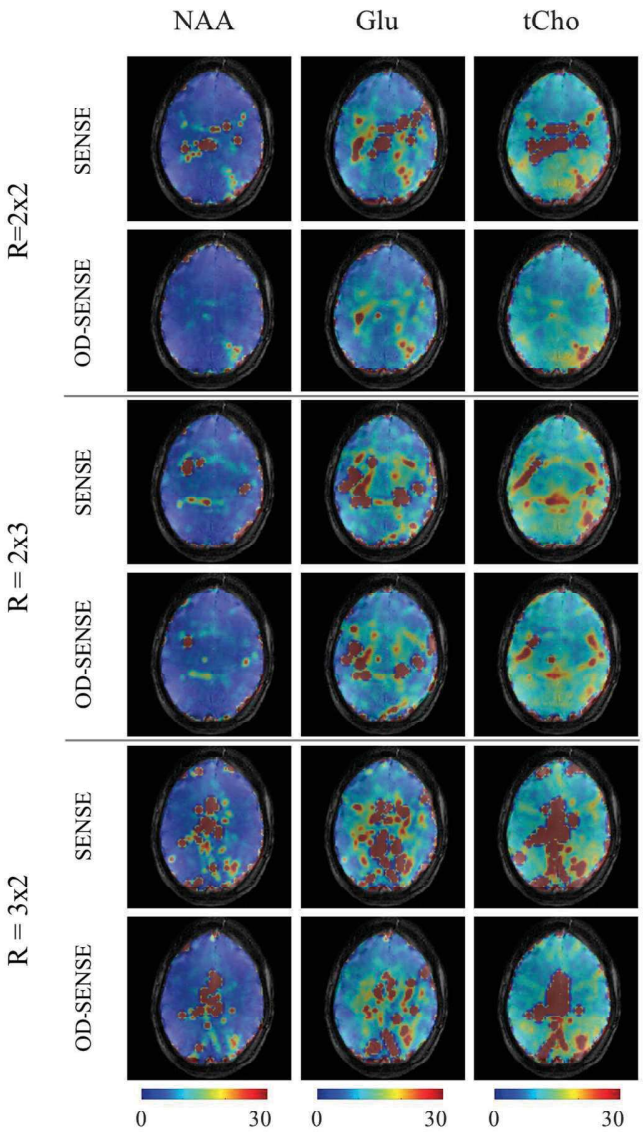

Figure 6- Effect of different acceleration factors and reconstruction schemes on the confidence of fitting: the CRLB maps corresponding to the metabolite maps of the three major metabolites in Figure 5. The maps are shown for the fully sampled, as well as accelerated datasets (accelerated in both phase-encoding directions, i.e. R = right-left x anterior-posterior) reconstructed with conventional SENSE, and with OD-SENSE.

86x144mm (300 x 300 DPI)

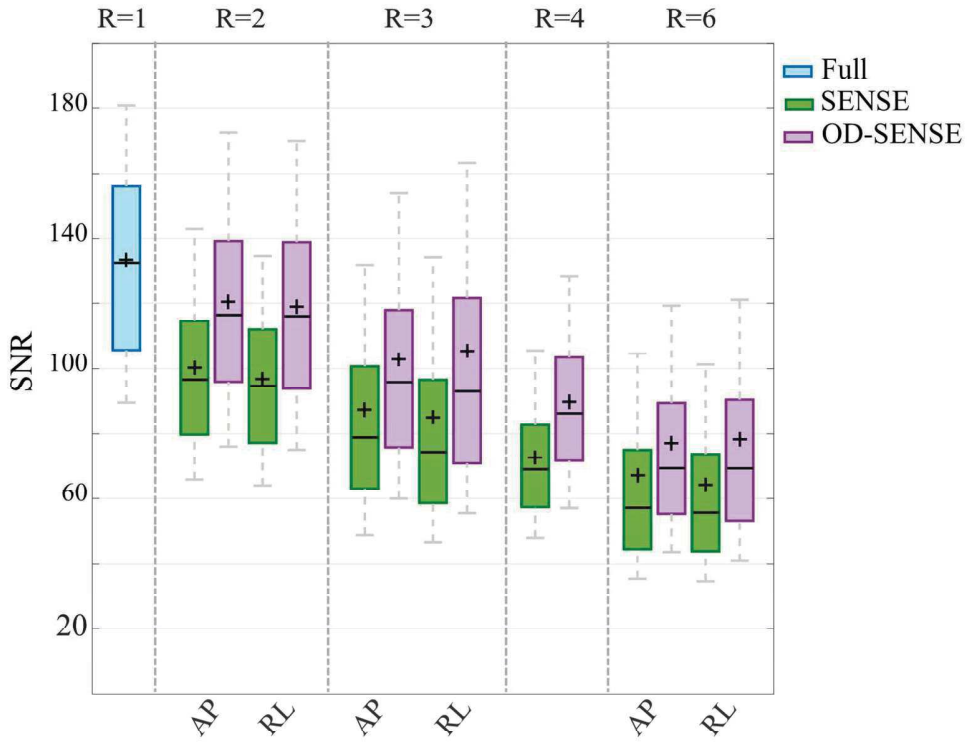

Figure 7- Box plot of SNR values resulting from different acceleration factors and reconstruction schemes: Each box includes the SNR values aggregated across the whole slice through the brain for four volunteers. The main acceleration direction (anterior-posterior or right-left) are indicated at the bottom of each box.

130x109mm (300 x 300 DPI)

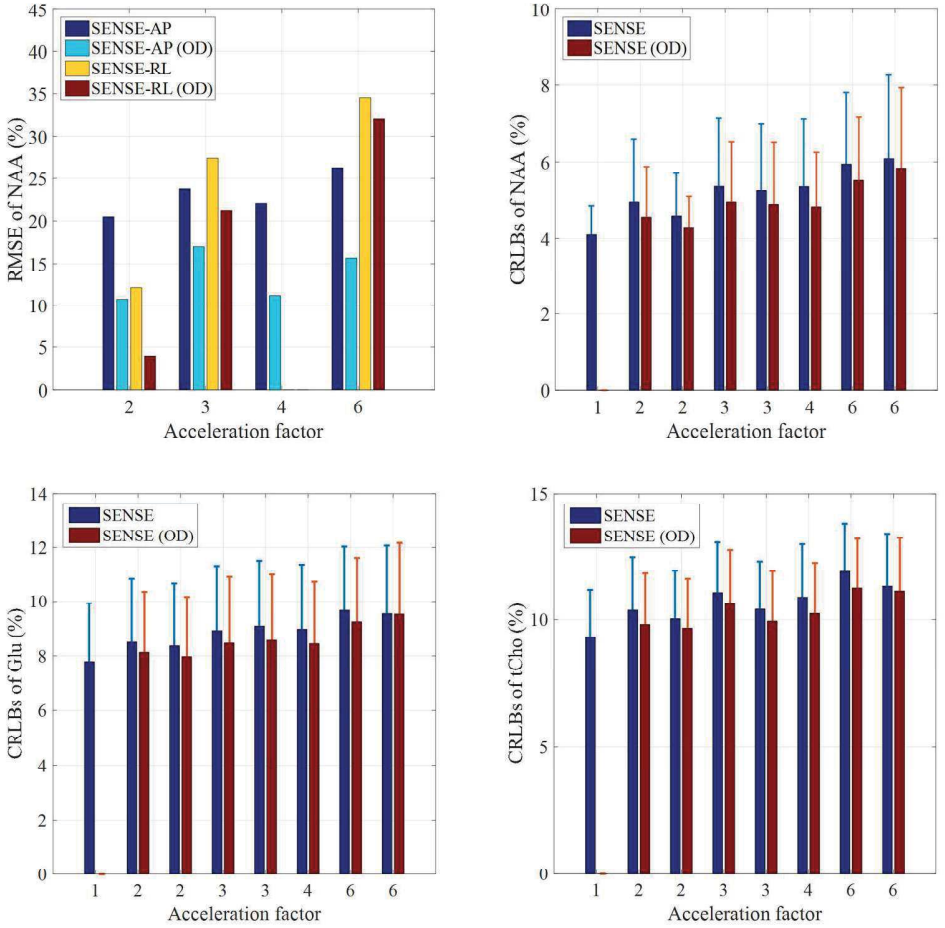

Figure 8- Quantitative comparison of the effect of different acceleration factors and reconstruction approaches: The RMSE of the NAA maps (the error between the accelerated and the fully sampled maps) versus different acceleration factors is shown on the left. The dark and light blue bars both correspond to more acceleration in the anterior-posterior (AP) direction, reconstructed with conventional SENSE (dark blue) and with OD-SENSE (light blue). The yellow and brown bars both correspond to more acceleration in the right-left (RL) direction, once reconstructed with conventional SENSE (yellow) and once with OD-SENSE (brown). The CRLB of NAA, glutamate, and total choline for different acceleration factors are also shown. Only the net acceleration factor is indicated on the x-axis but the exact acceleration factors from left to right written as "R = (right-left) x (anterior-posterior)" are: 1x1, 1x2, 2x1, 1x3, 3x1, 2x2, 2x3, and 3x2.

175x180mm (300 x 300 DPI)

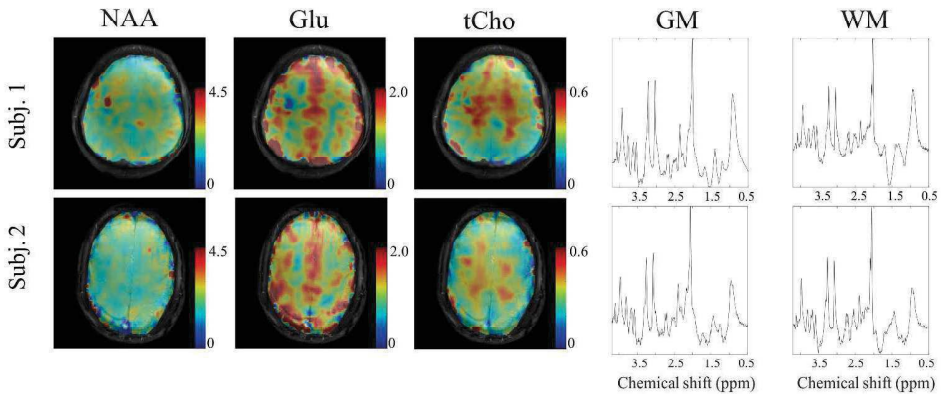

Figure 9- Accelerated (R=2x2) metabolite mapping using the OD-SENSE reconstruction at 9.4T: Ratio metabolite maps of three major metabolites (/Cre) acquired from two additional healthy volunteers are shown. Representative spectra chosen from white and gray matter voxels are also shown.

320x140mm (300 x 300 DPI)

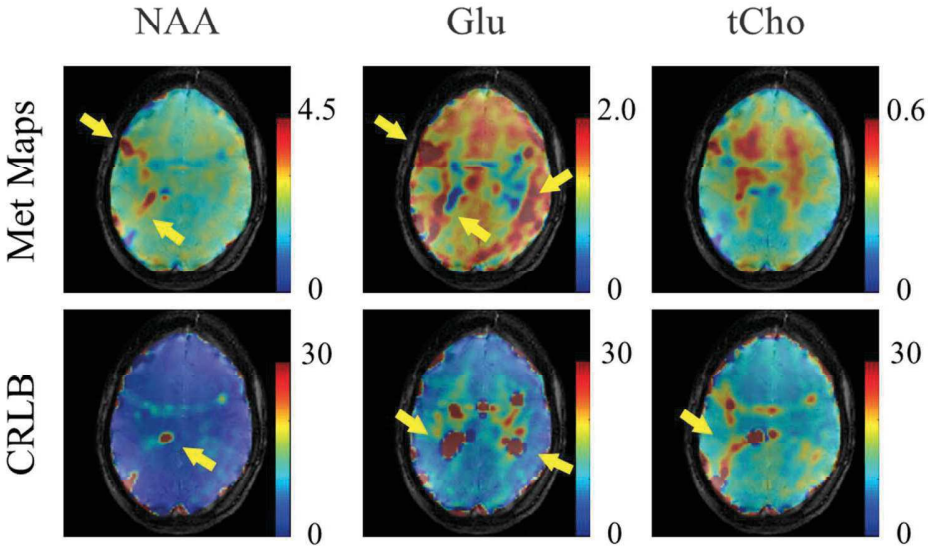

Figure 10- Comparison of OD-SENSE and GRAPPA reconstruction for an acceleration factor of 4 (R=2x2): Ratio metabolite maps (/Cre) and the corresponding CRLB maps of three major metabolites reconstructed using a 2D GRAPPA operator are shown for the same subject of which maps are depicted in Figure 3-6. Yellow arrows point to where clear residual aliasing artifacts are present in the maps. On the contrary the same maps obtained using the OD-SENSE reconstruction in Figure 5 and 6 do not show any significant aliasing artifact.

86x55mm (300 x 300 DPI)

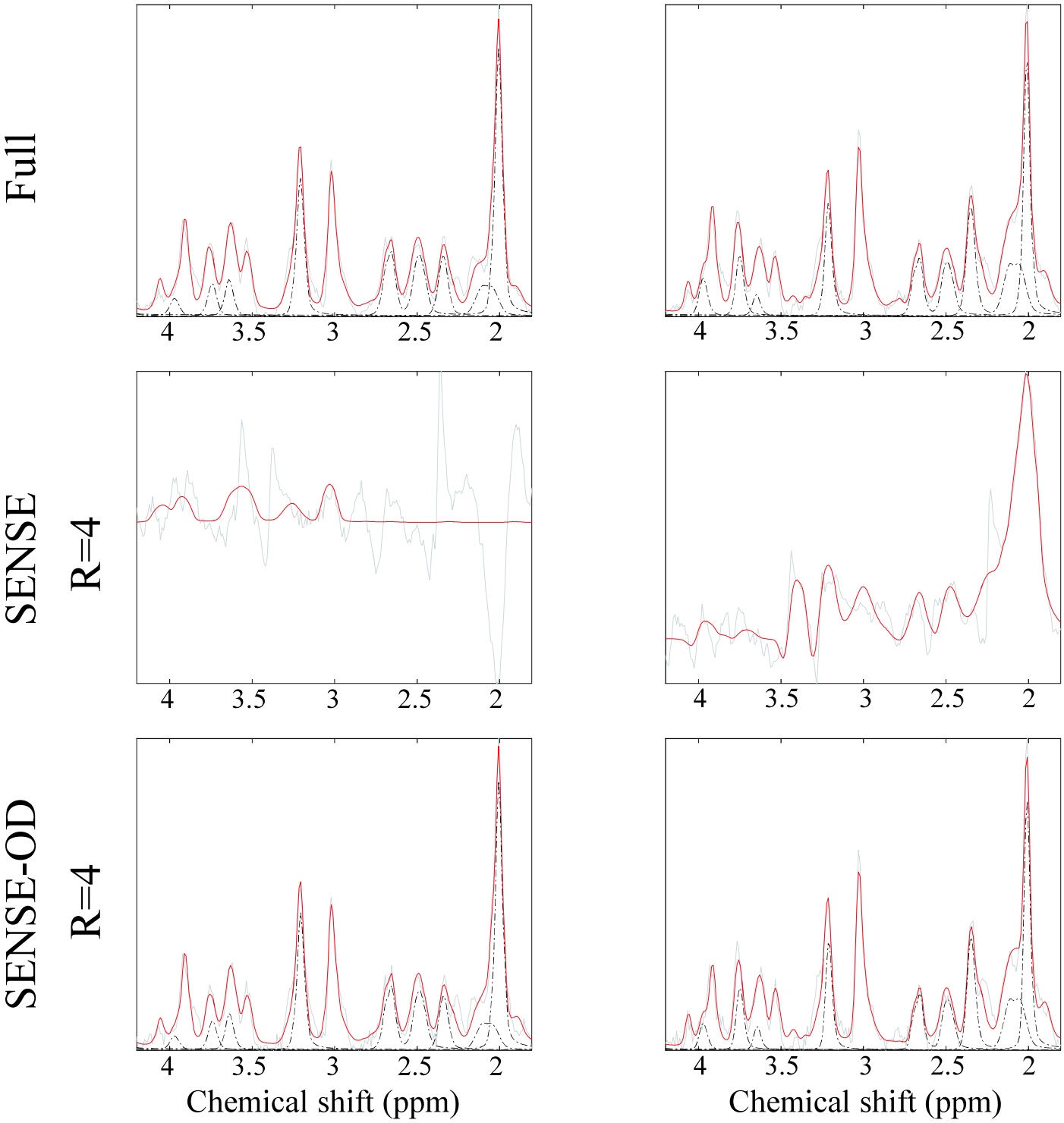

Figure S1- Representative spectra (gray) along with their LCMODEL fit (red) from white and gray matter voxels. The spectra are shown for the fully sampled case as well as accelerated with a factor of 4 reconstructed with conventional and OD SENSE. The LCMODEL fit for Glu, NAA, and tCho components are shown in dotted gray lines.

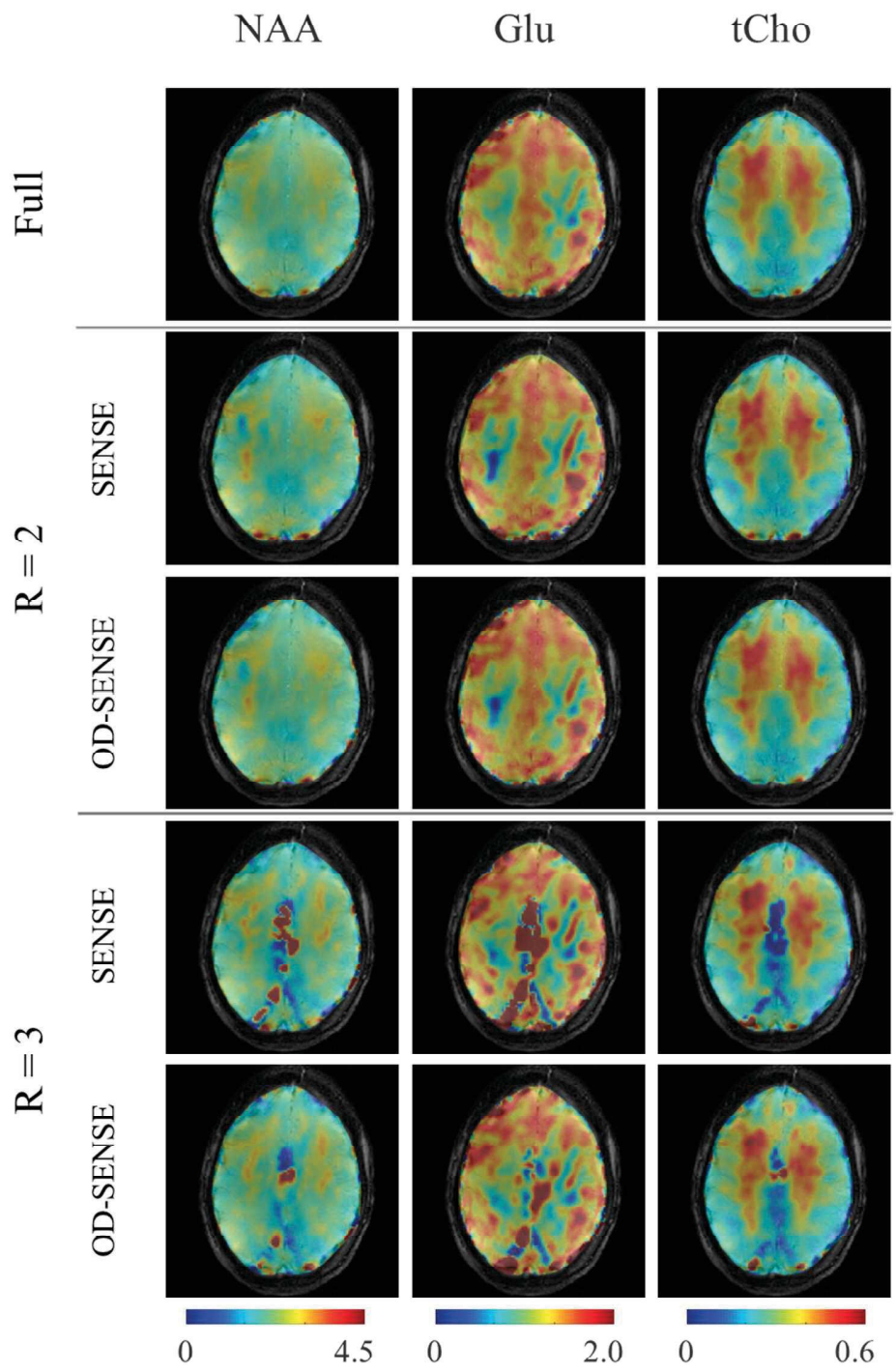

Figure S2- Effect of different acceleration factors and reconstruction schemes on metabolite mapping: Ratio metabolite maps of three major metabolites (/Cre) resulting from the fully sampled, as well as accelerated datasets (accelerated only in the right-left direction) reconstructed with conventional SENSE, and with OD-SENSE.

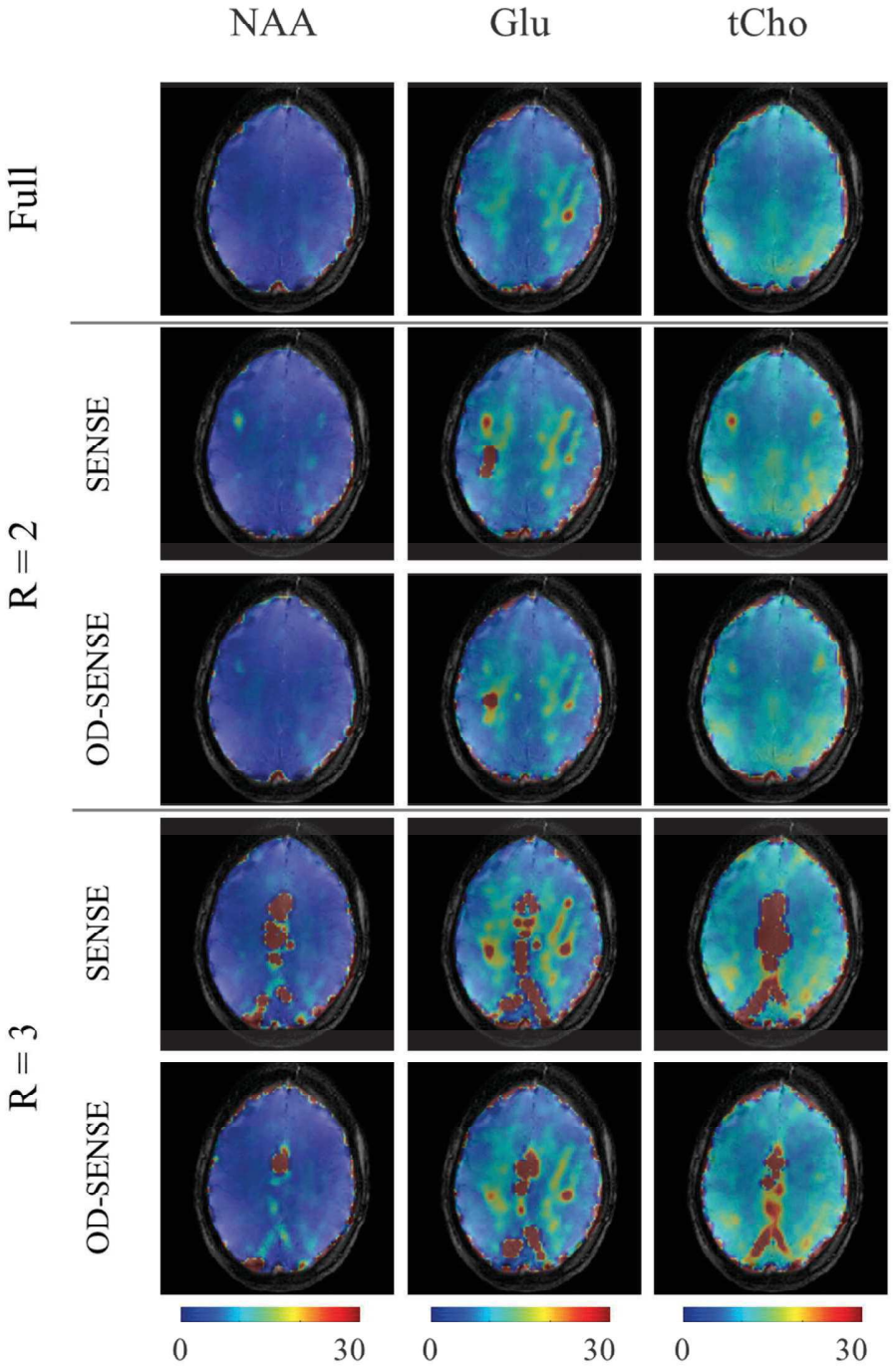

Figure S3- Effect of different acceleration factors and reconstruction schemes on the confidence of fitting: the CRLB maps corresponding to the metabolite maps of the three major metabolites of Figure S1 are shown. The maps are shown for the fully sampled, as well as accelerated datasets (accelerated only in the right-left direction) reconstructed with conventional SENSE, and with OD-SENSE.

Parameters used for LCMODEL fits:

chnot2(1)= 'Lip13c'

chnot2(2)= 'Lip13d'

chnot2(3)= 'Lip13e'

chnot2(4)= 'Gua'

degppm= 0

deltat= 1.250e-04

doecc= F

dows= F

hzpppm= 3.9972e+02

neach= 100

nnot2= 4

nunfil= 1024

ppmend= 1.8

ppmst= 4.2

sddegp= 0

wsppm= 2.95

Publication V

"MultiNet PyGRAPPA: Multiple Neural Networks for Reconstructing Variable Density GRAPPA (a ^{1}H FID MRSI Study)"

S Nassirpour*, P Chang*, A Henning

[in review]

MultiNet PyGRAPPA: Multiple Neural Networks for Reconstructing Variable Density GRAPPA (a ^{1}H FID MRSI Study)

Sahar Nassirpour†[1,2], Paul Chang†[1,2], Anke Henning[1,3]

[1] Max Planck Institute for Biological Cybernetics, Tübingen, Germany, [2] IMPRS for Cognitive and Systems Neuroscience, Eberhard Karls University of Tübingen, Tübingen, Germany, [3] Institute of Physics, Ernst-Moritz-Arndt University Greifswald, Greifswald, Germany

Corresponding author: *Sahar Nassirpour, email: sahar.nassirpour@tuebingen.mpg.de, address: Max Planck Institute for Biological Cybernetics, Max-Planck-Ring 11, Tübingen 72076, Germany.*

† These authors contributed equally to this work.

Abstract

Magnetic resonance spectroscopic imaging (MRSI) is a powerful tool for mapping metabolite levels across the brain, however, it generally suffers from long scan times. This severely hinders its application in clinical settings. Additionally, the presence of nuisance signals (e.g. the subcutaneous lipid signals close to the skull region in brain metabolite mapping) makes it challenging to apply conventional acceleration techniques to shorten the scan times. The goal of this work is, therefore, to increase the overall applicability of high resolution metabolite mapping using ^{1}H MRSI by introducing a novel GRAPPA acceleration acquisition/reconstruction technique. An improved reconstruction method (MultiNet) is introduced that uses machine learning, specifically neural networks, to reconstruct accelerated data. The method is further modified to use more neural networks with nonlinear hidden layers and is then combined with a variable density undersampling scheme (MultiNet PyGRAPPA) to enable higher in-plane acceleration factors of R=7 and R=9 for a non-lipid suppressed ultra-short TR and TE ^{1}H FID MRSI sequence. The proposed method is evaluated for high resolution metabolite mapping of the human brain at 9.4T. The results show that the proposed method is superior to conventional GRAPPA: there is no significant residual lipid aliasing artifact in the images when the proposed MultiNet method is used. Furthermore, the MultiNet PyGRAPPA acquisition/reconstruction method with R=7 results in reproducible high resolution metabolite maps (with an in-plane matrix size of 64x64) that can be acquired in 2.8 minutes on 9.4T. In conclusion, using multiple neural networks to predict the missing points in GRAPPA reconstruction results in a more reliable data recovery while keeping the noise levels under control. Combining this high fidelity reconstruction with variable density undersampling (MultiNet PyGRAPPA) enables higher in-plane acceleration factors even for non-lipid suppressed ^{1}H FID MRSI, without introducing any structured aliasing artifact in the image.

Keywords: MRSI, Metabolite Mapping, Acceleration, GRAPPA, Neural Networks

Introduction

Shortly after its introduction in 2002 (Griswold et al. 2002), the generalized partial parallel acquisition (GRAPPA) acceleration method was adopted by the magnetic resonance spectroscopy imaging (MRSI) community to accelerate the lengthy MRSI scans. Contrary to the sensitivity encoding (SENSE) (Pruessmann et al. 1999) acceleration method, GRAPPA does not require explicit knowledge of the receive coil sensitivity profiles. It is easy to implement and can be applied in any phase encoding direction. This makes it a suitable candidate for acceleration of MRSI sequences. GRAPPA was first incorporated in a localized MRSI sequence (Banerjee et al. 2006) in both phase-encoding directions to accelerate the scan by a net factor of R ~ 2. Later on, GRAPPA (still with moderate acceleration factors) was used in combination with proton echo-planar spectroscopy imaging (PEPSI) sequences (Tsai et al. 2008, Sabati et al. 2014) to accelerate the MRSI studies even further.

Given that applying PEPSI sequences at ultra-high fields is challenging due to higher gradient strength and receive bandwidth requirements, one of the most promising MRSI techniques at ultra-high fields is the slice-selective non-lipid suppressed ultra-short TR and TE ^{1}H FID MRSI sequence (Bogner et al. 2012, Boer et al. 2012, Nassirpour et al. 2018). Hence, the next natural step was to incorporate GRAPPA into this sequence to accelerate the scans even further. However, it was soon discovered that extra care should be taken in applying conventional parallel imaging (PI) methods such as GRAPPA to non-lipid suppressed ^{1}H MRSI sequence. The reason for this is the presence of strong lipid signals near the skull (for brain metabolite mapping) which can be orders of magnitude stronger than the metabolites of interest inside the brain. Any remaining unresolved and structured aliasing artifact resulting from reconstruction errors in the conventional PI acceleration methods can completely distort the signal inside the brain and make quantification impossible. To overcome this, Hangel et al (Hangel et al. 2015) suggested incorporating a double-inversion recovery (DIR) lipid suppression scheme into the ^{1}H FID MRSI sequence. The DIR method is very effective for reducing the lipid signals and hence enabling higher PI acceleration factors, however, the major limitation is the strict specific absorption

rate (SAR) limitations at ultra-high fields. As a result of this, the repetition time (TR) is prolonged by a significant factor which is only partially compensated by using higher GRAPPA acceleration factors.

The most recent development for accelerating ultra-high field MRSI using an ultra-short TR and TE ^{1}H FID MRSI sequence was when Strasser et al (Strasser et al. 2017) took another PI approach and used (2+1) D CAIPIRINHA to enable higher acceleration factors despite the presence of unsuppressed lipids. They accomplished this by controlling the aliasing pattern through optimizing the undersampling scheme. However, the high acceleration factor resulting from this method relies on simultaneous acquisition of signal from multiple slices, which limits the use of slice-wise B_0 shim updating. It was also shown that the method sometimes still suffers from residual lipid contamination artifacts.

Given that the remaining lipid aliasing artifacts are a direct result of inaccuracies in the GRAPPA reconstruction process, and in the interest of enabling slice-wise dynamic B_0 shim updating, in this study we take a different approach and try to enable high in-plane GRAPPA acceleration factors for non-lipid suppressed ^{1}H FID MRSI by introducing a novel and more accurate GRAPPA acquisition and reconstruction scheme.

Since the early years of GRAPPA, the imaging community has introduced several variations to the reconstruction process that would increase its accuracy. Among these advances was the realization that separating the reconstruction to the low and high frequency regions in k-space and having separate kernels for each, will increase the accuracy of the reconstruction and suppress the residual aliasing as well as noise amplification artifacts (Park et al. 2005, Miao et al. 2011). Park et al (Park et al. 2005) further used this property to introduce 1D variable density sampling with higher acceleration factors in the outer k-space without losing accuracy. Another group (Wang et al. 2005) used a multi-line, multi-column interpolation approach for finding a more accurate GRAPPA reconstruction kernel. By increasing the number of training points, this method improves the quality of reconstruction. Huang et al (Huang et al. 2008) used an image-support based approach for more accurate data recovery.

Additionally, regularization has been proven to be advantageous in PI reconstruction techniques and hence (Qu et al. 2006) used Tikhonov and singular-value decomposition to regularize the GRAPPA reconstruction optimization problem to control the trade-off between noise and residual artifacts in the resulting image. In another approach, Huo et al (Huo et al. 2008) introduced Robust GRAPPA, in which they assign weights to the training data in a way that would discount the contribution of the outliers to the coefficient estimation. Other groups used cross-validation (Nana et al. 2008) to better determine which neighboring lines and columns should be used in forming the reconstruction kernel. A more recent advance for improving the GRAPPA reconstruction was the introduction of nonlinear GRAPPA by Chang et al (Chang et al. 2012). All GRAPPA reconstruction methods so far assume a linear relationship between the acquired data points and the missing data, and hence, form a linear optimization problem to find the optimal reconstruction kernel. However, Chang et al. (Chang et al. 2012) observed a nonlinear relationship between the acquired auto-calibration signal (ACS) and the missing data points in the presence of noise. Their reconstruction optimization problem takes these nonlinearities into account by introducing up to 2nd order polynomial terms into the system of equations used for kernel optimization. Their reconstruction method proved superior to conventional GRAPPA for higher acceleration factors.

In this work we present a novel and improved GRAPPA reconstruction method (MultiNet GRAPPA) that combines the advantages of regularization, cross-validation, and localized coil calibration, and accounts for nonlinearities by using multiple neural networks in the reconstruction process. We show the advantages of this approach over the conventional GRAPPA reconstruction for accelerating non-lipid suppressed ultra-short TR and TE ^{1}H FID MRSI and further introduce a modified version combined with a variable density sampling scheme (MultiNet PyGRAPPA) that enables higher acceleration factors. Finally, we show the reproducibility of this approach for fast and high resolution metabolite mapping of the human brain at 9.4T.

Methods

Data Acquisition

High-resolution MRSI data were acquired using a slice-selective ^{1}H FID MRSI sequence (Henning et al. 2009, Bogner et al. 2012) with ultra-short TE and TR without any outer volume or lipid suppression schemes. An optimized 3-pulse water suppression scheme with a total duration of 62 ms was implemented in the sequence and optimized for a range of T_1 values and B_1 inhomogeneity levels between 50-150% (Nassirpour et al. 2018). Five healthy volunteers were scanned using a Siemens 9.4T whole-body human scanner (Erlangen, Germany). All volunteers gave their informed consent and were scanned in accordance with the local ethics committee regulations. An in-house built transceiver RF coil with 18 transmit and 32 receiver elements was used for all 9.4T scans (Avdievich et al. 2017). 2nd-order image-based B_0 shimming was performed on a rectangular shimming volume with the same dimensions as the imaging volume using the vendor implemented shimming routine.

Fully-sampled MRSI data from a single slice running through the periventricular white matter parallel to the Corpus Callosum was acquired from each volunteer using the described custom ^{1}H FID MRSI sequence with the following parameters: FOV = 200x200 mm; slice thickness = 10 mm; Flip angle = 30°; matrix size = 64x64; acquisition delay = 1.56 ms; TR = 300 ms; spectral bandwidth = 8000 Hz; acquisition time = 128 ms; total scan time = 15 mins. The nominal voxel size was 97µL.

After each MRSI scan, a high resolution reference anatomical image (at 4x4 times higher resolution than the MRSI data) with the same slice position and dimensions as the MRSI data was acquired using a 2D FLASH sequence with the following parameters: TR = 312 ms, TE = 9 ms, flip angle = 25°.

MultiNet GRAPPA: Multiple Neural Network based GRAPPA Reconstruction

The fully sampled MRSI data were retrospectively undersampled by a factor of 2 in each direction. In addition, an elliptical shuttered sampling was applied to further increase the acceleration. The effective acceleration factor was R=5.47 for a matrix size of 64x64 (Figure 1). Note that since acquiring fully sampled lines for use as ACS in the GRAPPA reconstruction methods would significantly add to the MRSI scan time, for all studies the anatomical reference image acquired through an imaging sequence was used as ACS data. This makes the net acceleration factors much higher, as imaging sequences run much faster than MRSI scans.

Neural networks (NN) were trained to predict the missing data points using the anatomical image as training data. Only the central k-space points of the high resolution anatomical data in a grid of 64x64 were used for training. Two neural networks were trained: one for cross-neighbors and another for adjacent-neighbors (as shown in Figure 2). The adjacent neighbors are the 4-connected voxels (i.e. voxels in the Von Neumann neighborhood). The cross-neighbors are the 8-connected voxels (i.e. voxels in the Moore neighborhood) excluding the 4-connected voxels. The neighbor voxels were used to train the networks to predict the voxel of interest. Single layer NN with 128 hidden nodes were used for each NN. A Broyden–Fletcher–Goldfarb–Shanno (BFGS) algorithm was used to calculate the weights.

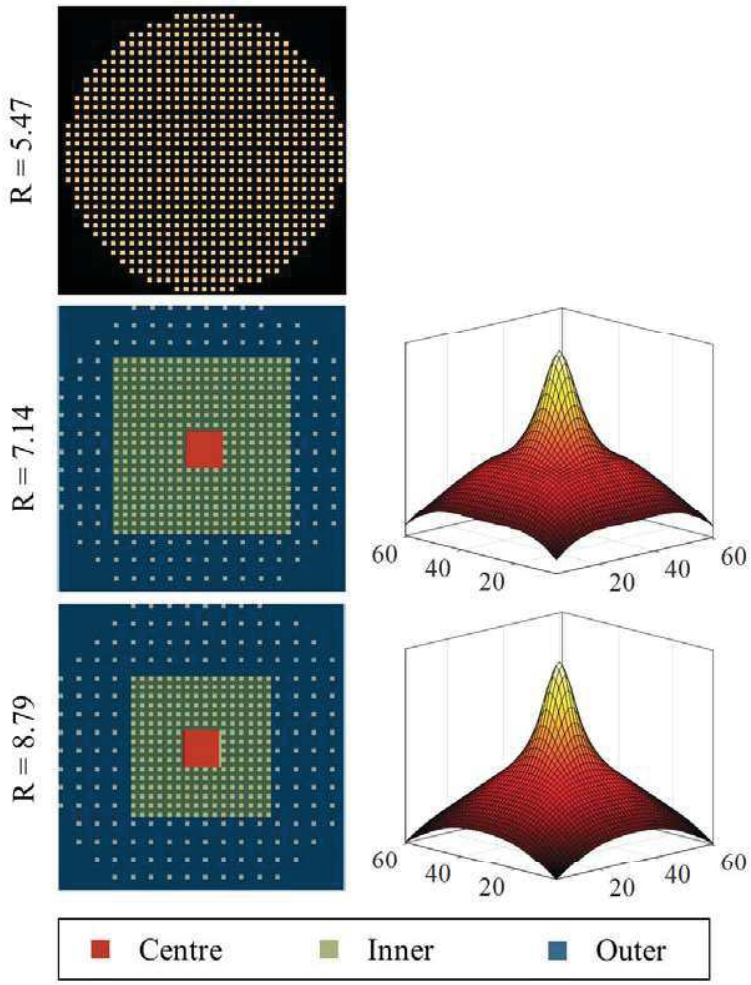

Figure 1- *k-space undersampling masks used in this study are shown in the left column for a regular undersampling scheme of R=2 in each direction resulting in a net acceleration factor of R~5 due to the additional elliptical shuttering mask (top row), a variable density PyGRAPPA undersampling scheme resulting in R~7 (middle row), and another one resulting in R~9 (bottom row). Three different regions in kspace are defined and annotated with different colors for the PyGRAPPA undersampling schemes. The Voronoi sampling density curves are shown for the two PyGRAPPA schemes in the right column. The normalized sampling density curves are shown between 0 and 1.*

To reconstruct the data, the cross-neighbor NN was first used to predict the missing k-space values. After these values were filled-in, the adjacent-neighbor NN was used to predict the remaining missing points.

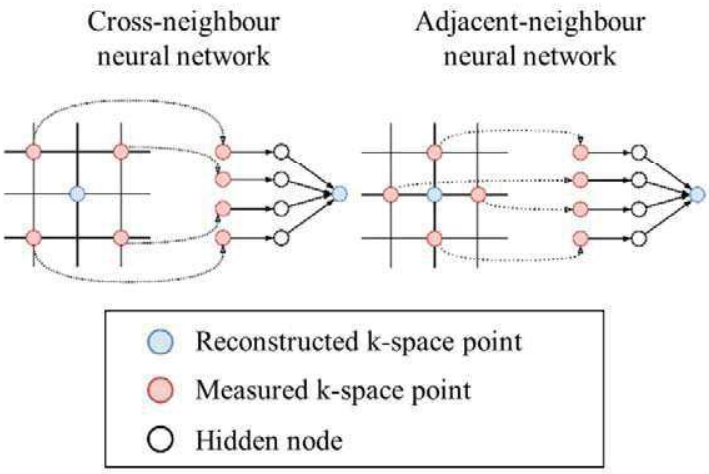

Figure 2- *Schematic depiction of the multiple neural network based GRAPPA reconstruction (MultiNet GRAPPA) using two neural networks: first a cross-neighbor neural network is trained and used to predict the central missing point in each grid (left), next, an adjacent-neighbor neural network is trained and used to predict the rest of the points (right).*

For comparison, a traditional GRAPPA reconstruction using the 2D-GRAPPA operator method (Blaimer et al. 2006) was performed, again using the anatomical scout image as ACS to calibrate the kernel weights.

The metabolite maps from the fully sampled, conventional GRAPPA reconstructed and multiple neural network based (MultiNet) GRAPPA reconstructed MRSI data were compared. The data were post-processed as described in (Nassirpour et al. 2018), which includes eddy current correction, automatic phase correction, residual water peak removal, and coil combination. The metabolite maps were generated by fitting the processed data using LCModel (Provencher 1993). The spectra were fit between 1.8 and 4.2 ppm. The basis-set was simulated using the GAMMA library (http://www.nmr.ethz.ch/Gamma.html) and included spectra of 18 brain metabolites (namely GPC, Tau, Cre, Glc, Naa, Asc, Lac, GABA, NAAG, GSH, Glu, PE, mI, PCh, Ala, Gln, Scyllo and Asp) with a linewidth of 5Hz. No T_1/T_2 correction was applied to the metabolite maps.

MultiNet PyGRAPPA: Enabling Higher Acceleration Using Variable Density Sampling

The centre of k-space contains the low spatial frequency information and determines the main contrasts in the image. Hence, it is more important and has more impact on the aliasing artifacts in the reconstructed image. On the contrary, the outer k-space which contains the high spatial frequency information determines detailed lines and edges. This is an important concept which is exploited in many acceleration schemes such as compressed sensing (Lustig et al. 2007). Similarly, with the neural network kernel-based GRAPPA approach described here, we can take advantage of this and sample different parts of the k-space with different sampling densities according to their contribution to the overall quality or artifacts in the image. The MultiNet GRAPPA reconstruction approach can easily be separated to different regions in k-space. Multiple neural networks with different properties can be trained for each k-space region. For example, by changing the hidden layer of the neural network to be nonlinear for the reconstruction of the outer k-space region, we can account for the nonlinear relationship between the missing and acquired data points due to higher levels of noise present in the outer regions of k-space. This will result in a more reliable reconstruction, which in turn enables higher net acceleration factors than those achievable through conventional GRAPPA.

Figure 1 shows two variable density undersampling schemes that were used to achieve higher acceleration factors in this study. In both schemes, the centre-most part of k-space was fully sampled, the "inner" k-space region was undersampled by a factor of 2x2 and the "outer" k-space region was undersampled by a factor of 4x4. The size of the centre was always kept to be 8x8, and the size of the inner region was 40x40 and 32x32 which resulted in effective acceleration factors of R=7.14 and R=8.79, respectively. These two undersampling schemes will be referred to as R=7 and R=9, respectively, in the remainder of this paper. The figure also shows the calculated sampling density function for each of the variable density undersmapling masks. The sampling density curves were calculated as the reciprocal of the area of the Voronoi cells at each kspace point. Due to the similarity of the shape of these density curves to a pyramid, the proposed acquisition scheme is hereafter referred to as PyGRAPPA.

To optimally reconstruct the data, firstly, the outer k-space points were filled in using the method described in the previous subsection. However, the difference is that the neighbour voxels are two voxel spaces away instead of one. After the outer k-space points are filled, the remaining missing points are the same as a 2x2 undersampling in the outer and inner regions. These missing points are then filled in using the NNs described previously. Therefore, a total of four NNs are required to reconstruct the data: a cross-neighbour NN in addition to an adjacent-neighbour NN with 2-voxel distance for filling the outer region, and a cross-neighbour and adjacent neighbour NN with 1-voxel distance for filling the inner region and the remaining missing points of the outer region. Figure 3 shows the step-by-step process of how the missing k-space points are reconstructed using the corresponding NNs.

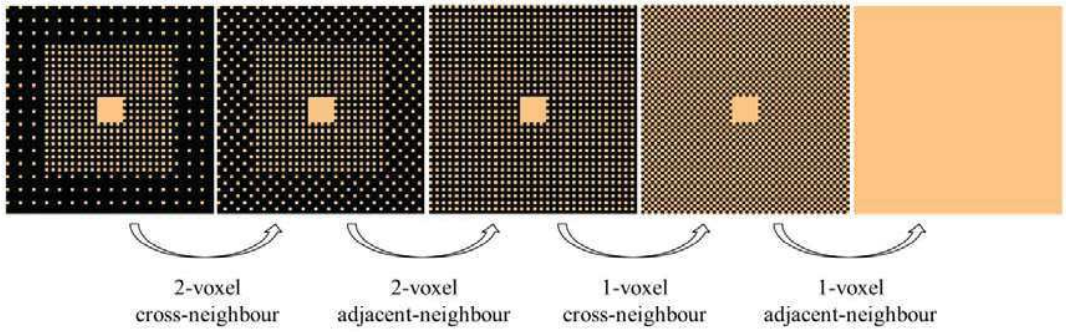

Figure 3- *Step-by-step process of MultiNet PyGRAPPA for predicting the missing points of the proposed variable density sampling schemes. The missing kspace points are shown in black. Four different neural networks are trained: First, a 2-voxel cross-neighbour neural network fills in some of the missing points in the outer region of kspace. Then, a 2-voxel adjacent-neighbour is used to predict more of the missing points in the outer region so that now almost all of the kspace is undersampled by a factor of 2x2. Next, a 1-voxel cross-neighbor neural network is trained and used to fill in the central missing point in each small grid, and finally, a 1-voxel adjacent-neighbour fills in the rest of the missing points to form the reconstructed data.*

Since the central k-space region is always fully sampled in these variable density sampling schemes, it can also be used as additional training data for the NNs. Similarly, the measured inner-region k-space samples can be used to train the 2-voxel distance NNs in the reconstruction of the outer region. Therefore, for training the 2-voxel distance NNs, the inner and central regions of the MRSI data were used in addition to the anatomical image. For training the 1-voxel distance NNs, the central region of

the MRSI data was used in addition to the anatomical image. Only the first 8 time points of the MRSI data were used for training due to their higher SNR.

For the hidden layer of the 1-voxel distance NNs the identity function was used. However, for the 2-voxel distance NNs, logistic functions were used for more flexibility and to account for possible nonlinearities.

Metabolite maps from the fully sampled, R=7, and R=9 MultiNet PyGRAPPA reconstructions were compared. The metabolite maps were generated using the same process as described in the previous subsection.

The different acceleration schemes were further quantitatively evaluated using four metrics: the lipid contamination power (LCP), SNR ratio (similar to g-factor), root-mean-square-errors (RMSEs) of three major metabolite maps (NAA, Cre, and Glu), and the corresponding Cramer-Rao lower-bounds (CRLBs). The lipid contamination power is defined as

$$LCP = 100 \cdot \frac{\sum_{ch} \sum_{\vec{r} \in mask} \sum_{f \in Fmask} \left| S_{accel}(ch, \vec{r}, f) - S_{full}(ch, \vec{r}, f) \right|}{\sum_{ch} \sum_{\vec{r} \in mask} \sum_{f \in Fmask} \left| S_{full}(ch, \vec{r}, f) \right|} \quad (1)$$

Where the coil channels, voxel position and spectral points are denoted by *ch*, *r*, and *f*, respectively. *Mask* is the spatial mask defined to contain only the brain region and *Fmask* is the frequency domain mask between (0.3 and 1.8 ppm) that contains most of the contribution of lipid signals. The spatial masks were manually defined for each subject. Lastly, S_{accel} denotes the accelerated data and S_{full} denotes the fully sampled data.

The SNR ratio metric is defined similarly to the g-factor and is approximated by:

$$\frac{RMS(noise_{accel})}{\sqrt{R} \cdot RMS(noise_{full})} \quad (2)$$

The RMSE of the metabolite maps is calculated for each metabolite by:

$$RMSE = 100 \cdot \sqrt{\frac{\sum_{\vec{r} \in mask} \left(\frac{C_{accel}(\vec{r}) - C_{full}(\vec{r})}{C_{full}(\vec{r})} \right)^2}{N}} \quad (3)$$

Where *C* is the concentration of the metabolite and *N* is the number of voxels in the spatial mask. The CRLBs are taken from the values reported from LCModel.

Results

MultiNet GRAPPA

Figure 4 shows the metabolite maps for NAA and Glutamate. The fully sampled data, conventional GRAPPA reconstructed data (R=2x2) and MultiNet reconstructed data (R=2x2) are shown in the figure for three subjects. The advantage of the proposed MultiNet reconstruction over the conventional GRAPPA reconstruction can be seen from the residual aliasing artifacts present in the metabolite maps resulting from the conventional GRAPPA reconstruction. The residual aliasing is especially prevalent in subject 3 for both metabolites. However, the residual aliasing can also be seen for subject 1 for Glutamate, and for subject 2 for NAA. The MultiNet reconstruction also results in metabolites maps that appear more similar to the fully sampled data by visual inspection than those resulting from conventional GRAPPA reconstruction.

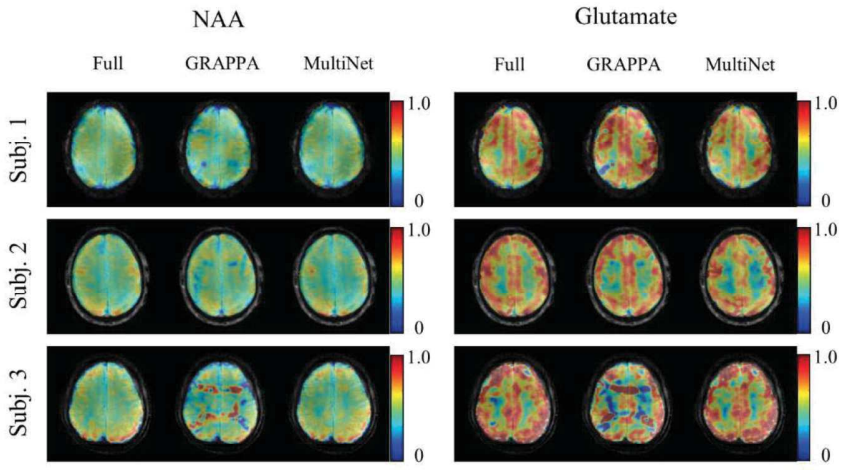

Figure 4- *Comparison of conventional GRAPPA reconstruction (denoted as GRAPPA) and the proposed neural network based GRAPPA reconstruction (denoted as MultiNet) for the case of R=2x2 acceleration: Metabolite maps are shown for two major metabolites in three subjects. All maps are normalized and shown between 0 and 1. The maps are shown for the fully sampled case (R=1) and the accelerated case (R=2x2) reconstructed once with GRAPPA and once with MultiNet.*

Figure 5 shows the lipid contamination maps for the same three subjects and for the different reconstruction methods. The lipid contamination is defined as the integral of the absolute signal between 0.3 to 1.8 ppm. The maps shown in the figure are normalized to their maximum value. The lipid contamination maps from the conventional GRAPPA reconstruction show more aliasing artifacts than the MultiNet GRAPPA. In comparison, the maps of the MultiNet GRAPPA and the fully sampled data look very similar. No visible aliasing artifacts are present in the MultiNet GRAPPA lipid contamination maps.

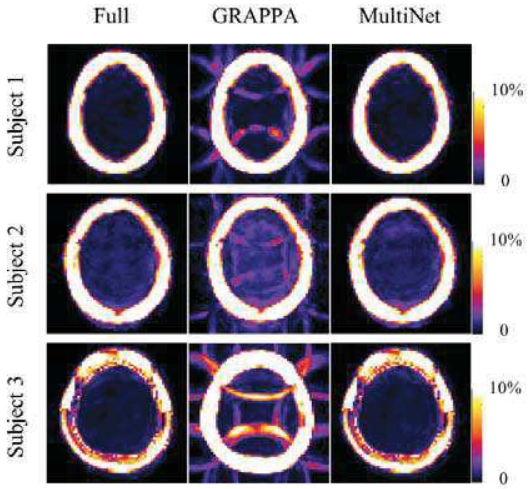

Figure 5- *Lipid contamination maps shown between 0 and 10% of the strongest lipid contribution near the skull region for better visualization. The maps are shown for three subjects for fully sampled (R=1) versus accelerated (R=2x2) acquisitions, once reconstructed with conventional GRAPPA, and once with the proposed neural network based GRAPPA (MultiNet).*

MultiNet PyGRAPPA

Figure 6 and 7 show the metabolite and CRLB maps of two major metabolites for the fully sampled, along with the highly accelerated R=7 and R=9 MultiNet PyGRAPPA reconstructions on three subjects. Compared to the fully sampled data, the accelerated maps show good consistency albeit slightly more noisy. The grey/white matter contrast and the anatomical structure can still be seen. The noise in the R=9 case is higher than in the R=7 case. Higher noise levels for higher accelerations also occurs for conventional GRAPPA reconstructions. However, the advantage of the MultiNet method as can be seen in this figure, is that it does not result in structured aliasing artifacts such as lipid rings.

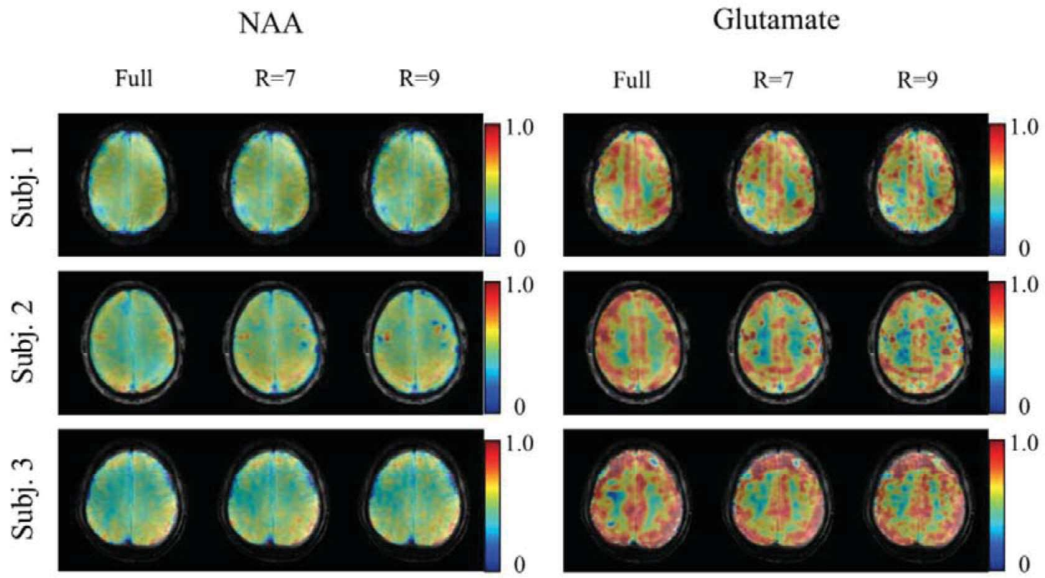

Figure 6- *Reproducibility of highly accelerated metabolite mapping using the proposed MultiNet PyGRAPPA method: metabolite maps of two major metabolites are shown for three volunteers and for three cases:* ***1)*** *fully sampled (R=1),* ***2)*** *variable density undersampled and multiple neural network GRAPPA reconstructed (MultiNet PyGRAPPA) with R=7, and* ***3)*** *R=9. All maps are normalized and shown between 0 and 1.*

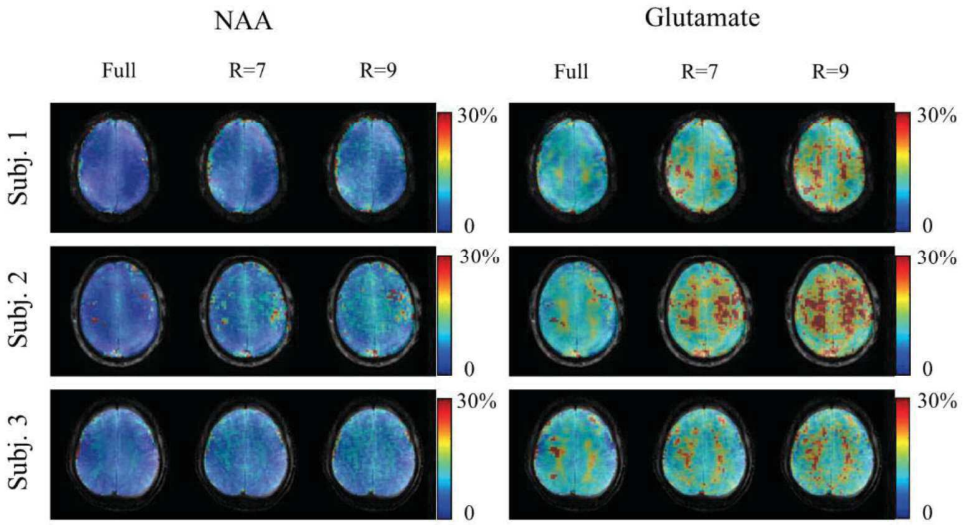

Figure 7- *Reproducibility of highly accelerated metabolite mapping using the proposed MultiNet PyGRAPPA method: CRLB maps of two major metabolites are shown for 3 volunteers and for three cases:* ***1)*** *fully sampled (R=1),* ***2)*** *variable density undersampled and multiple neural network GRAPPA reconstructed (MultiNet PyGRAPPA) with R=7, and* ***3)*** *R=9.*

Figure 8 shows the lipid contamination maps for the subjects for the R=7 and R=9 MultiNet PyGRAPPA reconstructions. Despite the high in-plane acceleration factors, there are no visible aliasing artifacts and lipid rings in these maps.

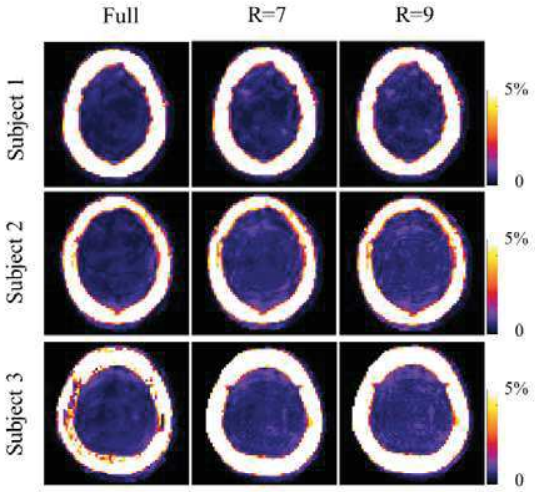

Figure 8- *Lipid contamination maps shown for three subjects between 0 and 5% of the strongest lipid contribution near the skull region for better visualization. The maps are shown for the case of fully sampled, and the proposed MultiNet PyGRAPPAacceleration method with R=7 and R=9.*

Table 1 shows the results for the quantitative assessment of the reconstructions using the metrics described above, namely: lipid contamination power, SNR ratio, RMSE of three major metabolite

maps, and the corresponding CRLBs. The values are averaged over five volunteers across the whole slice. An acceleration factor of 2x2 (R=4) with MultiNet reconstruction was compared to the R=7 and R=9 PyGRAPPA. On average, the lipid contamination power, RMSEs, and CRLBs increase as the acceleration factor increases. However, the lipid contamination power is not significantly affected by the acceleration factor. As expected, the CRLBs increase as the acceleration factor increases, however, the CRLBs are still quite low (typically between 6% and 12%).

The SNR ratio (equivalent to a g-factor calculation) for R=4 is approximately 1.1 when averaged over the whole slice and across volunteers. However, the SNR ratio is below 1.0 (approximately 0.8) for R=7 which indicates that the noise from acceleration increases at a lower rate than $\sqrt{R}$. For R=9, the SNR ratio is slightly higher, approximately 0.93 on average.

	R = 4	R = 7	R = 9
LCP	0.46	0.47	0.54
CRLB (Cre)	9.12 ± 0.97	9.14 ± 1.13	10.18 ± 1.44
CRLB (NAA)	6.21 ± 0.75	6.55 ± 0.80	6.98 ± 1.01
CRLB (Glu)	12.40 ± 1.58	12.54 ± 1.61	12.99 ± 1.52
RMSE (Cre)	7.45	8.77	12.13
RMSE (NAA)	5.29	5.79	7.92
RMSE (Glu)	9.94	11.30	15.93
SNR ratio	1.09 ± 0.25	0.81 ± 0.20	0.93 ± 0.22

Table 1- *Quantitative evaluation of the proposed MultiNet GRAPPA reconstruction method for a range of acceleration factors. Eight metrics are used for the evaluation (lipid contamination power, SNR ratio (similar to g-factor), RMSE (%), and CRLB (%) of the maps for three major metabolites). The values are averaged across five healthy volunteers.*

Discussion

Metabolite mapping using ^{1}H MRSI is a promising tool for assessing the spatial distribution of several metabolites in different regions of the brain in a non-invasive manner. To increase the clinical applicability of ^{1}H MRSI, it is crucial to increase the SNR and in general the data quality as much as possible, but also decrease the lengthy scan times. The slice-selective ultra-short TE and TR non-lipid suppressed ^{1}H FID MRSI sequence (Bogner et al. 2012, Boer et al. 2012, Nassirpour et al. 2018) seems to be a suitable candidate for achieving this goal since it can be easily implemented both at lower and ultra-high fields, is not SAR demanding, does not require specific hardware specifications, does not suffer from in-plane chemical shift artifacts and has negligible SNR loss due to T_2 relaxation as a result of very short echo times. As a result of all this, it is by nature a fast sequence which can be used with TRs as short as a few hundred milliseconds (Nassirpour et al. 2018, Hangel et al. 2018) or even as low as 50ms (Chadzynski et al. 2017). The resulting spectra from this sequence have already been shown to be of good quality and result in reliable and high resolution metabolite maps. The next step, of course, is to accelerate this sequence in order to enable high resolution metabolite mapping with multi-slice or whole brain coverage in a reasonable scan time.

At ultra-high field strengths, in-plane (2D) acceleration methods are preferable for accelerating this sequence, since any use of 3D or multi-band acquisition schemes will limit the ability of using tailored B_0 shim settings for each slice of the brain. This is due to the fact that signal is being simultaneously acquired from a bigger region in these acquisition schemes. This problem is more severe at ultra-high fields, since the air cavities close to the brain tissue especially when imaging the lower slice positions in the brain, will result in poor B_0 shimming. This, in turn, will result in poor spectral quality which severely hinders reliable metabolite quantification.

The challenge in using in-plane PI acceleration methods is that they suffer from residual aliasing artifacts and severe noise amplification at higher acceleration factors. The residual aliasing artifact is especially problematic since there are unsuppressed and strong lipid signals present near the skull region when no lipid suppression scheme is used. When folded into the brain, these signals can distort the spectra to the point where it is impossible for the fitting routine to resolve other metabolite peaks.

In this work, we present a novel acquisition and reconstruction method (MultiNet PyGRAPPA) for in-plane acceleration that enables acceleration factors as high as R=7 or 9 while keeping the noise levels under control and without introducing any structured aliasing artifacts. The method is based on a 2D variable density sampling acquisition scheme and the use of machine learning, specifically multiple neural networks with different hidden layers, to recover the missing data points as reliably as possible. To the best of the authors' knowledge, this is the first GRAPPA acceleration/reconstruction method that when used with non-lipid suppressed ^{1}H FID MRSI sequence, does not introduce lipid rings inside the brain resulting from residual aliasing artifacts. This eliminates the need for any SAR demanding lipid suppression schemes (Henning et al. 2009, Hangel et al. 2015) or post-processing lipid removal methods such as the L_2-regularized algorithm (Bilgic et al. 2014).

The use of neural networks for GRAPPA reconstruction (MultiNet GRAPPA) showed a clear improvement over the regular GRAPPA reconstruction. The aliasing artifacts were much less, which directly impacts the metabolite maps. The 1-voxel distance NNs use identity activation functions as the hidden layer. Although this reduces to a linear perceptron, using a NN to train and calculate the weights improves the robustness of the regression. In comparison, a regular multivariate regression is susceptible to noise and outliers.

In general, the higher the SNR of the training data, the better the weights of the network can be estimated, and thus the missing k-space points can be more accurately predicted. The predictive power of the NNs is dependent on the quality of the training data. In this study, an anatomical FLASH image was used for training but, in general, any anatomical image (such as GRE or MPRAGE sequences) can be used for this purpose. Even though the advantage of the proposed MultiNet GRAPPA reconstruction was shown for the specific case of non-lipid suppressed ^{1}H FID MRSI, this method can be used to reconstruct GRAPPA accelerated data for any MR imaging application, as the chosen application in this paper is in fact one of the most challenging ones in terms of resolving aliasing artifacts due to the strong contrast between the intensity of unsuppressed lipid signals and the metabolites of interest.

Compared to Cartesian regular undersampling, variable density sampling (pyGRAPPA) schemes result in a better spatial response function (SRF). The aliased peaks are further from the original peak and have less power compared to those resulting from regularly undersampled data with similar net acceleration factors. This means that if there are inaccuracies in the reconstruction process which would result in some percentage of the aliased peak to remain in the image, the power of the residual signal is much less than that of the regularly undersampled data. Controlling the artifact power in this manner is the key concept behind the idea of variable density sampling. So if there is a way to push the in-plane PI acceleration to achieve higher acceleration factor, especially in case of non-lipid suppressed MRSI sequences, it has to be through controlling the aliasing artifacts.

Conventional GRAPPA reconstruction itself can be applied to reconstruct the variable density undersampled data, however, by nature there will be severe noise amplification especially from the outer k-space regions if no regularization measure is taken. This is where the multiple neural network approach suggested in this work proves to be most advantageous.

In addition to the implicit regularization that is inherent to neural networks, the other advantage of NNs is the ability to use a nonlinear hidden function to capture nonlinearities. This is beneficial for the 2-voxel distance NNs where the relationship between the inputs are more nonlinear due to the presence of noise (Chang et al. 2012). This allows the NNs to predict the missing k-space points more

accurately and is the key benefit that enables the reconstruction of the highly accelerated data while keeping the noise levels under control. Note that since the regularization is implicit when using neural networks, no prior knowledge is needed to reconstruct the data reliably.

The SNR ratio (defined similar to g-factor) is even lower for PyGRAPPA with R=7 and R=9 compared to the R=4 regular undersampling scheme. This is likely due to the fact that for the R=7 and R=9 variable density schemes, the center of k-space is fully measured, whereas for R=4, the entire k-space is undersampled by 2x2. Since the center of k-space has the most contribution, if the center is undersampled, more noise will be introduced compared to undersampling outer k-space. Therefore the SNR ratio can be improved using a variable density sampling scheme rather than a uniformly undersampled k-space. Furthermore, the proposed sampling scheme reduces the aliasing artifacts: the lipid contamination traces are greatly reduced, even for higher acceleration factors of R=7 and R=9.

The proposed acceleration and reconstruction scheme incorporated into an ultra-short TR and TE ^{1}H FID MRSI sequence with a TR of 300ms, enabled high resolution metabolite mapping of the human brain. For a nominal voxel size of 97μL (matrix size of 64x64), the total scan time was 2 minutes 50 seconds with R=7, and 2 minutes 7 seconds for R=9. This is faster than the fastest accelerated ^{1}H FID MRSI published in the literature so far, which was reported using the (2+1) D CAIPIRINHA method (Strasser et al. 2017) to be 3.75 minutes for the same matrix size. Our proposed method is about 1.5 times and 2 times faster than this, with R=7 and R=9, respectively. This will make a great impact for multi-slice and whole brain coverage metabolite mapping.

The only factor limiting the achievable acceleration factor using the proposed method (beyond R=7 or R=9) is the limited initial SNR of the spectroscopy data. This is more of a limitation at lower field strengths since at ultra-high fields (≥7T) the initial SNR of the data is much higher than at lower fields. SNR boosting techniques such as any denoising method can be used to mediate this problem, and improve the quality of the metabolite maps, however, most denoising techniques come at the price of trading off spatial and spectral resolution for higher SNR. Recently, Kirchner et al (Kirchner et al. 2017) introduced a denoising method using over-discretized B_0 correction that improves the SNR while resulting in better line-shapes without sacrificing the spatial resolution. Using this technique, the MultiNet PyGRAPPA method presented in this paper can also be applied at a lower field strengths to enable fast and high resolution metabolite mapping.

A limitation of this study was that only 2nd order B_0 shimming was used for shimming at 9.4T. It is well know that using better B_0 shimming will improve the quality of the MRSI data (Pan et al. 2012, Chang et al. 2018), which will in turn enable more reliable acceleration due to the higher SNR and less lipid contamination in the original data.

Conclusion

This paper presents a novel acquisition and reconstruction scheme (MultiNet PyGRAPPA) for highly accelerated metabolite mapping using the non-lipid suppressed ^{1}H FID MRSI sequence. The proposed method is an improvement on conventional GRAPPA, combining a variable density sampling scheme with multiple neural networks to predict the missing data points. The machine learning based reconstruction method proves superior to conventional GRAPPA and results in less noise and residual aliasing artifacts. The proposed MultiNet PyGRAPPA method was applied at an ultra-high field of 9.4T for high resolution (matrix size = 64x64) metabolite mapping of the human brain and resulted in smooth and reliable maps acquired in 2.8 minutes (with R=7). MultiNet PyGRAPPA is compatible with dynamic slice-wise B_0 shim updating and can be used to increase the clinical applicability of ^{1}H MRSI.

Acknowledgements

This study was supported by the European Research Council Starting grant (project SYNAPLAST MR #679927) and the Horizon 2020 grant (project CDS_QUAMRI #634541).

References

Avdievich et al. 2018 Avdievich NI, Giapitzakis IA, and Henning A, "Combined Surface Loop/"Vertical" Loop Element Improve Receive Performance of a Human Head Transceiver Array at 9.4T: an Alternative to Surface Loop/Dipole Antenna Combination", NMR in Biomedicine 2018; 31(2).

Banerjee et al. 2006 Banerjee S, Ozturk-Isik E, Nelson SJ, and Majumdar S, "Fast magnetic resonance spectroscopic imaging at 3 Tesla using autocalibrating parallel technique", Proceedings of the 28th IEEE EMBS Annual International Conference, 2006; 1866-69.

Bilgic et al. 2014 Bilgic B, Chatnuntawech I, Fan AP, Setsompop K, Cauley SF, Wald LL, Adalsteinsson E, "Fast image reconstruction with L2-regularization", Journal of Magnetic Resonance Imaging 2014; 40(1): 181-91.

Blaimer et al. 2006 Blaimer M, Breuer FA, Mueller M, Seiberlich N, Ebel D, Heidemann RM, Griswold MA, Jakob PM, "2D-GRAPPA-operator for faster 3D parallel MRI" Magnetic Resonance in Medicine 2006; 56(6): 1359-64.

Boer et al. 2012 Boer VO, Klomp DWJ, Juchem C, Luijten PR, de Graaf RA, " Multi-slice ^{1}H MRSI of the human brain at 7 Tesla using dynamic B_0 and B_1 shimming", Magnetic Resonance in Medicine 2012; 68(3): 662-70.

Bogner et al. 2012 Bogner W, Gruber S, Trattnig S, Chmelik M, "High-resolution mapping of human brain metabolites by free induction decay ^{1}H MRSI at 7 T", NMR in Biomedicine 2012; 25(6): 873-82.

Chadzynski et al. 2017 Chadzynski GL, Bause J, Shajan G, Pohmann R, Scheffler K, Ehses P, "Fast and efficient free induction decay MR spectroscopic imaging of the human brain at 9.4 Tesla", Magnetic Resonance in Medicine 2017; 78(4): 1281-95.

Chang et al. 2018 Chang P, Nassirpour S, Henning A, "Modeling real shim fields for very high degree (and order) B_0 shimming of the human brain at 9.4 T", Magnetic Resonance in Medicine 2018; 79(1): 529-40.

Chang et al. 2012 Chang Y, Liang D, Ying L, "Nonlinear GRAPPA: A kernel approach to parallel MRI reconstruction", Magnetic Resonance in Medicine 2012; 68(3): 730-40.

Griswold et al. 2002 Griswold MA, Jakob PM, Heidemann RM, Nittka M, Jellus V, Wang J, Kiefer B, Haase A, "Generalized autocalibrating partially parallel acquisitions (GRAPPA)", Magnetic Resonance in Medicine 2002; 47(6): 1202-10.

Hangel et al. 2015 Hangel G, Strasser B, Považan M, Gruber S, Chmelík M, Gajdošík M, Trattnig S, Bogner W, "Lipid suppression via double inversion recovery with symmetric frequency sweep for robust 2D-GRAPPA-accelerated MRSI of the brain at 7 T", NMR in Biomedicine 2015; 28(11): 1413-25.

Hangel et al. 2018 Hangel G, Strasser B, Považan M, Heckova E, Hingerl L, Boubela R, Gruber S, Trattnig S, Bogner W, "Ultra-high resolution brain metabolite mapping at 7T by short-TR Hadamard-encoded FID-MRSI", NeuroImage 2018; 168: 199-210.

Henning et al. 2009 Henning A, Fuchs A, Murdoch JB, Boesiger P, "Slice-selective FID acquisition, localized by outer volume suppression (FIDLOVS) for ^{1}H-MRSI of the human brain at 7 T with minimal signal loss", NMR in Biomedicine 2009; 22(7): 683-96.

Huang et al. 2008 Huang F, Li Y, Vijayakumar S, Hertel S, Duensing GR, "High-pass GRAPPA: An image support reduction technique for improved partially parallel imaging", Magnetic Resonance in Medicine 2008; 59(3): 642-49.

Huo et al. 2008 Huo D, Wilson DL, "Robust GRAPPA reconstruction and its evaluation with the perceptual difference model" Journal of Magnetic Resonance Imaging 2008; 27(6): 1412-20.

Kirchner et al. 2017 Kirchner T, Fillmer A, Anke Henning. "Mechanisms of SNR and line shape improvement by B0 correction in overdiscrete MRSI reconstruction." *Magnetic resonance in medicine* 77, no. 1 (2017): 44-56.

Lustig et al. 2007 Lustig M, Donoho D, Pauly JM, "Sparse MRI: The application of compressed sensing for rapid MR imaging", Magnetic Resonance in Medicine 2007; 58(6): 1182-95.

Miao et al. 2011 Miao J, Wong WC, Narayan S, Huo D, Wilson DL, "Modeling non-stationarity of kernel weights for k-space reconstruction in partially parallel imaging", Medical Physics 2011; 38(8): 4760-73.

Nana et al. 2008 Nana R, Zhao T, Heberlein K, LaConte SM, Hu X, "Cross-validation-based kernel support selection for improved GRAPPA reconstruction", Magnetic Resonance in Medicine 2008; 59(4): 819-82.

Nassirpour et al. 2018 Nassirpour, Sahar, Paul Chang, and Anke Henning. "High and ultra-high resolution metabolite mapping of the human brain using ^{1}H FID MRSI", NeuroImage 2018; 168: 211-21.

Pan et al. 2012 Pan JW, Lo KM, Hetherington HP, "Role of very high order and degree B_0 shimming for spectroscopic imaging of the human brain at 7 Tesla", Magnetic Resonance in Medicine 2012; 68(4): 1007-17.

Park et al. 2005 Park J, Zhang Q, Jellus V, Simonetti O, Li D, "Artifact and noise suppression in GRAPPA imaging using improved k-space coil calibration and variable density sampling", Magnetic Resonance in Medicine 2005; 53(1): 186-93.

Provencher 1993 Provencher SW, "Estimation of metabolite concentrations from localized in vivo proton NMR spectra", Magnetic Resonance in Medicine 1993; 30(6): 672-79.

Pruessman et al. 1999 Pruessmann KP, Weiger M, Scheidegger MB, Boesiger P, "SENSE: sensitivity encoding for fast MRI", Magnetic Resonance in Medicine 1999; 42(5): 952-62.

Qu et al. 2006 Qu P, Wang C, Shen GX, "Discrepancy-based adaptive regularization for GRAPPA reconstruction", Journal of Magnetic Resonance Imaging 2006; 24(1): 248-55.

Sabati et al. 2014 Sabati M, Zhan J, Govind V, Arheart KL, Maudsley AA,"Impact of reduced k-space acquisition on pathologic detectability for volumetric MR spectroscopic imaging", Journal of Magnetic Resonance Imaging 2014; 39(1): 224-34.

Strasser et al. 2017 Strasser B, Považan M, Hangel G, Hingerl L, Chmelik M, Gruber S, Trattnig S, Bogner W, "(2+1) D-CAIPIRINHA accelerated MR spectroscopic imaging of the brain at 7T", Magnetic Resonance in Medicine 2017;78(2): 429–40.

Tsai et al. 2008 Tsai SY, Otazo R, Posse S, Lin YR, Chung HW, Wald LL, Wiggins GC, Lin FH, "Accelerated proton echo planar spectroscopic imaging (PEPSI) using GRAPPA with a 32-channel phased-array coil", *Magnetic Resonance in Medicine* 2008; 59(5): 989-98.

Wang et al. 2005 Wang Z, Wang J, Detre JA, "Improved data reconstruction method for GRAPPA", Magnetic Resonance in Medicine 2005; 54(3): 738-742.

Publication VI

"Accelerated Water Reference Acquisition for ^{1}H MRSI using Compressed Sensing"

S Nassirpour*, P Chang*, A Henning

[in preparation]

Highly Accelerated Water Reference Acquisition for ^{1}H MRSI using Compressed Sensing

Introduction

Proton magnetic resonance spectroscopic imaging (^{1}H MRSI) is susceptible to time-dependent magnetic field distortions produced by eddy currents. These eddy currents are mostly induced by time-varying gradients of the imaging sequence and are more severe for fast imaging sequences such as EPSI [1] or ultra-short TR ^{1}H FID MRSI [2, 3, 4]. To retrospectively correct for the distortions caused by these time-dependent frequency shifts in the acquired spectra, usually a non-water suppressed (NWS) reference image is acquired in the same session and is afterwards used for eddy current and automatic phase correction in a process known as Klose eddy current correction [5]. Additionally, for quantification purposes, the signal obtained from the unsuppressed water peak can be used for internal referencing.

Despite the advantages of acquiring a NWS reference image for every water-suppressed ^{1}H MRSI dataset, this naturally comes at the price of a significantly prolonged scan time, i.e. double the scan time in the case of 2D FID MRSI if a fully-sampled NWS image is acquired at the same spatial resolution as the metabolite image. To reduce this overhead scan time, conventionally a reduced resolution NWS image is acquired (e.g. at 2 times lower resolution in each phase encoding direction (e.g. [6]) resulting in the MRSI scan time being prolonged by 125% instead of 200%). Afterwards, the water signal from each voxel is used to correct for the spectra of four voxels in the original MRSI image. This proves to be sufficient for the purposes of eddy current and automatic phase correction as it has been previously shown to result in reliable metabolite maps [7]. However, for internal referencing and quantification purposes, this low resolution NWS image will be too coarse and suffer from severe partial volume effects. Furthermore, prolonging the scan by 25% may be feasible for low resolution or single-slice MRSI studies, but for high resolution metabolite mapping with larger coverage the additional 25% scan time will severely hinder the clinical use of such sequences.

Ideally, NWS reference images should be acquired at the same spatial resolution as the actual water-suppressed MRSI images in an accelerated manner. This can be achieved through conventional MRI acceleration methods. The NWS image is specifically suitable for acceleration as one of the key factors enabling high acceleration factors in any MR imaging application is high initial signal to noise ratio (SNR). The SNR of water in ^{1}H spectra is much greater than for other metabolites and therefore for water reference acquisition, k-space can be heavily undersampled. Furthermore, the water signal is spatially more uniform across the brain and therefore sparser than water-suppressed data where the lipid signals from the subcutaneous fat can dominate. This makes the water reference image even more compressible.

Recently, Birch et al [8] made an attempt at accelerating the acquisition of NWS reference images using parallel imaging, specifically using SENSE [9]. They compared a SENSE accelerated NWS acquisition method (R=3) to a reduced resolution approach (R=2) and showed that in addition to being faster, the SENSE accelerated approach succeeds in reliably reconstructing the NWS image at the same resolution as the original metabolite image and is hence more accurate than the reduced resolution approach.

Despite the successful application of SENSE for acceleration of NWS reference image acquisition, the acceleration factors achievable through parallel imaging methods are generally limited. For multi-slice and high resolution metabolite mapping these acceleration factors will not be enough. Instead, different acceleration approaches such as compressed sensing [10] seem more suitable for this purpose as they enable higher acceleration factors without introducing structured aliasing artifacts or noise amplification in the image. The high SNR and the sparse nature of the water image makes it a perfect candidate for this purpose.

The aim of this work is to highly accelerate the acquisition of NWS reference images (up to R=28) using compressed sensing. Different acceleration factors will be explored and the accuracy of the proposed method will be evaluated by comparing the compressed-sensing accelerated NWS images to the reduced resolution approach. The reproducibility of the proposed method will also be evaluated in the context of

high resolution metabolite mapping using an ultra-short TE and TR ^{1}H FID MRSI sequence at 9.4T. The results of this study enable the acquisition of single-slice high resolution NWS reference images in about 44 seconds.

Methods

Data Acquisition

Three healthy volunteers were scanned for this study in accordance with the local ethics committee regulations. Subjects were scanned on a whole-body Siemens Magnetom 9.4T human scanner (Erlangen, Germany). An in-house developed RF head coil with 16 transmit-only and 31 receive-only coil elements [11] was used for all scans. Single-slice ^{1}H MRSI data were acquired from the brains of each of the volunteers. The slice was always positioned above the Corpus Callosum as shown in Figure 1.

Water-suppressed ^{1}H MRSI data was acquired from each subject using a slice-selective ^{1}H FID pulse sequence [3, 7] with no lipid suppression and no outer volume suppression. The water suppression scheme consisted of three pulses with an interval of 20 ms between each pulse and the flip angle were optimized for a B_1^+ range of 50% to 150% [7]. The acquisition parameters were: 64x64 matrix size; 200x200 mm field of view (FOV); 10 mm slice thickness; 8000 Hz spectral bandwidth, 1.5 ms acquisition delay, and 300 ms repetition time (TR). The water-suppressed MRSI data were all acquired fully sampled and thus the acquisition time was approximately 15 mins.

For the first subject, a fully sampled water reference was also acquired with the same matrix size as the MRSI data. The acquisition parameters for the water reference were identical to the above mentioned MRSI sequence except without the water suppression pulses. The fully sampled water reference was then retrospectively undersampled using two undersampling factors of R=14 and R=28. To efficiently exploit the high SNR and sparsity of the water signal for acceleration of the water reference scan using compressed sensing, undersampling was realized through random variable-density undersampling masks generated for each acceleration factor as shown in Figure 1. Additionally, the resolution was retrospectively reduced to a 32x32 matrix size (denoted as the "reduced resolution" water reference) for comparison and proof of concept.

To test the reproducibility of the suggested accelerated NWS reference acquisition method, two water references were acquired for each of the following two subjects: a reduced resolution water reference (4 times less spatial resolution than the MRSI data) and a randomly undersampled compressed sensing mask with the highest acceleration factor (R=28). The acquisition time was 5 minutes for the reduced resolution and 44 seconds for the compressed sensing scan.

An anatomical reference image of the slice was also acquired after each MRSI scan using a 2D FLASH sequence. The FOV and position of the image were the same as for the MRSI data. The sequence parameters were: TR = 312 ms, TE = 9 ms, flip angle = 25°.

Data Reconstruction

The randomly undersampled k-space data was reconstructed using compressed sensing optimization where the objective function consisted of a data consistency term using a norm-2 metric, a total variation term using norm-1 and a sparsity term also using a norm-1 metric. The sparsity term was a 2D 4th order Debauchy wavelet in the spatial (image) domain and the total variation term was 3D (over the two spatial domains and the time domain). The total variation and sparsity terms were calculated on the coil combined data which used coil sensitivity maps to combine and uncombine the data. The data consistency term was calculated over all four dimensions, i.e. two k-space dimensions, the time domain and the coil channels. Formally, the objectively function was, therefore:

$$\min_x \|\mathcal{F}_u x - y\|_2 + \lambda_1 \|\Psi x\|_1 + \lambda_2 \|TV(x)\|_1 \qquad (1)$$

where $\mathcal{F}_u$ is the undersampled Fourier transform, y is the measured k-space data (for data consistency), Ψ is the sparsity transform, TV is the total variation, and λ_1, λ_2 are weighting factors for the sparsity terms. The weighting factors were chosen to be $\lambda_1 = 0.001$ and $\lambda_1 = 0.003$. For every reconstruction, the k-space data were normalized so the same weighting factors could be used for different datasets.

The coil sensitivity maps used in the compressed sensing reconstruction were calculated from the anatomical scout image. ESPIRiT [12] was used to generate these coil sensitivity maps using eigenvalue decomposition. Calculating the sparsity terms on the coil combined data rather than individual coil channels can improve the reconstruction since the higher SNR of the coil combined data allows the noise-like aliasing (due to the random undersampling) to be better resolved from the measurement noise.

A conjugate gradient descent method was used to minimize the objective function and reconstruct the missing k-space data. Four iterations of the gradient descent were performed before the gradients were reinitialized and run again. Sufficient convergence was reached after four iterations of reinitialization.

The compressed sensing water reference was compared to the reduced resolution water reference image. Each water reference was used for eddy current and phase correction of the MRSI data and their effect on the final metabolite maps were compared. The MRSI data was reconstructed and post processed following the steps described in [7] which involved spatial Hanning filter, eddy current correction, SVD coil combination and HLSVD water removal. No further smoothing or apodization filtering was performed. The reconstructed spectra were fit using LCModel [13] and a basis set of 18 metabolites simulated using the GAMMA library (https://scion.duhs.duke.edu/vespa/gamma). Metabolite maps were extracted from the LCMODEL fit results for each dataset.

Data Analysis

Bland-Altman plots were generated to compare the water peak amplitude between the fully sampled NWS reference image and the compressed sensing accelerated one. For comparison the same plot was generated for the reduced resolution reference image (interpolated in the image domain to the original resolution).

Furthermore, Bland-Altman plots were generated for the major metabolites that were fit with LCModel. The metabolite concentrations resulting from eddy current and phase correction once with the reduced resolution water reference and once with the highly accelerated compressed sensing water reference were compared. The percentage difference of the reduced resolution and the compressed sensing methods were calculated for the Bland-Altman plots as:

$$d = \frac{conc_{red.res.} - conc_{CS}}{mean(conc_{CS})} \quad (2)$$

Where the subscripts $red.res.$ and cs indicate concentrations resulting from the reduced resolution versus the compressed sensing method, respectively.

Results

For proof of concept, a fully sampled water reference was acquired and compared to the compressed sensing reconstruction of the water reference (using a randomly undersampled mask with two different acceleration factors). Figure 2 shows the water references for the fully sampled data, the compressed sensing reconstruction for the two acceleration factors and the reduced resolution data from the first subject. The magnitude images show the concentration of the water signal for the coil-combined data and the phase images show the phases of the first time point for the coil-combined data. Naturally, the reduced resolution image looks like a smoother version of the fully sampled case and shows less anatomical details. The compressed sensing water image with R=28 looks similar to the reduced resolution in the amount of blurring resulting from the high acceleration factor. The R=14 accelerated

image however, shows more anatomical details and appears to have a higher spatial resolution than the highly accelerated one. All of the phase images are in good agreement to the fully sampled high resolution NWS image and are almost identical.

To quantitatively evaluate the change in the water peak amplitude resulting from compressed-sensing acceleration versus reduced resolution NWS acquisition, Bland-Altman plots comparing each of these methods to the fully sampled high resolution NWS image are shown in Figure 3. Despite the fact that the compressed sensing in this case has an acceleration factor that is more than 3 times faster than the reduced resolution, the agreement limits of the reduced resolution ($R_{effective}$=4) and compressed sensing (R=14) are similar (less than 10% for most voxels).

Figure 4 shows the acquired reduced resolution ($R_{effective}$=4) and highly accelerated compressed sensing NWS reference image (R=28) for subjects 2 and 3. Once again, a comparison of the magnitude images between the reduced resolution and compressed sensing reconstruction is very similar despite the very high acceleration factor of the compressed sensing method. The phase images look almost identical.

Each of the different water references were used for eddy current and phase correction of the MRSI data that was acquired for the respective volunteers. The resulting metabolite maps were then compared for multiple metabolites. The ratio metabolite maps (/Creatine) for three major metabolites (NAA, Glutamate and total Choline) are shown in Figure 5. Three lower concentrated metabolites, namely, GABA, Scyllo-inositol and Taurine are also shown in this figure. The metabolite maps are shown for two subjects using the reduced resolution water reference for eddy current and phase correction versus the ones using the highly accelerated compressed sensing water reference. The difference between the reduced resolution and compressed sensing for eddy current and phase correction is virtually indistinguishable in the metabolite maps.

Analysis of the degree of agreement, between using the reduced resolution and compressed sensing water references for eddy current and phase correction, was performed using Bland-Altman plots. The Bland-Altman plots for the four major metabolites are shown in Figure 6. The concentrations of metabolites with CRLBs greater than 30% were discarded. The three horizontal lines show the mean (middle line) and the agreement limits (top and bottom lines). The agreement limits are defined as $1.965 * std.dev$ from the mean. The 95% confidence intervals of the mean and the agreement limits are also shown. The detailed data from the Bland-Altman plots are given in Table I. Since there are many samples, the confidence intervals are very small. This leads to statistically significant systematic biases between the two datasets (the reduced resolution and compressed sensing data). The mean biases are 0.52% for Glutamate, -0.2% for NAA, -0.15% for Creatine and -0.45% for total Choline. The standard deviations of the differences are 2.05% for Glutamate, 1.24% for NAA, 1.95% for Creatine and 2.92% for total Choline. The plots show that for Glutamate, NAA and Creatine, 95% of the differences between the two water references fall within a ±2% interval. For total Choline, which can be more difficult to reliably quantify, 95% of the differences fall within the ±3% interval. Therefore, there is a small overestimate of Glutamate when using the reduced resolution for eddy current correction compared to compressed sensing, and there is a small underestimation of NAA, Creatine and total Choline. These biases are all smaller than 1% of the respective mean concentrations.

Discussion

The purpose of this study was to reliably accelerate the acquisition of the water reference that is often acquired for ^{1}H MRSI studies. This water reference can be used for quantification as well as phase and eddy current correction. Despite what is usually done in the field (i.e. acquiring at a reduced spatial resolution equivalent to R=4), in this study the acquisition of the water reference was highly accelerated using a random and variable density undersampling scheme with effective acceleration factors of up to R=28. Whereas for eddy current and phase correction purposes only the phase of the water reference data is of use, for internal referencing and quantification purposes the magnitude of the water reference also needs to be accurate and ideally of high spatial resolution. The results of this study show that

depending on the application, by carefully choosing the acceleration factor for the compressed sensing method, these requirements can be met to a satisfactory extent while reducing the scan time well beyond what is conventionally used in the field. This reduction of overhead scan time will be of great value for high resolution multi-slice or whole brain coverage MRSI studies.

For eddy current and phase correction purposes, a compressed sensing water reference acquisition even with a high acceleration factor of R=28 works as well as a fully sampled and high resolution water image. This is due to the fact that the spatial phase distributions are even sparser than the magnitude images. Therefore, since it is only the phase that is used for eddy current correction (and correction of the phase 0), the compressed sensing water reference with even R=28 can be used for eddy current correction without any loss of accuracy. Compared to the conventional reduced resolution water reference, this offers 7 times shorter scan time (44 seconds compared to 5 minutes).

Indeed, when the reduced resolution and the highly accelerated (R=28) compressed sensing water references are used for eddy current correction, the metabolite maps fit with LCModel (using identical settings for both) resulted in very similar maps. A visual inspection of metabolite maps for the four major metabolites shown in this paper, show that there are no perceivable differences between the metabolite concentration maps.

The Bland-Altman plots of the metabolite concentrations (using the reduced resolution and highly accelerated compressed sensing water references for eddy current and phase correction) show that there are slight systematic biases between the two methods. Due to the large number of samples, the 95% confidence intervals of statistical significance are very narrow. However, the estimated biases are approximately 0.5% or less for each of the metabolites. The differences between the concentrations are very small. The agreement limits are also quite narrow: less than ±3% for the major metabolites.

For quantification purposes, the magnitude of the water reference data is also of importance. Even though the compressed sensing accelerated water references are acquired at the same high spatial resolution as the original MRSI data, the apparent resolution after reconstruction is lower than the fully sampled case. This is a known side-effect of the compressed sensing reconstruction for very high acceleration factors. The total variation term in the compressed sensing reconstruction is known to result in some spatial smoothing. Reducing the weighting factor for this term could improve the spatial resolution of the reconstruction at the price of having less SNR. Increasing the weighting factor of the data consistency term (by decreasing the weighting factors of the two other terms) could possibly also improve the spatial resolution. Another method of improving the compressed sensing reconstruction is simply to acquire more k-space points but this, of course, increases the scan time. The results of this study show that for a compressed sensing acceleration of R=14, the accuracy of the water amplitudes are similar to that of what is usually done in the field (reduced resolution approach). However, it is important to note that the acquisition time of the compressed sensing water reference for this acceleration factor was 3.5 times shorter than the reduced resolution approach. Needless to say, a compressed sensing acquisition with an acceleration factor of less than R=14, will result in more accurate water reference images than the reduced resolution approach while still requiring less scan time.

Previously, Birch et. al [8] also made an attempt at accelerating the acquisition of the water reference images.In this work, SENSE was used to accelerate the water reference acquisition for quantification purposes. However, the MRSI data in that study was acquired at a very low spatial resolution and therefore the resulting reduced resolution water reference was very inaccurate. Another difference is that Birch et al. [8] only achieved an acceleration factor of R=3, which is reasonable for a low resolution MRSI scan however, for multi-slice high resolution MRSI studies, this will not be enough. Instead of using parallel imaging which has a limited achievable acceleration factor in practice, in this study we exploited the sparsity of the water image to achieve much higher in-plane acceleration factors.

Conclusion

In this study the acquisition of the water reference image that is often needed for MRSI studies was accelerated through compressed sensing. Acceleration factors of up to R=28 were investigated and compared to what is commonly done in the field, i.e. a reduced resolution approach (equivalent to R=4). The Bland-Altman analysis results showed that for quantification and referencing purposes an acceleration factor of R=14 results in similar accuracy as the reduced resolution approach while reducing the scan time by a factor of 3.5. For eddy current and phase correction purposes however, an acceleration factor of R=28 using the proposed method can be reliably used without any loss in accuracy. This results in an acquisition time of 44 seconds for a high resolution matrix size (64x64). This can in turn greatly reduce the overhead scan time for multi-slice high resolution metabolite mapping.

Bibliography

[1] M. Sabati, S. Sheriff, M. Gu, J. Wei, H. Zhu, P. B. Barker, D. M. Spielman, J. R. Alger and A. A. Maudsley, "Multivendor implementation and comparison of volumetric whole-brain echo-planar MR spectroscopic imaging," *Magnetic resonance in medicine,* vol. 74, no. 5, pp. 1209-1220, 2015.

[2] W. Bogner, S. Gruber, S. Trattnig and M. Chmelik, "High-resolution mapping of human brain metabolites by free induction decay 1H MRSI at 7 T," *NMR in Biomedicine,* vol. 25, no. 6, pp. 873-882, 2012.

[3] A. Henning, A. Fuchs, J. B. Murdoch and P. Boesinger, "Slice-selective FID acquisition, localized by outer volume suppression (FIDLOVS) for 1H-MRSI of the human brain at 7 T with minimal signal loss," *NMR in Biomedicine,* vol. 22, no. 7, pp. 683-696, 2009.

[4] V. O. Boer, J. C. Siero, H. Hoogduin, J. S. van Gorp, P. R. Luitjen and D. W. Klomp, "High-field MRS of the human brain at short TE and TR," *NMR in Biomedicine,* vol. 24, no. 9, pp. 1081-1088, 2011.

[5] U. Klose, "In vivo proton spectroscopy in presence of eddy currents," *Magnetic Resonance in Medicine,* vol. 14, no. 1, pp. 26-30, 1990.

[6] G. L. Chadzynski, J. Bause, G. Shajan, R. Pohmann, K. Scheffler and P. Ehses, "Fast and efficient free induction decay MR spectroscopic imaging of the human brain at 9.4 Tesla," *Magnetic resonance in medicine,* 2016.

[7] S. Nassirpour, P. Chang and A. Henning, "High and ultra-high resolution metabolite mapping of the human brain using 1 H FID MRSI at 9.4 T," *NeuroImage,* 2016.

[8] R. Birch, A. C. Peet, T. N. Arvanitis and M. Wilson, "Sensitivity encoding for fast 1H MR spectroscopic imaging water reference acquisition," *Magnetic resonance in medicine,* vol. 73, no. 6, pp. 2081-2086, 2015.

[9] K. P. Pruessman, M. Weiger, M. B. Scheidegger and P. Boesinger, "SENSE: sensitivity encoding for fast MRI," *Magnetic resonance in medicine,* vol. 42, no. 5, pp. 952-962, 1999.

[10] M. Lustig, D. Donoho and J. M. Pauly, "Sparse MRI: The application of compressed sensing for rapid MR imaging," *Magnetic resonance in medicine,* vol. 58, no. 6, pp. 1182-1195, 2007.

[11] G. Shajan, M. Kozlov, J. Hoffman, R. Turner, K. Scheffler and R. Pohmann, "A 16-channel dual-row transmit array in combination with a 31-element receive array for human brain imaging at 9.4 T," *Magnetic resonance in medicine,* vol. 71, no. 2, pp. 870-879, 2014.

[12] M. Uecker, P. Lai, M. J. Murphy, P. Virtue, M. Elad, J. M. Pauly, S. S. Vasanawala and M. Lustig, "ESPIRiT—an eigenvalue approach to autocalibrating parallel MRI: where SENSE meets GRAPPA," *Magnetic resonance in medicine,* vol. 71, no. 3, pp. 990-1001, 2014.

[13] S. W. Provencher, "Estimation of metabolite concentrations from localized in vivo proton NMR spectra," *Magnetic resonance in medicine,* vol. 30, no. 6, pp. 672-679, 1993.

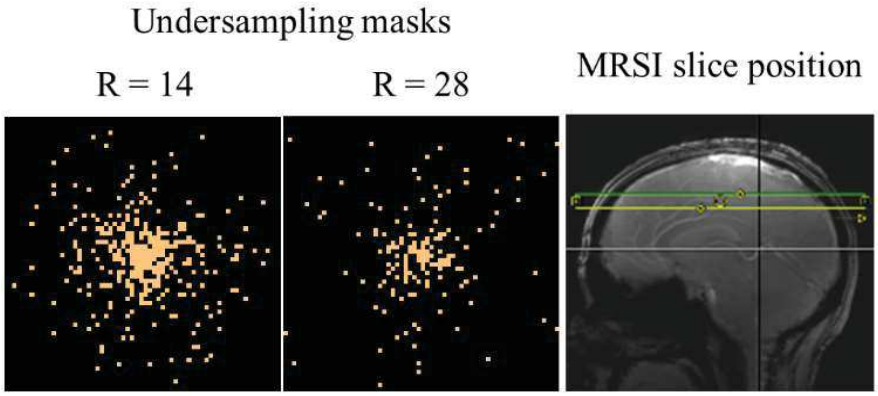

Figure 1- Right: Slice position (shown in yellow) and shim box (overlaid in green) of all MRSI scans done in this study, Left: Variable-density random k-space undersampling masks with effective undersampling factors of 14 and 28 used for compressed sensing acceleration. The acquired k-space points are shown in orange.

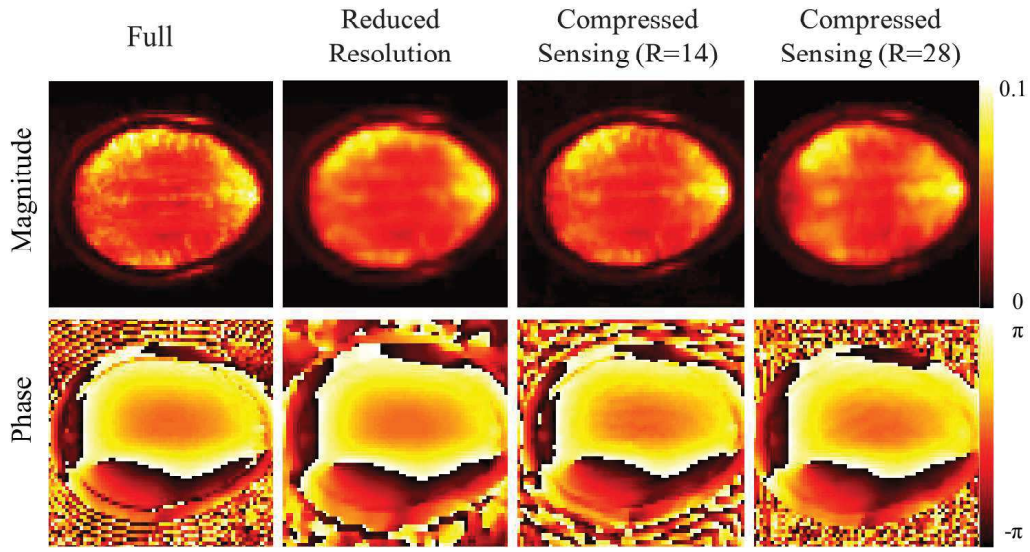

Figure 2- Comparison of the magnitude and phase of the non-water suppressed reference images acquired fully sampled at high resolution (first column), reduced spatial resolution with 2x2 times lower spatial resolution than the original MRSI scan (second column), and accelerated through compressed sensing by R=14 (third column), and R=28 (fourth column).

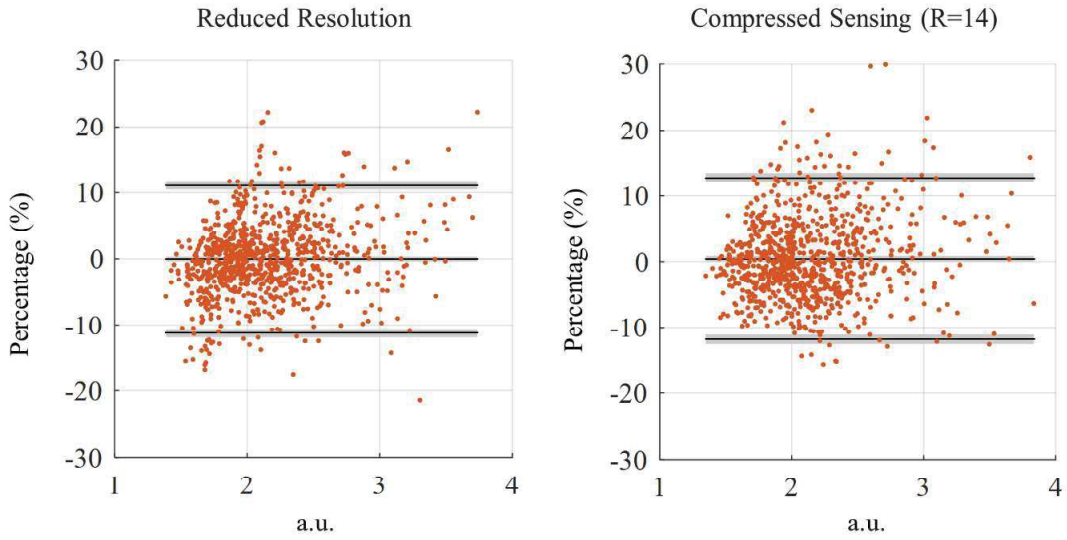

Figure 3- Bland-Altman plots showing the agreement between the fully sampled water reference image once with the reduced resolution (left) and once with the compressed sensing accelerated (right) water reference images. The y-axis shows the mean differences between water amplitudes resulting from the two methods (in percentage) and the x-axis shows the mean amplitude of water across the two methods. The limits of agreement are also indicated with black lines.

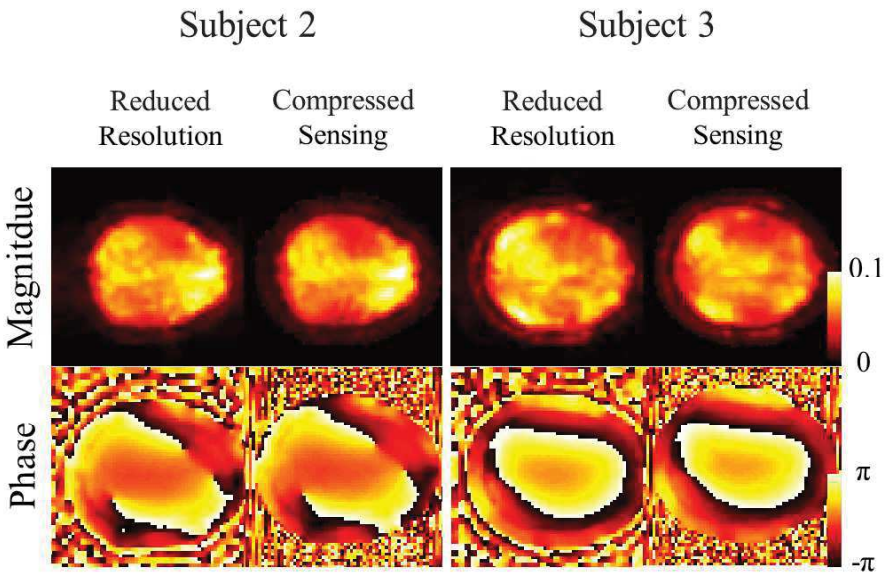

Figure 4- Reproducibility of the proposed method: comparison of the magnitude and phase of the non-water suppressed reference images acquired once at reduced spatial resolution and once with high acceleration through compressed sensing (R=28) shown for two additional volunteers.

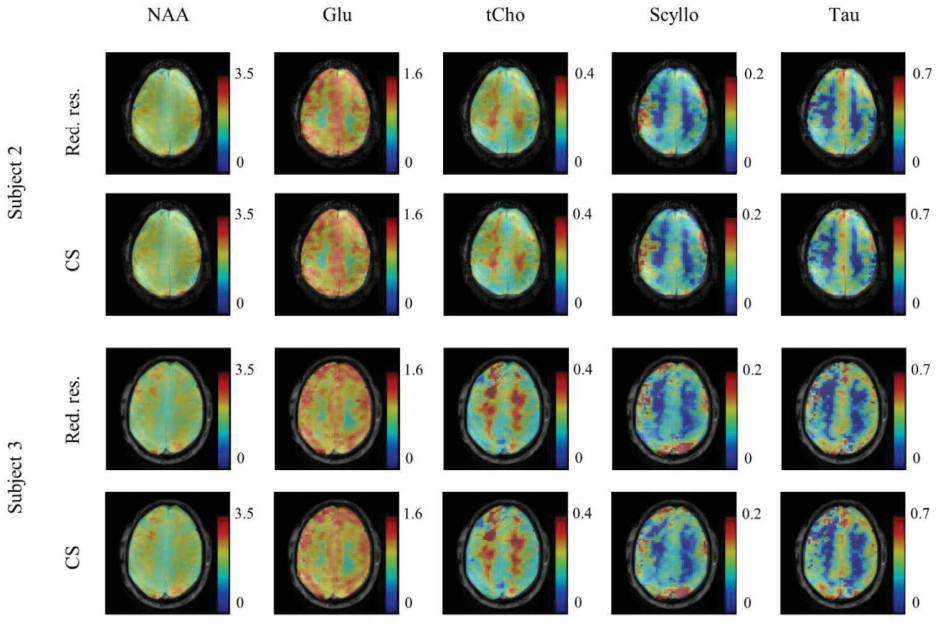

Figure 5- Comparison of eddy current and phase correction using the reduced resolution (R=4) versus compressed sensing (R=28) water reference images for metabolite mapping: ratio metabolite maps (/Creatine) of seven metabolites from two different volunteers are shown.

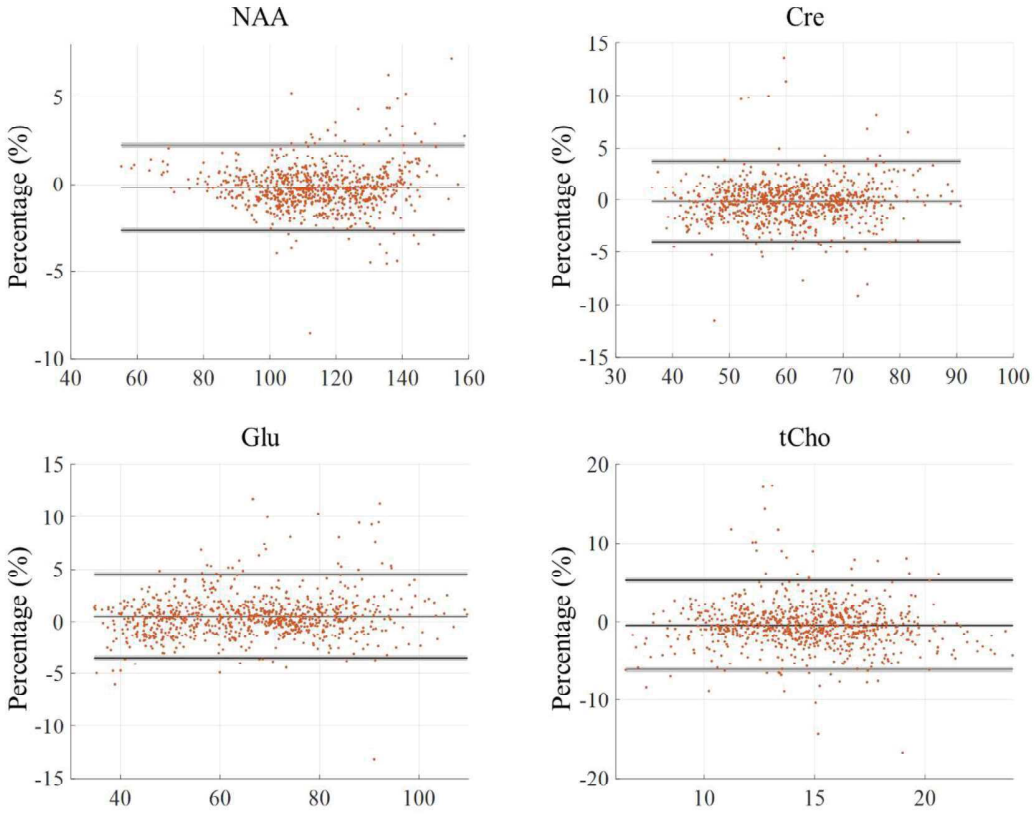

Figure 6- Bland-Altman plots for metabolite concentrations showing the agreement between the case of eddy current and phase correction using the reduced resolution (R=4) versus the compressed sensing (R=28) water reference image. The y-axis shows the mean differences between metabolite concentrations between the two cases in percentage and the x-axis shows the mean concentrations across the two methods. The limits of agreement are also indicated with black lines.

NAA					
				Confidence interval	
Parameter	Unit	Standard error	Confidence	from	to
difference mean (d)	-0.20	0.04	0.08	-0.28	-0.11
standard deviation (s)	1.24				
d-1.96s	-2.64	0.07	0.15	-2.78	-2.49
d+1.96s	2.24	0.07	0.15	2.09	2.38
Cre					
				Confidence interval	
Parameter	Unit	Standard error	Confidence	from	to
difference mean (d)	-0.15	0.07	0.13	-0.28	-0.02
standard deviation (s)	1.95				
d-1.96s	-3.98	0.12	0.23	-4.21	-3.75
d+1.96s	3.67	0.12	0.23	3.44	3.90
Glu					
				Confidence interval	
Parameter	Unit	Standard error	Confidence	from	to
difference mean (d)	0.52	0.07	0.14	0.38	0.66
standard deviation (s)	2.04				
d-1.96s	-3.45	0.12	0.24	-3.73	-3.25
d+1.96s	4.53	0.12	0.24	4.29	4.77
tCho					
				Confidence interval	
Parameter	Unit	Standard error	Confidence	from	to
difference mean (d)	-0.45	0.10	0.19	-0.65	-0.25
standard deviation (s)	2.92				
d-1.96s	-6.17	0.17	0.34	-6.52	-5.83
d+1.96s	5.27	0.17	0.34	4.92	5.61

Table 1- Bland-Altman plot statistics for the plot shown in Figure 6. For each metabolite the difference mean (d) and standard deviation (s) between the two methods are shown, along with agreement limits calculated as d±1.96s.

Publication VII

"In Vivo Whole Brain Proton Spectroscopic Imaging at 9.4T: A Focus on Dynamic Slice-wise B_0 Shimming"

P Chang*, **S Nassirpour***, A Aghaeifar, A Henning

[in preparation]

In Vivo Whole Brain Proton Spectroscopic Imaging at 9.4T: A Focus on Dynamic Slice-wise B_0 Shimming

Abstract

Purpose: To compare different B_0 shimming approaches at 9.4T and to evaluate their performance in the context of high resolution multi-slice metabolite mapping of the human brain with whole brain coverage.

Methods: Two different B_0 shimming approaches, namely, a very high degree spherical harmonic insert shim and a multi-coil system were used to perform B_0 shimming on the human brain at 9.4T. High-degree static shimming was compared to both low- and high-degree dynamic slice-wise shimming. Dynamic shimming using spherical harmonics was also compared to multi-coil slice-wise shimming. Based on the results, the optimal B_0 shim solution was used to perform whole brain metabolite mapping at 9.4T for the first time.

Results: Better B_0 homogeneity achieved through dynamic shimming using either of the shim systems resulted in a more accurate quantification of spectra. The dynamic shim quality obtained using 4^{th} degree spherical harmonics was comparable to the 16-channel multi-coil setup. The multi-coil setup was chosen for whole brain metabolite mapping study due to its more practical hardware setup, and high resolution metabolite maps acquired at 9.4T with whole brain coverage were presented.

Conclusion: Metabolite mapping at 9.4T benefits greatly from advanced B_0 shimming approaches. Dynamic shimming performed using a 4^{th} degree spherical harmonic shim system resulted in a similar quality as a 16-channel multi-coil system combined with 2^{nd} degree spherical harmonic shims. High resolution metabolite maps with whole brain coverage using the multi-coil approach show promise for the advance of MRSI at ultra-high fields.

Introduction

Proton magnetic resonance spectroscopic imaging (^{1}H MRSI) has a lot of potential for clinical applications and neuroscientific exploits. It offers a method to identify the neurochemical profile of the brain in a non-invasive manner. Spatial distributions of metabolites and amino acids, such as Glutamate and N-Acetylaspartic acid (NAA), that are involved in neurotransmission processes can be mapped using ^{1}H MRSI. Mapping metabolites in the human brain can further illuminate our understanding of how the human brain functions.

There are methods available for whole brain metabolite mapping at 3T, namely, echo-planar spectroscopic imaging (EPSI) [1] and Hadamard-encoded spectroscopic imaging [2]. While this has allowed research into metabolic function of Parkinson's disease [3] and traumatic brain injury [4], the low signal-to-noise ratio (SNR) results in poor spatial resolution and spectral specificity. Furthermore, while EPSI can be used for group studies, the low SNR means that metabolic information is often not reliable enough for single subject analysis.

In light of this, efforts have been made to perform MRSI at ultra-high field strengths, which offer super-linear increase in SNR with respect to the field strength. Single slice metabolite maps have been acquired using free induction decay (FID) MRSI at 7T [5, 6] and 9.4T [7], which showed improved metabolite maps at higher spatial resolutions.

However, despite the higher SNR and advances in ultra-high field (UHF) MRI, there are still many technical challenges that make whole brain metabolic mapping difficult. Without a spatially homogenous magnetic field, the many advantages of ultra-high field strengths cannot be fully exploited [8]. ^{1}H MRSI is, in general, very susceptible to inhomogeneities in the magnetic field and can suffer from insufficient water suppression performance [9, 10, 11], or poor quality spectra with broadened

linewidths and low signal to noise ratio (SNR) if insufficient B_0 shimming is performed. The poor quality of the spectra then directly affects the reliability of the fits for metabolite quantification and result in metabolite maps that do not fully reflect the underlying anatomy. Furthermore, B_0 inhomogeneities can affect the water suppression pulses and result in metabolites being suppressed rather than the water peak. In general, any spectrally selective pulses will be effected by B_0 inhomogeneities. Therefore, to acquire reliable metabolite maps, we need to first address the issue of B_0 inhomogeneity.

Koch et al. [11] and Boer et al. [9] addressed the issue of B_0 field inhomogeneity using dynamic B_0 slice-wise updating with a second- and third-degree spherical harmonic (SH) shim system, respectively. They showed improved spectra for multi-slice ^{1}H MRSI but did not show any metabolic maps. Pan et al. [12] used very high degree SH shim coils (up to full 4^{th} degree and partial 5^{th} and 6^{th} degree) to improve the B_0 homogeneity using a static global shim for MRSI at 7T. Again, no metabolite maps were shown.

In recent years, the B_0 shimming community has moved towards arrays of localized shim coils rather than using high degree spherical harmonic shim coils [13, 14]. The array of localized shim coils (or multi-coil system) can also be used to dynamically update the slice-wise B_0 shims of multi-slice sequences, which has been shown to be advantageous for B_0 shimming [14, 15]. While higher degree spherical harmonic shimming generally increases the homogeneity of the magnetic field over all, the multi coil setup can, depending on the design, produce local field patterns that more closely match the local inhomogeneities caused by the tissue susceptibility differences (e.g. close to the sinus air cavities) [14]. In other words, using higher degree spherical harmonics B_0 shimming systems likely provides more degrees of freedom for producing global field patterns that result in a more homogenous field distribution overall, whereas the multi-coil approach is more suited to producing locally complicated patterns.

The question of which B_0 shimming setup is optimal when imaging different regions of the brain is still a point of discussion in the field and a thorough comparison of the two methods for shimming different regions of interest is missing. Given the differences between the two shim approaches, for each MRI imaging application (depending on the focus being on a small region of the brain versus on multiple slices), a certain B_0 shim setup might be more beneficial over the other approach. Additionally, each of these shimming methods can be applied in a static or dynamic manner. While it is known that performing dynamic shim updates improves the quality of the images compared to static shimming, for some imaging applications such as 3D sequences, dynamic shim updating is not possible. Then the question is whether or not using more shim coils for static shimming can ever come close to the same shim quality as dynamic shimming (with fewer coils).

To the best of our knowledge, no previous study has directly compared the use of higher degree spherical harmonic B_0 shimming to the multi-coil approach for in-vivo human brain metabolite mapping at ultra-high fields using dynamic slice-wise B_0 shim updating.

In this work, we systemically compare the B_0 shimming quality using a very high degree SH shim system and the multi-coil approach. The two different shimming approaches were then used to acquire multi-slice MRSI data for comparison. Finally, using the optimal and most feasible B_0 shimming method, multi-slice MRSI data with whole cerebrum coverage were acquired from the human brain at 9.4T. For the first time, we present high resolution *in vivo* metabolite maps covering the whole cerebrum at ultra-high field.

Methods

Equipment

All measurements were performed on a Siemens Magnetom 9.4T whole-body human scanner (Erlangen, Germany). For all experiments, an in-house developed 18Tx/32Rx transceiver head RF coil [16] was used.

A multi-coil shim array with 16 identical circular shim coils arranged in two rows, as shown in Figure 1a, was used for the localized multi-coil (MC) B_0 shimming. The local shim coils were 100 mm in diameter and had 25 turns [17]. The multi-coil shim array was used in combination with the 1st and 2nd degree spherical harmonic shim coils from the vendor. Therefore, the system consisted of 2nd degree SH coils + 16 localized shim coils. Unless otherwise stated, any further mention of the MC shim system will refer to the 2nd degree SH coils + 16 MC coils.

An insert shim from Resonance Research Inc. (Billerica, MA) with complete 4th-degree SH shim coils and partial 5th- and 6th-degree shim coils was used for the very high-degree B_0 shimming. This insert shim system will be referred to as the very high order/degree shim (VHOS) system and is shown in Figure 1b. For a fair comparison with the MC system, only the 3rd- and 4th-degree shim coils of the insert shim were used, since this also amounts to 2nd degree SH coils + 16 VHOS SH coils. This system shall, henceforth, be denoted as the SH4 shim system. SH terms up to 2nd degree terms shall be denoted as SH2.

In this study, we investigated B_0 shimming in the human brain *in vivo* using two different approaches: very high-degree SH (up to 4th degree) shim coils and a 16 channel MC shim array. Therefore, both hardware setups used up to 2nd degree shim coils and 16 additional shim coils.

Reference Field Measurements

The reference B_0 maps produced by each of the 16 local shim coils is shown in Figure 2 [17]. These reference maps were acquired on an oil phantom and interpolated to a 1 mm isotropic resolution.

Reference field maps were also acquired for the VHOS system on a silicon oil spherical phantom. Each coil channel was driven with 0.5 A and the shim fields were measured using a 2D dual echo GRE with the following parameters: in-plane resolution = 1.56 x 1.56 mm^2; number of slices = 50; slice thickness = 4 mm (0% distance factor); FOV = 200 x 200 mm^2; TE = 4.00/4.76 ms; TR = 1200 ms; read-out bandwidth = 1500 Hz/Px. The reference shim fields were then modelled using spherical harmonic decomposition based on the Legendre functions as described in [18]. The SH shim fields for the 3rd and 4th degree terms are shown in Figure 2 (on a unit sphere in arbitrary units for illustrative purposes). Actual measured shim fields can be found in [18].

In vivo *B_0 Shimming Comparison*

To compare the quality of each of the B_0 shim setups *in vivo*, 3 healthy volunteers were scanned at 9.4T. All volunteers gave their written consent prior to the scan according to the regulations of the local ethics committee. On each volunteer B_0 field reference maps were acquired using a 2D GRE sequence with the same parameters as mentioned in the previous subsection from a 50 mm volume: 25 slices with 2 mm slice thickness (0% distance factor). The middle slice was placed above the *corpus callosum* with a transversal orientation. The two different B_0 shimming approaches (i.e. SH shimming and MC) were implemented on the volunteers as described below. Thereafter, for each shim setting, three MRSI slices were acquired: a top slice, center slice and bottom slice. Each MRSI slice had a thickness of 10 mm. Thus, each MRSI slice used 5 slices of the B_0 field reference map for shimming. The slices of the B_0 field maps and the MRSI slices are illustrated in Figure 3.

For SH B_0 shimming, we compared dynamic slice-wise B_0 shimming of both SH2 and SH4 systems on the three volunteers. The term “dynamic slice-wise” shimming and “dynamic” shimming will be used interchangeably in the remainder of this paper. In order to allow for the eddy currents to settle, a 5 second delay after each shim update was implemented in the sequence for all dynamically shimmed acquisitions in this study. Considering that even with the fastest sequence, the acquisition time for a high resolution MRSI slice is on the order of a few minutes, the effect of this delay on the total scan time was negligible. In addition, a static global SH4 B_0 shim was performed over the entire 200x200x50 mm volume for comparison as illustrated in Figure 3.

Spectroscopic imaging data were acquired for each slice and each of the shim configurations. An FID MRSI sequence without lipid or outer-volume suppression was used with the following parameters [7]: FOV = 200x200 mm^2; slice thickness = 10 mm; acquisition delay = 1.56 ms; nominal flip angle = 28°; repetition time (TR) = 300 ms; bandwidth = 4000 Hz; k-space matrix = 64x64. The flip angles and gradients of the water suppression were optimized for a range of B_1^+ values (between 50% and 150%), which was important due to the large B_1^+ inhomogeneity at 9.4T (especially at lower slices in the brain) [18]. The sequence was accelerated using elliptical shuttering and undersampling of k-space by a factor of R = 2x2 (in each phase encoding direction) except for the center 8x8 k-space points which were fully sampled. The reconstruction was performed using GRAPPA. A highly accelerated water reference spectroscopic image was also acquired for eddy current and phase correction. Further details of the processing and fitting of the spectral data and acquisition of the water reference spectra are described in the next section.

Additionally, an anatomical reference was acquired for each slice using a T_2-weighted 2D FLASH scout image (TR = 312 ms, TE = 9 ms, flip angle 25°) with the same slice position and properties as the MRSI sequence.

Therefore, the scanning procedure consisted of the following protocols:

1. Anatomical scout reference;
2. B_0 field reference maps;
3. FID MRSI on the top, middle and bottom slices with SH2 shim (slice-wise);
4. B_0 field maps of the top, middle and bottom slices with SH2 shim (slice-wise);
5. FID MRSI on the top, middle and bottom slices with SH4 shim (slice-wise);
6. B_0 field maps of the top, middle and bottom slices with SH4 shim (slice-wise);
7. FID MRSI on the top, middle and bottom slices with SH4 shim (global);
8. B_0 field maps of the top, middle and bottom slices with SH4 shim (global).

For MC B_0 shimming, we compared slice-wise dynamic B_0 shimming of SH2 to MC on the same 3 volunteers in another session. Therefore, the scanning procedure consisted of the same protocols as listed above except for steps 4 and 5 where an MC slice-wise was used and steps 7 and 8 were excluded.

Due to long scan times and different hardware setup requirements, the SH and MC measurements were conducted in different sessions. Therefore, the dynamic SH2 shims were used as references for the comparisons. The standard deviations of the B_0 field maps of each of the slices were used to evaluate the quality of the shims.

To evaluate the quality of the MRSI data acquired with different B_0 shim settings, the Cramer-Rao lower bound (CRLB) of the spectral fits as reported by LCMODEL, as well as the SNR values (calculated as the absolute peak of NAA over the root mean square of the noise) were compared.

Whole Brain Metabolite Mapping

To show the advantages of advanced B_0 shimming methods on ultra-high fields for *in vivo* metabolite mapping, the most optimal and feasible shimming method (as indicated by the results of the previous section) was used to acquire high resolution metabolite maps of the human brain with whole brain coverage at 9.4T. Three healthy volunteers were scanned for this purpose using ^{1}H MRSI.

As mentioned previously, a slice-selective ultra-short TE proton FID MRSI sequence was used to acquire the spectroscopic imaging data. For coverage over the whole cerebrum, the same sequence parameters were used as described in the previous section, except for the following changes: slice thickness = 8 mm; number of slices = 10; undersampling factor of R = 7. Therefore, the total coverage was an FOV of 200x200x80 mm in approximately 25 minutes.

Water reference MRSI spectra were acquired using a highly undersampled acceleration scheme for eddy current correction. An acceleration factor of R = 28 was achieved by randomly undersampling k-space

and reconstructing the data using compressed sensing as described in [19]. The scan duration for the water reference scan amounted to approximately 8 minutes.

The whole-brain data were acquired with slice-wise B_0 shimming using the MC setup. Again, a B_0 field reference map, from which the shim currents could be calculated, was first acquired. For practical reasons, a static global SH2 was first performed on the whole FOV, then the shim currents of the MC (only the 16 localized shim coils) were updated during the scan for each slice. The MRSI sequence was modified to enable communication with the MC shim coils using a standard user datagram protocol (UDP) [17]. The shim values were sent to the MC shim amplifiers before the beginning of each MRSI slice acquisition.

The MRSI data were then processed as previously described in [7]. LCModel [20] was used to fit the spectra and generate the metabolite maps. Again, the CRLBs and SNRs were used to evaluate the MRSI data quality.

An MP2RAGE sequence accelerated using CAIPIRINHA was used to acquire 600 um isotropic anatomical images in ~12 mins [21]. B_1^+ correction was performed on the anatomical maps using a B_1^+ map acquired using an AFI sequence [22] as described in [23].

Results

In vivo B_0 Shimming Comparison

For the first comparison, we looked at the VHOS system and compared high degree static (SH4) to both low (SH2) and high (SH4) degree dynamic B_0 shimming. The three slices with 10 mm slice thickness were evaluated. The comparison between static global shimming, dynamic slice-wise SH2 (D2) and dynamic slice-wise SH4 (D4) shimming are shown for a representative volunteer in Figure 4 (left). Clearly, the B_0 maps resulting from dynamic SH4 are much more homogeneous than dynamic SH2 for all slices with a 2 Hz improvement on the top slice and a 10 Hz improvement on both the center and bottom slices. The static global SH4 (S4) also shows some improvement over dynamic SH2, however the improvement is very small on the top slice. The figure also shows the histograms of the B_0 field distributions between -100 and 100 Hz. The histograms give a rough indication of the linewidth of the spectra acquired from the whole slice for each position and shim setting. Compared to dynamic SH2, the static SH4 and dynamic SH4 histograms have taller and thinner distributions.

In the next comparison, we looked at the difference between using a dynamic SH2 B_0 (D2) shimming and the dynamic MC (DMC) B_0 shimming for each of the slices. The results of this study are also shown for a representative volunteer in Figure 4 (right). As expected, the dynamic MC proves to be superior to dynamic SH2 on all slices. The dynamic SH2 results for this volunteer are similar to the volunteer shown for the VHOS system on the left of the same figure. However, the improvement over dynamic SH2 for the bottom slice was slightly more for dynamic SH4 than the dynamic MC (10 Hz compared to 7 Hz). The histograms, once again, show narrower linewidths for dynamic MC than dynamic SH2.

Table 1 shows the means and standard deviations of the frequency shifts in the shimmed B_0 maps averaged over all volunteers for each shim setting. The improvement from dynamic SH2 to dynamic SH4 is comparable to the improvement seen from dynamic SH2 to dynamic MC (approximately 3-4 Hz, 7-8 Hz and 8-9 Hz for the top, middle and bottom slices, respectively). This is similar to what was shown in Figure 4. The averaged standard deviations of dynamic SH2 vary slightly between the two comparisons due to different positioning of the heads mandated by the different hardware setups. Improvements can be seen on all slices for both dynamic SH4 and dynamic MC methods compared to dynamic SH2. However, the improvement is always less for the top slices compared to the center and bottom slices.

Comparison of static and dynamic shimming shows that, on average, static SH4 shimming outperforms dynamic SH2 shimming for the center and bottom slices. However, the improvement is traded-off for the homogeneity of the top slice, since the top slice of dynamic SH2 is better than the top slice of static

SH4. Furthermore, the improvement of static SH4 for the center and bottom slices is only about 4 or 5 Hz compared to the potential 8 to 9 Hz that could be achieved with dynamic SH4.

The resulting metabolite maps along with their respective Cramer-Rao lower bound (CRLB) maps for the VHOS comparisons are shown in Figure 5. The metabolite maps are shown for NAA, Glutamate and total Choline relative to the Creatine concentrations. The metabolite maps acquired from dynamic SH2 shimming are different to the maps acquired from dynamic SH4 shimming. For NAA on the bottom slice the signal dropout due to the residual B_0 inhomogenity from the nasal cavity is smaller when using dynamic SH4 than when using dynamic SH2. Also, in the CRLBs of NAA, more voxels could be reliably fit for the center and bottom slices when dynamic SH4 shimming was used. The effect of good shimming is more obvious for the Glutamate and total Choline metabolite maps. The Glutamate maps resemble the underlying anatomical structure much more closely for dynamic SH4 than SH2. This is evident in all the slices and is also reflected in the CRLB maps which have more voxels being reliably fit for the dynamic SH4 case. A similar effect can be seen for total Choline. CRLB values averaged across all volunteers are given in Table 1.

The resulting metabolite and CRLB maps for the same volunteer are shown for the MC comparisons in Figure 6. Compared to the VHOS metabolite maps, the slice position was slightly higher due to different hardware setups and the effect of the nasal cavity is less observed. Since the position was slightly higher, the metabolite maps from dynamic SH2 were already quite good for the center slice. However, we still see very good improvement of the dynamic MC over dynamic SH2 (particularly for the bottom slice). Again, the metabolite maps resemble the underlying anatomical structure better for the dynamic MC shimming, especially for Glutamate in the top and bottom slices, and for total Choline in all slices. The grey and white matter contrast is clearer in the total Choline maps for dynamic MC. Furthermore, the improved fitting is also clearly reflected in the CRLB maps for the bottom slice and the total Choline in the top slice. CRLB values averaged across all volunteers are given in Table 1.

The average (and standard deviation) CRLBs of Creatine and NAA, and the average (and standard deviation) SNR of the NAA averaged across the slice for all volunteers are summarized in Table 1 for each B_0 shim setting.

Overall, it is evident that better B_0 homogeneity not only improves the reliability of the quantification process (i.e. more voxels can be reliably fit due to higher SNR and better spectral lineshapes) but also with better B_0 shimming, the metabolite concentration maps are more reflective of the underlying anatomical structure.

Whole Brain Metabolite Mapping

The standard deviations of the shimmed B_0 field maps for each of the volunteers are shown for each slice in Table 2. These results were obtained using a global static SH2 B_0 shim in addition to slice-wise MC B_0 shim updates. It can be seen that with this shim setup, that the shim quality improves as we move away from the bottom slices (which are affected by the nasal air cavity), only to get worse as they approach the very top slices affected by the subcutaneous lipid layer.

The metabolite maps (over Creatine) for each of the slices are shown for a representative volunteer in Figure 7. The bottom- and top-most slices were omitted due to poor data quality. The metabolite maps show good gray/white matter contrast for metabolites such as Glutamate and total Choline. In Figure 8, sagittal and coronal cross sections of the metabolite maps can be seen to be in agreement with the underlying anatomical structures.

The same evaluation metrics as in the previous section were used to evaluate the quality of the MRSI data across each slice and the results are shown for all volunteers in Table 2. The SNR appears to be highest on the middle slices (where the shimming performance is the best). Overall, the SNR is sufficient for a reliable quantification of the metabolites with an average CRLB of 6.9% (±1.1%) for NAA and 9.8% (±1.1%) for Creatine across all datasets. The only exception is the two outer-most slices where the

B_0 shim quality achieved through this setup (static SH2 + dynamic MC) is still not sufficient for reliable quantification of the spectroscopy data.

Discussion

In vivo B_0 Shimming Comparison

The goal of this work was to provide further insight into the benefits of two different B_0 shimming concepts, namely very high degree SH and MC shimming setups, for performing B_0 shimming in the human brain at 9.4T.

The two B_0 shim setups were compared *in vivo* for dynamic slice-wise shimming by evaluating the B_0 field maps and spectroscopic imaging data. In addition, performing global shimming over the whole imaging volume (static SH4 shimming) was compared to performing dynamic slice-wise shim updating. In all cases dynamic slice-wise shim updating using SH2 shims was taken as a benchmark. The results showed that including more degrees of spherical harmonic (SH4) while performing static shimming improves the quality of the shim overall. The results showed that when it is not possible to perform dynamic slice-wise B_0 shimming (due to lack of driving hardware/software or due to acquisition sequence limitations), one can still achieve reasonable shim quality by including higher degree SH and performing global static shimming.

Alternatively, the shim quality can be further improved by performing dynamic shim updates using either the SH4 or MC systems. Unsurprisingly, this proves to always be consistently advantageous over dynamic SH2 shimming. The amount of improvement gained from going to higher degree SH versus including a MC design was comparable to each other for similar slice positions. The highest improvement was seen on inferior slice positions, where due to the susceptibility difference between the air in the nasal cavities and the brain tissue, severe B_0 inhomogeneities are present. This has also been confirmed before for the case of dynamic SH shimming by Koch et al. [11], Boer et al [9], and Pan et al [12].

It is well known that the quality of B_0 shimming directly affects the quality of the acquired spectra in MRSI applications [11, 12]. This can be due to the fact that as a result of lower local B_0 inhomogeneity, the spectral lines are sharper and the SNR is higher, which means that quantification is much more accurate. Additionally, the quality of water suppression is affected by B_0 inhomogeneity. In regions with high residual B_0 distortion, the water suppression will fail, leaving a strong residual water peak that will distort the quantification of the metabolites of interest. High resolution metabolite maps acquired with the two improved B_0 shim setups of this study further highlight the advantages of these advanced shim setups compared to dynamic slice-wise SH2 shimming. Qualitatively speaking, the maps acquired with dynamic SH4 shimming and dynamic MC shimming are similar. In all cases however, the maps look much more accurate than only performing dynamic SH2 shimming as they reflect the underlying anatomy much better. The white/gray matter contrasts are much clearer and the confidence in fits are higher as a result of improved B_0 shimming. The positioning of the slices between the datasets shown in Figure 5 and 6 are somewhat different, since the experiment was conducted in two different session with two different hardware setups and positioning limitations. The slice positions shown in Figure 5 are lower than in Figure 6, this could explain the less reliable fits (higher CRLBs) and noisier metabolite maps for the dynamic SH4 shimming than for the dynamic MC shimming results.

Additionally, the physical weight of the VHOS system when inserted into the bore, adversely affected the quality of the acquired MRSI data by shifting the frequency of the gradient modulation sidebands closer to the spectral range of interest. These modulation sidebands appear as spurious peaks in the acquired spectra as a result of the acoustic resonation of the gradient system. It was observed that by additional weight of the VHOS system to the exam table (~100 Kg), the sidebands were shifted to a lower frequency which resulted in the spurious peaks to overlap with the NAA peak. Since the NAA peak is often used as the reference for the fitting algorithm, the quality of the fits and the resulting maps were affected by the confound effect of this overlap. Given that the multi-coil setup is much lighter in

weight, such effect was not observed when using the MC shim system. This could further explain the less reliable fits for the dynamic SH4 shimming than for the dynamic MC shimming results.

It should further be noted that, even though the results of this study show that for multi-slice imaging in the brain at 9.4T, both the multi-coil plus 2nd degree spherical harmonics setup and the 4th degree spherical harmonics setup perform comparably well, the manufacturing of the local shim coils are in practice much easier than the higher degree SH. The requirements on manufacturing shim coils to generate spherical harmonic functions over a large spatial region are much more demanding than building local shim coils. Furthermore, SH shim coils are more prone to eddy currents due to their large inductance [18], while the local shim coils are smaller and have much less eddy currents that may be induced due to switching gradient or shim currents [24]. Using SH shim coils for dynamic B_0 shim updating often requires pre-emphasis and calibration of the system [9, 14, 25, 26] while the MC does not.

As a result of the limitations described above, for the whole-brain MRSI study of this work, we chose the more practical MC B_0 shimming setup.

Whole Brain Metabolite Mapping

Due to the practical hardware limitations of the system, the B_0 shimming for the whole brain study was performed using a static global SH2 shim along with the MC system which was used for dynamic shim updates. In comparison, the previous section where the SH2 shim coils were also dynamically slice-wise updated would result in slightly better B_0 homogeneity. Nevertheless, good metabolite maps could be acquired for major metabolites at high resolution with a coverage over the whole cerebrum. This is the first time that metabolite maps with such coverage have been shown at 9.4T.

The spectra from the very low or very high slices of the brain could not be reliably fit due to poor B_1 coverage and insufficient B_0 homogeneity. The hot spots in the low slices near the anterior of the brain result from signal dropout due to poor B_0 homogeneity. This is a common problem for B_0 shimming since this is close to the nasal cavity [15, 17, 27]. Therefore, for better brain coverage for whole brain metabolite mapping, we firstly need high SNR and transmit coverage from the RF coil which needs to be available for inferior positions in the brain, and secondly, we need B_0 shimming that can adequately compensate for the B_0 inhomogeneity caused by the nasal cavity. B_0 shimming can be improved for the multi-coil array by optimizing the positions of the coil loops [28] and shapes of the coils [29]. In general, there is still a need for better B_0 shimming techniques for UHF MRI [8].

Conclusion

In this study, we compared the performance of a very high degree spherical harmonic B_0 shim system to a 16-channel multi-coil setup for B_0 shimming of the human brain at 9.4T. The two different B_0 shimming approaches were compared *in vivo* for a slice-wise dynamically shimmed multi-slice MRSI application. High resolution metabolite maps were acquired from three slices across the human brain using each of the B_0 shimming methods. Both methods showed substantial advantages over low degree (up to 2nd) spherical harmonic dynamic shimming. The results emphasize the importance of slice-wise B_0 shimming for metabolite mapping at ultra-high fields and suggest that either of the two B_0 shimming approaches can be used to achieve similar results. However, given the practical limitations associated with the manufacturing of the VHOS system, the multi-coil system was chosen to perform whole-brain metabolite mapping of the human brain. For the first time, high resolution metabolite maps with high coverage of the human brain acquired at 9.4T are presented.

References

[1] A. A. Maudsley, C. Domenig, V. Govind, A. Darkazanli, C. Studholme, K. Arheart and C. Bloomer, "Mapping of brain metabolite distributions by volumetric proton MR spectroscopic imaging (MRSI).," *Magnetic Resonance in Medicine,* vol. 61, no. 3, pp. 548-559, 2009.

[2] O. Cohen, A. Tal and O. Gonen, "Three-Dimensional Hadamard-Encoded Proton Spectroscopic Imaging in the Human Brain Using Time-Cascaded Pulses at 3 Tesla," *Magnetic Resonance in Medicine,* vol. 72, pp. 923-933, 2014.

[3] B. E. Levin, H. L. Katzen, A. Maudsley, J. Post, C. Myerson, V. Govind, F. Nahab, B. Scanlon and A. Mittel, "Whole-Brain Proton MR Spectroscopic Imaging in Parkinson's Disease," *Journal of Neuroimaging,* vol. 24, no. 1, pp. 39-44, 2014.

[4] V. Govind, S. Gold, K. Kaliannan, G. Saigal, S. Falcone, K. L. Arheart, L. Harris, J. Jagid and A. A. Maudsley, "Whole-brain proton MR spectroscopic imaging of mild-to-moderate traumatic brain injury and correlation with neuropsychological deficits," *Journal of neurotrauma,* vol. 27, no. 3, pp. 483-496, 2010.

[5] A. Henning, A. Fuchs, J. B. Murdoch and P. Boesiger, "Slice-selective FID acquisition, localized by outer volume suppression (FIDLOVS) for 1H-MRSI of the human brain at 7 T with minimal signal loss," *NMR in Biomedicine,* vol. 22, no. 7, pp. 683-696, 2009.

[6] W. Bogner, S. Gruber, S. Trattnig and M. Chmelik, "High-resolution mapping of human brain metabolites by free induction decay 1H MRSI at 7 T," *NMR in Biomedicine,* vol. 25, no. 6, pp. 873-883, 2012.

[7] S. Nassirpour, P. Chang and A. Henning, "High and ultra-high resolution metabolite mapping of the human brain using 1 H FID MRSI at 9.4 T," *NeuroImage,* 2016.

[8] J. P. Stockmann and L. L. Wald, "In vivo B0 field shimming methods for MRI at 7 T," *NeuroImage,* vol. 168, pp. 71-87, 2018.

[9] V. O. Boer, D. W. Klomp, C. Juchem, P. R. Luijten and R. A. de Graaf, "Multislice 1H MRSI of the Human Brain at 7T using Dynamic B0 and B1 Shimming," *Magnetic Resonance in Medicine,* vol. 68, pp. 662-670, 2012.

[10] P. Chang, S. Nassirpour and A. Henning, "Modeling real shim fields for very high degree (and order) B0 shimming of the human brain at 9.4T," *Magnetic Resonance in Medicine,* 2017.

[11] K. M. Koch, L. I. Sacolick, T. W. Nixon, S. McIntyre, D. L. Rothman and R. A. de Graaf, "Dynamically Shimmed Multivoxel1H Magnetic ResonanceSpectroscopy and Multislice Magnetic ResonanceSpectroscopic Imaging of the Human Brain," *Magnetic Resonance in Medicine,* vol. 57, pp. 587-591, 2007.

[12] J. W. Pan, K.-M. Lo and H. P. Hetherington, "Role of Very High Order and Degree B0 Shimming for Spectroscopic Imaging of the Human Brain at 7 Tesla," *Magnetic Resonance in Medicine,* vol. 68, pp. 1007-1017, 2012.

[13] C. Juchem, T. W. Nixon, S. McIntyre, D. L. Rothman and R. A. de Graaf, "Magnetic field homogenization of the human prefrontal cortex with a set of localized electrical coils," *Magnetic Resonance in Medicine,* vol. 63, no. 1, pp. 171-180, 2010.

[14] C. Juchem, T. W. Nixon, S. McIntyre, V. O. Boer, D. L. Rothman and R. A. de Graaf, "Dynamic multi-coil shimming of the human brain at 7 T," *Journal of Magnetic Resonance,* vol. 212, pp. 280-288, 2011.

[15] J. P. Stockmann, T. Witzel, B. Keil, J. R. Polimeni, A. Mareyam, C. LaPierre, K. Setsompop and L. L. Wald, "A 32-Channel Combined RF and B0 Shim Array for3T Brain Imaging," *Magnetic Resonance in Medicine,* vol. 75, pp. 441-451, 2016.

[16] N. Avdievitch, I. A. Giapitzakis and A. Henning, "Combined Surface Loop/"Vertical" Loop Element Improve Receive Performance of a Human Head Transceiver Array at 9.4T: an Alternative to Surface Loop/Dipole Antenna Combination," *NMR in Biomedicine,* 2017.

[17] A. Aghaeifar, C. Mirkes, J. Bause, T. Steffen, N. Avdievitch, A. Henning and K. Scheffler, "Dynamic B0 shimming of the human brain at 9.4 T with a 16-channel multi-coil shim setup," *Magnetic Resonance in Medicine,* 2018.

[18] P. Chang, S. Nassirpour and A. Henning, "Modeling real shim fields for very high degree (and order) B0 shimming of the human brain at 9.4 T," *Magnetic Resonance in Medicine,* 2017.

[19] S. Nassirpour, P. Chang and A. Henning, "Highly Accelerated Water Reference Acquisition for 1H MRSI using Compressed Sensing," *Magnetic Resonance in Medicine.*

[20] S. W. Provencher, "Estimation of metabolite concentrations from localized in vivo proton NMR spectra," *Magnetic resonance in medicine,* vol. 30, no. 6, pp. 672-679, 1993.

[21] J. Bause, E. Philipp, G. Shajan, R. Pohmann and K. Scheffler, "Whole brain MPRAGE with 550 µm isotropic resolution in 9 minutes at 9.4 T," in *ISMRM Ultra high field workshop*, Heidelberg, 2016.

[22] V. L. Yarnykh, "Actual Flip-Angle Imaging in the Pulsed Steady State: A Method for Rapid Three-Dimensional Mapping of the Transmitted Radiofrequency Field," *Magnetic Resonance in Medicine,* vol. 57, pp. 192-200, 2007.

[23] G. E. Hagberg, J. Bause, T. Ethofer, P. Ehses, T. Dresler, C. Herbert, R. Pohmann, G. Shajan, A. Fallgatter, M. A. Pavlova and K. Scheffler, "Whole brain MP2RAGE-based mapping of the longitudinal relaxation time at 9.4T," *NeuroImage,* vol. 144, pp. 203-216, 2017.

[24] C. Juchem, S. U. Rudrapatna, T. W. Nixon and R. A. de Graaf, "Dynamic multi-coil technique (DYNAMITE) shimming for echo-planar imaging of the human brain at 7 Tesla," *Neuroimage,* vol. 105, pp. 462-472, 2015.

[25] S. J. Vannesjo, Y. Duerst, L. Vionnet, B. E. Dietrich, M. Pavan, S. Gross, C. Barmet and K. P. Pruessmann, "Gradient and shim pre-emphasis by inversion of a linear time-invariant system model," *Magnetic Resonance in Medicine,* vol. 78, pp. 1607-1622, 2017.

[26] A. Fillmer, S. J. Vannesjo, M. Pavan, M. Scheidegger, K. P. Pruessmann and A. Henning, "Fast Iterative Pre-Emphasis Calibration Method EnablingThird-Order Dynamic Shim Updated fMRI," *Magnetic Resonance in Medicine,* vol. 75, pp. 1119-1131, 2016.

[27] C. Juchem and R. A. de Graaf, "B0 magnetic field homogeneity and shimming for in vivo magnetic resonance spectroscopy," *Analytical Biochemistry,* vol. 529, pp. 17-29, 2017.

[28] J. Stockmann, B. Guerin and L. L. Wald, "Improving the efficiency of integrated RF-shim arrays using hybrid coil designs and channel placement and compression via a genetic algorithm," in *International Society for Magnetic Resonance in Medicine*, Singapore, 2016.

[29] I. Zivkovic, C. Mirkes and K. Scheffler, "B0 Shimming at 9.4T using a Multicoil Approach - Coil Design with Genetic Algorithm," in *International Society for Magnetic Resonance in Medicine*, Singapore, 2016.

[30] S. Nassirpour, P. Chang and A. Henning, "MultiNet PyGRAPPA: Multiple Neural Networks for Reconstructing Variable Density GRAPPA (a 1H FID MRSI Study)," *NeuroImage.*

[31] M. Bydder, G. Hamilton, T. Yokoo and C. B. Sirlin, "Optimal phased-array combination for spectroscopy," *Magnetic Resonance Imaging,* vol. 24, no. 6, pp. 847-850, 2008.

[32] U. Klose, "In vivo proton spectroscopy in presence of eddy currents.," *Magnetic Resonance in Medicine,* vol. 14, no. 1, pp. 26-30, 1990.

[33] S. A. Smith, T. O. Levante, B. H. Meier and R. R. Ernst, "Computer Simulations in Magnetic Resonance. An Object Oriented Programming Approach," *Journal of Magnetic Resonance, Series A,* vol. 106, no. 1, pp. 75-105, 1994.

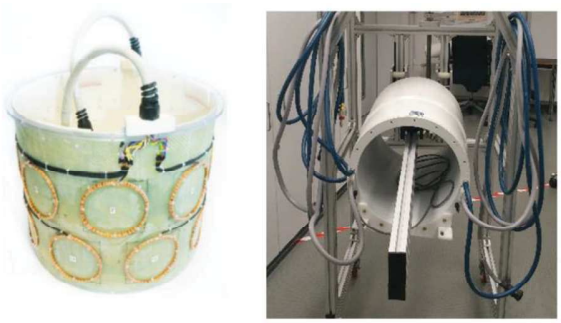

Fig. 1 (a) Localized multi-coil array and (b) the very high degree spherical harmonic insert shim array.

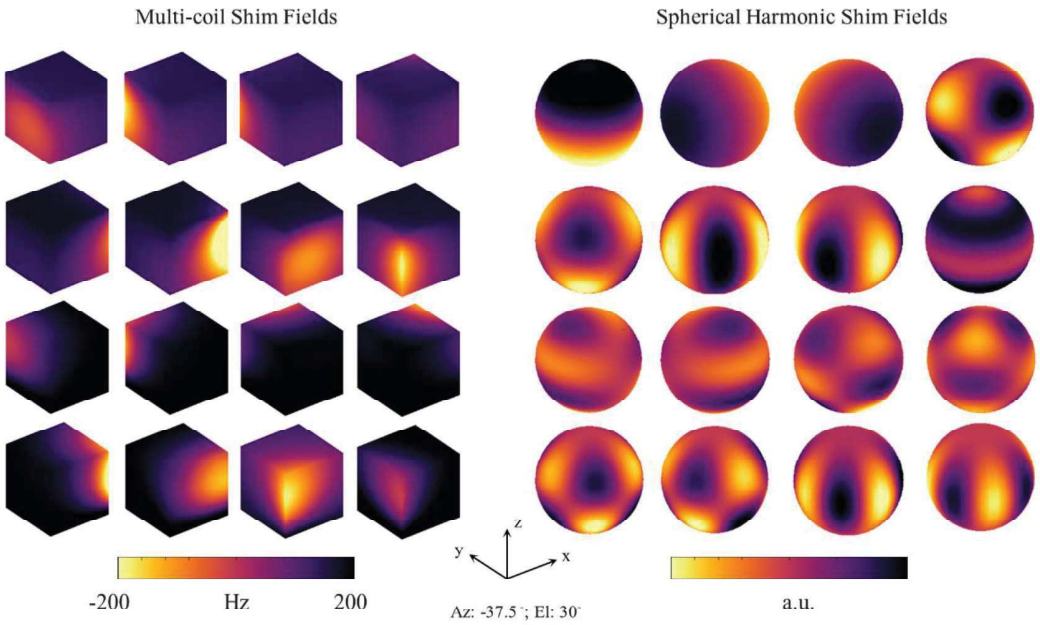

Fig. 2 (Left) Magnetic fields generated by each coil element of the MC shim array and (right) magnetic fields generated by the 3rd and 4th degree SH (on a unit sphere for illustrative purposes).

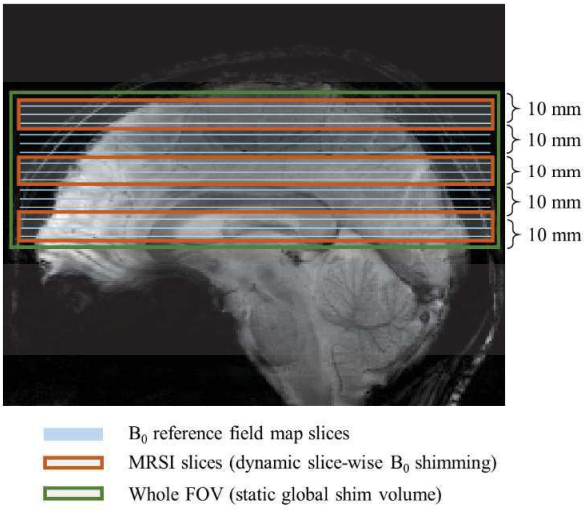

Fig. 3 Illustration of the slice placement for the top, middle and bottom slices of the MRSI data and the corresponding slices of the B_0 reference maps. The FOV used for global shimming is also shown.

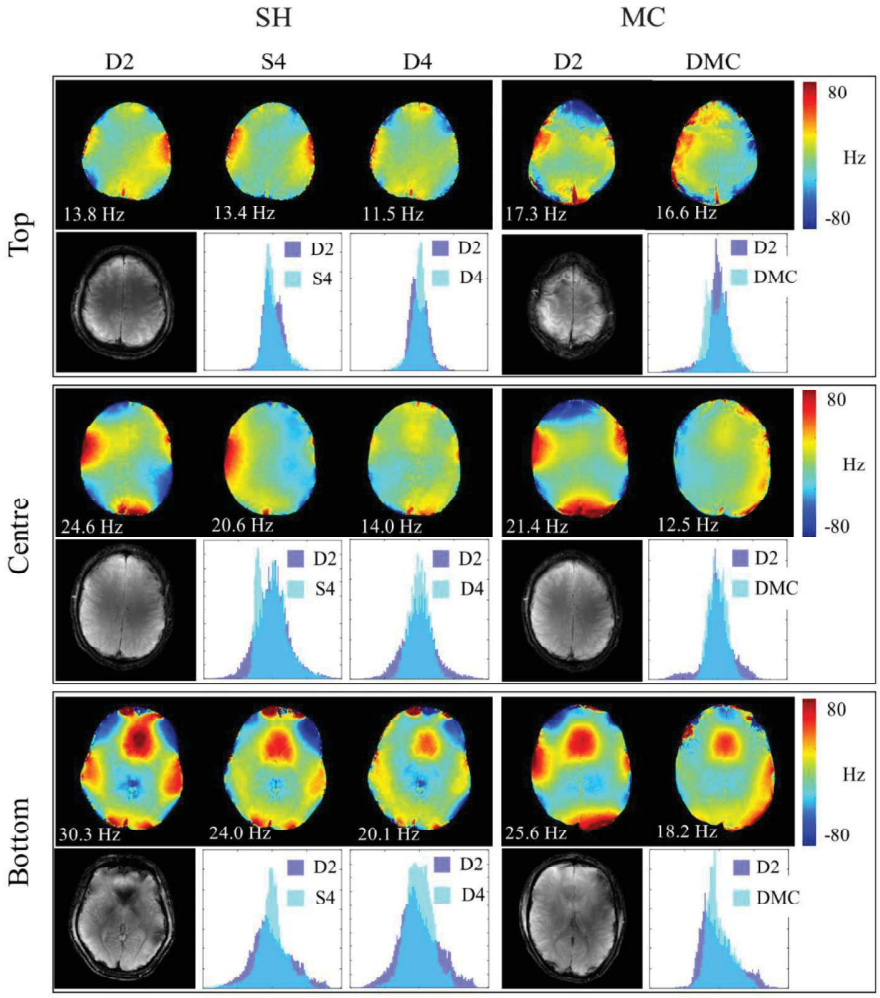

Fig. 4 B_0 fields and histograms after shimming with the global SH (S4) and dynamic SH (D4) with dynamic 2nd degree shimming as a reference (D2). Also, B_0 fields and histograms after dynamic slice-wise shimming with the MC shim array (DMC) with the dynamic 2nd degree shimming as a reference (D2).

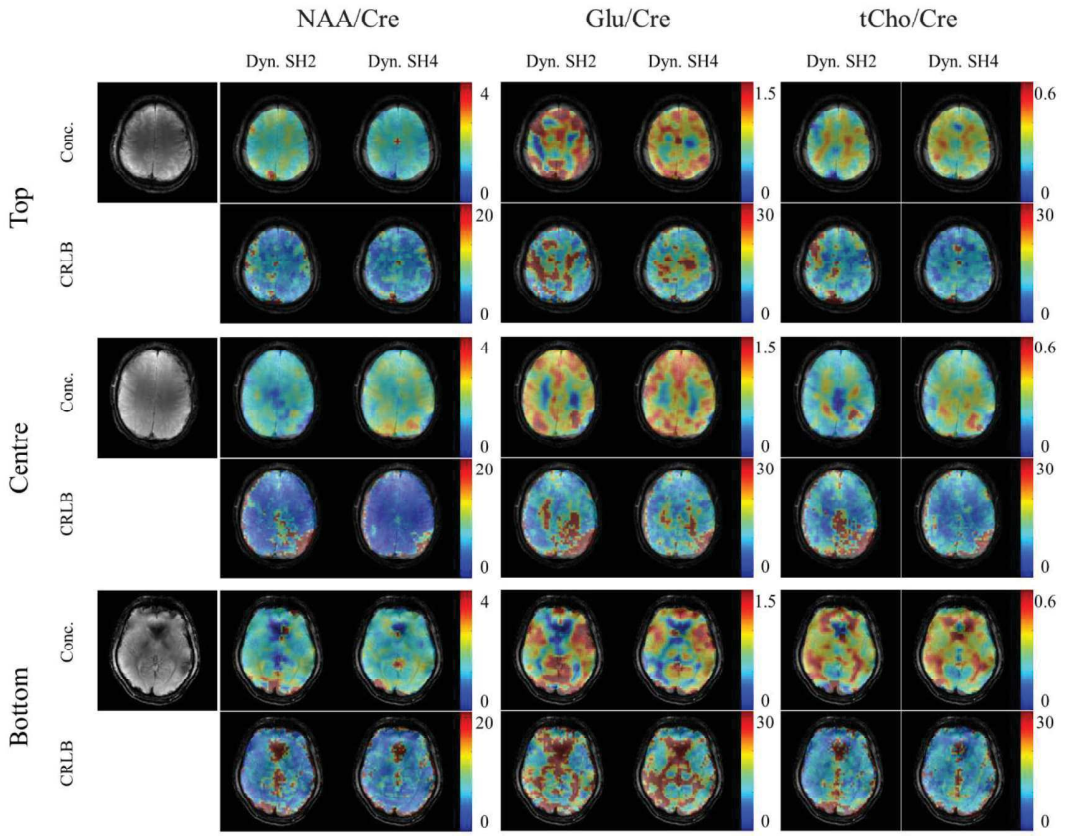

Fig. 5 Metabolite maps for NAA, Glutamate and total Choline (over Creatine) using SH shimming. CRLB maps are also shown (note: this are not shown over Creatine and are only shown for the corresponding metabolites: NAA, Glutamate and Choline). Dynamic slice-wise shimming using up to 2nd degree SH shim terms and also using up to 4th degree SH shim terms are shown for comparison.

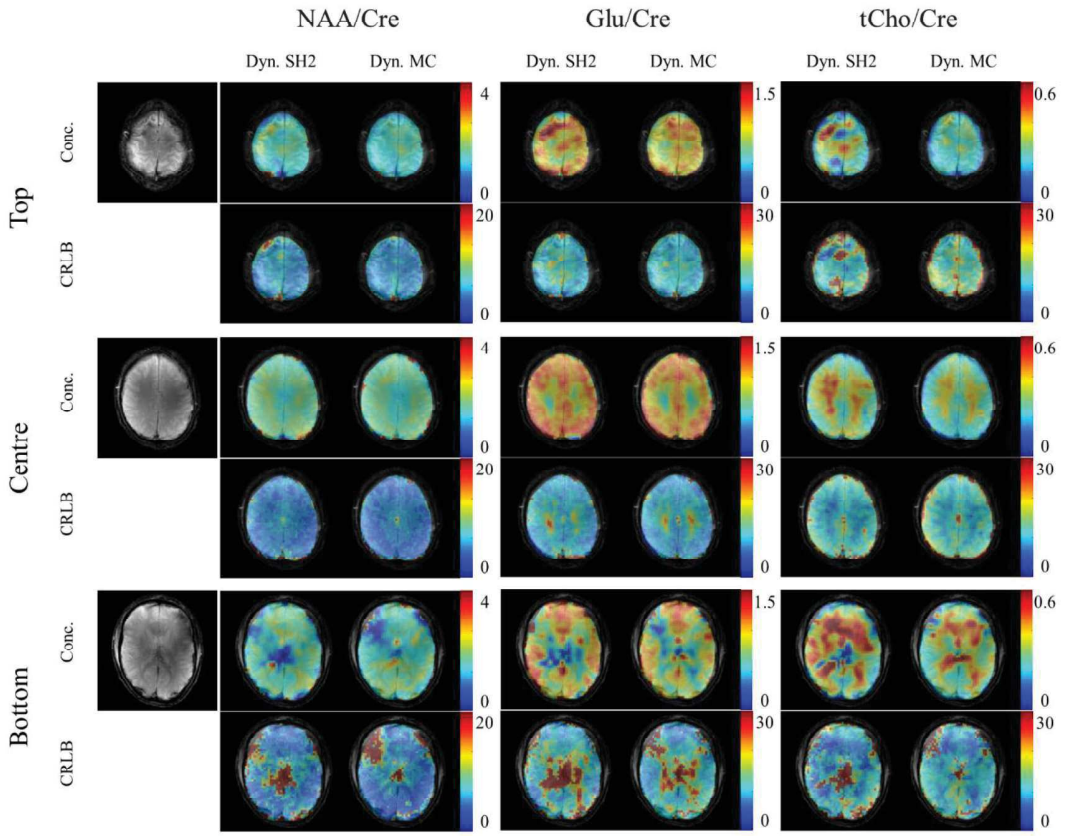

Fig. 6 Metabolite maps for NAA, Glutamate and total Choline (over Creatine). CRLB maps are also shown (note: this are not shown over Creatine and are only shown for the corresponding metabolites: NAA, Glutamate and Choline). Dynamic slice-wise shimming using up to 2nd degree SH shim terms are shown as a reference and compared to using dynamic slice-wise MC shimming.

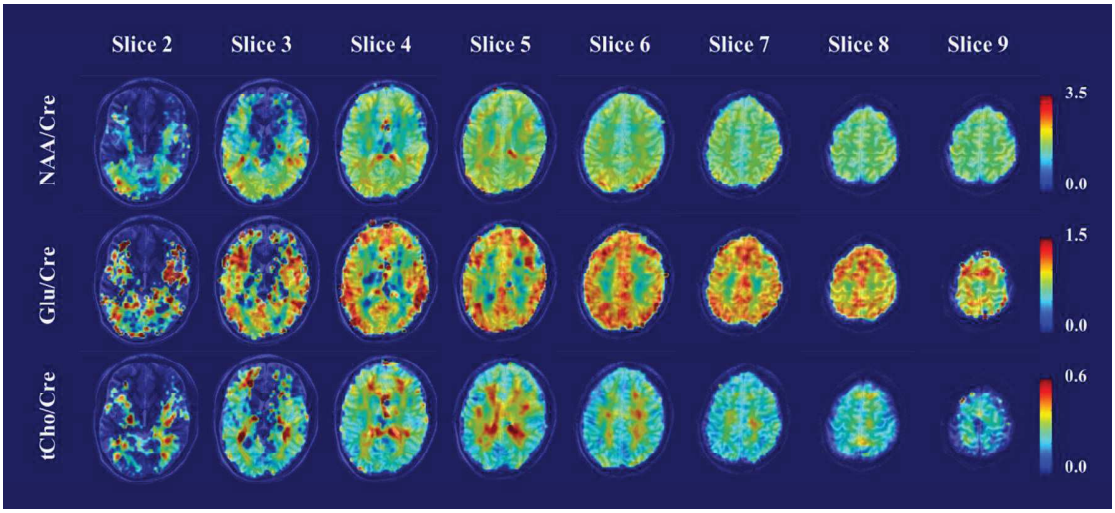

Fig. 7 Whole brain metabolite maps for NAA, Glutamate and total Choline (over Creatine). Slice 1 and 10 omitted due to poor data quality.

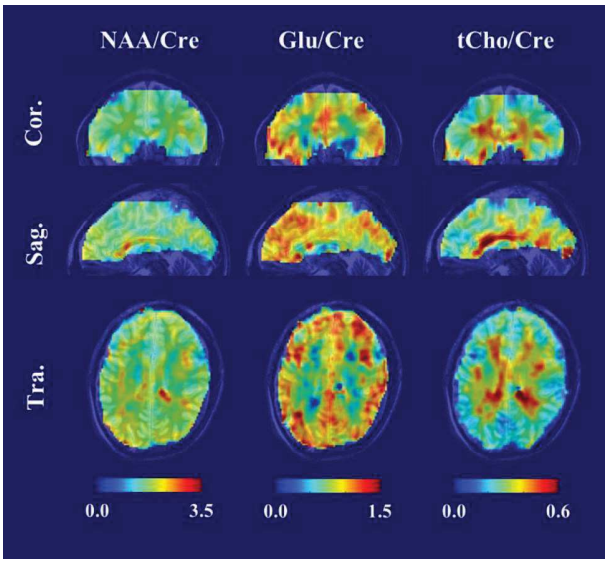

Fig. 8 Whole brain metabolite maps for NAA, Glutamate and total Choline (over Creatine) shown in the coronal, sagittal and transverse orientations.

Table 1 Comparison of the standard deviation of the B_0 maps, CRLBs of Creatine and NAA, and SNR of NAA for MC shimming and SH shimming averaged across three volunteers.

	SH			MC	
δB_0 (Hz)	**D2**	**S4**	**D4**	**D2**	**DMC**
Top	12.7 ± 2.1	13.6 ± 1.6	10.6 ± 2.4	18.1 ± 1.4	14.2 ± 3.8
Centre	22.3 ± 3.5	18.7 ± 2.6	14.5 ± 2.2	19.4 ± 1.4	12.7 ± 2.1
Bottom	29.6 ± 4.4	25.4 ± 4.0	20.5 ± 3.3	27.0 ± 1.8	19.4 ± 3.0
CRLB (Cre)					
Top	10.3 ± 1.5	-	9.4 ± 1.3	8.5 ± 1.7	7.7 ± 1.0
Centre	8.6 ± 1.4	-	8.2 ± 1.2	8.3 ± 1.2	7.0 ± 0.7
Bottom	9.1 ± 1.7	-	8.1 ± 1.5	9.2 ± 1.9	8.2 ± 1.5
CRLB (NAA)					
Top	7.0 ± 1.6	-	6.8 ± 1.5	6.2 ± 1.9	5.8 ± 1.4
Centre	6.0 ± 1.7	-	5.7 ±1.4	5.0 ± 1.0	4.7 ± 0.8
Bottom	7.0 ± 1.9	-	6.5 ± 1.6	5.8 ± 2.2	5.3 ± 2.0
SNR					
Top	34 ± 9	-	39 ± 11	41 ± 10	43 ± 10
Centre	42 ± 10	-	49 ± 12	51 ± 15	60 ± 16
Bottom	27 ± 11	-	34 ± 10	36 ± 14	40 ± 13

Table 2 Comparison of the standard deviation of the B_0 maps, CRLBs of Creatine and NAA, and SNR of NAA for whole brain MRSI using global 2nd degree shimming + dynamic slice-wise MC shimming for three volunteers.

	Slice #									
	1	**2**	**3**	**4**	**5**	**6**	**7**	**8**	**9**	**10**
δB_0 (Hz)										
Subject 1	60.98	44.60	23.98	11.86	10.99	13.43	11.05	9.10	13.34	19.00
Subject 2	66.67	46.70	25.50	14.20	9.33	8.60	13.84	11.19	14.95	21.38
Subject 3	60.47	56.23	36.28	23.96	15.43	12.66	8.84	9.79	12.70	28.00
CRLB (Cre)										
Subject 1	-	12.0±2.2	11.5±1.9	11.3±1.8	9.6±1.8	9.2±1.6	9.4±1.5	10.1±1.4	9.9±1.8	-
Subject 2	-	11.8±2.4	11.1±2.0	10.4±1.9	9.7±1.7	8.7±1.3	8.7±1.1	9.2±1.2	9.3±1.3	-
Subject 3	-	11.0±1.9	10.5±2.1	10.6±2.0	8.7±1.8	8.3±1.4	8.3±1.1	8.0±1.0	10.2±1.8	-
CRLB (NAA)										
Subject 1	-	8.7±2.2	7.7±2.4	7.1±1.8	7.0±1.4	6.4±1.3	6.7±1.1	7.0±1.3	8.6±2.3	-
Subject 2	-	9.1±2.6	7.9±2.4	7.1±1.9	6.4±1.4	5.9±1.0	5.8±1.1	6.4±1.3	7.2±1.8	-
Subject 3	-	7.7±2.8	6.9±2.6	7.6±2.0	6.0±1.0	5.2±0.9	5.1±1.1	5.3±0.8	7.9±2.0	-
SNR										
Subject 1	-	15.4±3.6	25.3±5.2	31.3±5.3	37.0±4.8	39.6±3.5	35.2±3.5	27.2±2.2	27.0±5.2	-
Subject 2	-	14.1±2.9	21.2±5.1	27.7±4.9	32.17±4.4	41.2±5.3	37.7±4.3	31.0±2.5	30.5±4.8	-
Subject 3	-	19.0±3.0	24.2±4.8	33.3±5.8	33.8±5.1	45.3±4.4	39.1±3.6	34.3±3.7	32.2±4.7	-